University of Alberta

Design and Microfabrication of Robust and Highly Integrated Thermal Lab-On-A-Chip Polymeric Systems for Genetic Diagnosis

by

Jose Martinez-Quijada

A thesis submitted to the Faculty of Graduate Studies and Research
in partial fulfillment of the requirements for the degree of

Doctor of Philosophy
in
Microsystems and Nanodevices

Department of Electrical and Computer Engineering

©Jose Martinez-Quijada
Spring 2014
Edmonton, Alberta

Permission is hereby granted to the University of Alberta Libraries to reproduce single copies of this thesis and to lend or sell such copies for private, scholarly or scientific research purposes only. Where the thesis is converted to, or otherwise made available in digital form, the University of Alberta will advise potential users of the thesis of these terms.

The author reserves all other publication and other rights in association with the copyright in the thesis and, except as herein before provided, neither the thesis nor any substantial portion thereof may be printed or otherwise reproduced in any material form whatsoever without the author's prior written permission.

Abstract

The lab-on-chip (LOC) technology could transform and greatly enhance the health care system by making genetic diagnosis tests fast, accurate and readily accessible. However, most LOC systems are not prepared to resist variations of their external environment, as they depend upon many uncontrollable boundary variables. This dependence causes alterations of the temperature profile of the system. In critical applications that require precise temperature control, such as genetic diagnosis for disease detection, or in portable devices in which adequate thermal isolation is difficult to provide, those alterations degrade the reliability of the system. Expensive infrastructure is then required to maintain repeatable external conditions. Moreover, costly and invasive calibration methods are required to estimate the true temperature in the system. These challenges prevent the cost-effective manufacture of LOC systems.

We have developed a new thermal control technology to produce manufacturable LOC systems. In this approach, the system depends upon a single dominant external variable that can be easily controlled, making the system robust to all other external variables. Operation in uncontrolled environments with minimum infrastructure is then feasible. With this concept we built a LOC system for genetic amplification in a new polymer chip architecture. In this system a thin film heater that is also a sensor is highly integrated to the reaction chamber. This integration plus the homogeneous temperature provided by the heater results in unusual temperature sensing accuracy, and a greatly simplified calibration process. By keeping tight microfabrication tolerances, the repeatability of the system is further ensured, eliminating per-device calibration. Reducing the complexity and cost of calibration to this level allows for mass production of ready-to-use, affordable devices. Other technologies that support our robust control approach were also developed, including an automated method to precisely distribute heat in the system space. This method enabled the use of aluminum for the fabrication of planar heaters/sensors, replacing expensive metals that are commonly used. The use of aluminum makes our technology CMOS-compatible. CMOS integration will enable a fully contained system that could be packaged in a USB key and cost a few dollars. Such a system would certainly revolutionize the practice of Medicine.

Acknowledgements

I would like to thank my supervisor, Dr. Chris Backhouse for giving me the opportunity to work in his group, providing me with support and invaluable guidance. He transmitted to me his enthusiasm for the project and taught me the art of composing ideas in a clear and structured manner. Throughout my work Dr. Backhouse led me to think critically and maintain scientific rigor. His lessons will be enormously valuable in my professional career and in my everyday life. I would like to thank Dr. Duncan Elliot, who guided my work at the University of Alberta along with Dr. Backhouse and provided very valuable ideas that enriched my project substantially. I would like to thank Dr. Dan Sameoto for his insightful thoughts during our group meetings and for his help in the review and writing of the articles this thesis is based on. I am especially grateful to Saul Caverhill-Godkewitsch, who helped me with extensive simulation work in the final stages of my program. He came when I called him and provided an effective and smart work that led us to develop successfully the devices presented in Chapter 9 and 10. Later Saul helped me to carry out several tests in the devices and his help was also key in our articles related to this work. I would like to thank Matt Reynolds for carrying out the experiments that led us to choose aluminum as the best alternative for polymer metallization. His expertise in the cleanroom was also key in the success of our work. I would like to thank David Sloan for his help performing lifetime tests on the devices and for validating my MATLAB code after the development of heater design method. I would like to recognize the work of Tianchi Ma and Gordon Hall from the group of Dr. Backhouse at the University of Waterloo for developing the test platform for our devices and test the U 1550 design by fluorescence thermometry, which provided the final validation to my modeling and simulation work. I would like to thank Luis Gutierrez-Rivera for his hard work in the cleanroom when we developed the CAF bonding technique. Our work on KMPR multilayer structures and microvalves allowed me to understand many aspects of polymer microfabrication. I would like to thank all the members of our group, including Govind Kaigala, Mohammad Behnam, Abraham Jang, Eva Sant, Sunny Ho, Samira Movahedian, Ayo Olanrewaju, Robert Johnstone, Nilufar Poshtiban, Reza Banaei, Shane Groendahl and Viet Hoang. Their help was key in many aspects my work. I would like to thank the generous support of Alberta Innovates Technology Futures from 2009 to 2012, which allowed my family and me have a satisfactory quality of life over these years.

My deepest acknowledgement is for my family, who walked along with me in this adventure. My wife Verónica Elizabeth Camacho Zúñiga, my son, José Martínez Camacho and my parents, María del Carmen Quijada Cisneros and José Martínez Pichardo, were my support in all aspects of my life during these years. Eli, Pepito, Mamá y Papá, a través de esta tesis quiereo expresarles todo mi amor y agradecimiento. Por ustedes es por quienes yo realmente he hecho este gran esfuerzo. Cada día a lo largo de estos seis años tan difíciles ustedes han estado en mi mente y en mi corazón. Siéntanse orgullosos de lo que hemos logrado.

Pepito, eres un niño mágico. Gracias por tantas horas en que jugamos juntos a los trenes. Gracias por reírte tanto y ser mi mejor amigo. Desde que llegaste, como un bebé milagro, has llenado mi vida de luz. En los momentos difíciles me imagino sosteniendo tu manita, esa es mi fuerza. Soy un papá muy feliz. Te dedico mis números y mis letras, los que están aquí y los que he de escribir, para que cuando seas un hombre te sirvan de inspiración. Te amo Pepi.

Eli, has sido la luz de mis ojos y de mi corazón. Gracias por tu impulso diario y tu inmenso amor, por caminar de mi mano y transformar mi vida. Me diste mucho más que un hijo: me diste un hijo feliz, un niño mágico. Eres la alegría y el calor de nuestro hogar, que nos ha llevado muy lejos a los tres. Le agradezco a Dios que haya unido nuestros caminos. Soy un soñador y tu eres parte de mis sueños, en los que volamos juntos, por los campos de maíz. Te amo Eli.

Papá y Mamá, gracias por traerme a este mundo brillante, en el que he encontrado retos, pero también mucha felicidad. Soy inmensamente afortunado de que ustedes sean mis papás. Con su amor, trabajo diario y ejemplo me han traído hasta aquí, a la cima del triunfo. Desde niño tuve un sueño, ser un científico, hoy lo he cumplido. Seguiré conectando mis pilas y mis motorcitos, como en mis primeros años, con la motivación y la tenacidad que han sembrado en mi. Soy muy feliz, gracias, los amo.

México, familia, amitos, los llevo muy profundamente en mi corazón. Este trabajo lo he hecho por y para ustedes, pensando en que de esta forma algún día contribuiremos a hacer que la vida del hombre sea mas larga, más saludable y más feliz. Gracias.

Table of Contents

1 Introduction ... 1

2 Background ... 8

2.1 Lab-On-Chip and Integration ... 8

2.2 PCR Genetic Amplification ... 9

2.3 The Central Problems of LOC Thermal Systems ... 9

2.4 Sensitivity to Ambient Conditions ... 12

2.5 References ... 14

3 Standard Approach for Thermal Control in LOC ... 17

3.1 System Description ... 17

3.2 The Need for a Tc(Th) Mapping ... 20

3.3 Sensitivity to Fabrication Error and Misalignment ... 21

3.4 Sensitivity to External Variables ... 23

3.4.1 Heatsink and Ambient Temperature Variations ... 24

3.4.2 Thermal Contact Variations ... 26

3.5 Time Response ... 27

3.6 Effect of Temperature Shifts and Non-Uniformities on PCR ... 29

3.7 Appendix A: PCR/CE-4 Simulation Details ... 32

3.8 References ... 34

4 A Three-Layer Chip for USB-powered Instruments ... 35

4.1 Appendix A: USBPCR-1 Simulation Details ... 39

5 Thermal Calibration ... 40

5.1 Observer Effect ... 41

5.2 Inaccuracy of Simulation Models ... 45

5.3 Delta Calibration Method ... 46

5.4 Practical Implementation and Results ... 49

5.4.1 Step 1: Temperature Measurement ... 49

5.4.2 Step 2: Calculation of Δ ... 50

5.4.3 Step 3: Temperature Correction ... 52

5.4.4 Improvement of the PCR Performance ... 53

5.5 Conclusion ... 55

5.6 References ... 57

6 A New LOC Multilayer Polymer Technology ... 58

6.1 A Low Power Genetic Analysis Platform ... 60

6.2 A Flow-Through PCR Chip with Built-in Thermal Control ... 67

6.3 Appendix A: PC6-K and FTC-1 Simulation Details ... 75

6.4 References *77*

7 A Novel Multilayer Bonding Process 78

7.1 Introduction *79*

7.2 Fabrication *81*

7.3 Results and Discussion *82*
7.3.1 Lithography of KMPR 82
7.3.2 Film Uniformity 82
7.3.3 Conformal Adsorbate Film (CAF) 83
7.3.4 Multilayer Bonding Characterization 84
7.3.5 Leakage and Bonding Strength Tests 85

7.4 Conclusions *86*

7.5 References *88*

8 Polymer Metallization 90

8.1 Introduction *90*

8.2 Fabrication *94*

8.3 Experimental *95*
8.3.1 Calibration 95
8.3.2 Joule Heating 96

8.4 Results and Discussion *98*
8.4.1 Characteristics of the Al Film on KMPR 98
8.4.2 Resistance Behavior 100
8.4.2.1 First Calibration Cycle and Joule Heating Test 100
8.4.2.2 Second Calibration Cycle and Joule Heating Test 102
8.4.3 Resistivity and TCR 104
8.4.4 Resistance Repeatability and Measurement Precision 106
8.4.4.1 Same Chip Repeatability 106
8.4.4.2 Chip-to-Chip Repeatability 106
8.4.4.3 Batch to Batch Repeatability 107
8.4.5 Al-KMPR Adhesion 107
8.4.6 Electromigration Effects 109
8.4.7 Resistive vs. Batch Annealing 111

8.5 Conclusions *111*

8.6 References *113*

9 A Novel Design Method for Thin Film Heaters 117

9.1 Introduction *118*

9.2 Target System *122*

9.3 Heater Design Methodology *123*
9.3.1 Step 1: Calculation of the Q Field 125
9.3.2 Step 2: Discretization and Automatic Layout Generation 128
9.3.3 Step 3: Verification 132

9.4 Results and Discussion *134*
9.4.1 Heater Extension and Calculation of the Q Field 134
9.4.2 Discretization 139
9.4.3 Steady State Uniformity 140
9.4.4 Current Density Considerations 143

9.4.5 Selectivity ... 144
9.4.6 Experimental Results ... 145
9.4.6.1 Device Lifetime ... 146

9.5 Conclusion ... 148

9.6 Appendix A: Heater Extension Based on Relative Uniformity ... 149

9.7 Appendix B: Heater Track Widths and Current Densities ... 151

9.8 Appendix C: Layout Verification ... 153
9.8.1 Virtual Connection Test ... 153
9.8.2 Physical Connection Test and Optimization ... 154

9.9 References ... 156

10 A Robust and Manufacturable LOC Thermal System ... 158

10.1 Introduction ... 159

10.2 Design, Methods and Materials ... 162
10.2.1 System Description ... 162
10.2.2 Analytical Model ... 164
10.2.3 Physical Layout ... 170
10.2.4 3D Simulation of the System ... 171
10.2.5 Power Considerations ... 173
10.2.6 Electrical Temperature Measurement ... 175
10.2.6.1 Temperature Measurement from Power ... 175
10.2.6.2 Temperature Measurement from Resistance ... 175
10.2.7 TCR Measurement ... 177
10.2.8 IR Temperature Measurement ... 178
10.2.9 Fluorescence-based Temperature Measurement ... 178

10.3 Simulation Results ... 179
10.3.1 Calculation of Correction Factors via 3D Simulation ... 179
10.3.2 Temperature Uniformity in 3D ... 183

10.4 Experimental Results ... 184
10.4.1 Determination of TCR ... 185
10.4.2 IR Temperature Measurement ... 186
10.4.3 Fluorescence-based Temperature Measurement ... 190
10.4.4 Measurement Error ... 191

10.5 Conclusion ... 193

10.6 Appendix A: Device Fabrication ... 195

10.7 Appendix B: Details of the IR Imaging Experiments ... 197

10.8 Appendix C: Moisture Sensitivity ... 199

10.9 References ... 207

11 A CMOS-Ready PCR System ... 210

11.1 Design Considerations ... 211

11.2 Preliminary Results and Specifications ... 212

12 Conclusions ... 218

List of Tables

Table 1. Calculation of absolute and relative differences under influence of the simulation error. In this example 94 ºC and 92 ºC have been predicted by simulating the system with water or air+TLC in the PCR chamber. The simulation error, *e*, is estimated to be ±10 %. The relative difference Δ is independent of *e*. 47
Table 2. Thermal conductivities (*k*) of materials used in simulation. 50
Table 3. Sample temperature matrix obtained by solving the H2O model for different combinations of *Th* and *Ths*. Ts_{H2O} is centered at *Th* = 94, 71 and 59 ºC and *Ths* = 22 ºC. *Th* – heater temperature; *Ths* – heatsink temperature; $Ts_{H2O\ ave}$ – average chamber temperature. 51
Table 4. Coefficients of the Ts_{H2O} and Ts_{TLC} functions obtained by simulation. 52
Table 5. Correction of the measured temperatures made to estimate the true temperature in the chamber T_{H2O}. The first column is the measured temperature that serves as an absolute reference. *Th* and *Ths* are the heater and heatsink temperatures recorded along with T_{TLC} . Δ is calculated at these *Th* and *Ths* through the functions Ts_{H2O} and Ts_{TLC} . The value of Δ is essentially constant. 53
Table 6. First Joule heating results of a prototype Al heater on KMPR. At each step, the current was turned on, held for the times specified in the second column, turned off to allow the heater to reach room temperature, and finally turned on again. Resistances were measured with the applied current and the mismatch between the two values reflects the film's stability. 102
Table 7. Second Joule heating test results of a prototype Al heater on KMPR. At each step the current was turned on, held for the times specified in the second column, turned off, allowing the heater to reach room temperature, and finally turned on again. Resistances were measured with the applied current, and the mismatch between the two values reflects the film's stability. 104
Table 8. Mean temperature coefficient of resistivity and resistivity at room temperature of Al on KMPR after annealing. Values for other film and bulk materials are shown for comparison. 105
Table 9. Dimensions and type of power density distribution of the designed heaters. The power, uniformity (ΔT) and average chamber temperature (Tc_{avg}) were calculated on the 2D model of the system driven by an ideal heater. *Ths* = 30 ºC. For NU 750 and NU 1450 *Th* = 95 ºC. For U 850 and U 1550 *Q* = 6.314 x 10^{5} W/m^2. 136
Table 10. Specifications of the heater designs, as obtained from the discretization process. Heaters were designed with Th = 95 ºC and Ths = 30 ºC. For uniform power density heaters *Q* = 6.314 x 10^{5} W/m^2. 140
Table 11. Absolute and relative chamber temperature uniformity of the designed heaters (applicable to Step 1 of the process), calculated on the 2D model of the system driven by an ideal heater. 151
Table 12. Properties of the materials in the system. The values in bold were used in analytical calculations. 165
Table 13. Estimated resistances of the system using a U 1550 heater design, whose chamber and heater radii are 1200 µm and 1550 µm, respectively. 168
Table 14. Correction factors determined from 3D simulation for U 1550. The parameters β and γ are defined in section 10.2.2 (Eq. 26 and Eq. 28, respectively). The parameter ε is defined in section 10.2.6.2. 182
Table 15. Estimated error in chamber temperature measurements due to different sources of variability, estimated for the U 1550 design at *Tc* = 95 ºC, *Ths* = 20–30 ºC and *Tamb* = 20 ºC. 192
Table 16. Old Al/KMPR fabrication processes used in the work of Chapter 8 (section 8.2). The heater chips were fabricated by Luis Gutierrez-Rivera and tested by the author. 203
Table 17. New Al/KMPR fabrication processes used in the work of Chapter 10 (section 10.6). The devices were fabricated by Matthew Reynolds and recently tested by him and David Sloan. 205

Table 18. Major differences between the old and new Al/KMPR fabrication processes. 206
Table 19. Parameters calculated in the analytical model of the system with *Tc* = 95 ºC, *Ths* = 30 ºC, *htc* = 5.6 W/m^2 K. The parameters C_{Si},, *Cb, C2, Cc* and *C4* are the heat capacities associated to the Si substrate, airbridge, layer 2, the chamber and layer 4, respectively. The parameter τ Is the time constant of the system. 214
Table 20. Properties of air. The values in bold were used in analytical calculations. 214

List of Figures

Figure 1. The PCR/CE-4 LOC platform for genetic analysis. (a) Layout of the chip. The channels intersecting on the left constitute the CE stage; at the center, the PCR chamber (red) is surrounded by the thin film Pt heater/sensor (orange). The thicker red channel on the right is the sample preparation stage. (b) Cross section of the chip, showing the components of the thermal system. 19
Figure 2. Photograph of the fabricated PCR/CE-4 device. Holes in the glass were water-jet drilled to allow for access to the heater contact pads, pneumatic connections to the valves and fluid ports. 19
Figure 3. Temperature distribution on the cross section of PCR/CE-4, showing the difference between heater/sensor and chamber temperatures when the chamber is at denaturation temperature (94 ºC). The arrows indicate the direction of the heat flux. In this simulation the top surface and sidewalls of the chip are prescribed a boundary condition of heat loss by natural convection with h=5.6 W/m^2-K (typical value for free convection for heated plates facing up [1]. The bottom surface is imposed a thermal isolation boundary condition in an area of 3.5 mm radius aligned to the heater and chamber. The rest of the bottom surface area is prescribed a uniform temperature boundary condition (22 ºC) to mimic an ideal heatsink, ... 20
Figure 4. (a) Chamber-heater misalignment occurring during chip bonding. (b) chip-heatsink misalignment occurring during chip placement. Blue – chamber; red – heater; yellow – heatsink. 22
Figure 5. Simulation of the effect of heatsink and ambient temperature variations on the average chamber temperature (at denaturation). The horizontal axis corresponds to the variable that is allowed to change. Red – *Ths* and *Tamb* change simultaneously; blue – *Ths* changes, while *Tamb* is kept at 22 ºC; black – *Tamb* changes, while *Ths* is kept at 22 ºC. A controller that is not aware of changes of *Ths* would keep *Th* constant (168.16 ºC), but *Tc* would shift. At room temperature (22 ºC), Tc_{ave} falls on the target denaturation temperature (94 ºC). 26
Figure 6. (a,c) Surface profiles of the copper heatsink of two different instruments obtained by optical profilometry. (b,d) Micrographs of the scanned surfaces. The differences in surface roughness caused differences in contact resistance that shifted the system temperatures. 27
Figure 7. Simulation of PCR/CE-4 showing the average heater and chamber temperatures 4 over time. The units of the vertical and horizontal scales are ºC and seconds, respectively. Blue – *Th*; Red – *Tc*. *Tc* reaches the steady state in approximately 5τ = 30 s........ 29
Figure 8. 3D simulation of the Taq concentration and diffusion in the PCR chamber of PCR/CE-4 due to a 2 ºC temperature non-uniformity. The arrows indicate the direction and magnitude of the diffusive flux. 30
Figure 9. Relative concentration of Taq in the PCR chamber over the duration of a typical PCR run, calculated by 3D simulation at Tc_{ave} = 94 ºC (a) and at Tc_{ave} = 97 ºC. The fast depletion of Taq is caused by combined thermal degradation and diffusion effects. Blue – concentration at the coldest point; green – concentration at the hottest point; dashed line – average concentration. 31
Figure 10. Simulation of the decay in Taq concentration along a real PCR run at different denaturation temperatures. 31
Figure 11. USBPCR-1 system, which integrates a Pt heater/sensor, PCR chamber and micro-valves/pumps. This is the PCR-only variant of the device. Other variants were built with SP and CE sections too. 36
Figure 12. USB-powered instruments enabled by USBPCR-1. (a) Compact PCR instrument that integrates solenoid valves and the pressure/vacuum system necessary to actuate the valves in the chip, as well as the circuitry for thermal and fluid control (dimensions: 2.25” x 2.5” x 3”). (b) Compact CE instrument (dimensions: 3” x 2.25” x 1.5”). (c) Compact PCR/CE system that integrated the functionalities of (a) and (b). 37

Figure 13. (a) Comparison of chamber and heater size of USBPCR-1 and PCR/CE-4, showing the area of the PCR chamber (blue). The drawings are shown in real proportion. The radius of the hole in the heatsink (3.5 mm) was kept unchanged. The radius of the chamber, inner radius of the heater and heater width was, 1.5 mm, 1.15 mm and 100 µm, respectively. For USBPCR these dimensions were 750 µm, 950 µm and 100 µm.........(b) Bottom plate of USBPCR-1 along a coin of $1 CAN. 37
Figure 14. Electropherogram of a successful PCR of BK virus template run on USBPCR-1. The PCR product (blue line) shows a peak size of ~300 bps. A DNA ladder (red line) is run under identical electrophoretic conditions to estimate and validate the size of the PCR product. 38
Figure 15. Effect of different materials filling the PCR chamber, calculated by 3D simulation. To emulate closed loop control the heater temperature *Th* is maintained at 168.16 ºC, which produces 94 ºC in a water-filled chamber. The heatsink temperature *Ths* is kept at 22 ºC). The plot shows the temperature at the center of the PCR chamber from bottom to top. The horizontal axis indicates the vertical distance from the bottom (0 µm) to the top (90 µm) of the chamber. The top of the chamber is also the top of the TLC layer. Filling the chamber with a layer of air and TLC causes an abrupt change in the vertical temperature gradient. 42
Figure 16. Effect of a thermocouple inserted in the PCR chamber, calculated by 3D simulation. *Th* and *Ths* are maintained at 168.16 ºC and 22 ºC, respectively. In the simulation the 70 µm thick metallic junction of the thermocouple is placed at the center of the chamber. The plot shows the temperature at the center of the PCR chamber from bottom to top, passing through the junction. The horizontal axis indicates the vertical distance from the bottom (0 µm) to the top (90 µm) of the chamber. The temperature is highly homogeneous within the junction due to its high conductivity. The thermocouple positioned exactly in the middle of the chamber would report ~96 ºC for oil or ~100 ºC for air. 44
Figure 17. Conceptual diagram of the *Delta Method*. H2O and TLC (top squares) represent the chip filled with the PCR mix and with air+TLC, respectively. The relative temperature difference Δ is a metric of the observer effect, and it is calculated from FEM models of the system. (bottom squares). These models only include the most important characteristics of the systems. Δ is then used to estimate the true chamber temperature T_{H2O} from the measured reference temperature T_{TLC}. 48
Figure 18. Comparison of the old and new calibration schemes. (+) Measured reference temperature T_{TLC} ; (*) estimated true temperature T_{H2O} ; dashed line – *Tc* predicted by the old *Tc(Th)* relation. For clarity, the third dimension of the new relation (*Ths*) is not shown, but its value is indicated. 54
Figure 19. Structure of a PCR LOC system made in the new multilayer polymer architecture. A thin film heater between layers 1 and 2 underlies a PCR chamber patterned in layer 3.. 59
Figure 20. Cross section of the PC6-K system. The PCR chamber is patterned in layer 3 and a thin film heater suspended on an air bridge that is patterned in layer 1. On the right portion of the diagram there is a pneumatic microvalve structure that comprises a flexible diaphragm and a cavity underneath where either vacuum or pressurized air are applied to open/close the valve. A non-adhesive area is required to prevent the diaphragm from sticking permanently to the valve seat. 61
Figure 21. (a) Layout of the PC6-K system, a 4-layer polymer chip based on PCR/CE-4. (b) Temperature field of the heater at full power (~100 mW). The heater is composed of three concentric rings connected in parallel. (c) Mask layout of the heater and 4-point sensor. The innermost ring in (b) is the 4-point sensor, with two (thicker) tracks for the drive current and two (thinner) tracks for voltage sensing. The gaps between the three heater rings were filled with unconnected metal to improve temperature uniformity. 62
Figure 22. Radial temperature profile at the heater and chamber levels, obtained by 3D simulation, showing the high power concentration and selectivity achieved by the use of a thin polymer structure. The use of an air bridge made possible reaching 100 ºC within the small heated area with only a fraction of the power required by the PCR/CE-4 and USBPCR-1 platforms. 64

Figure 23. Radial temperature profile at the heater and chamber levels, showing the closeness between chamber, heater and sensor temperatures. 64
Figure 24. Cross section of FTC-1, a continuous flow PCR system. Air bridges are patterned under the reaction channel in order to control power consumption. 68
Figure 25. Cross section of FTC-1, showing the temperature zone of one heater. H – hot zone (94 ºC); C – cold zone (60 ºC); W – warm zone (70 ºC). The reaction channel (blue) is 50 µm high and is separated by 50 µm of KMPR from the heater elements (red). The heater elements are separated by a 100 µm airbridge from the substrate. The chip is supported on a flat heatsink. The arrows indicate conductive heat flux. 69
Figure 26. Layout of FTC-1. The PCR brew flows from the input well (large circle) to the waste reservoir by capillary forces. The small circle represents an air-exhaust port. Each heater contains three zones at PCR temperatures: H – 94 ºC, C – 60 ºC, W – 70 ºC. 71
Figure 27. (a) Layout of a 3-zone thin film heater (for one PCR cycle). The heater tracks (blue) are to be connected in series. The dashed lines show the profile of the channels in real proportion. The solid line rectangles show the air bridge areas. (b) Some tracks would be used as 4-point temperature sensors, by adding voltage probe lines. 72
Figure 28. Longitudinal temperature profile for PCR at the heater and channel (top and bottom) levels, produced by the heater layout of Figure 27(a), as predicted by 3D simulation. This profile will generate one amplification cycle on the moving PCR sample. 74
Figure 29. Longitudinal temperature profile for MCA, at the heater and channel (top and bottom) levels, predicted by 3D simulation. 74
Figure 30. Contact angle on the surface of a crosslinked KMPR film, (a) without CAF and (b) coated with the CAF. 84
Figure 31. Devices fabricated with the CAF technique. (a) 4-layer chip for complete genetic analysis that integrates PCR, CE and SP sections, 45 x 17.5 mm. (b) 4-layer chips for CE analysis and detection, located at the center of the wafer. The logo area, on the top right corner of each chip, as well as the alignment marks on the opposite corner, were excluded when measuring the bonding yield in this center portion of the wafer. 85
Figure 32. Capillary filling of DI water in KMPR microchannels. The arrow indicates the direction of the advancing meniscus. The water column was digitally colored. 86
Figure 33. Optical image of an Al heater on KMPR during Joule heating tests. No discernible changes were detected in the metal at this level of magnification. In this heater, the defect on the right-hand side, possibly a bubble in KMPR, did not affect resistance stability, because there was good coverage of metal. 99
Figure 34. Optical images of ridges on the Al film, formed by compressive stresses on insufficiently hard-baked KMPR (120ºC for 15 minutes). (a) Ridges on heaters caused significant hysteresis and nonlinear temperature vs. resistance curves; (b) zoomed-in image of the rectangular region in (a). Baking at 130ºC for 30 minutes raised T_g sufficiently to avoid such deformations. 99
Figure 35. First calibration cycle of a typical Al heater on KMPR, comprising three calibration runs in a row. The plot contains three curves that show a trend between calibration runs of ncreasing resistivity. Blue – run #1; green – run #2; red – run #3. 101
Figure 36. Second calibration cycle of a typical Al heater on KMPR, comprising three calibration runs in a row. The plot contains three curves that overlap each other. It is clear that resistive annealing substantially improves the heater performance. 103
Figure 37. Aluminum on KMPR (right quarter wafer) and Al on SU-8 (left quarter wafer) tape-test. Both polymers were layered on silicon substrates. Al is completely removed from the SU-8 but remains on the KMPR, clearly showcasing exceptional metal-polymer adhesion. 109
Figure 38. Coupled Joule-heating/heat-transfer 3D simulation of an Al heater on KMPR in normalized values. The area of highest combined current density and temperature is at the ring-pad interconnect. Electromigration will occur at the highest rate in these areas. (a) normalized temperature; (b) normalized current density. The simulation was performed in COMSOL 3.5a using the base model of PCR/CE-4 described in section 3.7. The Electrical Conduction in Shells physics was added to the base model to simulate Joule heating, much as described in section 4.1. 110

Figure 39. Optical images of Al heaters on KMPR. The size and density of hillocks due to electromigration increase with operation time. (a) Film before application of current; (b) film after 1 hr of ~165 ºC Joule heating; (c) film after 6 hr of ~160 ºC Joule heating. Deliberate shallow scratches to the film (d, e, f) confirmed that hillocks proliferate on defects.......... 111
Figure 40. Schematic cross-section of the target PCR system. The thickness of the KMPR layers is (from 1 to 4) 20, 20, 20 and 25 µm. The thickness of the sealing polypropylene layer and Si substrate are 40 µm and 500 µm, respectively. The thin-film Al heater is 100 nm thick.......... 123
Figure 41. (a) Parallel-type heater (b) Series-type drive wheel heater. *Q* – power density along the metal tracks; *V* and *I* – applied voltage and current; *h* – thickness of the metal film; *ρ* – resistivity of the metal film; *l* and *w* – length and width of the tracks.......... 124
Figure 42. (a) Discretization of the *Q* field into segments. The circular area represents the non-zero elements of the matrix. (b) Segment structure. Each segment in the heater is comprised of a track segment and an empty space on each side. *L* – segment length; *s* – segment width; *w* – track width. *L* and *s* are controlled independently. (c) Effective area A_e that the heater occupies in an edge segment.......... 128
Figure 43. Stack of polygons forming a grid heater (only ¼ of the heater is shown). The x and y resolution can be freely selected. In this example the tracks are all connected in parallel. Far from the center the tracks become shorter, thus they need to become thinner to limit the current and maintain the same power input.......... 132
Figure 44. Trade-off between chamber temperature uniformity (ΔT), power consumption (*P*) and extension distance (Δrh), for uniform and non-uniform power density heaters. The curves were obtained from 2D simulation using an ideal heater. (a) Curves for designs with a 500 µm radius chamber. (b) Curves for designs with a 1200 µm radius chamber. At Δrh = 0 the radius of the heater is equal to the radius of the chamber. For NU designs a uniform temperature condition of value *Th* = 95 ºC is prescribed along the heater. For U designs a uniform power density condition of value $Q = 6.32 \times 10^{5}$ W/m^2 is prescribed along the heater. *Ths* = 30 ºC, *Tamb* = 22 ºC.......... 135
Figure 45. Temperature along a 500 µm PCR chamber induced by a 500 µm (circles) and 750 µm (no markers) radius ideal heater. The temperature of the ideal heater is maintained at 95 ºC across its entire surface.......... 137
Figure 46. Heat flux along the surface of the ideal NU 750 heater. This is the power density field necessary to maintain uniform temperature in the PCR chamber. An exponentially increasing power density radially towards the edge compensates for the high losses outside the heater.......... 138
Figure 47. (a) Layout of the NU 1450 design. The blue circle in (a) indicates the perimeter of the 1200 µm radius chamber. The drive current is applied through terminals A and B; the output voltage is probed between terminals C and D. The circles indicate points of contact for terminals (pogo pins). The inset in (a) is a zoom-in of the heater's edge, where the tracks thin down to increase the power input. (b) 3D FEM model used to characterize the designed heaters. The full layout of the heaters is embedded in the model; the chamber is indicated in blue.......... 141
Figure 48. Temperature field at the bottom of the PCR chamber, predicted by 3D heat-transfer/Joule-heating simulation of the full layouts. (a) NU 750, (b) U 850, (c) NU 1450, (d) U 1550. The voltages applied to reach an average *Tc* = 95 ºC are: 3.89, 3.95, 9.72, 10.62 The heaters in the full layout require higher voltages than those shown in Table 10, due to the voltage drops introduced by the power bus and elbows; therefore the voltages need to be adjusted to reach 95 º in the chamber.......... 142
Figure 49. Histograms of temperatures across the entire volume of the PCR chamber of non-uniform (a) and uniform (b) power density heaters. The temperatures in > 94 % of the chamber volume fall within a 1 ºC band in all cases, while the volume outside this band is negligible.......... 143
Figure 50. Temperature along the middle of the chamber and heater. (a) NU 750; (b) NU 1450. 143

Figure 51. Current density field in the NU 1450 heater. Notice the sharp increase at the track ends. The current density on the elbows and connections to the power bus is 1-2 orders of magnitude lower than the densities found on the tracks. 144
Figure 52. *Tc* and *Th* of NU 750 over a chip-wide scope for an applied voltage of 2, 3, 4 V. At a distance 250 µm from the edge of the heater the chip remains at the temperature of the heatsink. Uniformity is better at lower temperatures. Other objects can be placed in contact or other structures can be built in the chip at this distance without affecting the thermal system. This establishes the potential for building several chambers in the same chip. 145
Figure 53. (a) Photograph of the fabricated target system (U 1550) as a silicon die, including the KMPR microfluidic layer. (b) Zoomed-in image of the NU 1450 aluminum traces showing the narrowing of tracks towards the heater perimeter. (c) U 850 heater tracks with no KMPR fluidics. (d) U 1550 configuration including KMPR fluidics. 146
Figure 54. Trade-off between relative chamber temperature uniformity (*B*), power consumption (*P*) and extension distance (Δrh), for uniform and non-uniform power density heaters. The curves are calculated using the data obtained from the 2D simulations of section 9.4.1. (a) Curves for designs with a 500 µm radius chamber. (b) Curves for designs with a 1200 µm radius chamber. 150
Figure 55. (a, b) Automatically generated NU 750 and U 850 heater tracks. (c, d) Width of the tracks for the NU 750 and U 850 heaters. Note the significant tapering of track width near the heater edge. (e,f) Current density along the tracks. 152
Figure 56. (a) Temperature field at the bottom of the PCR chamber in U 1550. (b) Histogram of the temperatures across the volume of the PCR chamber. The heater tracks are connected through zero-resistance virtual connections. The uniformity is good which validates the result of the discretization and generated layout. 153
Figure 57. Temperature field at the bottom of the PCR chamber in the NU 750, using a pitch of 50 µm (30 tracks resolution). 154
Figure 58. Temperature field at the bottom of the PCR chamber in U 1550, when the physical connections are added. The voltage drop at the end group at the bottom, caused by the large number of elbows, was corrected by reducing the length of the first track. The top group was not corrected, in order to show the difference. The non-uniformity in this group reaches ~ 5 ºC. 155
Figure 59. Construction of the thermally robust LOC system. (a) Cross sectional view of the stack of KMPR layers forming the system. The device is placed onto a heatsink prior to operation. (b) Top view schematic of the system, showing the PCR chamber, the heater and the polypropylene lid that seals the chamber. The wells and microchannels are part of the fluidic system intended to fill up the PCR brew into the chamber and perform capillary electrophoresis on the PCR product. 163
Figure 60. Analytical model of the system, with layers as labeled in Figure 59.......................... 165
Figure 61. Layout of the U 1550. The horizontal lines at the center of the figure are the heater tracks. The blue circle at the center of the figure indicates the perimeter of the 1200 µm radius chamber. The driving current is applied through terminals A and B; the output voltage is probed between terminals C and D. 171
Figure 62. Average chamber temperature vs. resistance curves calculated by 3D simulation for U 1550. In the simulation the applied voltage is ramped from 1.5 to 12 V for three different values of *Ths*, causing *R* and *Tc* to increase. The plot shows the three sets of data corresponding to *Ths* = 20, 30, 40 ºC. A line is fitted to each data set (dashed lines) and these lines overlap on each other, indicating a very small sensitivity to changes in *Ths*. 180
Figure 63. Zoomed-n image of the plot in Figure 62. If a controller keeps *R* constant, *Tc* would shift by 0.76 ºC with variations of 20 ºC in *Ths*. 181
Figure 64. Temperature field at the bottom of the PCR chamber in U 1550, predicted by 3D simulation. Applying a voltage of 10.62 V gives an average chamber temperature of 95 ºC and a uniformity of ±1.25 ºC. 184
Figure 65. Photograph of the fabricated device. 184

Figure 66. (a) Infrared image of U 1550 using driven by 3.34 ± 0.01 W power. (b) Temperature sampled along a horizontal line crossing through the heater in (a). ... 187
Figure 67. Temperature corrected for the real emissivity in U 1550. ... 189
Figure 68. (a) Infrared image of a U 1550. The image was taken with no power applied. (b) Temperature sampled along a horizontal line crossing through the heater in (a). ... 198
Figure 69. Cross section of the CMOS PCR system. ... 212
Figure 70. Heat flux along the surface of the ideal NU 600 heater. This is the power density field necessary to maintain uniform temperature in the PCR chamber of the LOC CMOS system. The exponential increment of power density towards the edge compensates for the high losses at the heater's edge. The heat loss at the pillar locations is also compensated with sharp power steps. ... 217
Figure 71. Automatically generated NU 600 heater tracks for the CMOS PCR system. The algorithm compensates for the high heat loss through the pillars by thinning the tracks at the pillar locations. This design demonstrates the flexibility of our heater design method. ... 217

List of Abbreviations

CAF	Conformal Adsorbate Film
CCD	Charge-Coupled Device
CE	Capillary Electrophoresis
CMOS	Complementary Metal-Oxide-Semiconductor
CTE	Coefficient Of Thermal Expansion
DC	Direct Current
DI	Deionized Water
DMM	Digital Multimeter
DNA	Deoxyribonucleic Acid
FEM	Finite Element Method
HCL	Highly Conductive Layer
IR	Infrared
ITO	Indium Tin Oxide
LOC	Lab-On-Chip
LTCC	Low Temperature Co-fired Ceramics
MCA	Melting Curve Analysis
MEMS	Microelectromechanical Systems
NIST	National Institute of Standards and Technology
PCB	Printed Circuit Board
PCR	Polymerase Chain Reaction
PDMS	Polydimethylsiloxane
PEB	Post Exposure Bake
PET	Polyethylene Terephtalate
PMMA	Poly(Methyl Methacrylate)
POC	Point-Of-Care
qPCR	Quantitative Real Time PCR
RMS	Root Mean Square
RTD	Resistance Temperature Detector
SMT	Surface Mount Technology
SP	Sample Preparation
TBE	Tris/Borate/EDTA
TCR	Temperature Coefficient Of Resistance
TiW	Titanium-Tungsten
TLC	Thermochromic Liquid Crystals
USB	Universal Serial Bus

1 Introduction

In recent years the cost of genetic analyses for disease detection has decreased significantly. However the laboratory infrastructure and equipment necessary to perform these analyses is extremely expensive. The integration of the lab-on-chip (LOC) and microelectronics technologies could enable the mass-fabrication of complete genetic analysis instruments fully contained in a single chip. Such instruments would replace an entire laboratory setting, enabling handheld devices that would make it possible to perform rapid and accurate screening of disease-specific genes at the point of care, and at a minimum cost.

Amplification of genes in the clinical sample through the polymerase chain reaction (PCR) is a fundamental operation in genetic diagnosis devices. The efficiency of PCR relies strongly on precise temperature control, as well as high temperature uniformity in the PCR chamber. However, many implementations of LOC thermal systems suffer from a dependence on a myriad of ill-defined boundary conditions and external variables (see discussion and references in section 2.3). One of such boundary conditions could include thermal contact, wherein the inability to control surface roughness or contact pressure leads to variations of contact resistance. Other sources of boundary variability are the fluctuations in air temperature and flow velocity. Most of these variables are difficult to measure and control, or are not repeatable, and may cause significant variations of the in-system temperatures. Such variations deteriorate the performance and reproducibility of PCR, leading to inaccurate diagnosis. This vulnerability is a central problem in LOC systems and has limited them to operate in the laboratory setting, where external conditions such as the ambient temperature are controlled to be high stable. We believe that in order to enable the reliable operation of LOC systems in uncontrolled environments, such as the doctor’s office, the system must be robust to variations of boundary conditions. By eliminating the need for specialized infrastructure and equipment that maintain stable or repeatable boundary conditions, the cost of the system can be

dramatically reduced. Such a cost reduction would enable the mass-manufacturability of LOC systems, and with this allow for access of the population to affordable genetic diagnosis tests.

In typical LOC thermal systems there is also a need for estimating the temperature of the PCR chamber from the reading of a nearby temperature sensor. An accurate estimation, therefore, requires fine calibration of the chamber temperature vs. the sensor temperature. However, conventional calibration methods may be biased by the observer effect, i.e. the disturbance caused by the calibration transducer that impedes observing the true temperature of the system. Other non-contact methods are expensive, bulky and require extensive pre-calibration. Moreover, once an estimation relationship is obtained, the non-robustness of the system as well as fabrication error cause the real temperature to deviate from the estimated temperature. As a consequence, per-instrument and per-device calibration need to be performed, increasing enormously the cost of the system. A manufacturable LOC implementation, should, therefore, be designed to minimize the calibration requirements. We believe that this could be achieved by keeping tight microfabrication tolerances and ensuring an intimate integration of the heat source, temperature sensor and PCR chamber.

The goal of this work is to establish a new direction in thermal design for LOC systems that leads to new levels of temperature measurement accuracy as well as robustness to external conditions. High integration and thermal robustness could be the key to the mass manufacture of devices capable of yielding fast and reliable diagnoses. A more advanced thermal control could certainly transfer the LOC technology to the doctor's office, making genetic diagnosis for the first time widely accessible.

To accomplish this goal, we initially worked on thermal modeling, design and simulation to develop a high level of understanding that would allow us to go further than what is normally done in LOC systems. This work became the

foundation of a large number of projects and activities in our group, and allowed us to identify the central limitations of thermal LOC systems.

Along this research we designed and fabricated a low power microchip that enabled the construction of a family of low-cost highly miniaturized genetic analysis instruments that can be powered from the USB port of a laptop computer. Later we implemented a new and unusually accurate way of sensing temperature in PCR microreactors, which improved the PCR efficiency by a factor of four (discussed in section 5.4.4). This method enabled our group to implement new genetic analysis applications such as qPCR (Quantitative Real-time PCR) and MCA (Melting Curve Analysis).

The knowledge that we developed was central in the migration of our technologies to a new multilayer polymer architecture, which allows for a significant reduction of fabrication cost, manufacturability and more efficient thermal control. Also, the low thermal conductivity environment in this architecture allows a significant reduction of power consumption, and consequently, new levels of miniaturization. Moving towards implementing a functional LOC system in the new polymer architecture the author and coworkers (listed in page 6, articles 1–4) developed new technologies, including a method to produce stable aluminum heaters/sensors on polymer and a technique to design thin film heaters deterministically. With these tools, we designed and fabricated a robust CMOS-compatible PCR LOC system.

The polymer structure is built on a high conductivity substrate that becomes the primary heatsink of the system. The system is then designed so that the substrate temperature, which can be easily measured, dominates over all other boundary conditions. In addition, the system is miniaturized to minimize its interaction with the environment. With these strategies all external variables, apart from the substrate temperature, have negligible influence on the system. Once this robustness is achieved, the only variables that remain affecting the system are

internal, e.g. layer thickness, material properties, lithography/bonding alignment, etc. These parameters, however, can be adjusted to a high precision in the cleanroom. In this way, we have designed a system that depends only on variables that can be fully controlled. As a result, the system can become reproducible, eliminating the need for per-device and per-instrument calibration.

Miniaturizing the system also results in a close integration of the heater/sensor to the PCR chamber. This integration allows for knowing the temperature in the chamber from the heater/sensor reading very accurately, with a small correction from simulation. Remarkably, this accuracy is achieved without the need for an empirical estimation function obtained from the invasive methods typically used, as described in Chapter 2. The main variables affecting the accuracy become the material properties of the heater, i.e. the temperature coefficient of resistivity (TCR), which can be stabilized within a very narrow range during production (< 1.7 % as measured in our in-house process). Furthermore, the careful control of current densities of the heater/sensor made it possible to replace platinum by aluminum, with excellent operation performance. Such an achievement reduces production costs significantly since aluminum is inexpensive and can be patterned with standard microfabrication techniques. Most importantly, the use of aliminum makes our technology compatible with the CMOS microelectronics technology.

The system is also designed to create a highly uniform temperature environment in the chamber (within 1 ºC in > 94 % of the chamber volume), even at high temperatures (95 ºC). Such uniformity ensures high temperature measurement accuracy and high PCR efficiency, and enables specialized analysis such as real time quantitative PCR (qPCR) and melting curve analysis (MCA). With this system we have also enabled, at least in terms of thermal behavior, for the first time the possibility of completing a full 35-cycle, 3-step PCR in 3 min, while a typical PCR LOC device takes ~1 hr.

The design flow of the system was automated to the point that the layout of the heater/sensor is generated automatically from a finite element model of the device. The algorithm ensures that the heater will produce 1 ºC uniformity in > 94 % of the PCR chamber volume. The heater layout generated by the algorithm can be readily transferred to the photolithography mask for fabrication. This design method is deterministic and can produce heaters of arbitrary size and shape, as well as with different temperature profiles. This method is currently being used to further miniaturize the system in preparation to fabricate a single-chip LOC CMOS instrument that could be packaged in a USB key and cost a few dollars, which is well beyond the state of the art.

In this work we demonstrate what we believe is the first manufacturable solution to the fundamental thermal control challenge of LOC systems. To our knowledge, we have demonstrated for the first time the feasibility of building a LOC PCR system that can run on a CMOS chip, reliably. Reaching such a degree of miniaturization could change the landscape and direction of LOC systems, and could certainly make possible meeting the high demand for genetic tests at the point-of-care.

This thesis is based on the following refereed journal publications:

(1) Chapter 7 Published	L. Gutierrez-Rivera*, **J. Martinez-Quijada***, R. Johnstone, D. Elliott, C. Backhouse, and D. Sameoto, "Multilayer Bonding Using a Conformal Adsorbate Film (CAF) for the Fabrication of 3D Monolithic Microfluidic Devices in Photopolymer," Journal of Micromechanics and Microengineering, Vol. 22, No. 8, 085018 (12 pp.), Aug. 2012. *Equal contribution.
(2) Chapter 8 Published	**J. Martinez-Quijada**, S. Caverhill-Godkewitsch, M. Reynolds, L. Gutierrez-Rivera, R. W. Johnstone, D. G. Elliott, D. Sameoto, and C. J. Backhouse, "Fabrication and Characterization of Aluminum Thin Film Heaters and Temperature Sensors on a Photopolymer for Lab-On-Chip Systems", Sensors and Actuators A: Physical, Vol. 193, pp. 170–181, Apr. 2013.
(3) Chapter 9 In final preparation	**J. Martinez-Quijada**, S. Caverhill-Godkewitsch, M. Reynolds, D. Sloan, C. J. Backhouse, D. G. Elliott, and D. Sameoto, "Non-Iterative Design of Thin Film Grid Heaters for Precise Spatial Temperature Control In Lab-On-Chip Systems".
(4) Chapter 10 In final preparation	**J. Martinez-Quijada**, S. Caverhill-Godkewitsch, M. Reynolds, D. Sloan, D. Sameoto, D. G. Elliott, and C. J. Backhouse, "Robust Thermal Control for CMOS-based Lab-On-Chip Systems".

The author of this work focused on the thermal design, modeling and simulation of thermal systems. He also participated actively in the development of fabrication processes to understand the fabrication constraints and feed this information back into the design process. He also contributed to the experimental testing of the fabricated devices.

S. Caverhill-Godkewitsch contributed with extensive simulation work for the designs and methods presented in Chapters 9 and 10. He also contributed to the experimental testing of the devices presented in Chapters 9 and 10.

L. Gutierrez-Rivera, R. Johnstone and M. Reynolds focused on the development of microfabrication processes. R. Johnstone contributed to the development of the 4-layer KMPR process. M. Reynolds also contributed to the fabrication and experimental testing of the devices presented in Chapters 9 and 10.

Dr. Chris Backhouse contributed a large number of key ideas in all chapters. Dr. Duncan Elliott contributed significantly to the work in chapters 9, 10 and 11. Dr. Dan Sameoto participated actively in the work of chapters 9, 10 and 11 and in the review and writing of the articles this thesis is based on.

Thesis Organization

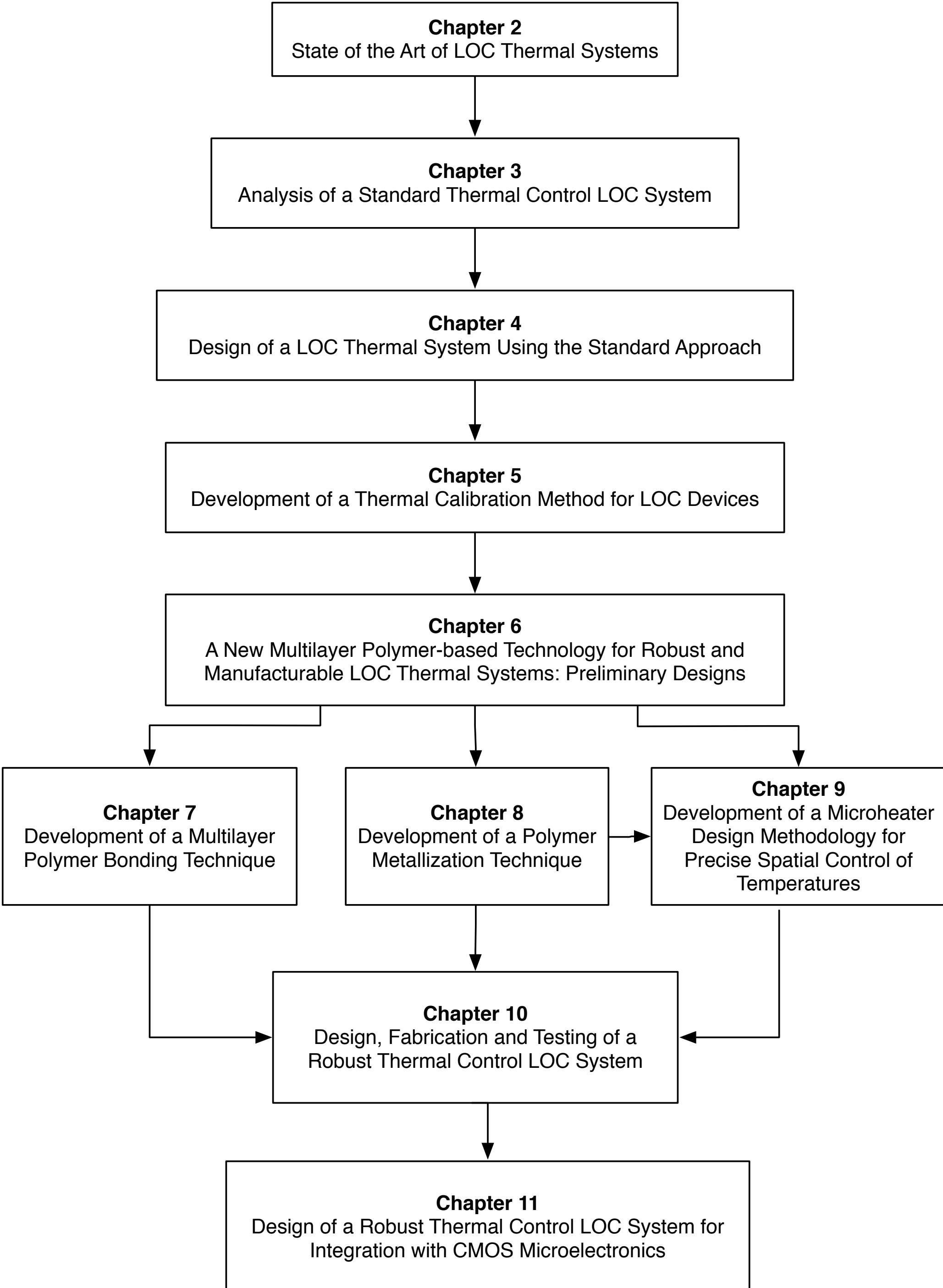

2 Background

2.1 Lab-On-Chip and Integration

Today there is a huge need for early and accurate diagnosis of cancer, infectious diseases and other conditions such as adverse drug reactions. This has driven the development of lab-on-a-chip (LOC) systems for genetic analysis. The goal of this technology is to make genetic tests affordable and readily accessible for the population, through the integration and automation of the fundamental molecular biology operations.

A fully integrated LOC system would employ minute amounts of the expensive reactants commonly used in genetic assays. Only fractions of microliter of clinical sample would be required for the test. These low volumes of liquid in a small chip could then be processed in minutes, reducing the analysis time dramatically. Moreover, by carrying out all the analysis steps in the same chip the risk of contamination would be minimized, thus enhancing the reliability of the test. The analysis could then be fully automated, making the test transparent for users with minimal training. Integration could then allow for the realization of inexpensive portable instruments that substitute for an entire laboratory, greatly reducing the high cost, complexity and long lead times currently associated to genetic tests.

However, true integration has not been achieved, since most LOC implementations to date require considerable infrastructure and a controlled environment. These limitations make LOC systems bulky and costly. The external infrastructure of a typical LOC system often includes a hydraulic/pneumatic system that controls the fluid in the chip, usually through a set of built-in micro-valves/pumps; heaters, temperature sensors, fans and other components used to control temperature; and electronic boards for temperature measurement, data acquisition, control, and other functions e.g. optical imaging and detection.

If all these components could be integrated in a single chip, LOC systems could be mass-manufactured and could then reach widespread use. We believe that such a level of integration is feasible through the design of robust thermal control systems and the union of the LOC and microelectronics (CMOS) technologies.

2.2 PCR Genetic Amplification

Genetic amplification through the polymerase chain reaction (PCR), is a fundamental molecular biology operation indispensable in a fully integrated molecular diagnosis microsystem. In this operation, a solution containing clinically relevant DNA fragments is subjected to temperature changes in a repeated sequence, causing replication of the DNA molecules by billions. In a typical LOC device, the PCR product is often transferred to the analysis/detection section of the chip, where DNA fragments of different sizes are separated by capillary electrophoresis (CE). In this process the DNA fragments bound to a fluorescent molecule are driven by an electric field past an optical detector. The detected light intensity plotted as a function of time forms an electropherogram whose peaks provide information on the size of the fragments.

The exponential amplification of DNA copies in the PCR process greatly enhances the sensitivity of the CE analysis/detection subsystem, making possible the use of extremely small volumes of clinical sample. PCR, therefore, is a central operation that allows for performing genetic analysis on a chip. The success and yield of PCR, however, strongly depends on rapid and precise temperature control.

2.3 The Central Problems of LOC Thermal Systems

A version of this section will be submitted for publication as part of Article 4 – J. Martinez-Quijada 2014.

As stated in a review by Yager *et al*. [1], a low cost lab-on-chip (LOC) implementation of efficient polymerase chain reaction (PCR) would enable the

widespread use of genetic analysis for point-of-care (POC) disease detection and other applications. The efficiency of PCR in terms of yield and selectivity relies on fast temperature cycling and precise control of the temperature levels [2]. To achieve precise temperature control at a low cost, a new approach for heating and temperature sensing is needed where two key aspects must be considered. Firstly, the system should be robust to allow operation outside the laboratory setting [1], [3], [4]; thereby it is crucial to produce a system that is largely unaffected by changes in the external environment [5]. Secondly, it is essential to implement an accurate temperature measurement method; nevertheless, one of the critical problems in temperature measurement is that it is easy to perturb the system and offset its temperature.

Non-invasive and semi-invasive thermometry systems have been developed to measure the temperature of a PCR sample with minimal or no physical contact, and so minimize perturbation [6], [7], [8]. These systems, however, require considerable pre-calibration and bulky external instrumentation that make them extremely expensive or impractical for use in portable, battery operated LOC-based instruments. Significant efforts using these techniques have been made by researchers such as Kim *et al.* [9] in Raman spectroscopy, Roper *et al.* [10] in infrared thermometry; and Schaerly *et al.* [11] in fluorescence lifetime thermometry, but these techniques remain expensive.

Probes such as wire-based thermocouples and semiconductor transducers are inexpensive, but are *invasive* in the sense that they require direct contact with the chip or the PCR sample [7]. This contact loads the system and can dramatically change its temperature profile [12]. Despite this fact, direct measurements are still common. Recently, Hu *et al*. [13] inserted a resistance temperature detector (RTD) to probe temperature in PCR wells and Hilton *et al*. [3] inserted either an RTD or a thermocouple in a water-filled PCR chamber to calibrate an integrated sensor. Small probes such as thin thermocouples [14], [15] and microfabricated sensors [16] can be embedded in the system as a way to minimize the disturbance.

However, such probes must be isolated from the PCR sample to avoid contamination and PCR inhibition [7]. This isolation causes a difference between the sensor's reading and the target chamber temperature.

The sensor's reading then needs to be corrected to provide an estimate of the true chamber temperature. A correction mapping is typically obtained by inserting a commercial thermocouple in the chamber [2], [16], [17], [18]. Wang *et al.* [16] for instance, calibrated microfabricated sensors against a thermocouple inserted in the PCR chamber; Kim *et al*. [2] calibrated an external thermocouple affixed to the chip against a second thermocouple inserted in the PCR reactor. This strategy, however, is not ideal, because contact with the thermocouple loads the system and shifts the temperature, giving a biased value.. As the LOC technology moves forward, PCR volumes are tending to decrease, and the use (for the purpose of calibration) of commercial wire-based thermocouples and other methods like thermochromic liquid crystals (TLC) [19], [20] is rapidly becoming unfeasible. A mapping can also be obtained by simulation [15], [21], [22], but in many cases the boundary conditions cannot be adequately captured, as they depend on multiple variables that are difficult to measure and control, e.g. ambient temperature, airflow rate and thermal contact, which may vary from device to device. As a result, mappings obtained by simulation are marginally accurate, especially for systems in which the sensor has a significant thermal separation from the chamber.

A temperature correction mapping is also highly dependent on a range of system boundary variables that are difficult to control or are not reproducible, including ambient temperature, airflow rate, thermal contact, surface temperature gradients, etc. Therefore, it is often the case that a particular correction mapping is only valid for a specific operating environment. Consequently, LOC thermal systems are vulnerable to varying external conditions [3], [4], [5], i.e. they are not thermally robust. This is a central problem for which, to date, there has been no

solution reported that is compatible with an inexpensive, mass-producible implementation.

2.4 Sensitivity to Ambient Conditions

In most LOC systems the environmental parameters need to be control to ensure repeatable performance. Many PCR LOC systems rely on natural convection as the primary heat release mechanism [5], [23], [24], [25], [26], [27], which renders them sensitive to variations in ambient temperature and airflow rate. Although these variables were considered in the modeling of some of these systems [26], [27], the effect of their variation was not reported. Continuous flow PCR systems are especially vulnerable to environmental parameters since the heated area in contact with the ambient is typically large [26], [27]. For example, Chen *et al.* [26] developed a glass-PDMS continuous flow PCR system of 26 x 76 mm that needed to be enclosed in a box to shield the device from ambient thermal disturbances. The sensitivity to those disturbances was not quantified. The authors also noted that the temperatures in the system could not be predicted accurately by simulation. The inaccuracy was attributed to a dependence on the thermal contact resistance between the chip and the heating/cooling surfaces, as well as the uncertainty in the actual value of the convective heat transfer coefficient.

It has been recognized that accurate temperature sensing and closed loop feedback are required to ensure appropriate thermal control under varying ambient conditions [5]. Sadler *et al.* [5] reported a continuous flow PCR chip made in a multi-layer low temperature co-fired ceramics (LTCC) architecture with integrated Ag-Pd heaters. Surface mount transistors placed on top of the chip were used for temperature monitoring. Each temperature zone in the system was individually controlled in closed loop. The authors confirmed (with thermocouples inserted in the PCR channels) that temperature can be maintained stable to within ± 0.5 ºC in all zones, irrespective of changing ambient conditions. However they did not provide details about such conditions. and there is no

indication that the system was built for thermal robustness, e.g. the heat flow was not steered in a way that one external variable dominates over all others.

2.5 References

[1] P. Yager, T. Edwards, E. Fu, K. Helton, K. Nelson, M. R. Tam, and B. H. Weigl, “Microfluidic diagnostic technologies for global public health,” *Nature*, vol. 442, no. 7101, pp. 412–418, Jul. 2006.

[2] J. Kim, D. Byun, M. G. Mauk, and H. H. Bau, “A disposable, self-contained PCR chip,” *Lab Chip*, vol. 9, no. 4, p. 606, 2009.

[3] C. D. Chin, V. Linder, and S. K. Sia, “Lab-on-a-chip devices for global health: Past studies and future opportunities,” *Lab Chip*, vol. 7, no. 1, pp. 41–57, Dec. 2006.

[4] C. P. Price and L. J. Kricka, “Improving Healthcare Accessibility through Point-of-Care Technologies,” *Clinical Chemistry*, vol. 53, no. 9, pp. 1665–1675, Sep. 2007.

[5] D. J. Sadler, R. Changrani, P. Roberts, C.-F. Chou, and F. Zenhausern, “Thermal Management of BioMEMS: Temperature Control for ceramic-based PCR and DNA Detection Devices,” *IEEE Transactions on Components and Packaging Technologies*, vol. 26, no. 2, pp. 309–316, Jun. 2003.

[6] P. R. N. Childs, P. R. N. Childs, J. R. Greenwood, J. R. Greenwood, C. A. Long, and C. A. Long, “Review of temperature measurement.,” *Review of Scientific Instruments*, vol. 71, no. 8, 2000.

[7] C. Zhang and D. Xing, “Miniaturized PCR chips for nucleic acid amplification and analysis: latest advances and future trends,” *Nucl. Acids Res.*, vol. 35, no. 13, pp. 4223–4237, Jul. 2007.

[8] C. Gosse, C. Bergaud, and P. Löw, “Molecular Probes for Thermometry in Microfluidic Devices,” in *Thermal Nanosystems and Nanomaterials*, 2009, pp. 301–341.

[9] S. H. Kim, J. Noh, M. K. Jeon, K. W. Kim, L. P. Lee, and S. I. Woo, “Micro-Raman thermometry for measuring the temperature distribution inside the microchannel of a polymerase chain reaction chip,” *J. Micromech. Microeng.*, vol. 16, no. 3, pp. 526–530, Mar. 2006.

[10] M. G. Roper, C. J. Easley, L. A. Legendre, J. A. C. Humphrey, and J. P. Landers, “Infrared Temperature Control System for a Completely Noncontact Polymerase Chain Reaction in Microfluidic Chips,” *Analytical Chemistry*, vol. 79, no. 4, pp. 1294–1300, Feb. 2007.

[11] Y. Schaerli, R. C. Wootton, T. Robinson, V. Stein, C. Dunsby, M. A. A. Neil, P. M. W. French, A. J. deMello, C. Abell, and F. Hollfelder, “Continuous-Flow Polymerase Chain Reaction of Single-Copy DNA in Microfluidic Microdroplets,” *Analytical Chemistry*, vol. 81, no. 1, pp. 302–306, Jan. 2009.

[12] J. Noh, S. W. Sung, M. K. Jeon, S. H. Kim, L. P. Lee, and S. I. Woo, “In situ thermal diagnostics of the micro-PCR system using liquid crystals,” *Sensors and Actuators A: Physical*, vol. 122, no. 2, pp. 196–202, Aug. 2005.

[13] K. Hu, Z. Chen, and J. Huang, “Research on temperature measuring positions selection and verification for Polymerase Chain Reaction instruments,” in *2011 4th International Conference on Biomedical Engineering and Informatics (BMEI)*, 2011, vol. 3, pp. 1165 –1169.
[14] C. J. Easley, J. A. C. Humphrey, and J. P. Landers, “Thermal isolation of microchip reaction chambers for rapid non-contact DNA amplification,” *J. Micromech. Microeng.*, vol. 17, no. 9, pp. 1758–1766, Sep. 2007.
[15] L. Gui and C. L. Ren, “Analytical and Numerical Study of Joule Heating Effects on Electrokinetically Pumped Continuous Flow PCR Chips,” *Langmuir*, vol. 24, no. 6, pp. 2938–2946, Mar. 2008.
[16] J.-H. Wang, L.-J. Chien, T.-M. Hsieh, C.-H. Luo, W.-P. Chou, P.-H. Chen, P.-J. Chen, D.-S. Lee, and G.-B. Lee, “A miniaturized quantitative polymerase chain reaction system for DNA amplification and detection,” *Sensors and Actuators B: Chemical*, vol. 141, no. 1, pp. 329–337, Aug. 2009.
[17] L. Chen, J. West, P.-A. Auroux, A. Manz, and P. J. R. Day, “Ultrasensitive PCR and Real-Time Detection from Human Genomic Samples Using a Bidirectional Flow Microreactor,” *Analytical Chemistry*, vol. 79, no. 23, pp. 9185–9190, Dec. 2007.
[18] Z.-Y. Wu, K. Chen, B.-Y. Qu, X.-X. Tian, X.-J. Wang, and F. Fang, “A thermostat chip of indium tin oxide glass substrate for static polymerase chain reaction and in situ real time fluorescence monitoring,” *Analytica Chimica Acta*, vol. 610, no. 1, pp. 89–96, Mar. 2008.
[19] V. N. Hoang, G. V. Kaigala, and C. J. Backhouse, “Dynamic temperature measurement in microfluidic devices using thermochromic liquid crystals,” *Lab Chip*, vol. 8, no. 3, p. 484, 2008.
[20] G. V. Kaigala, M. Behnam, A. C. E. Bidulock, C. Bargen, R. W. Johnstone, D. G. Elliott, and C. J. Backhouse, “A scalable and modular lab-on-a-chip genetic analysis instrument,” *Analyst*, vol. 135, no. 7, pp. 1606–1617, 2010.
[21] G. Hu, Q. Xiang, R. Fu, B. Xu, R. Venditti, and D. Li, “Electrokinetically controlled real-time polymerase chain reaction in microchannel using Joule heating effect,” *Analytica Chimica Acta*, vol. 557, no. 1–2, pp. 146–151, Jan. 2006.
[22] K. H. Chung, S. H. Park, and Y. H. Choi, “A palmtop PCR system with a disposable polymer chip operated by the thermosiphon effect,” *Lab Chip*, vol. 10, no. 2, pp. 202–210, 2010.
[23] D. S. Lee, S. H. Park, H. S. Yang, K. H. Chung, T. H. Yoon, S. J. Kim, K. Kim, and Y. T. Kim, “Bulk-micromachined submicroliter-volume PCR chip with very rapid thermal response and low power consumption,” *Lab on a Chip*, vol. 4, no. 4, pp. 401–407, 2004.
[24] J. P. Hilton, T. Nguyen, M. Barbu, R. Pei, M. Stojanovic, and Q. Lin, “Bead-based polymerase chain reaction on a microchip,” *Microfluid Nanofluid*, vol. 13, no. 5, pp. 749–760, Nov. 2012.
[25] T. Deng, M. Li, C. Zhao, J. Qin, C. Guo, and Z. Liu, “Characteristic investigation of a static micro polymerase chain reaction chip based on in

situ electrochemical detection," *IET Micro Nano Letters*, vol. 7, no. 12, pp. 1226–1229, 2012.

[26] J. J. Chen, C. M. Shen, and Y. W. Ko, "Analytical study of a microfludic DNA amplification chip using water cooling effect," *Biomed Microdevices*, vol. 15, no. 2, pp. 261–278, Apr. 2013.

[27] S. Kumar, M. A. Cartas-Ayala, and T. Thorsen, "Thermal modeling and design analysis of a continuous flow microfluidic chip," *International Journal of Thermal Sciences*, vol. 67, pp. 72–86, May 2013.

3 Standard Approach for Thermal Control in LOC

This chapter introduces the standard non-robust thermal control approach for LOC systems. The challenges and disadvantages of this approach are identified through the analysis of a typical LOC platform. The analysis shows the need for reducing the number of variables that affect the reliability of the LOC system. The factors that complicate measuring accurately the temperature in the PCR chamber are also illustrated. Those factors have a direct impact on the reliability of genetic diagnosis tests, and increase enormously the costs for calibration. Most if not all LOC systems have been affected by these problems.

The author modeled and analyzed the PCR/CE-4 genetic analysis platform, developed previously by other members of the Advanced Miniaturization Laboratory. Abraham Jang, fabricated the devices and performed measurements such as misalignment distance and surface roughness. The author contributed sensitivity analyses and transient and diffusion simulations.

3.1 System Description

The PCR/CE-4 system, depicted in Figure 1 and Figure 2, is a standard LOC system developed by the Backhouse group at the University of Alberta to test a large number of genetic analysis protocols. This platform is representative of most LOC systems reported to date, which are commonly formed by stacking layers of Polydimethylsiloxane (PDMS) and/or glass with patterned microchannels, microreactors and other fluidic components. It is important to note that some specific features of this platform, such as the ring-shaped heater or the heatsink configuration are not common to all thermal LOC systems. Other heater shapes or external cartridge heaters may be used. The heater may or may not be used as a sensor. The design of thermal LOC systems may vary significantly form one device to another, but most of them suffer from the same fundamental issues of the system presented herein.

The PCR/CE-4 system is comprised of three stages: sample preparation (SP), genetic amplification (PCR) and detection by capillary electrophoresis (CE), which were sufficient to performing a complete genetic diagnosis test. The fluid in the chip was controlled by microvalves actuated pneumatically. A circular thin film Pt element or 5 mm diameter, 200 nm thickness accomplished heating of the PCR sample and temperature sensing simultaneously. The temperature of the heater *Th* could be measured very accurately (±0.15 ºC) from its resistance vs. temperature curve obtained in an isothermal waterbath. The chip was fabricated from a 254 µm PDMS membrane, sandwiched between 1.1 mm thick etched glass plates. This flexible membrane forms the moving part of the microvalves that opens or closes the flow of liquid by the application of vacuum or positive air pressure, respectively.

The bottom plate (control layer) contains the heater/sensor as well as pneumatic channels and cavities cut for the membrane to displace and open the valves upon the application of vacuum (see Figure 2). The top plate (fluidic layer) contains fluidic channels and the 3 mm diameter, 90 µm high PCR chamber.

The chip was placed on top of a finely polished copper heatsink that absorbed the vast majority of the generated heat. The heatsink had a 3.5 mm radius hole (or compartment) in the middle that provided thermal isolation under the heater and chamber. This design allowed heating only the center region of the chip, within the perimeter of the hole, while keeping the rest of the chip at room temperature. The heatsink also accomplished the important role of speeding up temperature stabilization and cooling.

Although the PCR/CE-4 system made possible to carry out complete genetic analyses for the detection of several infections diseases, it is not a manufacturable solution due primarily to the high cost of labor in calibration. The cost of fabrication was also significant since it required glass etching in $HF:HNO_3$ (hydrofluoric + nitric acid), as well as water-jet glass drilling, per-chip manual

assembly and platinum lift-off. The high cost of calibration, processing and materials made the device extremely expensive for mass-production.

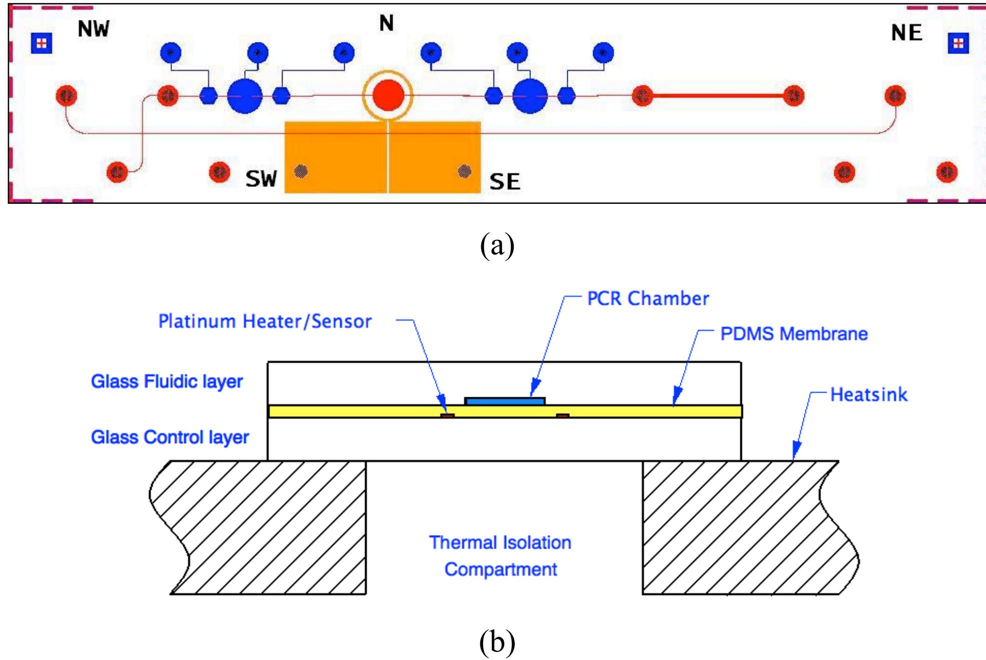

Figure 1. The PCR/CE-4 LOC platform for genetic analysis. (a) Layout of the chip. The channels intersecting on the left constitute the CE stage; at the center, the PCR chamber (red) is surrounded by the thin film Pt heater/sensor (orange). The thicker red channel on the right is the sample preparation stage. (b) Cross section of the chip, showing the components of the thermal system.

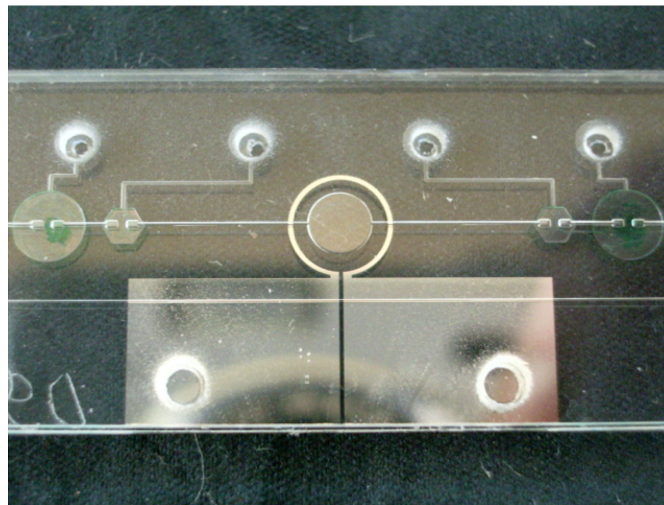

Figure 2. Photograph of the fabricated PCR/CE-4 device. Holes in the glass were water-jet drilled to allow for access to the heater contact pads, pneumatic connections to the valves and fluid ports.

3.2 The Need for a Tc(Th) Mapping

The PDMS membrane had an important role in the thermal system. This membrane spreads out the generated heat, producing homogeneous temperature in the chamber (within a 2 ºC difference between the maximum and minimum temperatures in the chamber). The radius of the heater extending far beyond the chamber's boundary also contributes to create an isothermal environment. The membrane keeps the heater/sensor isolated from the chamber in order to avoid contamination and PCR inhibition.

The use of the PDMS membrane, however, results in a large thermal separation between the heater/sensor and the chamber, which deteriorates the accuracy of the measurement. As shown in Figure 3, it is necessary to reach ~170 ºC in the heater in order to obtain denaturation temperatures (94 ºC) in the chamber. Therefore, although the temperature of the heater/sensor (*Th*) could be measured very accurately, a *Tc(Th)* relation needed to be obtained in order to estimate the true temperature of the chamber. The difference between *Tc* and *Th* also caused a significant waste of power, so reaching denaturation temperature required 2 W.

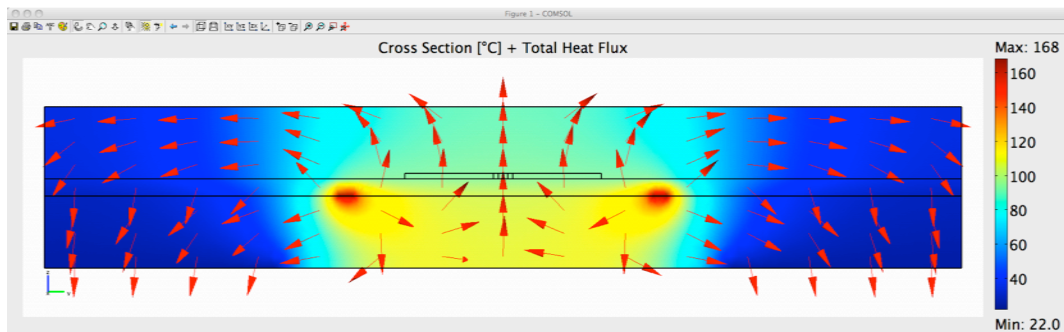

Figure 3. Temperature distribution on the cross section of PCR/CE-4, showing the difference between heater/sensor and chamber temperatures when the chamber is at denaturation temperature (94 ºC). The arrows indicate the direction of the heat flux. In this simulation the top surface and sidewalls of the chip are prescribed a boundary condition of heat loss by natural convection with h=5.6 W/m^2-K (typical value for free convection for heated plates facing up [1]. The bottom surface is imposed a thermal isolation boundary condition in an area of 3.5 mm radius aligned to the heater and chamber. The rest of the bottom surface area is prescribed a uniform temperature boundary condition (22 ºC) to mimic an ideal heatsink,

The *Tc(Th)* relation calculated by simulation was $Tc = 0.559\ Th$. The relation actually programmed into the instruments was determined experimentally.

This relation, however, predicted *Tc* with significant error (1–6 ºC) with respect to experimental measurements. *Tc* was measured using thermochromic liquid crystals (TLC) deposited in the chamber. These crystals undergo a color transition at specific temperatures. The *Tc(Th)* relation was then obtained by detecting visually the color transition and then correlating the corresponding *Tc* to *Th* [1]. However, the color transition occurred gradually and presented hysteresis effects, preventing the accurate measurement of *Tc*.

3.3 Sensitivity to Fabrication Error and Misalignment

We found by 3D simulation that the temperature levels and uniformity of the PCR chamber are strongly affected by fabrication error and geometry variations. We studied the effect of misalignments and PDMS thickness variations on the average chamber temperature *Tc* and the temperature uniformity ΔTc. *Tc* was defined as the integral of the temperatures in the chamber volume divided by the total volume and ΔTc as the difference between the maximum and minimum temperatures found in the chamber.

Misalignment of the PCR chamber with respect to the heater, as shown in Figure 4(a), was one of the most common defects found in the fabricated devices, and occurred during chip assembly. In this operation the glass plates had to be visually aligned and rapidly bonded by-hand onto the membrane right after plasma activation of the PDMS. A simulation of the system operating at $Tc = 94$ ºC showed that *Tc* varies only by < 0.25 ºC with misalignments between 0 to 750 µm. However ΔTc grows by ~0.56 ºC with misalignments larger than 250 µm. Microscope images revealed that this chamber-heater misalignment was often greater than 250 µm and could reach ~ 600 µm in some cases.

Misalignment of the heater and chamber with respect to the hole in the heatsink, as shown in Figure 4(b), was also common. This system-level defect occurred when placing the chip on the heatsink prior to a PCR run. Simulation showed that *Tc* decays quadratically as this misalignment increases since the chamber and

heater get closer to the heat-sunk area. Thus, while a misalignment of 500 µm would cause *Tc* to decrease from 94 ºC to 93.5 ºC, a misalignment of 1 mm would drop *Tc* to 91.5 ºC. The parameter Δ*Tc* is significantly affected, growing linearly by 0.74 ºC per 100 µm of alignment error. Measuring this error was very difficult since there was no clear visual reference around the heatsink hole and refraction through the glass and PDMS hindered precise positioning of the chip. Due to this refraction we estimate the misalignment could easily reach 500 µm.

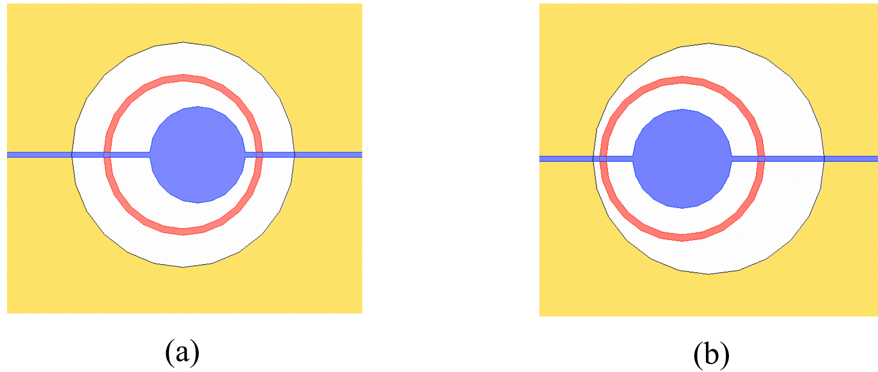

Figure 4. (a) Chamber-heater misalignment occurring during chip bonding. (b) chip-heatsink misalignment occurring during chip placement. Blue – chamber; red – heater; yellow – heatsink.

The PDMS membrane was fabricated in-house by spinning and curing the liquid PDMS mixture. The final thickness of this layer varied by ±20 µm from the target 254 µm. This error was found to be critical, causing *Tc* to shift by -0.054 ºC/µm, resulting in a total shift of ±1.08 ºC. Notably, the uniformity in the chamber improved with thicker PDMS by 0.0076 ºC/µm (the difference between the maximum and minimum temperatures decreased).

In a worst-case scenario, the shift in chamber temperature at denaturation (94 ºC), caused by the combination of PDMS thickness error and misalignments, was estimated to be +4 ºC, and the non-uniformity could reach 4 ºC, dangerously taking the liquid close to the boiling point.

The data obtained from the sensitivity analysis for the defects described above were used to formulate equations that aimed to enable our instruments to correct

for the temperature shifts caused by such defects. This approach was discontinued since it required measuring precisely misalignments and thickness error for each device and enter these parameters prior to a PCR run. Three poorly controlled geometric variables were yielding non-repeatable devices. It was clear that the only way for the instrument to estimate accurately the chamber temperature would be to calibrate each device, i.e. obtain a *Tc(Th)* individually, which increased enormously the cost of the system.

These results showed that maintaining tight control of the fabrication parameters is crucial to obtain repeatable temperatures and reproducible PCR across devices. In other words, a manufacturable design should avoid the need and cost for per-chip calibration. We realized through this analysis that a lithography-only process that avoids any manual assembly could yield reproducible devices, and this would require moving to an entirely new technology.

3.4 Sensitivity to External Variables

The AML group observed in the PCR/CE-4 significant variability in PCR product intensity [2]. PCR was often irreproducible or totally suppressed. This behavior was first attributed to inadequate surface passivation, but later the thermal system was found to be sensitive to factors not considered before, which introduced run-to-run variability. The temperature in the chamber of PCR/CE-4 was estimated from the relation $Tc = 0.559\ Th$, obtained by simulation and fine-tuned experimentally, as explained in section 3.2. The simulation, however, did not account for variations in the boundary conditions. It assumed, for example, complete thermal contact between chip and heatsink. However, experiments and further simulation revealed a significant dependence of *Tc* on variations in the boundary conditions, which made the relation above inaccurate and non-applicable to all the instruments. These difficulties made necessary to calibrate each instrument individually and periodically, increasing significantly the operation cost.

3.4.1 Heatsink and Ambient Temperature Variations

PCR/CE-4 was designed so that heat conduction into the heatsink dominated over convection loss at the top of the chip. Therefore the heatsink temperature *Ths* would mostly determine the rest of the temperatures in the chip. However, variations of heatsink temperature were thought to be negligible, thus *Ths* was not included as a predictor of *Tc*.

Our group indeed observed warming of the heatsink up to 7 ºC above room temperature (22 ºC) over the duration of a PCR run (~1 hr) [3]. To account for this variation, *Tc* was calibrated (with TLC) once the heatsink had stabilized at 30 ºC. Running PCR, therefore, required pre-warming the heatsink with the chip empty for several minutes. The value of *Ths*, however, shifted slowly or did not stabilize at the same level across different instruments, depending on the particular configuration of its ventilation system. The plot in Figure 5, obtained by simulation, shows the effect of variations of *Ths* on *Tc* when a closed loop controller keeps *Th* at ~168 ºC. In these conditions *Tc* would change at a rate of $Tc \approx 0.5\ \Delta Ths$. According to this, a drift of 4 ºC in *Ths* would take the average *Tc* to 96 ºC, but some regions in the chamber would see 97 ºC due to its 2 ºC internal gradient. At those regions, the lifetime of the Taq polymerase would decrease from 40 to 8.4 min. The effects of temperature on Taq lifetime and PCR efficiency will be detailed in section 3.6. Clearly, we required measuring *Ths* accurately and compensating for its variation in real time to obtain an accurate estimate of *Tc*.

PCR/CE-4 was thought to be insensitive to ambient temperature fluctuations, since the heated area in contact with the ambient was apparently very small (3.5 mm radius). It was assumed that by heat- sinking most of the bottom surface of the chip (outside the 3.5 mm radius hole), would constrain the heated volume to a cylinder of 3.5 mm radius through the thickness of the chip. However, the relatively high conductivity of glass caused heat to spread on a greater region, increasing substantially the effective heated area. With a greater area exposed to

the ambient, The system would certainly be more sensitive to varying airflow and ambient temperature.

Fluctuations in ambient temperature *Tamb* were found to shift *Tc* at a rate of $\Delta Tc \approx 0.04\ \Delta T_{amb}$, as shown Figure 5. In our lab where *Tamb* was nearly stable at 22 ºC this sensitivity to ΔT_{amb} could be neglected. However, in uncontrolled environments in different geographies *Tamb* may change dramatically. Variations from 10 to 50 ºC, for example, would shift *Tc* by ~1.6 ºC. For a complete immunity to *Tamb* variations is therefore necessary to reduce this sensitivity and this can be achieved by reducing the effective heated area. Changes of *Tc* were also detected to occur due to random environmental airflow around the chip, as well as air currents leaking from the fans in the instrument. This airflow increased the loss by convection on top of the chip, reducing system temperatures, but its effect could not be quantified accurately, since the velocity/direction of airflow was very difficult to measure.

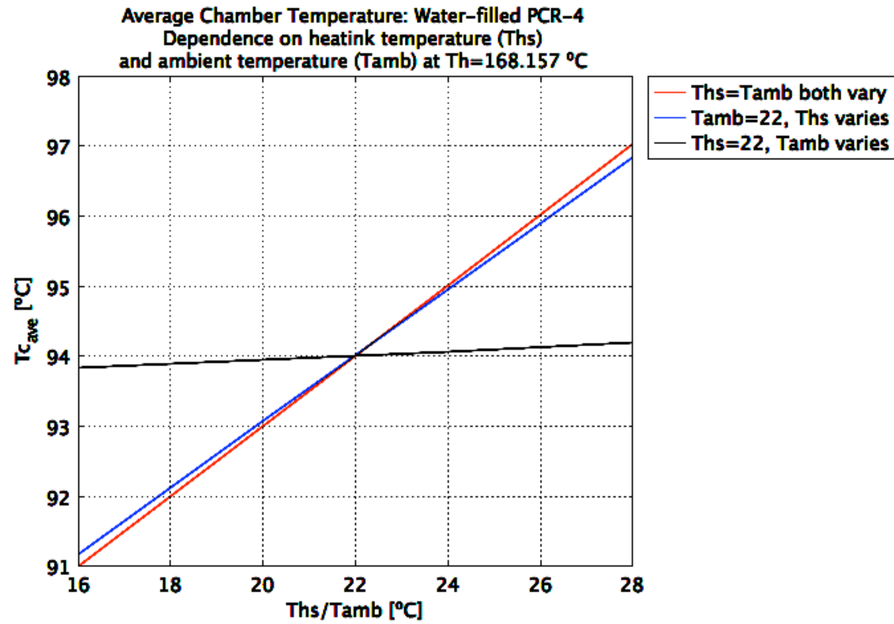

Figure 5. Simulation of the effect of heatsink and ambient temperature variations on the average chamber temperature (at denaturation). The horizontal axis corresponds to the variable that is allowed to change. Red – *Ths* and *Tamb* change simultaneously; blue – *Ths* changes, while *Tamb* is kept at 22 ºC; black – *Tamb* changes, while *Ths* is kept at 22 ºC. A controller that is not aware of changes of *Ths* would keep *Th* constant (168.16 ºC), but *Tc* would shift. At room temperature (22 ºC), Tc_{ave} falls on the target denaturation temperature (94 ºC).

3.4.2 Thermal Contact Variations

We observed significant uncertainty (± 2 ºC) in measurements performed with TLC due to variations in contact between the chip and the heatsink from instrument to instrument. These variations were mainly caused by differences in heatsink surface roughness/flatness and other factors such as contact pressure and microscopic particles. Significant efforts were made to quantify the thermal contact resistance analytically. Such resistance would be included in the simulation model in order to obtain a more accurate *Tc(Th)* relation. However the results from simulation and from mathematical models in literature could not be associated to the measured surface roughness (~1.26 µm RMS). Figure 6 shows sample surface profiles of the heatsink of two different instruments. Although the RMS value is similar between the surfaces, the pattern is different and this caused a difference in contact resistance. A thermal paste was used in order to improve contact and make it more repeatable. However the paste film shifted the

temperatures by up to 4 ºC, depending on its thickness. This thickness was not reproducible, so the use of thermal paste was discontinued. The thermal contact resistance proved to be one of the most difficult boundary variables to determine and control in order to make it reproducible. Later it was found that the large thicknesses of the bottom glass plate along with its relatively low thermal conductivity were responsible for the sensitivity of the system to thermal contact resistance.

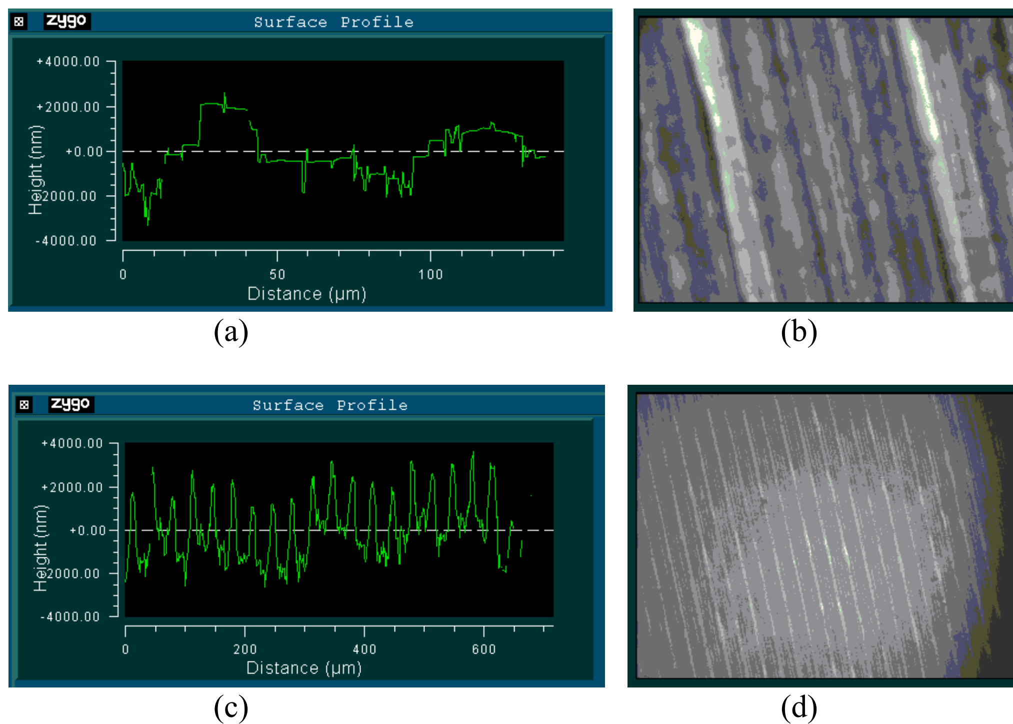

Figure 6. (a,c) Surface profiles of the copper heatsink of two different instruments obtained by optical profilometry. (b,d) Micrographs of the scanned surfaces. The differences in surface roughness caused differences in contact resistance that shifted the system temperatures.

3.5 Time Response

Although the PCR chamber in PCR/CE-4 was fairly small (1.5 mm radius, 90 µm high), the heated volume was substantially larger, due to the thick glass plates and PDMS layer used to build the chip. Considering the heated volume to be a cylinder of 3.5 mm) radius (defined by the heatsink hole) and thickness of 2.454 mm (total thickness of the chip), the heated volume was 94.4 µL, while the

chamber volume was 636.2 nL. In reality the effective heated volume was larger due to heat spreading through glass, as discussed in the previous section. Thus, for the chamber to reach thermal equilibrium it was necessary to mobilize heat in a volume of material two orders of magnitude larger. The large heat capacity of such a volume, combined with the high thermal resistance of PDMS caused the system to respond very slowly. With a time constant of ~ 6 s for *Tc*, a 3-step PCR cycle required ~110 s to complete and a full 30-cycle PCR required ~ 1 hr. Figure 7 shows a dynamic simulation of PCR/CE-4 with hold times as established in our PCR protocols. This simulation made clear that at the chamber level the hold times were actually shorter than expected (10 s), due to the long transient. The programmed time was not allowing for *Tc* to stabilize at the target temperature (94 ºC). The hold times at annealing (20 s, 54 ºC) and extension (20 s, 70 ºC) seemed to be barely respected. The shortening of the hold times, especially at denaturation in this case, could certainly be an important factor that affected the efficiency and reproducibility of PCR.

We learned that in a fast system the top-view area of the heated region should be constrained as much as possible to within the perimeter of the heater, and this required minimizing the horizontal heat spreading through the glass. Moving to a much thinner chip architecture would be also necessary, so as to make the heated volume approximately equal to the chamber volume. Such a reduction of the heated volume would also yield benefits in power consumption.

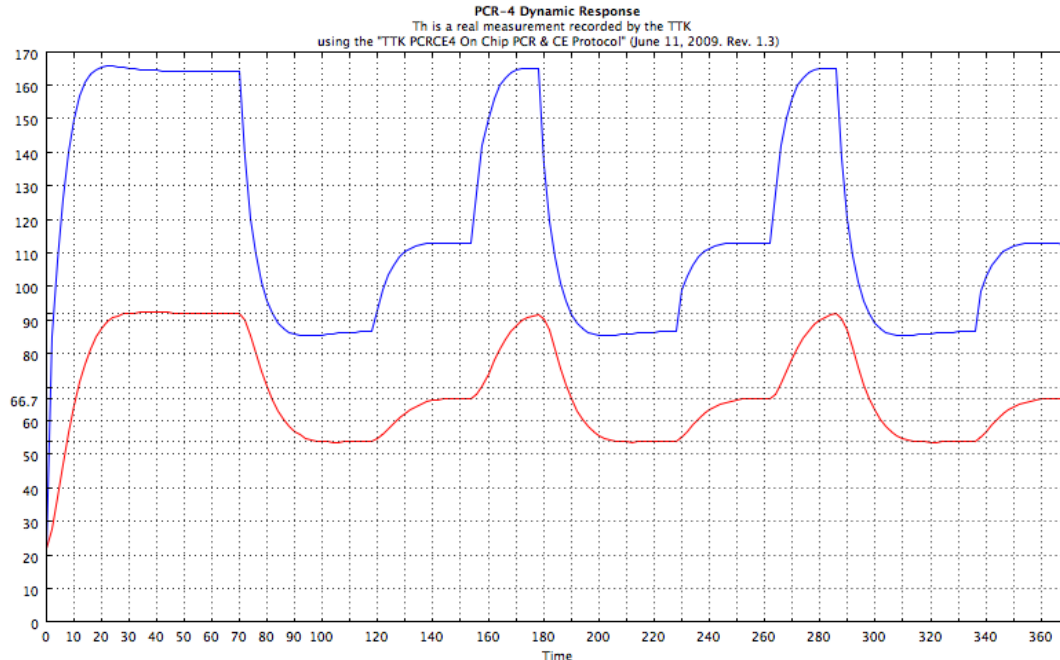

Figure 7. Simulation of PCR/CE-4 showing the average heater and chamber temperatures 4 over time. The units of the vertical and horizontal scales are ºC and seconds, respectively. Blue – *Th*; Red – *Tc*. *Tc* reaches the steady state in approximately $5\tau = 30$ s.

3.6 Effect of Temperature Shifts and Non-Uniformities on PCR

The variations of *Tc* as well as the temperature gradients in the chamber affect directly the lifetime of the Taq polymerase. Taq is the key enzyme that makes possible the replication of DNA fragments in the PCR reaction. The half life of this enzyme, however, decays quadratically with temperature [4]. Thus the stage at which the fastest degradation occurs is at denaturation, when Tc ≈ 94 ºC. As a result the availability of Taq in the PCR brew is reduced during the reaction, making necessary to control its initial concentration and thermal degradation rate.

As shown in the previous sections, temperature shifts and non-uniformities can be caused by variations in the boundary conditions and fabrication error. In order to evaluate the effect of these variations on the PCR reaction, the spatial Taq concentration in the PCR chamber as a function of temperature was simulated. Temperature uniformity is a measure of the magnitude of the temperature gradients in the chamber and was defined as the difference between the maximum

and minimum temperatures across the chamber volume. It was found that the temperature gradients in the chamber could reach more than 2 ºC at denaturation (94 ºC). It was estimated from the manufacturer's generic specifications for Taq [4] that the half life corresponding to these gradients could range from 100 min in the colder regions to 40 min in the hotter regions, without considering diffusion effects.

However, the simulation results, depicted in Figure 8, showed that a 2 ºC non-uniformity in the chamber causes significant concentration gradients of the enzyme. This uneven concentration in turn drives diffusion of Taq towards the hotter regions, where Taq is further degraded. This diffusion effect was found to accelerate degradation and cause a strong decay in the Taq concentration, as shown in Figure 9.

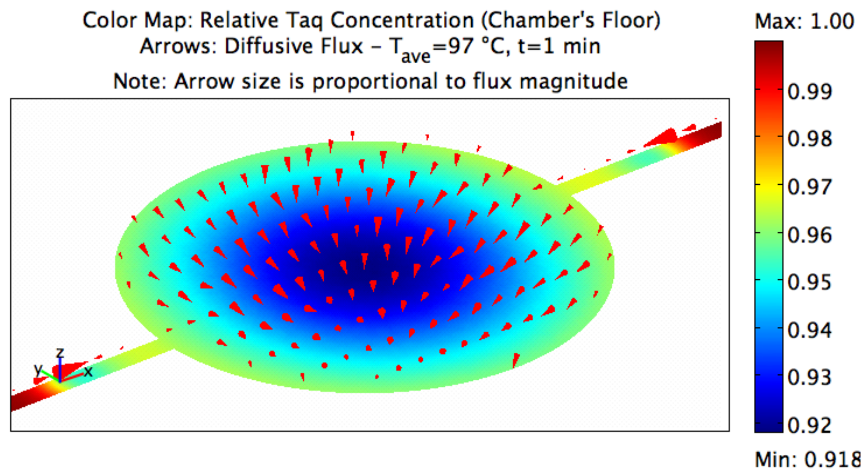

Figure 8. 3D simulation of the Taq concentration and diffusion in the PCR chamber of PCR/CE-4 due to a 2 ºC temperature non-uniformity. The arrows indicate the direction and magnitude of the diffusive flux.

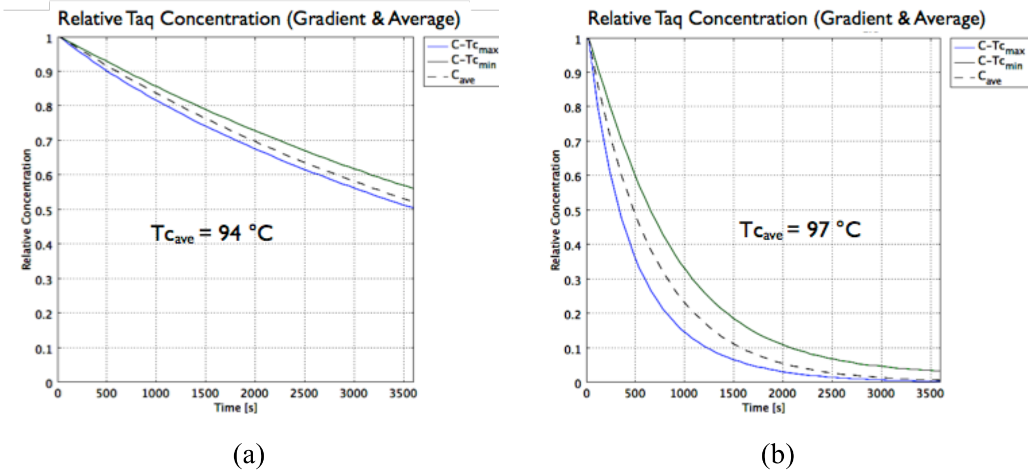

(a) (b)

Figure 9. Relative concentration of Taq in the PCR chamber over the duration of a typical PCR run, calculated by 3D simulation at Tc_{ave} = 94 ºC (a) and at Tc_{ave} = 97 ºC. The fast depletion of Taq is caused by combined thermal degradation and diffusion effects. Blue – concentration at the coldest point; green – concentration at the hottest point; dashed line – average concentration.

The logical solution to the loss of Taq is to increase the initial concentration. However there is a limit in the amount of Taq that can be added to the PCR brew before Taq starts to interfere chemically with itself. The concentration of Taq along a real PCR run at different denaturation temperatures was simulated and the results are shown in Figure 10.

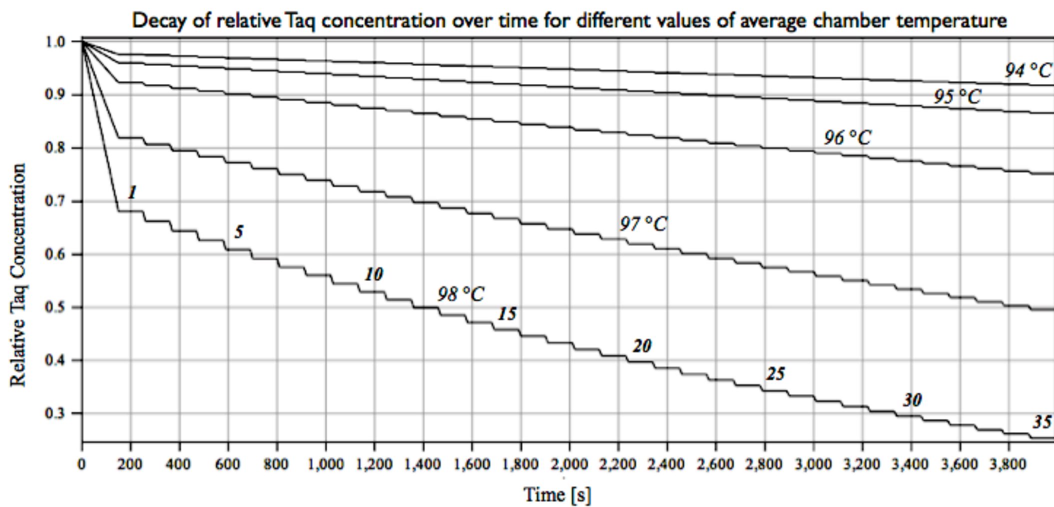

Figure 10. Simulation of the decay in Taq concentration along a real PCR run at different denaturation temperatures.

The obtained curves can be used to choose the best combination of initial concentration as well as denaturation temperature/hold-time for maximum Taq utilization. Most importantly, the results of this analysis show that temperature non-uniformities and shifts of a few degrees of the center temperature may have a profound impact on the success and performance PCR reaction. Besides causing premature depletion of Taq, a poor thermal control could take temperatures above the boiling point of water, leading to failure by evaporation of the PCR mix or destruction of the device.

For these reasons it is crucial to minimize the effect of external variables on the system temperatures. Equally important is to obtain accurate measurements of the chamber temperature, maintain tight microfabrication tolerances and provide high temperature uniformity.

3.7 Appendix A: PCR/CE-4 Simulation Details

The simulations in this chapter were performed on a 3D model of PCR/CE-4 using COMSOL 3.5a and its Heat Transfer module. The properties of the materials in the model are listed in Table 2. Uniform temperature of value *Ths* = 22 ºC was prescribed at the bottom surface of the chip, and convective heat loss on all the other external boundaries. The convective heat loss boundary condition is defined as *Q* = *htc (Ts -Tamb)*, where *Q* is the outward heat flux, *htc* the heat transfer coefficient (5.6 W/m^2-K), *Ts* the surface temperature and *Tamb* the ambient temperature (22 ºC). The heater is modeled as a closed ring surface and imposed a boundary condition of uniform temperature of value *Th* = 168.2 ºC. The heater is also imposed a Highly Conductive Layer (HCL) boundary condition with the thermal conductivity of platinum (72 W/m-K) and 200 nm thickness. The circular hole of 3.5 mm diameter in the heatsink is modeled as a thermal insulation (*Q* = 0) boundary condition at the bottom surface of the chip. For sensitivity analysis the relative position of the chamber and heater, as well as the thickness of the PDMS membrane, were varied while maintaining all other parameters constant.

For the transient simulation along a real PCR run the heater was prescribed a boundary heat source condition (instead of uniform temperature), and through this condition a power of 1.967, 0.927 and 1.31 W was applied for the chamber to reach an average temperature of 94, 70 and 54 ºC, respectively. The hold times at denaturation, annealing and extension were set to 10, 20 and 20 s, respectively. The simulation was run with a variable time resolution of 1–5 s. The average chamber temperature was calculated as the volume integral of the temperatures in the chamber divided by the total chamber volume. The average heater temperature was calculated as the surface integral of the temperature on the heater divided by the total surface area.

For Taq diffusion-degradation analysis a fully coupled heat-transfer/diffusion simulation was performed. The diffusion coefficient for Taq was dynamically calculated from the Stokes Einstein equation as a function of the temperature, viscosity of water and molecular radius of Taq. The simulation tool was set to calculate the viscosity of water pointwise as a function of temperature and a molecular radius of 37.12×10^{-10} m was considered. The half-life of Taq (τ) was calculated by COMSOL from $\tau = 216\, T^2 - 1.6 \times 10^5\, T + 2.98 \times 10^7$. This relation was obtained by fitting a curve to the temperature vs. half-life data for Platinum® Taq (Life Technologies Corp.). The relative Taq concentration and diffusive flux were computed along time for different average values of chamber temperature until the relative concentration reached less than 1 %.

3.8 References

[1] Fontes, J., “Temperature Sensors,” in *Sensor Technology Handbook*, 2005th ed., Oxford: J.S. Wilson, Elsevier Inc., pp. 531–562.
[2] V. N. Hoang, G. V. Kaigala, and C. J. Backhouse, “Dynamic temperature measurement in microfluidic devices using thermochromic liquid crystals,” *Lab Chip*, vol. 8, no. 3, p. 484, 2008.
[3] G. V. Kaigala, M. Behnam, A. C. E. Bidulock, C. Bargen, R. W. Johnstone, D. G. Elliott, and C. J. Backhouse, “A scalable and modular lab-on-a-chip genetic analysis instrument,” *Analyst*, vol. 135, no. 7, pp. 1606–1617, 2010.
[4] V. N. Hoang, G. V. Kaigala, A. Atrazhev, L. M. Pilarski, and C. J. Backhouse, “Strategies for enhancing the speed and integration of microchip genetic amplification,” *Electrophoresis*, vol. 29, no. 23, pp. 4684–4694, 2008.
[5] “Invitrogen, Speifications for Taq DNA Polymerase.” [Online]. Available: http://www.invitrogen.com/site/us/en/home/Products-and-Services/Applications/PCR/pcr-enzymes-master-mixes/taq-dna-polymerase-enzymes/taq_dna_polymerase.html. [Accessed: 27-Aug-2012].

4 A Three-Layer Chip for USB-powered Instruments

As we learned from the analysis of PCR/CE-4, reducing the extent of the heated area would result in a more robust and faster system. Miniaturizing the thermal system could also reduce power consumption, and chip footprints. We undertook the challenge of designing a smaller thermal system using our established glass-PDMS chip architecture. The system had to reach PCR temperatures (60–94 ºC), but with lower power and voltage than its predecessor PCR/CE-4. The target was to fit these requirements to within the capabilities of the USB port of a personal computer (5 V, 500 mA, 2.5 W), yet leaving enough power for the control electronics. The feasibility of building such a device was questionable, because PCR/CE-4 alone exceeded by far the voltage available in a USB port and required 2 W for Tc = 94 ºC, and its control electronics was being powered separately.

In this work the author designed and modeled the thermal system of the presented device. The author laid out the fabrication mask and Abraham Jang fabricated the device. The compact genetic analysis instruments were developed by Govind Kaigala, Mohammad Behnam, Sunny Ho and other members of the group. They also performed the PCR experiments on the developed device.

After testing several designs we succeeded in developing a new LOC platform for low voltage and low power operation. The device (named USBPCR-1), shown in Figure 11, was fabricated with the same process and layer thicknesses as those used for PCR/CE-4. The low electrical requirements of the new chip enabled the use of low power electronics and with this smaller printed circuit boards (PCB), leading to the construction of highly compact genetic analysis instruments powered by the USB port of a laptop computer (shown in Figure 12. The chip dimensions were also reduced considerably with respect to PCR/CE-4, (18 x 95 mm to 19 x 47 mm –SP/PCR/CE, or 12 x 35 mm –PCR), which allowed

instrument miniaturization and portability levels not reached before. Figure 13 compares the size of the thermal system of USBPCR-1 and PCR/CE-4.

The voltage/power requirement (for *Tc* = 94 ºC) were reduced from ~15 V, 2W in PCR/CE-4 to 4.2 V, 0.87 W in USBPCR-1. These requirements are well within the power budget of the USB port, and the remaining available power (1.h3 W) was in fact enough to power the instrument's electronic boards, enabling the USB port to be the only power supply needed by the system. We achieved a substantial reduction of the voltage requirement by splitting the heater ring into two arcs connected in parallel. The total resistance in this configuration is ¼ the resistance of a whole-ring. Thinning the heater and reducing the gap between the heater and the chamber reduced the power requirement.

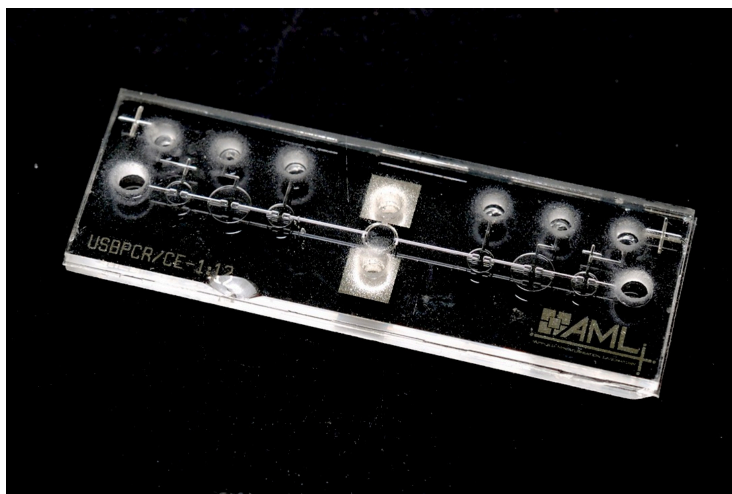

Figure 11. USBPCR-1 system, which integrates a Pt heater/sensor, PCR chamber and micro-valves/pumps. This is the PCR-only variant of the device. Other variants were built with SP and CE sections too.

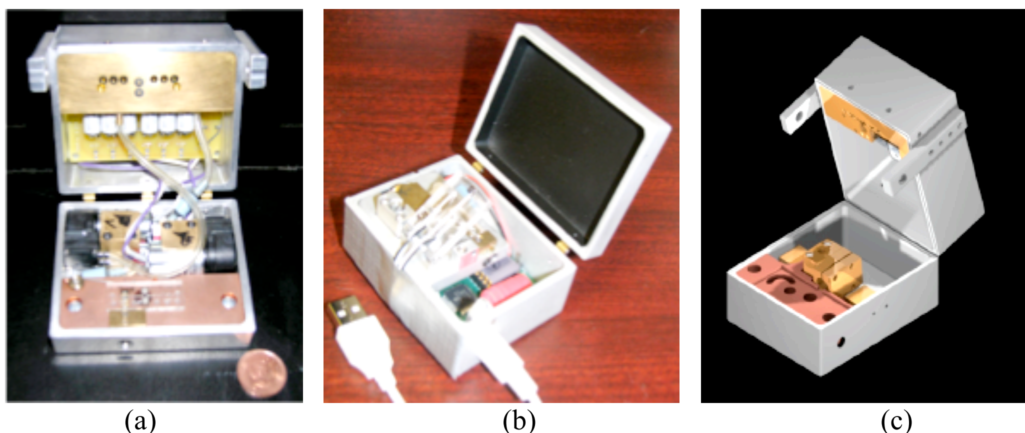

Figure 12. USB-powered instruments enabled by USBPCR-1. (a) Compact PCR instrument that integrates solenoid valves and the pressure/vacuum system necessary to actuate the valves in the chip, as well as the circuitry for thermal and fluid control (dimensions: 2.25" x 2.5" x 3"). (b) Compact CE instrument (dimensions: 3" x 2.25" x 1.5"). (c) Compact PCR/CE system that integrated the functionalities of (a) and (b).

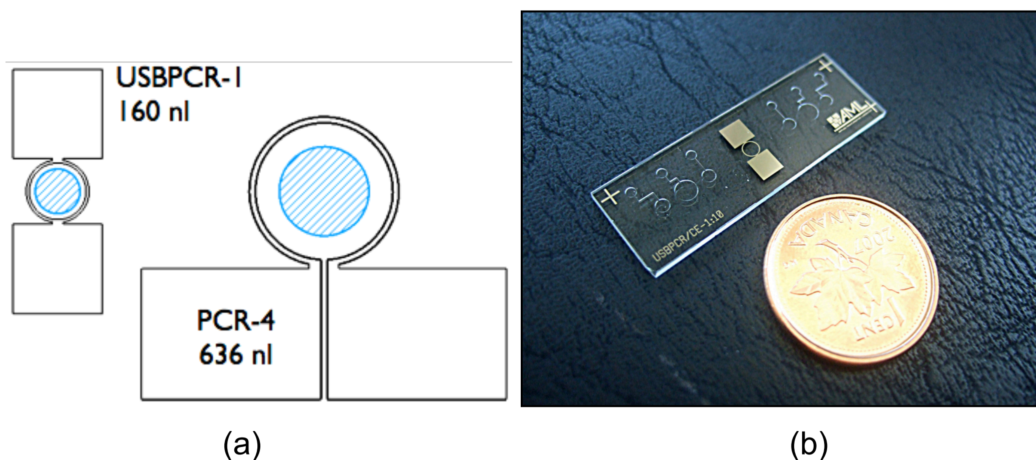

Figure 13. (a) Comparison of chamber and heater size of USBPCR-1 and PCR/CE-4, showing the area of the PCR chamber (blue). The drawings are shown in real proportion. The radius of the hole in the heatsink (3.5 mm) was kept unchanged. The radius of the chamber, inner radius of the heater and heater width was, 1.5 mm, 1.15 mm and 100 µm, respectively. For USBPCR these dimensions were 750 µm, 950 µm and 100 µm. (b) Bottom plate of USBPCR-1 along a coin of $1 CAN.

Remarkably, the analytical calculations and FEM simulations of the design agreed well with experimental measurements in the fabricated device at the first iteration. The target temperatures, as measured with TLC, were met satisfactorily. As a result, a positive PCR run was obtained in the first experiment on this chip, yielding a clear product peak, as shown in Figure 14. This test demonstrated the feasibility of performing PCR in a 160 nL sample volume.

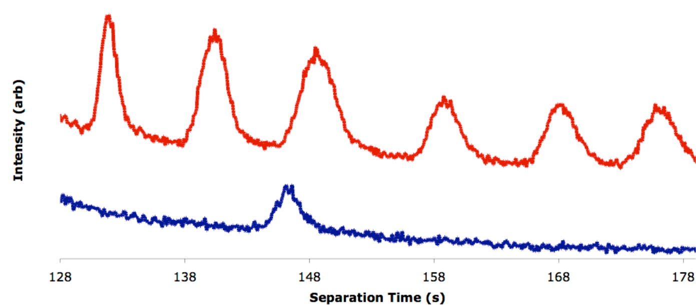

Figure 14. Electropherogram of a successful PCR of BK virus template run on USBPCR-1. The PCR product (blue line) shows a peak size of ~300 bps. A DNA ladder (red line) is run under identical electrophoretic conditions to estimate and validate the size of the PCR product.

The devices, however, did not show significant improvement in robustness or time response, because the heated volume/top-area were approximately the same as for PCR/CE-4. The reason is that with a lower power input, higher thermal isolation was needed to reach the same temperatures. Thus, the size of the thermal isolation area in the heatsink was kept unchanged.

In addition, the devices still required per-chip and per-system *Tc(Th)* calibration, which we performed using TLC. Repeatable devices were also harder to produce with our existing process, since the smaller thermal system required tighter fabrication tolerances. Manual alignment, for example, became very complicated. Also, the holes (~2 mm diameter) for the pogo-pin terminals used to contact the heater had to be drilled very close to the chamber/heater, leaving very small room for error. As the water-jet equipment used to drill through glass did not have enough positioning accuracy, the holes often overlapped the chamber/heater rendering the device unusable. We had clearly reached the limits of our chip architecture. Any further miniaturization of the thermal system would require a profound change of our technology. Nevertheless, producing a truly manufacturable, robust and fast system would require more than just making the chamber and heater smaller. One of the most important factors to control would be the heat spreading radially outside the perimeter of the heater.

4.1 Appendix A: USBPCR-1 Simulation Details

To design the USBPCR-1 system a series of Joule-heating/heat-transfer simulations were performed in COMSOL 3.5a, using its Heat Transfer and AC/DC modules. The model of PCR/CE-4 was used as a base model. Only the diameter of the chamber and shape of the heater were changed and the Current Conduction in Shells physics was added. All other model definitions, including materials and boundary conditions remained unchanged. A Ground and Electrical Potential (~ 4.2 V) boundary conditions were prescribed on the pogo-pins contact points (on the heater pads). The shape, width and radius of the heater, as well as the distance to the pogo-pin contact points were varied until the design specifications were met. Being an iterative method that starts from a best-guess, it was particularly complex to achieve an optimal combination of the geometric variables. After an optimal design had been obtained, the model was used to carry out other studies, such as transient and sensitivity analysis.

5 Thermal Calibration

Our group demonstrated successful genetic amplification in our glass-PDMS platforms [1]–[3]. The PCR process, however, lacked reproducibility and often failed. Inaccurate thermal control was suspected to be a major cause for this problem, which motivated the investigation and development of the method presented herein.

For efficient thermal control we required a non-invasive way of measuring the temperature in the PCR chamber accurately. This would enable our instruments to estimate the true temperature of the PCR mix from the easily measured heater/sensor temperature. The instrument could then compensate for changes of the external environment using a closed loop control, potentially gaining a degree of robustness. Conventional non-invasive measurements, however, are expensive and require elaborate pre-calibration procedures. On the other hand, any direct (invasive) measurement of Tc would be biased by the *observer effect,* which is caused by the interaction between the system and the temperature transducer. This interaction disturbs the temperature distribution of the system, which results in the measured value being different from the actual value [4]. In addition to observer effect issue, the estimation of Tc is typically valid for the specific set of boundary conditions present during calibration. If such conditions change, the real chamber temperature deviates from the estimated one.

The method presented herein is capable of yielding an accurate estimation of Tc, while allowing for boundary conditions to change without affecting the accuracy of the estimation. To do this in an affordable manner, a direct, invasive temperature measurement method is used to obtain a reference value, from which the true Tc is then determined. The first sections of this chapter introduce the methods that we used to measure Tc and the associated observer effect, as well as the challenges involved in estimating Tc by simulation.

The author quantified by simulation the perturbation caused by invasive measurements performed with TLC and thermocouples. The author performed a series of simulations that led to the development of the Delta method, including thermal contact resistance analyses. The author developed and implemented the method and produced calibration equations to replace those used previously by the group. The TLC calibration chips were fabricated by Abraham Jang, Mohammad Behnam and Shane Groendahl. Mohammad and Shane performed the measurements on the calibration chips that the author employed to generate the new calibration equations. Mohammad, Allison and other members of the group carried out the PCR experiments in the instruments calibrated with the new method.

5.1 Observer Effect

TLC was used in our group for long as an economical means to obtain a direct measure of the temperature in the PCR chamber, in order to build a *Tc(Th)* relation. However the observer effect induced by this method had been neglected. In principle, if this effect could be precisely quantified, the measurement could be corrected in order to determine the true *Tc*.

Depositing TLC in the PCR chamber was a complicated process. With the top glass plate facing up, the TLC slurry was applied on the chamber, then scraped and dried. This process always left the chamber partially filled, due to the loss of volume of the slurry in the drying process. After deposition, the glass plates were bonded to the PDMS membrane. A thick air layer then remained trapped in the non-filled portion of the chamber, between the TLC layer and the PDMS membrane.

Air and TLC have thermal conductivities significantly different from that of the PCR brew, which is mostly water. This difference could certainly change the temperature distribution in the PCR chamber and bias the measurement. We studied by simulation the effect of replacing water in the chamber by air, TLC and

other fillers with a controller maintaining the heater temperature constant. The analysis was performed at denaturation (95 ºC), since the largest gradients in the chamber are observed at this temperature. Mineral oil was also included in the analysis for comparison, as it was used as a filler in measurements performed with thermocouples. The results are shown in Figure 15. The temperature at the 90 µm point (top of the chamber and TLC layer) is of especial interest, since the temperature is measured with an spectrometer that images the top surface of the TLC film. The base 3D FEM model of PCR/CE-4 used for the simulations in this chapter is described in section 3.7 Appendix A: PCR/CE-4 Simulation Details.

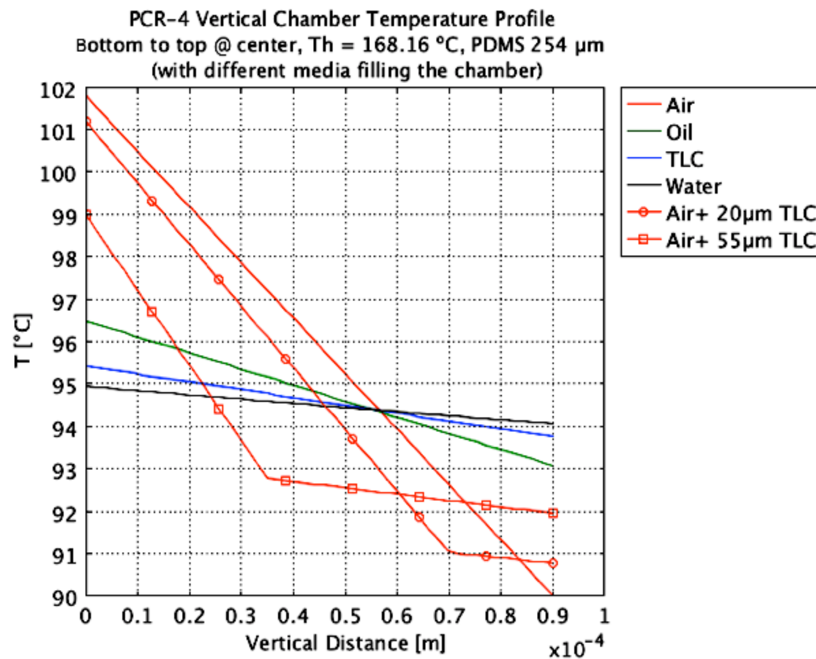

Figure 15. Effect of different materials filling the PCR chamber, calculated by 3D simulation. To emulate closed loop control the heater temperature *Th* is maintained at 168.16 ºC, which produces 94 ºC in a water-filled chamber. The heatsink temperature *Ths* is kept at 22 ºC). The plot shows the temperature at the center of the PCR chamber from bottom to top. The horizontal axis indicates the vertical distance from the bottom (0 µm) to the top (90 µm) of the chamber. The top of the chamber is also the top of the TLC layer. Filling the chamber with a layer of air and TLC causes an abrupt change in the vertical temperature gradient.

From these results we concluded that the presence of air in the chamber caused a huge temperature gradient along the height of the PCR chamber, due to the low thermal conductivity of air (~0.025 W/m-K). All previous simulations made by

the group had considered water, which produces a vertical gradient of only 1 ºC, owing to the relatively high conductivity of water (0.7 W/m-K). It was clear that the measurements done so far were being significantly biased by the presence of air in the chamber.

The TLC layer, having a conductivity of 0.2 W/m-K (~10 times higher than that of air), reduced the total gradient. However in the best case this layer could only fill 61 % (55 μm) of the chamber. Since the optical spectrometer imaged the chamber from the top, the temperature seen by the instrument was 3.2 ºC colder than the temperature that would actually exist if the chamber was filled with the PCR sample. Since the *Tc(Th)* relation had been obtained without taking into account this bias, the electronic controller could be increasing *Tc* by ~3.2 ºC at denaturation, reaching close to 97 ºC. At this temperatures the concentration of Taq could certainly be dramatically reduced, as explained in section 3.6, leading to low PCR efficiency and reproducibility.

The analysis also showed that the measurement could be far more precise if the chamber was completely filled with TLC, as it would produced approximately the same gradient as water (see blue and black curves in Figure 15). Many efforts were made to improve our TLC deposition protocol but the TLC layer could not be made thicker than 55 ± 5.5 μm, as measured with an optical profilometer. With this thickness, the optical spectrometer would still see a chamber 2 ºC colder. Our calibration method should then be able to correct for this shift in order to estimate the true *Tc.*

TLC was limited to detect only one specific temperature, so we used three TLC slurries, sensitive at different temperatures. Therefore three TLC chips had to be prepared, from which we obtained only three data points to construct a calibration curve. To overcome this limitation we considered the use of thermocouples, as this method seemed to be easier and cheaper, and would yield a large number of data points to build a more representative curve.

A thermocouple was inserted in a chip through the PDMS layer until reaching the center of the chamber. Water was pumped into the chamber to create more realistic conditions. However keeping water in the chamber with the thermocouple inserted and the heater turned on proved to be very difficult, due to evaporation. Maintaining the chamber hermetically sealed was no longer possible. The measurements were then performed either with air or mineral oil in the chamber. Oil was preferred because its conductivity is similar to that of water.

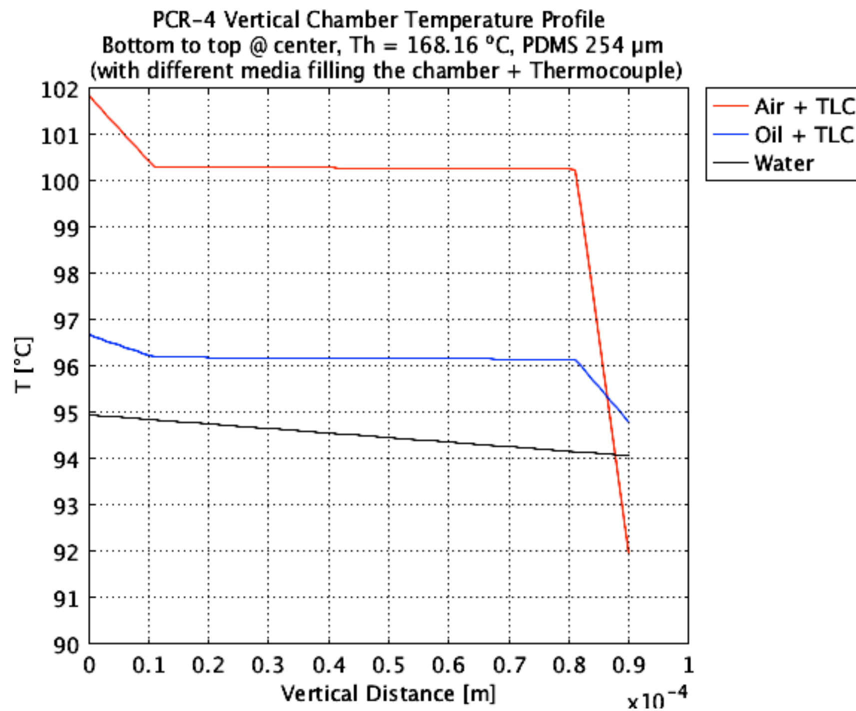

Figure 16. Effect of a thermocouple inserted in the PCR chamber, calculated by 3D simulation. *Th* and *Ths* are maintained at 168.16 ºC and 22 ºC, respectively. In the simulation the 70 µm thick metallic junction of the thermocouple is placed at the center of the chamber. The plot shows the temperature at the center of the PCR chamber from bottom to top, passing through the junction. The horizontal axis indicates the vertical distance from the bottom (0 µm) to the top (90 µm) of the chamber. The temperature is highly homogeneous within the junction due to its high conductivity. The thermocouple positioned exactly in the middle of the chamber would report ~96 ºC for oil or ~100 ºC for air.

The observer effect caused by the thermocouple was quantified by simulation, with the thermocouple's geometry and material properties included in the 3D model of the chip. The results for the junction positioned in the middle of the

chamber are shown in Figure 16. The thermocouple biases the measurement positively, i.e. the measured temperature is higher than the temperature that would exist in absence of the thermocouple, in a chamber containing only water. The reason for the positive bias is that the thermocouple wires cross above the heater ring, transferring additional heat to the junction and chamber. The bias, in addition, is highly dependent on the vertical position of the junction. Notice from Figure 16 that with air in the chamber, the measured value would vary from 102 ºC at 0 µm (junction in contact with PDMS), to 92 ºC at 90 µm (junction in contact with glass). This large uncertainty could be reduced to ~2 ºC (94.8—96.8 ºC) if the filler was oil. In practice the position of the junction could not be determined accurately. Indeed, the measurements performed with thermocouples were significantly less repeatable than with TLC, and varied over time by ~3 ºC, likely due to small displacements of the junction. Other factors such as the oil being constantly replaced, due to leakage, also affected the measurement. With such variability the use of thermocouples was discontinued.

The methods aforementioned were strongly invasive, and the observer effect could not be neglected. Yet TLC was far more repeatable, owing to its stability and relatively small thickness deviation (±5.5 µm), and hence it was kept as the method of choice for calibration. Nevertheless, using this method would require precise quantification of the observer effect.

5.2 Inaccuracy of Simulation Models

Instead of measuring *Tc* using a temperature sensor, *Tc* could be calculated by simulation using a comprehensive mathematical model of the system, thereby avoiding the obersver effect. Such a model would need to describe with great detail the boundary conditions, material properties and geometry of the system. However, the development of very accurate models is considerably expensive, since many of the variables in the system need to be measured precisely. Moreover, changes on these variables need to be tracked for the model to keep predictive power.

Our 3D FEM models captured the fundamental characteristics of the system, but had limited prediction accuracy as they did not include several variables difficult to define or measure or that are not repeatable. We estimated that our models could reach 10–12 % prediction error, arising from assuming ideal boundary conditions and neglecting factors such as: temperature dependence of material properties; chip-heatsink contact resistance; contact resistance gradients; gradients of heatsink temperature; velocity of the surrounding air; and fabrication defects like those described in Chapter 3. Other simplifications included the use of a constant heat transfer coefficient *htc* to model natural convection. This coefficient actually depends on several factors, such as the difference between surface and ambient temperatures and it is difficult to measure, thus a typical value was used. Due to this uncertainty our models could not be used to predict absolute temperatures accurately, but they could still be used to predict relative differences in order to quantify the observer effect.

5.3 Delta Calibration Method

As explained in the previous section, our models have moderate prediction accuracy in the absolute sense, So rather than using the absolute predicted values, we determine the percentage of change due to the observer effect. The percentage of change or *relative difference* is denoted Δ. This factor allows us to isolate the effect of the perturbation caused by the invasive measurement from other variables in the system.

Consider a chip in two states, one in which the chamber is filled with water (the PCR mix), and one in which the chamber is filled with air and TLC. Due to differences in thermal conductivities, the system shows in the chamber a temperature T_{H2O} in the first state and a temperature T_{TLC} in the second state. In section 5.1 we determined by simulation that at denaturation T_{H2O} = 94 ºC and T_{TLC} = 92 ºC. However this result could easily have an absolute error, e , of ±10%, as we estimated in section 5.2. In other words, the error in T_{H2O} and T_{TLC} would be

±9.4 ºC and ±9.2 ºC, respectively. By subtracting T_{TLC} from T_{H2O} we notice that the absolute difference varies with the simulation error. Since the simulation error is significant and its exact value is unknown the absolute difference cannot be used to estimate T_{H2O} accurately. However the relative difference, Δ, defined as the ratio of T_{H2O} to T_{TLC} , is a constant, as shown in Table 1. Therefore Δ depends on the characteristics of the system such as geometry, material properties and boundary conditions, and is a measure of the perturbation caused by the observer effect. Since Δ is independent of the simulation error, it can be used to estimate T_{H2O} if T_{TLC} is known, at any temperature.

	T_{H2O} [ºC]	T_{TLC} [ºC]	Absolute difference $T_{H2O} - T_{TLC}$ [ºC]	Relative difference $\Delta = T_{H2O} / T_{TLC}$
$T + e$	103.4	101.2	2.2	1.022
T	94	92	2	1.022
$T - e$	84.6	82.8	1.8	1.022

Table 1. Calculation of absolute and relative differences under influence of the simulation error. In this example 94 ºC and 92 ºC have been predicted by simulating the system with water or air+TLC in the PCR chamber. The simulation error, *e*, is estimated to be ±10 %. The relative difference Δ is independent of *e*.

The reason for which Δ is unaffected by the simulation error is that by defining Δ as a ratio the error cancels out:

$$\Delta = \frac{T_{H2O} \pm T_{H2O}\ e}{T_{TLC} \pm T_{TLC}\ e} = \frac{T_{H2O}}{T_{TLC}} \qquad \textbf{Eq. 1}$$

This means that the relative difference, Δ, can be predicted accurately using models that capture the most important characteristics of the system, but not necessarily include all the details and variables of it. The relative difference can then be used to obtain a good estimate of the true temperature in the chamber T_{H2O} from the measured temperature T_{TLC}, which serves as an absolute reference. The application of this method, or course, requires the systems (water-filled and air+TLC-filled) to be linear, and maintain a linear relation between them. Therefore we believe that the estimation is valid in steady state conditions, where the systems can be described as a linear combination of thermal resistances.

Figure 17 is a visual representation of the method. TLC is the calibration chip where the reference temperature T_{TLC} is measured. H2O is the chip filled with the PCR mix, where the true temperature T_{H2O} needs to be estimated. Δ is the relative difference between T_{TLC} and T_{H2O} , and it is calculated from approximate 3D FEM models of TLC and H2O. Δ is then used to estimate T_{H2O} from the reference temperature measured in TLC.

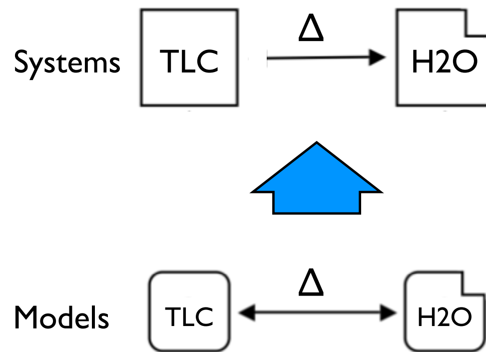

Figure 17. Conceptual diagram of the *Delta Method*. H2O and TLC (top squares) represent the chip filled with the PCR mix and with air+TLC, respectively. The relative temperature difference Δ is a metric of the observer effect, and it is calculated from FEM models of the system. (bottom squares). These models only include the most important characteristics of the systems. Δ is then used to estimate the true chamber temperature T_{H2O} from the measured reference temperature T_{TLC}.

As suggested by **Eq. 1**, if some difficult-to-measure boundary variables are excluded from the models the value of Δ will be unaffected. Therefore, to first order, the true chamber temperature can be estimated accurately using Δ, even if those variables change. The variables that can be excluded are those that do not define a fundamental characteristic of the system, such as contact resistance and others mentioned in section 5.2. Therefore, enabling our instruments to estimate *Tc* in this way reduces the sensitivity of the system to changes of the external environment. Boundary variables, e.g. airflow rate, can of course change, but a closed loop control can adjust the power level to maintain *Tc* stable, effectively eliminating the influence of boundary variables. In addition, since most of the generated heat flows into the heatsink, its temperature dominates over all other boundary variables. By reducing the number of variables that affect the system to

a single dominant variable that can be easily controlled the system becomes robust.

5.4 Practical Implementation and Results

The Delta Method was used to obtain a relation for the PCR/CE-4 platform that enabled the electronic controller to estimate the true temperature in the PCR chamber. As mentioned in section 3.4.1, the temperature of the heatsink *Ths* is the second more important variable that determines *Tc*, but had not been included in the calibration process. *Ths* is now included in this new calibration approach and therefore the estimation relation is *Tc(Th,Ths)*. The practical implementation of the method is divided into three steps: Temperature measurement, Calculation of Δ and temperature correction.

5.4.1 Step 1: Temperature Measurement

A uniform 55 ± 5.5 µm layer of TLC was deposited in the PCR chamber, remaining a ~35 µm thick air layer trapped between the PDMS membrane and the TLC layer. Three different TLC formulations were used that undergo a color transition approximately at 59, 71 and 94 ºC. The exact color transition temperatures were determined by spectral analysis as explained below. The color transition temperatures are indeed the absolute reference T_{TLC}.

The chips were mounted on a holder with an optical probe focusing the top of the TLC film, and then immersed in an isothermal waterbath calibrated with a NIST-certified RTD. The probe illuminated the TLC film and transmitted a ~1 mm diameter image of the TLC film to an spectrometer. In the spectrum of the emission, two distinctive intensity peaks appear at ~460 nm (blue) and ~550 nm (green). As temperature approaches T_{TLC} , both peaks grow by different amounts. In this context we define T_{TLC} as the temperature at which the ratio of the intensity of the green peak *Ig* to the intensity of the blue peak *Ib* reaches a maximum.

The waterbath was ramped in a 5 ºC window around 59, 71 and 94 ºC, in steps of 0.2 ºC. The temperature was allowed to stabilize for 5 min at each step before recording spectrum data. T_{TLC} was then determined by finding the spectrum with the highest Ig/Ib ratio in the 5 ºC window. Once the TLC chips were calibrated, each chip (59, 71 and 94 ºC) was set in the instrument, with the optical probe attached. The instrument then applied a current through the heater, ramping up its temperature to the point of finding the maximum intensity ratio Ig/Ib. At that point, the temperatures of the heater Th and heatsink T*hs* were recorded. This process was repeated for the three TLC chips. The temperature of the heater was calculated from its resistance vs. temperature curve, obtained by waterbath calibration. This curve was obtained for each chip. The heatsink temperature was measured with two waterbath-calibrated thermocouples taped to the heatsink at the edge of the chip. The readings of the thermocouples were averaged to obtain Ths.

5.4.2 Step 2: Calculation of Δ

Two 3D FEM heat-transfer models of PCR/CE-4 were constructed. In the first model, called H2O the entire chamber was given the thermal conductivity of water. In the second one, denoted TLC the chamber was divided into two domains of 35 µm and 55 µm thickness, with the conductivity of air and TLC, respectively. Table 2 shows the conductivity of the materials used in simulation.

Material	*k* [W/m-K]
Air	0.0252
Water	0.58
TLC (average in the range 0.2-0.4)	0.3
PDMS	0.18
Borosilicate glass (B_2O_3, 65-70 % SiO_2, at 100 ºC)	1.1
Oil (generic)	0.138

Table 2. Thermal conductivities (k) of materials used in simulation.

The output of the H2O model is Ts_{H2O} , which is the average chamber temperature. In the simulation context Ts_{H2O} is defined as the volume integral of

the temperature in the chamber divided by its total volume. The output of the TLC model is Ts_{TLC} , which is the average image temperature . T_{TLC} is defined as the surface integral of the temperature along the surface on top of the TLC layer imaged by the spectrometer, divided by its total area (1 mm diameter). Δ is calculated as the ratio of these two temperatures:

$$\Delta = \frac{Ts_{H2O}}{Ts_{TLC}} \quad \textbf{Eq. 2}$$

Ts_{H2O} and Ts_{TLC} are functions of *Th* and *Ths*. The evaluation of these functions will give one value of Δ to correct each measured temperature T_{TLC}.

To construct the Ts_{H2O} and Ts_{TLC} functions the models were solved for different combinations of *Th* and *Ths*. The result is two matrices of temperatures. Table 3 shows the matrix for Ts_{H2O}. The matrices were then fitted to a linear model of the form:

$$Ts_{H2O} = a_1 + a_2 Th + a_3 Ths \quad \textbf{Eq. 3}$$

Th [ºC]	*Ths* [ºC]	Ts_{H2O} [ºC]
168.157	16	91.0061
168.157	20	93.0096
168.157	24	95.0139
168.157	28	97.019
121.425	16	68.0198
121.425	20	70.0299
121.425	24	72.041
121.425	28	74.0531
97.044	16	56.0086
.044	20	58.022
97.044	24	60.0364
97.044	28	62.0518

Table 3. Sample temperature matrix obtained by solving the H2O model for different combinations of *Th* and *Ths*. Ts_{H2O} is centered at *Th* = 94, 71 and 59 ºC and *Ths* = 22 ºC. *Th* – heater temperature; *Ths* – heatsink temperature; $Ts_{H2O\ ave}$ – average chamber temperature.

The same combinations of *Th* and *Ths* are used to obtain the matrix for Ts_{TLC}. The coefficients of the functions resulting from surface fitting are shown in Table 4.

Coefficient	Ts_{H2O}	Ts_{TLC}
a_1	0.2452	0.3074
a_2	0.4919	0.4775
a_3	0.5025	0.5155

Table 4. Coefficients of the Ts_{H2O} and Ts_{TLC} functions obtained by simulation.

The fitted functions allow for calculating Δ for any combination of *Th* and *Ths* in the next step of the process. The simulation of the TLC model showed that the temperature in the TLC layer is highly uniform (~0.13 ºC difference between maximum and minimum temperatures) across the imaged area. Therefore it is reasonable to describe the entire TLC layer as a single temperature value.

5.4.3 Step 3: Temperature Correction

A Δ value must be calculated to correct each of the measured data points. This calculation is performed by evaluating the Ts_{H2O} and Ts_{TLC} functions at the *Th* and *Ths* recorded for each data point. Δ is then calculated from **Eq. 2**. Finally the T_{TLC} of each data point is multiplied by its corresponding Δ in order to estimate the true temperature T_{H2O} ;

$$T_{H2O} = \Delta\, T_{TLC} \qquad \textbf{Eq. 4}$$

Table 5 shows the data points [T_{TLC},*Th*,*Ths*] obtained experimentally, the corresponding Δ and the estimated true temperature T_{TLC} . The largest error due to the observer effect is ~2 ºC, and is observed near denaturation temperature, as expected. By fitting a plane to the corrected T_{H2O} data (columns 2, 3 and 5 in Table 5), the final *Tc(Th, Ths)* relation is obtained, which is directly programmed in the instrument. *Tc(Th, Ths)* is a polynomial of the same form of **Eq. 3**. The deviation of Δ is very small (±0.0021 around an average of 1.0205), which confirms that this parameter is essentially a constant.

T_{TLC} [ºC]	*Th* [ºC]	*Ths* [ºC]	Δ	T_{H2O} [ºC]
58.4	98.86	23.1	1.0178	59.44
58.0	99.74	23.3	1.0178	59.03
70.4	127.02	22.7	1.0202	71.82
70.4	127.36	23.0	1.0201	71.81
93.6	177.16	22.4	1.0227	95.72
93.6	177.97	23.1	1.0225	95.71
93.6	179.50	23.4	1.0225	95.71

Table 5. Correction of the measured temperatures made to estimate the true temperature in the chamber T_{H2O}. The first column is the measured temperature that serves as an absolute reference. *Th* and *Ths* are the heater and heatsink temperatures recorded along with T_{TLC} . Δ is calculated at these *Th* and *Ths* through the functions Ts_{H2O} and Ts_{TLC} . The value of Δ is essentially constant.

5.4.4 Improvement of the PCR Performance

Rather than trying to validate by experiment the temperatures that we calculated, we observed the effects of the new calibration on the PCR reaction. Experimental validation would require very expensive non-invasive thermometry, which we aim to avoid with the method presented herein.

The implementation of the Delta Method resulted in significantly improved thermal control, which we perceived as a substantial enhancement of the reproducibility and strength of the PCR product peak intensity, across our different instruments and PCR protocols. The three calibrated instruments had different arrangement of their ventilation system, heatsink finish and material (polycarbonate or brass) of the gantry that interfaces the chip to the pneumatic/electrical subsystems. The instruments were operated in laboratories with different ambient temperature and airflow conditions. Despite this external variability, PCR experienced a remarkably high success rate and efficiency, which is consistent with the expected robust behavior.

We use the relative yield as a metric of the PCR efficiency. The relative yield is the percentage of primers in the PCR brew that were actually used to synthesize new DNA in the reaction. From the electropherogram of the PCR product we calculate the relative yield as the ratio of the product peak height to the sum of the

heights of the product peak and primer peak [5]. With the old calibration scheme the relative yield was typically 8.1 % and increased to 25.8 % immediately after calibrating the systems with the Delta Method. For details of the PCR experiments refer to [5]. The improved thermal control then enabled a long series of real time PCR (qPCR) and melting curve analysis (MCA) experiments documented in [6].

Although the chamber temperature cannot be easily measured, it is possible to draw some conclusions by contrasting the estimated true temperature with the *Tc(Th)* relationship, programmed previously into all our systems. Figure 18 shows a plot of the old relation (dashed line), along with three points of T_{TLC} measured in the new calibration, with the corresponding estimated true temperature T_{H2O} .

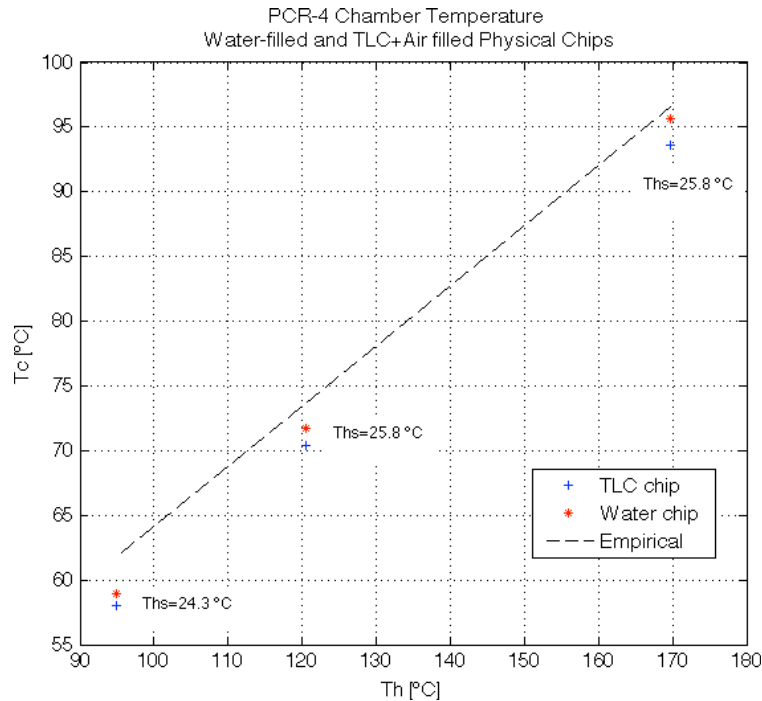

Figure 18. Comparison of the old and new calibration schemes. (+) Measured reference temperature T_{TLC} ; (*) estimated true temperature T_{H2O} ; dashed line – *Tc* predicted by the old *Tc(Th)* relation. For clarity, the third dimension of the new relation (*Ths*) is not shown, but its value is indicated.

These results reveal that with the old relation the chamber was running cold at least by ~3 ºC at annealing (lower range), ~2 ºC at extension (middle range) and ~1 ºC at denaturation (upper range). It was colder because the temperature controller erroneously estimated *Tc* to be higher than the what we consider is the

true value, so it responded by lowering *Th* in its effort to reach the target temperature.

Low annealing temperatures may produce nonspecific amplification or reduce PCR yield. On the other hand, although the chamber seemed to run cold at denaturation, the old relation did not consider the heatsink temperature. Therefore the system could not compensate for shifts of *Ths*, as well as variables that affect *Ths*, such as ambient temperature. Shifts of *Ths* and other factors, such as the 2 ºC gradient in the chamber, as well as the inadequate control of fabrication error in our process could easily take the chamber to the upper denaturation range, where Taq lifetime decays rapidly. Moreover, the old relationship is essentially incorrect, because it does not converge to 22 ºC at *Th* = 22 ºC, i.e. when the heater is unpowered. Thus, it is reasonable to assume that the old calibration process was responsible for the erratic behavior of PCR.

5.5 Conclusion

Many thermal LOC systems suffer from the observer effect, caused by invasive calibration methods. This effect is difficult to quantify and it is often neglected, leading to poor thermal control. We developed a method that enables a LOC instrument to estimate the true temperature of the PCR chamber in a non-invasive way. This is achieved by using two approximate FEM models and a reference temperature system. A correction factor Δ calculated by simulation is used to estimate the true temperature in the PCR chamber from the measured reference temperature. The factor Δ is defined multiplicative, i.e. as a relative difference, in order to quantify (as a percentage) the change in chamber temperature caused by the observer effect. In this way the value of Δ is valid for any temperature and is independent of the simulation error. Therefore the value of Δ and the accuracy of the estimation are unaffected by difficult to measure variables not included in the models. Defining Δ as additive, i.e. as an absolute difference, does not yield these advantages, as explained at the beginning of section 5.3. This calibration method

yielded clear benefits in PCR efficiency and reproducibility, and appeared to provide a significant degree of robustness to the system.

Despite this success, the calibration process is still very complex and expensive for a manufacturable LOC implementation. The root of this problem is the large difference between the heater/sensor and chamber temperatures. This problem cannot be solved simply by placing these elements next to each other, as this would cause dramatic temperature non-uniformities in the chamber – something that a closed loop control cannot fix. Those gradients would in turn deteriorate the accuracy of the measurement. Therefore the solution should lie in immersing the three elements, chamber, heat source and temperature sensor in a local isothermal environment, so that the sensor reading effectively represents the entire temperature of the system. In a truly robust system such an isothermal space should keep high temperature uniformity irrespective of varying boundary conditions.

Note: In this work the temperatures were calculated with respect to 0 ºC. In future work the method could be improved by calculating temperatures with respect to a reference temperature To. For example, T_{H2O} would become T_{H2O} - To. This would allow obtaining accurate values for Δ in any temperature measurement system, e.g. degrees Kelvin. The initial heatsink temperature could be taken as the reference To.

5.6 References

[1] G. V. Kaigala, V. N. Hoang, A. Stickel, J. Lauzon, D. Manage, L. M. Pilarski, and C. J. Backhouse, “An inexpensive and portable microchip-based platform for integrated RT–PCR and capillary electrophoresis,” *Analyst*, vol. 133, no. 3, p. 331, 2008.

[2] G. V. Kaigala, Jingbo Jiang, C. J. Backhouse, and H. J. Marquez, “System Design and Modeling of a Time-Varying, Nonlinear Temperature Controller for Microfluidics,” *IEEE Transactions on Control Systems Technology*, vol. 18, no. 2, pp. 521–530, Mar. 2010.

[3] G. V. Kaigala, M. Behnam, A. C. E. Bidulock, C. Bargen, R. W. Johnstone, D. G. Elliott, and C. J. Backhouse, “A scalable and modular lab-on-a-chip genetic analysis instrument,” *Analyst*, vol. 135, no. 7, pp. 1606–1617, 2010.

[4] P. R. Childs, *Practical Temperature Measurement*. Oxford, UK: Butterworth-Heinemann, 2001.

[5] A. C. E. Bidulock, *Scalable, modular, integrated genetic analysis systems*. University of Alberta (thesis), 2011.

[6] A. O. Olanrewaju, *Towards a portable and inexpensive lab-on-a-chip device for point of care applications*. University of Alberta (thesis), 2011.

6 A New LOC Multilayer Polymer Technology

As we learned from the previous work, robust thermal control requires isolation from the external environment as well as microfabrication repeatability. Polymers such as SU-8 and KMPR support rapid and inexpensive fabrication of three-dimensional structures and can provide strong thermal isolation due to their low thermal conductivity. They can also be directly photo-patterned, which allows for precise alignment of features - one of the main issues of our earlier technology. KMPR in particular is well suited for LOC applications as it is resistant to moisture [1]. These characteristics enable the fabrication of repeatable, mechanically stable, high-resolution structures.

In this work the author participated actively in the development of the multilayer polymer architecture in a joint effort with Robert Johnstone, and Luis Gutierrez-Rivera. The author designed and simulated the thermal system of the PC6-K device. The author designed and simulated the FTC-1 device. Robert Johnstone developed a 4-layer KMPR process that was later improved by the author and Luis Gutierrez-Rivera. The author and Luis performed capillary filling experiments in 3-layer KMPR chips to obtain the filling velocity data necessary to design the FTC-1 chip. The author and Luis made significant efforts to develop KMPR-based microvalves using a selective bonding process proposed by the author. The author and Luis fabricated the microvalves and tested them using a pneumatic actuation system developed by the author.

Aiming to produce truly robust and manufacturable devices we developed a radically new chip architecture, which consists of stacking and bonding several pre-patterned layers of KMPR onto a substrate. The basic structure of a PCR system made in this architecture is shown in Figure 19. In the system a thin film heater underlies a fluid chamber encapsulated between KMPR layers 2, 3 and 4.

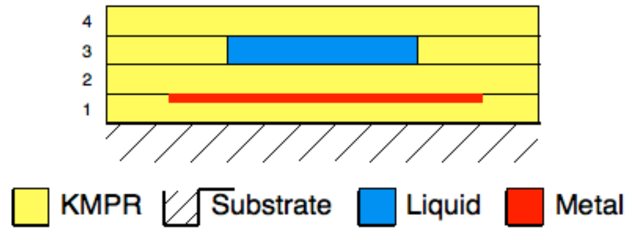

Figure 19. Structure of a PCR LOC system made in the new multilayer polymer architecture. A thin film heater between layers 1 and 2 underlies a PCR chamber patterned in layer 3.

By pre-patterning the individual KMPR layers it is possible to fabricate intricate structures containing a variety of interconnected microfluidic components, e.g. microchannels, microreactors and potentially microvalves. Moreover, patterned metal films can be embedded between layers, making possible the integration of electrical components, e.g. electrodes, heaters and sensors, increasing enormously the functionality of the device. With these elements it is possible to construct more complex components, such as electrostatic valves or capacitive pressure sensors.

The thickness of every layer in this architecture can be adjusted independently with micrometer precision. This flexibility allows for regulating and guiding the heat flux to fit the particular needs of the system. Moreover, the effective thermal mass of the system can be fine-tuned to achieve higher heat transfer rates. By thinning the structure a more intimate coupling between the PCR chamber and heater/sensor can also be achieved, which is key in eliminating complex and expensive calibration procedures. From this we believe that multilayer polymer architectures are the key to design manufacturable devices with highly precise and robust thermal control.

A remarkable advantage of this new technology is that the processing of KMPR, as well as the metal deposition (by sputtering), are carried out at low temperatures (< 200 ºC) that do not damage CMOS components. If in addition the metal is compatible with a CMOS process, LOC functionalities could be integrated onto a CMOS die, and with this create a monolithic, self-contained genetic analysis

instrument. Such a single-chip instrument could be packaged in a USB-key or memory card format and cost a few dollars.

As we moved towards a manufacturable and robust system we needed to understand the requirements of the new technology. For this purpose, we carried out preliminary designs of two multilayer LOC systems that are presented in the next sections. These designs showed the need for several new technologies. Namely, methods to fabricate reliable multilayer structures, to metalize polymers and to design thin film heaters/sensors. The developed methods are presented in chapters 7, 8 and 9.

6.1 A Low Power Genetic Analysis Platform

A 4-layer polymer system, denoted PC6-K, was designed to replicate the functionality of the PCR/CE-4 platform. The system integrated in a single chip SP, PCR and CE sections, as well as pneumatic microvalves for fluid control. These elements would be sufficient to perform a full genetic analysis. The cross section of the PCR system connected to one of the microvalves is displayed in Figure 20. The layout of the whole device is shown Figure 21(a). We made significant efforts to develop working KMPR valves capable of maintaining a strong seal at the pressures generated within the PCR chamber, However the fabrication of KMPR valves is challenging and is the subject of ongoing research. The development of PC6-K also aimed to test KMPR for its chemical compatibility with the PCR reaction in a chamber of high surface to volume ratio.

In this design we introduced the concept of *air bridges*, i.e. air-filled cavities built within the polymer structure. Air can provide roughly ten fold stronger thermal isolation than KMPR. Therefore suspending the heater and PCR chamber on an air bridge can yield substantial power savings.

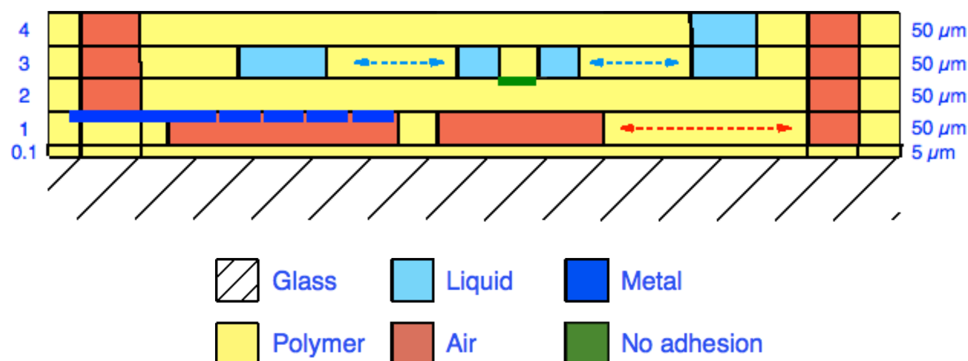

Figure 20. Cross section of the PC6-K system. The PCR chamber is patterned in layer 3 and a thin film heater suspended on an air bridge that is patterned in layer 1. On the right portion of the diagram there is a pneumatic microvalve structure that comprises a flexible diaphragm and a cavity underneath where either vacuum or pressurized air are applied to open/close the valve. A non-adhesive area is required to prevent the diaphragm from sticking permanently to the valve seat.

Highly manufacturable devices would require the use of metals cheaper than platinum and compatible with a CMOS process. This thought motivated the investigation of TiW and aluminum as an alternative to platinum, commonly used for the fabrication of heaters and temperature sensors in the LOC field. We found that direct metallization on polymers involves several challenges and discarded the use of TiW, since the film was not mechanically and electrically stable on KMPR. We successfully developed a method to produce stable Al heaters/sensors on KMPR that are suitable for PCR. This method was key in making our technology compatible with the CMOS technology. The method is discussed in Chapter 8.

The heater in PC6-K consisted of three concentric rings connected in parallel, as shown in Figure 21(b-c). An independent temperature sensor was patterned on the same metal layer of the heater, The heating and sensing functions were separated in order to measure temperature only within the small region below the PCR chamber, which was much smaller than the heater. In this design we also explored for the first time the use of a 4-point mode temperature sensor, wherein a current is passed through and the voltage is measured across the element to derive its resistance. 4-point measurements are very accurate since the error produced by parasitic resistances is practically eliminated. Some significant parasitic

resistances are those of wires and connectors and the contact resistance of terminals on the metal film. Similarly as in the glass-PDMS devices, PC6-K required a heatsink with a hole to thermally isolate the heater and PCR chamber.

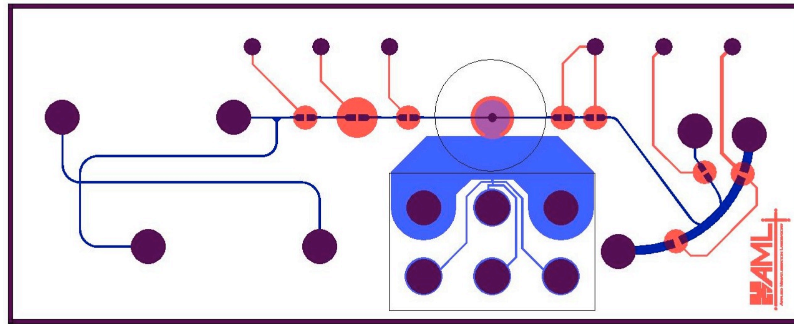

(a)

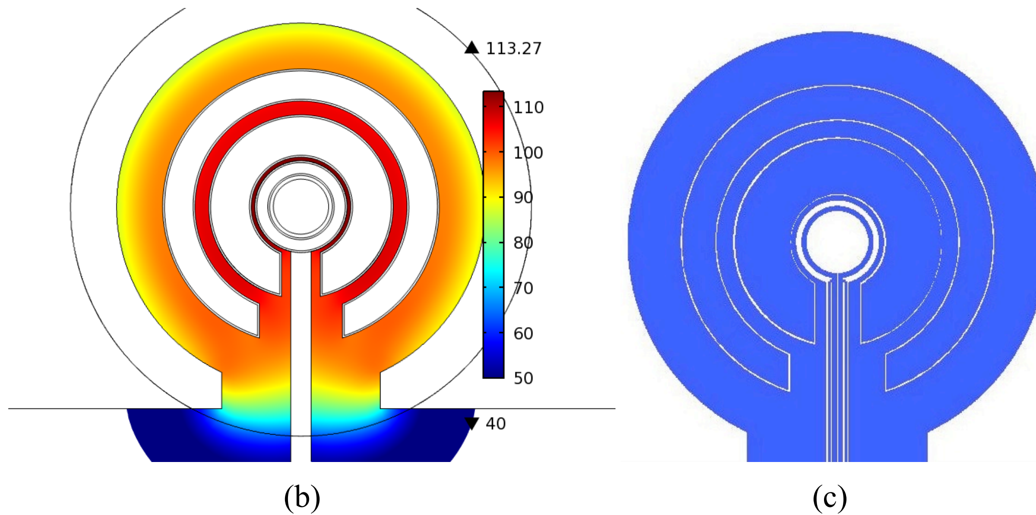

(b) (c)

Figure 21. (a) Layout of the PC6-K system, a 4-layer polymer chip based on PCR/CE-4. (b) Temperature field of the heater at full power (~100 mW). The heater is composed of three concentric rings connected in parallel. (c) Mask layout of the heater and 4-point sensor. The innermost ring in (b) is the 4-point sensor, with two (thicker) tracks for the drive current and two (thinner) tracks for voltage sensing. The gaps between the three heater rings were filled with unconnected metal to improve temperature uniformity.

Simulation of the system showed that a 100 μm deep air bridge could reduce the power consumption to 100 mW at the highest PCR temperature (94 ºC). This level of power consumption was a significant achievement, as it was nearly nine times lower than the power requirement of USBPCR-1. The low power consumption of PC6-K enabled the design of a driving circuitry for the heater and

sensor based entirely on surface mount technology (SMT) components. The circuit board would use a single +5V power supply and would be several times smaller than the equivalent board for PCR/CE-4 and USBPCR-1. The final heater and sensor specifications are listed below:

- **Heater and chamber specifications** – 100 mW power consumption at Tc=100 ºC (200 mA and 0.5 V); 2.5 Ω total resistance; 200 nm aluminum film, 20, 75 and 250 µm wide tracks; 30, 55 and 115 mA per track; 500 µm diameter, 10 nL volume chamber; 2 mm diameter, 200 nm thickness heater; 2.5 mm diameter, 100 µm height airbridge; 50 µm thick layer 2, 3 and 4; 4.2 ºC chamber temperature uniformity (maximum minus minimum temperature) at Tc = 100 ºC.

- **Sensor specifications** – 150 µm inner radius; 20 µm width; 72 µV/ºC sensitivity; 5.6 mV voltage variation with 10 mA current in the range of 22–100 ºC; 250 mV voltage across terminals at 22 ºC; 733 total gain required to cover ADC range with a 4.096 V reference.

We observed that the thin polymer structure had the effect of forcing heat to flow in the vertical direction. The entire KMPR structure was only 250 µm thick and its thermal conductivity was ~ 18 % the conductivity of glass. This combination produced a very high horizontal resistance to heat flow. At the same time, the thinness of the structure produced a small vertical resistance, even in presence of the air bridge. This high horizontal to vertical resistance ratio favored vertical conduction. As a result, most of the generated heat concentrated tightly in a region of only 2 mm diameter, as shown in Figure 22 and Figure 23. We realized that this highly selective heating could represent a major advantage for thermal control by constraining the heated area to a well defined perimeter. Highly selective heating could potentially enable the integration of several PCR chambers and other thermally sensitive components in a single chip, with minimum crosstalk.

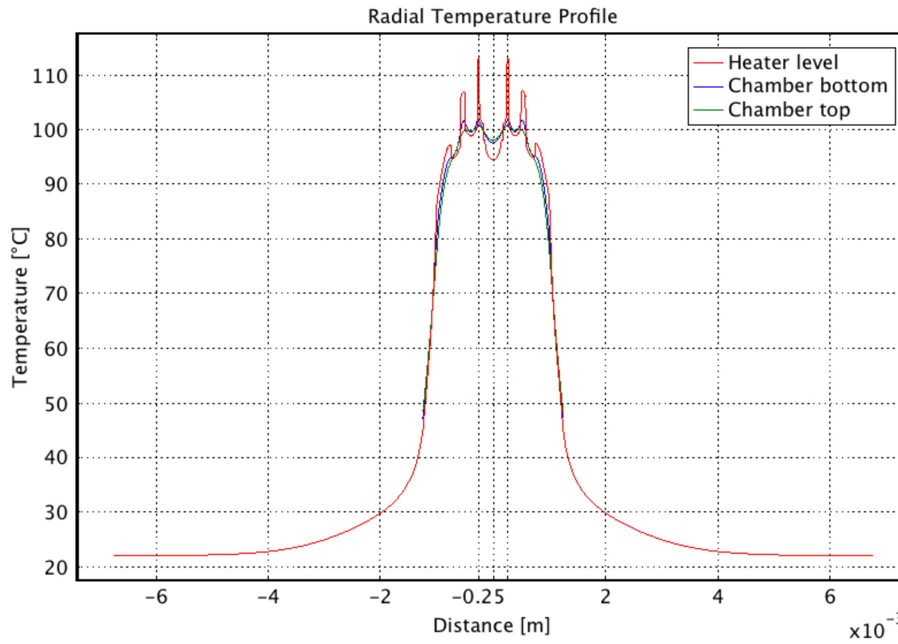

Figure 22. Radial temperature profile at the heater and chamber levels, obtained by 3D simulation, showing the high power concentration and selectivity achieved by the use of a thin polymer structure. The use of an air bridge made possible reaching 100 ºC within the small heated area with only a fraction of the power required by the PCR/CE-4 and USBPCR-1 platforms.

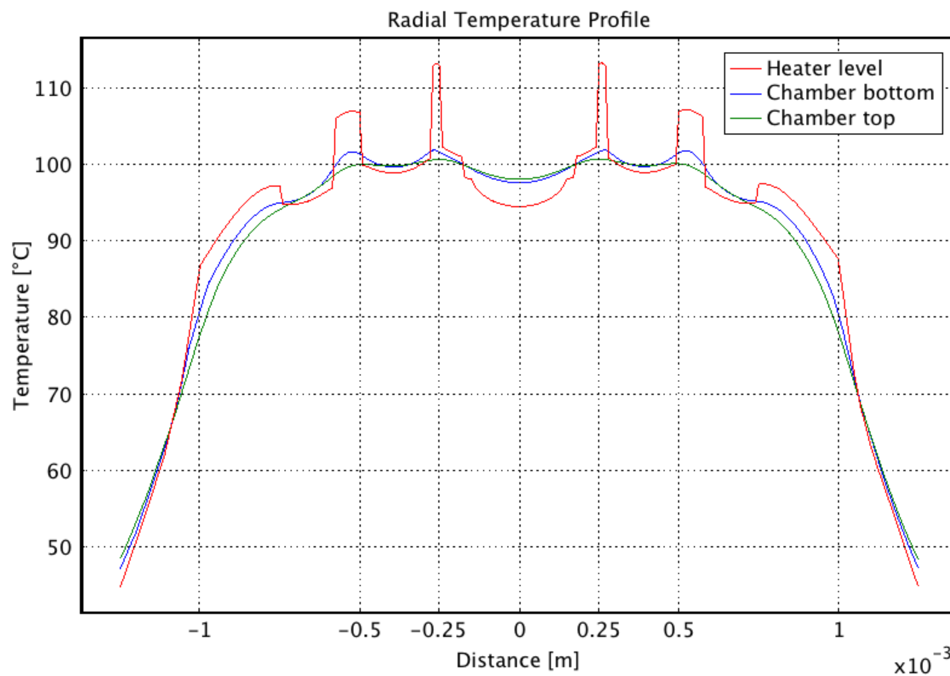

Figure 23. Radial temperature profile at the heater and chamber levels, showing the closeness between chamber, heater and sensor temperatures.

Owing to the high horizontal resistance the heated area was reduced from >7 mm diameter in the glass-PDMS platforms to ~2 mm diameter. The effective area on

top of the chip where convection occurs was dramatically reduced. The system therefore became more insensitive to variations in airflow. Since the chip outside the heater was heat sunk, anything occurring outside this area, such as an object touching the chip, would not affect the system.

The design showed that *Tc* could be taken very close to *Th*, as well as to *Ts* (the temperature seen by the sensor), as shown in Figure 23. This was achieved by (1) using a thin KMPR layer between the heater and chamber (layer 2) ; and (2) by reducing the size of the heated area, which increased substantially the resistance due to convection. In PCr/CE-4 the chamber and heater were separated by 254 µm of PDMS, while in PC6-K they were separated only by 50 µm of KMPR. By making *Th* close to *Tc,* we were for the first time designing an easy-to-calibrate system that was capable of overcoming the observer effect.

One of the main concerns at this stage of the project was the vulnerability of aluminum to electromigration, since the electromigration rates accelerate at high temperatures and current densities [2]. For pure Al a conservative electromigration limit is 1–2 mA/µm^2 for conductors at 110 ºC [1]. Simulation showed that the inner ring of the heater would be exposed to the highest temperature and current density (113 ºC, 7.97 mA/µm^2 when *Tc* = 94 ºC), which exceeded by far the above limit. We lacked experimental data to support the feasibility of producing aluminum heaters that operate at such current densities for a useful time. However we expected that by reducing the *Th* requirement (from ~ 170 ºC in PCR/CE-4 to an average of ~100 ºC in PC6-K), the electromigration rate would be reduced substantially, since it depends exponentially on the temperature [1]. In other words, ensuring a close coupling of *Tc* to *Th* could also enable the use of aluminum, making the design CMOS-compatible. Keeping *Th* low also ensures the integrity of the polymer and extends the device lifetime.

One of the major difficulties in this design was to obtain uniform temperature in the chamber using only three heater rings. Filling the space between rings with aluminum spread heat and improved substantially the uniformity. However, as

shown in Figure 23, the temperature still decays rapidly between rings. This decay could be compensated with additional rings, however the connection in parallel made very difficult to choose an appropriate spacing and track width. To design the heater we followed the conventional approach in which an initial heater geometry is proposed, then tested by simulation and modified repeatedly until reaching an optimal design. This technique proved to be extremely time consuming and ineffective. These difficulties showed the need for a method to control the spatial distribution of heat precisely. For this purpose we developed a method to produce controlled power density thin film heaters, discussed in Chapter 9.

A major cause for the loss of -uniformity was the rapid temperature decay at the edge of the heater. This decay made necessary to reduce the size of the chamber to 250 µm radius, but even with this reduction the best uniformity achieved was ~ 4 ºC (the maximum minus minimum temperatures in the chamber). Although a thick air bridge in fact reduced power consumption substantially, its high resistance limited vertical conduction and created a significant horizontal heat loss, making the edge cooler. It was clear that the structure, as well as the air bridge, should be thinned further, in order to increase the horizontal to vertical resistance ratio. At this stage of the project we were not prepared to produce KMPR layers thinner than 50 µm repeatably.

The design of the PC6-K system was finished and was considered a viable design for fabrication. The ability of the system to make $Tc \approx Th$ represented an enormous advantage, since there would be no need for calibrating Tc vs Th using TLC or any other invasive method. Calibrating the sensor temperature vs. resistance in a waterbath would be enough to estimate Tc with good accuracy. The extremely low power consumption of the design made it also a good candidate for fabrication. However, some technologies, such as aluminum metallization on KMPR, were not fully developed. In addition, factors such as the low uniformity, small chamber volume (10 nL) and high surface to volume ratio (2 times larger

than for PCR/CE-4), could have risked the performance of PCR. Thus we decided to develop the required technologies prior to the fabrication of a prototype.

6.2 A Flow-Through PCR Chip with Built-in Thermal Control

One of the challenges of static PCR is the need for micro-valves/pumps. The designs presented previously in this work require these components to convey the PCR brew into the chamber, seal the chamber during the reaction to prevent evaporation and perform other liquid handling tasks. Actuation of the microvalves is typically carried out by means of an external pneumatic system that includes solenoid valves, pressurized air sources, pumps and tubing, which increase the size and cost of the instrumentation considerably. As an alternative that would not require valves, we designed a highly manufacturable continuous-flow or *flow-though* PCR chip with built-in thermal control.

In the continuous-flow PCR technique the liquid is passed through a long channel over three different zones heated at the PCR temperatures [3].. The channel is typically patterned in a zigzag with as many loops as cycles are required for the reaction. Upon the application of an external pressure, the temperature of the liquid is cycled, as it is forced to travel through the temperature zones. These zones are typically large in order to accommodate a long channel with many loops, resulting in large chip footprints. The liquid must be pumped by a pressure system, such as a syringe or a micropump [3], [4],, strong enough to overcome the resistance of the channel. Of course, the higher the pressure, the faster the PCR process will be. Our approach is to design a flow-through chip in which the only necessary operation is to place a drop of the PCR mix on the inlet and wait for the reaction to complete, relying exclusively on capillary forces to drive the liquid in. The cross section of the device, denoted FTC-1, is shown in Figure 24.

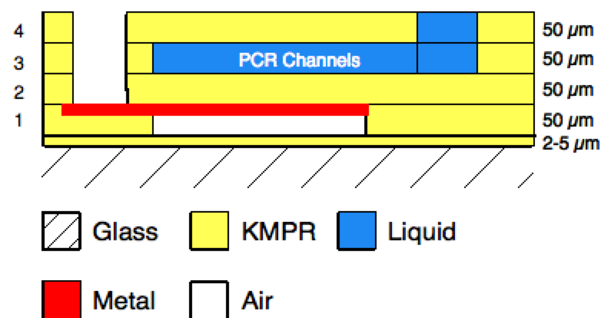

Figure 24. Cross section of FTC-1, a continuous flow PCR system. Air bridges are patterned under the reaction channel in order to control power consumption.

Our design is inspired in the spiral continuous-flow topology. Many PCR devices based in this topology have been reported, but even the most recent, such as those presented by Wu and Lee in 2013 [5] and Chung *et al.* in 2014 [6], still require syringe pumps to mobilize the liquid. Our system employs airbridges to limit power consumption and provide highly selective heating, which reduces dramatically the number of loops in the spiral and the overall device size. To our knowledge a continuous flow PCR system that combines the use of airbridges and capillary forces as a pumping mechanism has not been reported.

This structure in Figure 24 is similar to that of PC6-K, but does not contain valves/pumps or any moving parts, and hence does not require an external pneumatic system. Capillary forces convey the PCR brew into the chip, along a channel where the temperature is cycled, eliminating the need for external pressure sources or microfabricated pumps. The elimination of valves also facilitates the fabrication considerably, because it is not necessary to create local non-adhesion areas, which is difficult to achieve. This process simplification can certainly increase substantially the fabrication yield. Other problems associated with valves would also be eliminated, e.g. leaking, bubble trapping, tear/deformation of the diaphragm and introduction of dead volumes. In terms of thermal control, this design would have the great advantage of not requiring an elaborate temperature controller, since the heater temperatures are fixed. After powering the device, the temperature zones would stabilize within few seconds and the device would be ready to use. Since this device easy to control, requires

minimum external infrastructure and its fabrication is simpler than for PC6-K, the cost of the system could be dramatically reduced.

Since FTC-1 is constructed in the same way as PC6-K, including materials and layer thicknesses, the thermal behavior of the system is very similar. A more detailed view of the thermal system in FTC-1 is depicted in Figure 25.

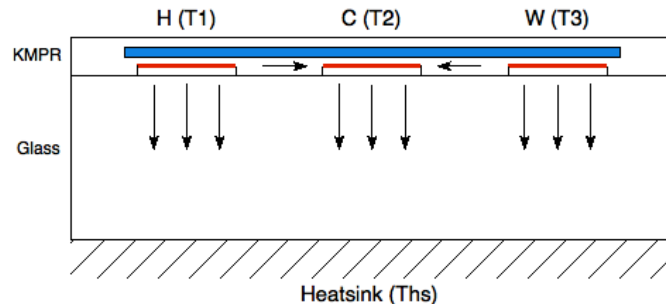

Figure 25. Cross section of FTC-1, showing the temperature zone of one heater. H – hot zone (94 ºC); C – cold zone (60 ºC); W – warm zone (70 ºC). The reaction channel (blue) is 50 µm high and is separated by 50 µm of KMPR from the heater elements (red). The heater elements are separated by a 100 µm airbridge from the substrate. The chip is supported on a flat heatsink. The arrows indicate conductive heat flux.

A major difference between PC6-K and FTC-1 is that in the latter the heatsink does not have a hole underlying the heated area. Therefore the air bridges provide most of the thermal isolation from the heater to the heatsink, and a small percentage is provided by the substrate. The horizontal resistance in FTC-1 is also high, which constrains the heated area closely to the perimeter of the heater, reducing connection of the system to the external environment. On the other hand, since the entire device's bottom surface is now in contact with the heatsink, vertical conduction dominates even more strongly over convective losses. In this device in particular, the interfaces with the macro-world have been substantially minimized, as it does not require a pneumatic system. Therefore the system is largely dependent on a single dominant boundary variable: the heatsink temperature *Ths*. For this reasons, FTC-1 is a step forward in terms of thermal robustness. It is also more manufacturable because the heatsink can be any flat metal surface, and no alignment procedure is required. By eliminating the error due to chip-to-heatsink misalignment - a major source of variability in our old

technology, the system is also more repeatable than all previous designs in this work.

The layout of the chip is shown in Figure 26. The reaction channel forms a 2-loop spiral. This configuration is more efficient than the zigzag or reciprocal designs, commonly found in literature [1], because there are no *return loops*. Those loops are needed to take the liquid back to the first temperature zone, so the liquid can move always in the amplification direction, i.e. denaturation (94 ºC) to annealing (60 ºC) to extension (70 ºC). Conversely, in the FTC-1 design the liquid travels always in the amplification direction.

The process starts when a drop of the PCR sample is deposited on the input well (large circle in Figure 26). The hydrophilicity of the polymer, surface tension of the liquid and narrow cross section of the channel cause a capillary pressure that pulls the liquid in. Each rectangle in Figure 26 is a thin film heater with three temperature zones denoted H (94 ºC), C (60 ºC) and W (70 ºC). With four of these heaters on each side of the spiral and two loops of the channel the PCR brew can be cycled 30 times, which is sufficient for typical amplification schemes.

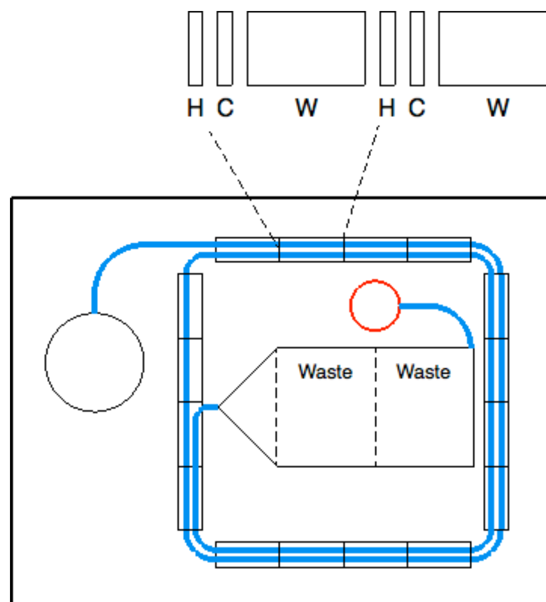

Figure 26. Layout of FTC-1. The PCR brew flows from the input well (large circle) to the waste reservoir by capillary forces. The small circle represents an air-exhaust port. Each heater contains three zones at PCR temperatures: H – 94 ºC, C – 60 ºC, W – 70 ºC.

To continue pulling the liquid when the capillary meniscus reaches the end of the channel, a waste reservoir is included in the device. This reservoir is a compartment populated with posts very close to each other, forming a capillary pump, i.e. a sponge. The volume of the reservoir is calculated so that its volume equals the volume of liquid in the channel. More than one reservoir can be coupled in order to empty the channel more than once. The compatibility of the polymer surfaces can be assured by passing a coating solution followed by the PCR brew. The first waste reservoir would fill up with the coating, removing it from the channel, and the second reservoir would fill up with the PCR brew.

Similarly as in PC6-K, the heater elements are suspended on an air bridge to reduce power consumption and provide localized heat concentration. The heaters are intended to connect in series to a common regulated current source. The series connection allowed for much easier control of the power density and temperature profile. Some of the tracks would be used as a 4-point temperature sensor. The temperatures would need to be finely adjusted prior to running the reaction. Since the temperature zones are fixed, the adjustment could be done by a very simple

controller, whose main role would be to compensate for variations of *Ths*. Temperatures could even be adjusted manually if the system is covered from air drafts and *Ths* is kept stable with an adequately large heatsink.

The specification for the hold time at H, C and W were 1, 1 and 10 seconds, respectively. These hold times along with the capillary filling velocity determine the length of the temperature zones. We fabricated 3-layer KMPR chips with microchannels and measured a maximum capillary filling velocity of ~100 µm/s for water in channels pre-treated with alcohol. The alcohol treatment was necessary to render the KMPR surface hydrophilic. This velocity was approximately constant over a ~16 mm long channel. Ideally the widths of the zones at the measured velocity would be 100, 100 and 1000 µm for H, C and W. However, the moving liquid requires some extra time to change its temperature as it passes through the temperature zone, due to its thermal mass. The width of the zones was therefore extended to account for this extra time. Figure 27(a) shows the heater designed to produce three temperature zones. The tracks are designed to be connected in series with wide elbows (connection not shown), and some tracks would have an extra pair of terminals to serve as 4-point sensors, as shown in Figure 27(b). The temperature profile produced by the heater, as predicted by simulation, is shown Figure 28.

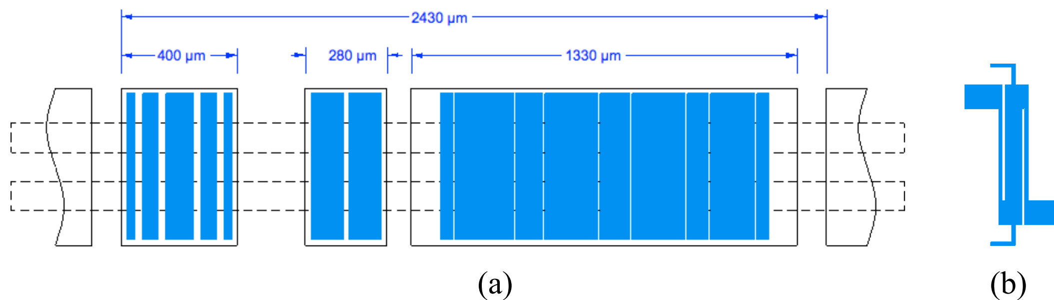

Figure 27. (a) Layout of a 3-zone thin film heater (for one PCR cycle). The heater tracks (blue) are to be connected in series. The dashed lines show the profile of the channels in real proportion. The solid line rectangles show the air bridge areas. (b) Some tracks would be used as 4-point temperature sensors, by adding voltage probe lines.

A heater that produces a linear ramp of temperatures could be placed at the end of the channel, and with this enable the system to perform melting curve analysis

(MCA). This analysis would be performed by adding to the PCR brew a fluorescent dye that binds to DNA. To this end we designed a heater (not shown) that can produce the linear ramp shown in Figure 29. Equipped with these different heaters the device could have the ability to run PCR, qPCR and MCA simultaneously. The calculated final specifications of the design are shown below:

- 2 loops, 30 cycles
- 100 µm x 50 µm channels
- ~ 1x1 cm chip area
- ~ 8 cm channel length, 400 nL channel volume
- 33 mW, 1.56 V per 3-zone heater (700 µm wide)
- 533 mW total power consumption, 21 mA driving current
- ~ 15 min total reaction time

Thermal calibration in a continuous flow PCR device can be even harder than for a static PCR system, because only a dissolved temperature sensitive marker, such as TLC or a fluorescent dye, can be passed through the thin channel, requiring the use of expensive contactless thermometry equipment. In PC6-K, however, the temperatures of the heater and channel are very close to each other, particularly on the center tracks. Those tracks can then be used to estimate the temperature in the channel, with a small correction factor obtained by simulation. Again, this thermal proximity would have the great benefit of reducing the calibration procedure to a measurement of the temperature vs. resistance curve of the heater elements.

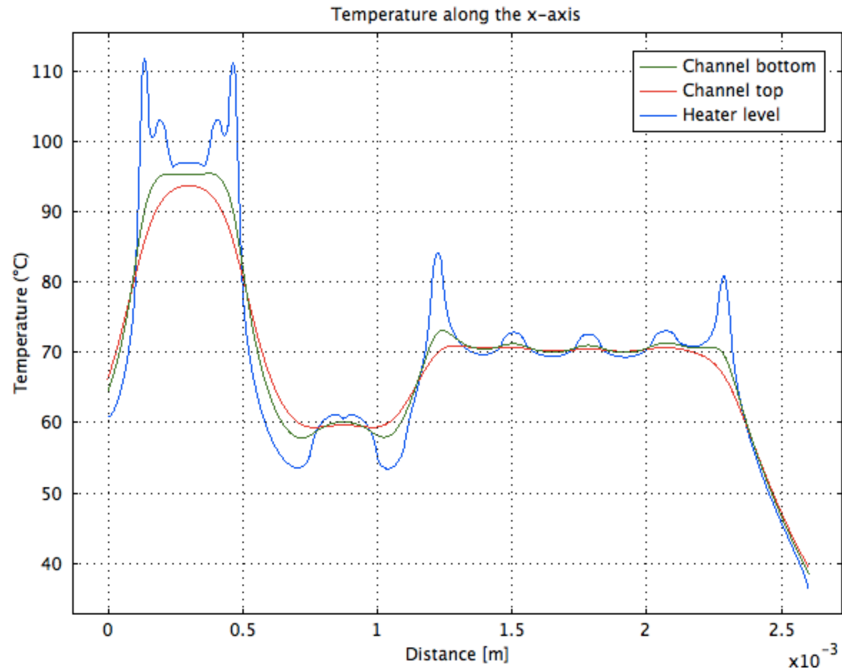

Figure 28. Longitudinal temperature profile for PCR at the heater and channel (top and bottom) levels, produced by the heater layout of Figure 27(a), as predicted by 3D simulation. This profile will generate one amplification cycle on the moving PCR sample.

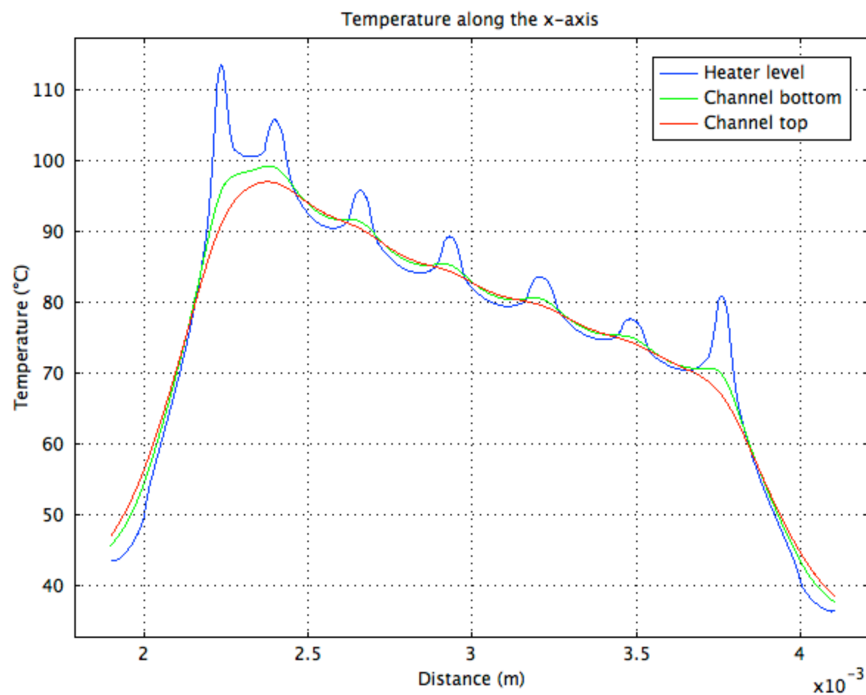

Figure 29. Longitudinal temperature profile for MCA, at the heater and channel (top and bottom) levels, predicted by 3D simulation.

FTC-1 was certainly a more robust and manufacturable system. However, its structure and airbridge were still thick, causing a rapid edge cooling. This made

difficult to obtain uniform temperature in the small zones (H and C), as show in Figure 28. In addition, the system was still vulnerable to gradients in chip-heatsink thermal contact, due to the relatively low conductivity of the substrate. From this we understood that if the substrate could be eliminated or replaced by a highly conductive material, such as silicon, the system could become robust to this variable. Finding the optimal /spacing of heater tracks was also very difficult, as we relied on repeated testing of the design through FEM simulation. This again showed the urgent need for a method to design heaters that enable precise control of the spatial temperature distribution. We decided to develop this and other methods associated to the new technology before fabricating prototypes of FTC-1.

6.3 Appendix A: PC6-K and FTC-1 Simulation Details

The PC6-K system was modeled in COMSOL 3.5a as a 4-layer KMPR structure built on a glass substrate. A 2D axisymmetric model was built for quick assessment of the designed heater rings. A 3D model was built to simulate the system with the actual heater layout. The Heat Transfer and AC/DC modules of COMSOL were used.to enable coupled heat-transfer/Joule-heating simulation on shell structures (i.e. thin films). The layers of the KMPR structure had a thickness (from bottom to top) of 100, 50, 50 and 50 μm. Since the thermal conductivity for KMPR has not been reported the KMPR structure was assigned the conductivity of SU-8 (0.2 W/m-K, see Table 12) - a photopolymer similar to KMPR. Other material properties used in the model are listed in Table 2. The airbridge in KMPR layer 1 was placed directly under the PCR chamber and was assigned the thermal conductivity of air, which is calculated by the simulation tool pointwise as a function of temperature.

The heater was modeled as a 200 nm thick Highly Conductive Layer located at the top of the airbridge (separated from the chamber by layer 2), and was assigned the conductivity of Al (237 W/m-K). For the axisymmetric model the heater rings were assigned a Boundary Heat Source condition. The power density on each ring was calculated separately in a spreadsheet. For the 3D model, Ground and Electric

Potential boundary conditions were prescribed on the pogo-pin contact points on the heater pads. Uniform temperature of value *Ths* was prescribed over the entire bottom surface of the chip and convective heat loss was prescribed on all other external boundaries. The 3D model for FTC-1 is identical in terms of materials and boundary conditions. The major differences are the geometry of airbridges and heaters, and the substitution of the chamber by microchannels.

6.4 References

[1] V. M. Blanco Carballo, J. Melai, C. Salm, and J. Schmitz, “Moisture resistance of SU-8 and KMPR as structural material,” *Microelectronic Engineering*, vol. 86, no. 4–6, pp. 765–768, Jun. 2009.

[2] N. H. E. Weste and D. F. Harris, *CMOS VLSI design: a circuits and systems perspective*. Boston, US: Pearson/Addison-Wesley, 2005.

[3] C. Zhang and D. Xing, “Miniaturized PCR chips for nucleic acid amplification and analysis: latest advances and future trends,” *Nucl. Acids Res.*, vol. 35, no. 13, pp. 4223–4237, Jul. 2007.

[4] C. Zhang, D. Xing, and Y. Li, “Micropumps, microvalves, and micromixers within PCR microfluidic chips: Advances and trends,” *Biotechnology Advances*, vol. 25, no. 5, pp. 483–514, Sep. 2007.

[5] W. Wu and N. Y. Lee, “Two-layer microdevice for parallel flow-through {PCRs} employing plastic syringes for semi-automated sample injection and a single heater for amplification: Toward process simplification and system miniaturization,” *Sensors and Actuators B: Chemical*, vol. 181, no. 0, pp. 756 – 765, 2013.

[6] K. H. Chung, Y. H. Choi, and S. Park, “Development of a continuous-flow polymerase chain reaction device utilizing a polymer disk with a spiral microchannel of gradually varying width,” *Sensors and Actuators B: Chemical*, vol. 191, no. 0, pp. 75 – 85, 2014.

7 A Novel Multilayer Bonding Process

A version of this chapter has been published (Article 1 – L. Gutierrez-Rivera 2012. Journal of Micromechanics and Microengineering, Vol. 22, No. 8).

Eliminating device-level calibration is key for a manufacturable LOC implementation and this requires the fabrication of repeatable devices. In our multilayer architecture the bonding between layers must be strong and uniform to ensure repeatability, as well as good thermal and fluidic performance. Weak or incomplete bonding leads to the formation of air pockets, which can severely affect the thermal system by creating large temperature gradients, as explained in section 5.1. Strong bonding is also critical to prevent delamination and leakage due to the high pressures generated in the PCR chamber. The pressurized air used for microvalve actuation can also delaminate layers creating air pockets - another good reason to design devices without valves, like FTC-1.

We developed a photopolymer bonding process to build high quality microfluidic structures of up to six pre-patterned layers. The process consists of growing a conformal adsorbate film (CAF) of ~15 nm thickness on a patterned KMPR layer, acting as an ultra-thin adhesive layer. Unlike previously reported methods, crosslinked, hardened and smooth KMPR layers can be bonded, resulting in high quality structures. An optimized partial-crosslinking bonding method was also developed and used to evaluate the performance of the CAF method. The partial-crosslinking method is suitable for devices with few layers that do not include valves, and it is the method used in our latest developments. Experiments of capillary filling of water into microchannels of structures made with the CAF technique were performed, without discernible leakage between layers. These results were used in the design of FTC-1, as explained in section 6.2.

Chapter 7 - The author and Luis Gutierrez-Rivera conceived and developed jointly the multilayer bonding technique presented herein. Luis performed a series

of bonding experiments with feedback from the author. The author contributed to the writing of the corresponding publication and produced figures and photographs. The author and Luis performed leakage and bonding strength experiments and the author developed a pneumatic test tool for these experiments.

7.1 Introduction

Integration of microchannel networks [1], microvalves [2], sensors [3] and other components in the same device is becoming increasingly important in the LOC field. We believe that multilayer polymer architectures would be key to achieve maximum integration, and with this produce highly functional yet manufacturable LOC systems. Polymers, however, require careful control of their material properties such as wettability, transparency, dielectric strength, thermal conductivity, mechanical stiffness and biocompatibility. Multilayer structures, particularly, require strong bonding between layers to avoid leakage and delamination. If the system requires thin film heaters/sensors, strong adhesion of metals on the polymer must be ensured. The adhesion to metals and between layers, as well as the structural integrity of the polymer, must be unaffected by moisture since aqueous solutions are to be handled. KMPR has excellent adhesion to metals like Al and Cu, and shows high resistance to moisture [4-6], so it appears to be suitable for the fabrication of multilayer LOC systems.

Techniques to encapsulate microchannels made in photopolymers like KMPR or SU-8 include adhesive bonding [7, 8-10]; carrier-release via low-adhesion layer [8-9], sacrificial wet-etch layer [8-9, 11], and thermal decomposition sacrificial layer [12]; and lamination [13-14]. Conventional adhesive layers may form bubbles at the bonding interface or flow into the channels/cavities and clog them. In sacrificial layer methods the etchant and the dissolved/decomposed material can contaminate the device, rendering it unusable for biological applications. A technique that combines carrier-release by low adhesion layer and lamination bonding is appropriate for the fabrication of multilayer structures for biological applications. In this technique each layer is built separately and then stacked onto

each other. The layers are patterned individually on a carriers substrate coated with a material with relatively low adhesion to the structural material. The layers are bonded by lamination and then released from the carrier [13- 14]. Some low adhesion layers used to transfer photopolymer layers are polyester foil (PET) [13-14], Kapton film [15] and PDMS [16].

Lamination is often used to encapsulate photopolymer microchannels by transferring uncrosslinked [13] or partially crosslinked [14] layers, and then crosslinking them together by applying heat and pressure to produce a permanent attachment. These techniques require careful control of baking time and temperature to achieve acceptable bonding while preventing deformation of the structures or filling of the channels with the photopolymer. These difficulties arise because the photopolymer is soft when it has been prebaked but not crosslinked (or only partially crosslinked) and thus can easily deform or flow with the application of heat and pressure. Due to the softness of these films, the bonding pressure cannot be increased above a certain limit to enhance contact. In the case of lamination with partially crosslinked layers, the photopolymer can be hardened further by increasing post-exposure bake time/temperature, but as the crosslinking level of the film increases the bonding yield and strength decreases.

With the partial crosslinking lamination technique, multilayer bonding yields of ~80%, in terms of bonded area, have been obtained after three bonding steps [15]. In terms of number of finalized bonded chips, multilayer bonding yields of 80% have also been reported [14]. The bonding yield is known to decrease with the number of bonding steps, which can be attributed to the accumulated surface unevenness after successive thermo-compressive bonding steps [15]. Unevenness is created by the deformation, under high pressures, of the partially crosslinked layers, which are mechanically less resistant than highly crosslinked layers. The quality of bonding therefore depends largely on both the level of partial crosslinking of the photopolymer established before bonding, and the planarity of the layers before and after bonding [15].

We have developed a novel CMOS-compatible bonding process for the fabrication of complex multilayer KMPR structures with at least six layers individually patterned and bonded one by one, with 90-100% bonded area after five bonding steps. This approach does not require strict control of the pre-bake parameters and is independent of the crosslinking level of the photopolymer layers. The process could potentially permit the fabrication of microvalves and thin film heaters/sensors embedded between layers, enabling cost-effective manufacture of fully integrated single-chip LOC systems.

7.2 Fabrication

The process to fabricate a multilayer KMPR structure requires two substrates called *device wafer* and *carrier wafer*. Onto the device wafer, we build the bottom layer by photolithography, and the layer is highly crosslinked with a post exposure bake (PEB) at ~100 ºC for 5 min. On the carrier wafer, a cured ~5 μm thick PDMS film is formed. On the PDMS film a second KMPR layer is patterned up and also highly crosslinked. A surface treatment is performed on the carrier wafer to deposit a conformal adsorbate film (CAF). The device and the carrier wafers are then aligned and brought into contact. An embosser is used to heat at 100 ºC and press with 25 kN the layers against each other, and crosslink the CAF at the bonding interface, joining them permanently. After bonding, the carrier wafer can be released due to the poor adhesion between PDMS and KMPR. After release, two layers of the final device are completed. The process is repeated by patterning the subsequent layers on different carrier wafers and bonding them on the stack one layer at a time until the structure is completed on the device wafer.

Notice that differently from previous demonstrations, in this process all the photopolymer layers are fully crosslinked before bonding, which gives them the stiffness to resist the bonding pressure without being deformed. The CAF treatment is the key of this process. It forms a barely polymerized molecular-scale KMPR conformal film (CAF) of ~15 nm thickness. The film is grown by immersing the wafer in a very diluted solution of KMPR and cyclopentanone.

KMPR monomers are adsorbed on the surface of the structural KMPR layers. The wafer with the CAF is pre-baked and exposed to UV light to produce the catalyst that will trigger polymerization during bonding. This leaves a nanometric layer of barely crosslinked KMPR on all the surfaces of the structural KMPR. For a detailed description of the fabrication process please refer to [17].

7.3 Results and Discussion

7.3.1 Lithography of KMPR

Crosslinked ~56 μm KMPR layers were obtained in the lithography process. The transparency of PDMS made especially difficult finding an optimal exposure dose to obtain layers with enough mechanical hardness to withstand the bonding pressure. In addition to the CAF technique we built multilayer structures using an optimized partial-crosslinking bonding method. For best results the PEB temperature (90 ºC) should be lower than the bonding temperature (100 ºC) in order to leave a large number of free monomers in the surface of the film, sufficient to achieve bonding. PEB lower than 90 ºC gives patterned structures with poor resolution after development. The crosslinking of the layer is then completed inside the embosser.

7.3.2 Film Uniformity

High uniformity and flatness of the KMPR layers are necessary to achieve a high bonding yield. However the dewetting of KMPR on PDMS, made it difficult to form high quality KMPR surfaces. During pre-bake dewetting caused the KMPR film to collapse under its own surface tension, which was stronger than its adhesion to PDMS. We overcome this problem by sputtering gold at the perimeter of the wafer, which acted as an anchor for the KMPR film. However multiple small depressions appeared on the KMPR film during pre-bake that deteriorated surface uniformity. These depressions seemed to be caused by the KMPR film flowing or sliding freely on PDMS due possibly to temperature gradients. For a KMPR film 56 μm thick, we minimized these effects by performing the pre-bake in periods of 29 min at 60, 80 and 100 °C to evaporate the solvent slowly.

7.3.3 Conformal Adsorbate Film (CAF)

The creation of the CAF allocates a substantial amount of open-chain KMPR monomers and catalyst along the surface of the patterned KMPR. If the monomers and catalyst are uniformly distributed, effective linkage of the mating layers can be achieved during thermo-compression. The thickness of the CAF depends on the concentration of monomers in the KMPR-cyclopentanone solution. A concentration of 1:4 is the most appropriate and results in a CAF thickness of ~15 nm. Larger amounts of solvent lead to detachment of the patterned KMPR from the PDMS, which hinders bonding. Conversely, higher concentrations of KMPR may produce a non-uniform coating with clumps.

A surface with monomers whose bonds are free will show higher energy than a surface in which most of the bonds have been passivated by the linking to other bonds. Since higher surface energies manifest in lower contact angles, we expected that the CAF would show low contact angles, approaching those of soft-baked KMPR, and hence would have similar bonding potential. The measured contact angle of DI water on the CAF is in fact very similar to that of a regular soft-baked KMPR film (~60 º). Figure 30 illustrates the variation of contact angle before (79°) and after (60°) of the surface treatment. When KMPR is crosslinked, the contact angle increases and therefore the hydrophobicity.

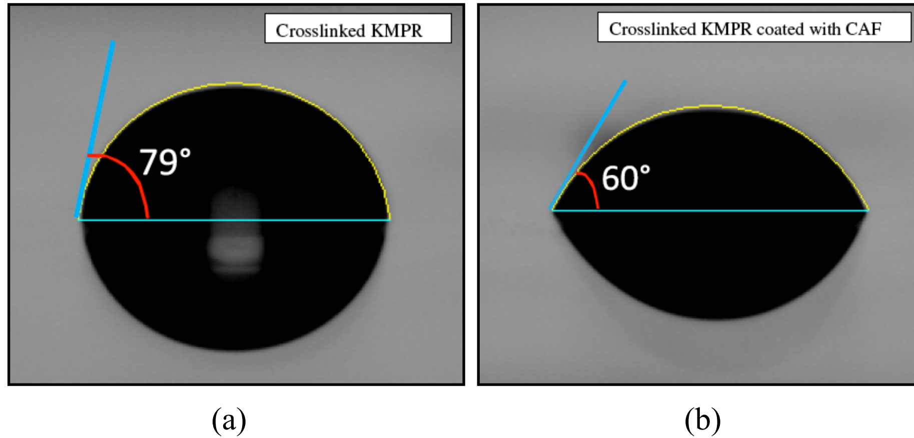

(a) (b)

Figure 30. Contact angle on the surface of a crosslinked KMPR film, (a) without CAF and (b) coated with the CAF.

7.3.4 Multilayer Bonding Characterization

The quality of bonding was assessed in terms of the percentage of bonded area, measured after each bonding step over the entire bonded layer (all layers have a total footprint of 8 x 8 cm). Two major bonding processes were performed at the same bonding temperature (100°C):

Optimized Partial crosslinking method. The PEB temperature of the patterned KMPR was reduced progressively until obtaining the highest yield for three bonding steps, while maintaining sufficient stiffness of the structure to withstand the bonding pressure without being deformed. The yield increased from the 70 % of a standard process to 96 % when reducing the PEB temperatures from 100 ºC and 90 ºC, respectively.

CAF method. Each layer to be bonded was crosslinked with a 100°C PEB for3 min, and thereafter the CAF were created on the surface. After three bonding steps, a bonded area of 99 % was measured. Fourth and fifth bonding steps (five and six-layer structures) were also performed with the CAF technique and the bonded areas were 97 % and 90 %, respectively. We attribute the decay of bonded area to the accumulated loss of flatness at the corners and edges over repeated thermo-compression cycles, which reduces the quality of bonding in subsequent

layers. However, at the center of the wafer the bonded area approached 100 % in a 4.5 x 4.5 cm area across five bonding steps.

Figure 31(a) shows a complete 4-layer chip with PCR chamber, microvalves and fluidic/pneumatic microchannels and ports. Figure 31(b) shows 4-layer chips for CE located at the center of the wafer. These devices were fabricated with the CAF method.

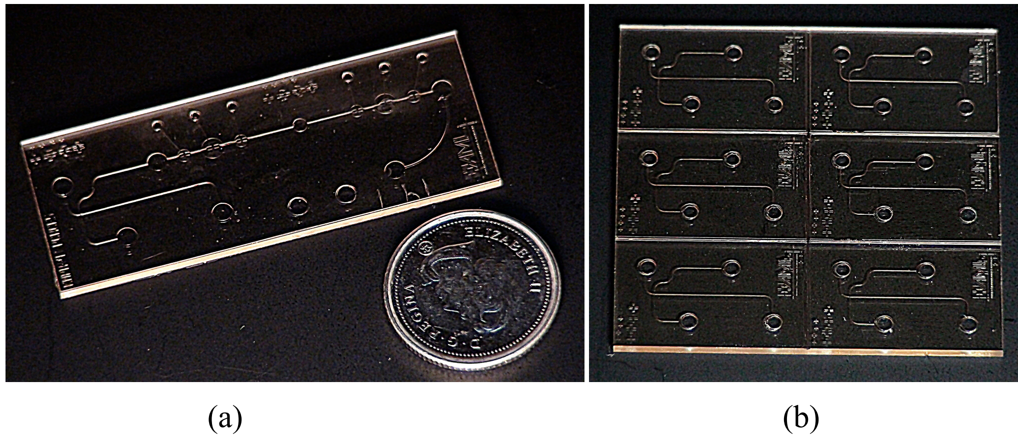

(a) (b)

Figure 31. Devices fabricated with the CAF technique. (a) 4-layer chip for complete genetic analysis that integrates PCR, CE and SP sections, 45 x 17.5 mm. (b) 4-layer chips for CE analysis and detection, located at the center of the wafer. The logo area, on the top right corner of each chip, as well as the alignment marks on the opposite corner, were excluded when measuring the bonding yield in this center portion of the wafer.

7.3.5 Leakage and Bonding Strength Tests

We carried out capillary filling experiments in microchannels of three and four-layer chips built with the CAF technique. The channels self-filled at a rate of 74 μm/s with DI water, showing no discernible leaks between layers. The experiments were repeated after passing isopropanol through the channels and allowing it to evaporate. This treatment increased filling velocity of DI water to 110 μm/s. Again, no leakage of isopropanol or water was observed, indicating a tight seal of the layer-layer interfaces. Figure 32 shows a microscope snapshot of the capillary filling in microchannels. Bonding strength was tested by applying pressurized air into 100 x 50 μm channels closed at one end, in chips of four 56 μm thick layers, finding that the structure starts to delaminate at 65 psi (~448 KPa). For SU-8 micro-channels, liquid pressure up to 600 KPa before leakage has

been reported [29-15]. Since no leakage was observed during capillary filling and the maximum pressures that we use to actuate microvalves in the chip is 30 psi (~206 KPa), we believe that the CAF bonding technique is well suited to build multilayer structures for microfluidic applications.

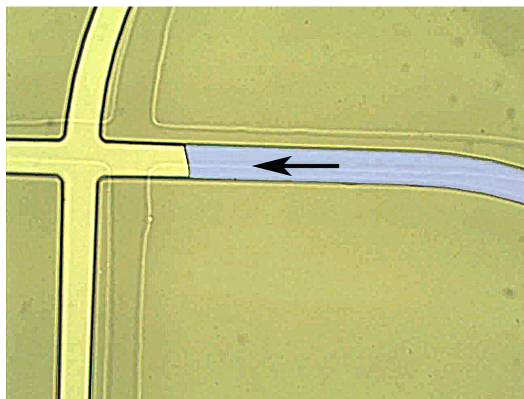

Figure 32. Capillary filling of DI water in KMPR microchannels. The arrow indicates the direction of the advancing meniscus. The water column was digitally colored.

7.4 Conclusions

We presented a new approach for the fabrication of multilayer structures by joining patterned and crosslinked KMPR layers using a novel conformal adsorbate film (CAF) bonding technique. This technique enables cost-effective fabrication of LOC systems with complex microchannel networks, microreactors, inter-layer vias, microvalves, and other microfluidic components. Being a low-temperature high bonding yield process, the CAF technique allows integration of microfluidics and CMOS microelectronics in a single-chip.

To build a multilayer structure, individual KMPR layers are fabricated on a carrier wafer and subsequently bonded onto each other. The CAF technique consists in the formation of a thin conformal film of ~15 nm thickness on the surface of one of the bonding KMPR layers. This film substantially increases the availability of open polymer chains at the bonding interface, enhancing the probability of linkage between mating layers. The technique has shown a maximum bonding yield of 99 % over the total area of the patterned layers after three bonding steps

(four-layer structure), and 90% after five bonding steps (six-layer structure). The yield decays due to delamination and lower pressure at the corners of the wafer, while the central, defect-free, portion of the wafer has a near 100% yield after 5 bonding steps. Unlike previously reported photopolymer bonding methods that rely on partial crosslinking of one of the bonding layers, the CAF technique allows high quality bonding of pre-patterned and crosslinked KMPR layers. Therefore it is not necessary to keep strict control of softbake and post-exposure bake parameters of the layers to be bonded. Besides the CAF technique, we developed an improved partial crosslinking bonding method that reaches 96 % bonding yield after three bonding steps. With PEB at 90 °C and bonding at 100 °C this method shows similar performance to the CAF technique. However, in the partial crosslinking method temperature control is critical because at higher PEB temperatures the bonding yield decays rapidly, and at lower temperatures the structure can easily be deformed by the bonding pressure. Conversely, the CAF technique allows bonding of smooth, patterned and hardened layers while still providing enough potential chemical bonds to produce good strength after a thermocompressive bonding step. This decoupling of optimal conditions for bonding and structural stability make the CAF technique better suited to build high quality multilayer structures.

7.5 References

[1] K. H. Kang, *et al.*, "Continuous separation of microparticles by size with direct current-dielectrophoresis," *Electrophoresis* vol. 27, pp. 694–702, 2006.

[2] C. Aracil, *et al.*, "Pneumatic impulsion device for microfluidic systems," *Sensors and Actuators A: Physical,* vol. 163, pp. 247-254, 2010.

[3] N. C. Tsai and C. Y. Sue, "SU-8 based continuous-flow RT-PCR bio-chips under high-precision temperature control," *Biosensors and Bioelectronics,* vol. 22, pp. 313-317, 2006.

[4] *Microchem Corp.* Available: http://www.microchem.com/products/kmpr.htm

[5] V. Blanco-Carballo, *et al.*, "Moisture resistance of SU-8 and KMPR as structural material," *Microelectronic Engineering* vol. 86, pp. 765-768, 2009.

[6] C. Salm, *et al.*, "Reliability aspects of a radiation detector fabricated by post-processing a standard CMOS chip," *Microelectronics Reliability,* vol. 48, pp. 1139-1143, 2008.

[7] L. Convert, *et al.*, "Rapid prototyping of integrated microfluidic devices for combined radiation detection and plasma separation," in *Microsystems and Nanoelectronics Research Conference*, Ottawa, Ont., 2008, pp. 105 - 108.

[8] F. Blanco, *et al.*, "Novel three-dimensional embedded SU-8 microchannels fabricated using a low temperature full wafer adhesive bonding," *Journal of Micromechanics and Microengineering,* vol. 14, pp. 1047-1056, 2004.

[9] S. Tuomikoski and S. Franssila, "Free-standing SU-8 microfluidic chip by adhesive bonding and release etching," *Sensors and Actuators A* vol. 120, pp. 408-415, 2005.

[10] J. Carlier, *et al.*, "High pressure-resistant SU-8 microchannels for monolithic porous structure integration," *Journal of Micromechanics and Microengineering,* vol. 16, pp. 2211-2219, 2006.

[11] S. Metz, *et al.*, "Polyimide and SU-8 microfluidic devices manufactured by heat-depolymerizable sacrificial material technique," *Lab on a Chip* vol. 4, pp. 114-120, 2004.

[12] S. Martel and L. Quellet, "European Patent Application 10150112," 2010.

[13] P. Abgrall, *et al.*, "A novel fabrication method of flexible and monolithic 3D microfluidic structures using lamination of SU-8 films," *Journal of Micromechanics and Microengineering,* vol. 16, pp. 113-121, 2005.

[14] J. Steigert, *et al.*, "A versatile and flexible low-temperature full-wafer bonding process of monolithic 3D microfluidic structures in SU-8," *Journal of Micromechanics and Microengineering,* vol. 18, p. 095013, 2008.

[15] M. Agirregabiria, *et al.*, "Fabrication of SU-8 multilayer microstructures based on successive CMOS compatible adhesive bonding and releasing steps," *Lab on a Chip,* vol. 5, pp. 545-552 2005.

[16] J. N. Patel, et al., "PDMS as a sacrificial substrate for SU-8-based biomedical and microfluidic applications," *Journal of Micromechanics and Microengineering*, vol. 18, p. 095028, 2008.
[17] Gutierrez-Rivera, J. Martinez-Quijada, R. Johnstone, D. Elliott, C. Backhouse, and D. Sameoto, “Multilayer Bonding Using a Conformal Adsorbate Film (CAF) for the Fabrication of 3D Monolithic Microfluidic Devices in Photopolymer,” Journal of Micromechanics and Microengineering, vol. 22, no. 8, p. 085018 (12 pp.), Aug. 2012.

.

8 Polymer Metallization

A version of this chapter has been published (Article 2 – J. Martinez-Quijada 2013. Sensors and Actuators A: Physical, Vol. 193).

In order to develop manufacturable devices we required a reliable method to produce low-cost, corrosion-resistant, thermally-stable metal films that can be embedded in polymer structures. In addition, the electrical properties of such films, namely the temperature coefficient of resistivity (TCR), must be highly repeatable across devices in order to eliminate the need for per-device calibration. Patterning metals on polymer microstructures is, however, much more challenging than doing so on conventional substrates such as silicon or glass. This chapter presents the method that we developed for patterning a film of aluminum on KMPR and treating the film to stabilize its resistivity. The films are suitable for use as heaters and/or temperature sensors at temperatures up to 165 ºC – well beyond the required temperatures for PCR.

The author performed the TCR measurements, all calculations and writing of the corresponding article. Luis Gutierrez-Rivera fabricated the heater chips. Shane Groendahl and the author performed the Joule heating tests. Robert Johnstone developed the automated waterbath calibration system. Saul contributed to the revision, correction and writing of the article. Dan Sameoto designed the adhesion test and Matthew Reynolds fabricated the films for the adhesion test. Prior to this work Matthew Reynolds carried out a series of experiments that showed the feasibility of depositing aluminum on KMPR.

8.1 Introduction

Microfluidic technologies are quickly developing around polymers due to the low cost and ease of processing of these materials [1]. Moreover, the low thermal conductivity of polymers can substantially reduce device power consumption. Indeed, many state of the art LOC systems employ polymers as structural

materials [2], [3], [4]. Further development of affordable LOC) technologies demands low cost, stable metal films that can be easily integrated in polymer structures. Many polymeric LOC devices require resistive metal films that can operate at elevated temperatures. However, metallization is generally performed on non-polymeric substrates such as glass or silicon, not directly on the polymer, and this limits the functionality and design of these devices.

Metallization on polymers is a challenging process. Polymers are often vulnerable to attack by the organic solvents and developers used in wet processing, often leading to the detachment of the metal film from the polymer [5]. PDMS (polydimethylsiloxane), one of the most commonly used polymers in LOC systems, swells when exposed to most common solvents [1], preventing metal films on their surface from being patterned by standard lithography. Techniques such as microstenciling can be used to pattern metal films onto polymers (such as polyethylene, polystyrene, polycarbonate, polymethyl methacrylate (PMMA), and polyamide), but for some, like PMMA, adhesion to metals is poor [6], and most of them are not photo-patternable. In addition to the difficulty of patterning, metal films on polymers are prone to cracking due to the polymer's flexibility. For instance, Au/Cr tracks patterned on PDMS will crack and lose conductivity irreversibly when the PDMS is strained by 10% [7]. Metal cracking may also be caused by the large difference in the coefficient of thermal expansion (CTE) of polymers and metals. SU-8 and PMMA, for example, have CTE of 52–150 ppm/K [8] and 90–162 ppm/K [9], respectively, while inorganic substrates e.g. Si and borosilicate glass have CTE of 2.5 ppm/K [9] and 3.7 ppm/K [10], respectively. For thin film heaters this CTE mismatch is even more critical, and there is the additional constraint of the low glass transition and melting/decomposition temperatures of common polymers.

Commercial polyimide foils, e.g. Dupont's™ Kapton®, are thermally stable [11], so they are readily used to produce flexible heaters. As manufactured, these foils are not suitable for building integrated heaters and temperature sensors in LOC systems, because they contain intrinsic and extrinsic contaminants that cannot be

completely removed by cleaning [11]. These contaminants produce surface peaks tens to hundreds of nanometers high, with frequency of about 1–10 per cm^2 for peak sizes of 100–200 nm [11], which is typically the thickness of an integrated heater/sensor. Moreover, thermal processing such as resist baking in lithography, may result in shrinkage [11], and the deposition of metal tends to create compressive stresses [12], [13] that may wrinkle the foil or delaminate it from the carrier. Cu-metallized Kapton foils like Pyralux® are designed for low resistance electronic interconnects, so its Cu layer is thick (≥ 9 μm [14]). Thus, patterning the metal will leave a varied topography that makes difficult the bonding/deposition of subsequent layers in multilayer thin structures. Cu films, in addition, might be very susceptible to oxidation, and hence destruction.

In the LOC field there have been few examples of polymer metallization. Heaters were fabricated on Kapton® by sputtering a Ti/Pt film on top of the polymer [13]. However, patterning required ion-milling and stresses in the Pt film caused detachment from the Kapton®. Geiger *et al*. [1] successfully patterned Au heaters on microfluidic chips made of cyclic olefin copolymer (COC) and demonstrated the heaters operating at 30–40 ºC. However, in a typical geometry of a LOC system for genetic analysis, heater temperatures must reach above 100º C in order to obtain PCR temperatures in the microreactor (60–95 ºC). To our knowledge, in the LOC field there has been no demonstration of a stable heater on photopolymer capable of reaching more than 100 ºC.

For PCR applications, thin film Pt has been used for heaters and sensors in chips made using SU-8 [15] and PDMS [16], [17], but the metal was patterned on glass and does not form part of the polymer structure. Alternatives like indium tin oxide (ITO) on glass have also been used for PCR [18], [19], but Pt is by far the most widely used material due to its high resistivity, high temperature coefficient of resistivity (TCR), linearity and resistance to corrosion. However Pt is extremely expensive in terms of the material and processing cost. A Pt sputtering target of 3” diameter, 0.063” thickness and 99.99 % purity is 13,689.00 USD [20], which gives a cost per unit volume of 1.88 USD/mm^3. For the fabrication of thin film

heaters a typical sputtered metal film (as used in this work) is 200 nm thick. A film of this thickness deposited on a 4” x 4” wafer has a volume of 2.06 mm^3. Assuming a waste volume as large as the deposited volume, the required volume of metal would be 4.12 mm^3 and the cost of the film (for material only) would be 7.75 USD. In addition to its high cost, Pt requires a Ti or Cr adhesion layer, and must be patterned by lift-off [21] stenciling, or wet etch in boiling *aqua regia* [17], presenting undesirable processing conditions. Furthermore, Pt must be annealed at temperatures higher than the operation temperature for the stabilization of its resistivity [22], [23], which can cause problems for the underlying polymer structure including loss of mass [24]. All these factors complicate the incorporation of Pt in a polymer LOC process.

KMPR is a photopatternable polymer with high resistance to moisture [25], which makes it suitable for LOC devices. KMPR has also a strong adhesion to Al, and this adhesion increases with a hard-bake [25]. Thus, Al is a good candidate for metallization of KMPR-based LOC systems. Al is inexpensive: an Al sputtering target of 3” diameter, 0.25” thickness and 99.99 % purity is 166.40 USD [20], which gives a cost per unit volume of 0.0057 USD/mm^3. Following the same considerations as for Pt above, the cost of a 200 nm Al film deposited on a 4” x 4” wafer is 0.02 USD. Moreover, Al can be easily patterned by standard lithography, stenciling or lift-off and exhibits low residual stress [26]. Al also forms a highly stable surface passivation oxide that stops corrosion [27]. We believe that the fabrication of highly integrated LOC systems and their adaptation to CMOS technologies is possible using KMPR as a structural material and Al as a metallization material.

The use of Al for integrated heating and sensing in the LOC field has been hindered by the difficulties of polymer metallization as well as the high susceptibility of Al to electromigration at relatively low current densities, a problem that is exacerbated by Joule heating [28]. The electromigration resistance of Al can be increased up to ten times by adding Cu in a small percentage [29], however Al-Cu alloys offer little protection to corrosion as they form weak or

unstable self-passivating oxides [27], [30]. Furthermore, the resistivity of Al is lower than for Pt [31], which might reduce the performance of heaters and sensors.

In this chapter we demonstrate for the first time an affordable, stable, non-noble thin film fabricated on a photopolymer that can be used as a heater or temperature sensor in a wide array of thermal operations in LOC systems, including PCR. The stability of the film is demonstrated by the ongoing characterization of its resistivity and TCR in the range of 22–165 ºC, and the exceptional adhesion of Al on KMPR is qualitatively verified.

8.2 Fabrication

We produced an Al film on KMPR and patterned heater rings of 1.15 mm inner radius and 100 µm width as follows: A 50 µm layer of KMPR 1025 (MicroChem Corp. Newton MA, USA) was spun on a cleaned and dehydrated glass substrate. The layer was then soft-baked for 20 min at 105 ºC, followed by a blanket 365 nm UV exposure with a 1000 mJ/cm^2 dose. The film was then cross-linked by baking at 105 ºC for 3 min and then at 130 ºC for 30 min. We sputtered onto the KMPR film a 200 nm metal layer containing Al (and oxide) from an Al target (purity 99.9995%) in a chamber with a significant base pressure (i.e. we expected a significant degree of oxygen incorporation in the form of oxides). By adding moderate amounts of oxygen, we aimed to produce a film of higher resistivity, without risking rendering the film dielectric. A higher resistivity film allows for higher power output per unit current, as well as higher sensitivity when used as a sensor. To achieve this, the chamber of our sputtering system (1998, Kurt J. Lesker Co.), was pumped down to a base pressure of 1.4 µTorr prior to initiating sputtering with an Ar gas feed. During sputtering, we held a 7 mTorr deposition pressure by setting 30 sccm Ar flow rate, and used 300 W, 380 V deposition power and voltage, to deposit 7 nm/min. In preparation for sputtering the wafers were inserted upside-down in the sputtering system above a 99.9995% purity Al target at an approximate distance of 15 cm. The Al film was then patterned using a positive photoresist exposed through a mask with a dose of 180 mJ/cm^2 of 365

nm UV light. After development the Al film was etched for 6 min in a 16:1:1:2 solution of phosphoric acid, nitric acid, acetic acid and water. The positive resist was stripped in acetone for 10 s. Details of the fabrication process are available in [32].

8.3 Experimental

We analyzed the behavior of the Al film on KMPR and determined its resistivity characteristics by calibrating the heater's electrical resistance vs. absolute temperature and then subjecting the heaters to significant Joule heating. This process was carried out twice, and the Joule heating hold time was increased substantially in the second test.

8.3.1 Calibration

The aluminum heater-on-KMPR chips were clamped in a holder equipped with round-tip spring-loaded Au-coated "pogo" pins of 1 mm diameter (Interconnect Devices Inc.), which make contact with the heater terminals without scratching the metal. The holder was sealed in a plastic bag and immersed in an isothermal waterbath (Haake C25P), which in turn was calibrated with a NIST-certified (National Institute of Standards and Technology) RTD (resistance temperature detector). The resistance was measured with a digital multimeter (HP-34401A, Hewlett Packard) set in 4-wire mode using two leads for voltage and two for current. Because the pins are relatively large, to minimize the overall size of our devices we used only two pins. The leads reach down only to the back end of the pins, thus the pin resistance and contact resistance of the pin on the metal film are part of the measurement. However, by virtue of the use of the Au-coated pins, the contact resistance was estimated to be ~0.3 Ω, which is much less than the resistance of the heater (15 to 22 Ω) in the test temperature range.

In a calibration run, the system first measured room temperature resistance, and then ramped the temperature up to 80 ºC in steps of 20 ºC. Before reading the resistance, the system allowed enough time for the temperature to stabilize at each step, approximately thirty seconds. At the end of the process, the system allowed

the waterbath to stabilize back to room temperature before taking the final reading. We use the difference of the resistance measured at room temperature at the beginning and at the end of a calibration run as a metric of the hysteresis of the heater. A complete calibration cycle consisted of three consecutive runs without moving the connections or taking the chips out of the waterbath.

8.3.2 Joule Heating

The heater chips were placed on the copper heatsink of our custom-made test instrument (described in section 3.1) and clamped with a gantry carrying pogo pins that connected to the circuitry. Two thermocouples (5TC-TT/K/40.36, Omega Engineering Inc.), calibrated in the waterbath, were taped onto the heatsink with adhesive pads (Omega Engineering Inc.) at opposite points next to the chip. The average of the readings of the two thermocouples was a good indicator of the room temperature.

To induce heating, a regulated current was passed through the heaters and increased in steps up to 172 mA. The resistance was calculated from the reading of a digital multimeter (DMM) measuring the applied current and a second DMM measuring the voltage at the ends of the pogo pins. The temperature along the heater was estimated from the calibration data and measured heater resistance using:

$$T = T_{rt} + \frac{R - R_{rt}}{m} \qquad \textbf{Eq. 5}$$

Where T_{rt} is the room temperature measured at the beginning of the experiment [ºC]; R is the measured resistance [Ω]; R_{rt} is the room temperature resistance [Ω]; and m is the slope of the calibration curve of runs #3 or #6 [Ω/ºC]. With the relation above and the known room temperature, we corrected for variations of the reference resistance R_{rt} for the same chip across the two instruments (waterbath and Joule heating test instrument). Although the calibration curve does not cover the entire operating temperature range of the heater, we believe that the high linearity observed in the calibrated range of 20–80 ºC holds at higher

temperatures, at least to the limit of the KMPR degradation point (200 ºC [24]). The reason to believe this is that in preliminary tests at low currents (0.33 to 123 mA in steps of ~24 mA) the heaters repeatedly showed the same resistance (within ~ 40 mΩ) and temperature (within 1 ºC) for the same applied currents over successive experiments, and this repeatability persisted at higher currents (148 to 172 mA). A current of 123 mA produced approximately 19 Ω, corresponding to 86 ºC as calculated from Eq. 5. Additionally, the resistance and estimated temperature showed a quadratic relation with current (with a correlation of 0.9998) that continued along the same curve beyond 123 mA. At temperatures near the KMPR degradation point the polymer experiments a significant loss of mass [24], which may deteriorate the Al film and change its properties.

To test how reproducibly the heater could reach the same resistance at a given temperature, the current through the heater was raised, held for a defined hold time, turned off, and then raised again to the previous value. A period of 30 s for heating and 3 min for cooling back to room temperature was allowed for the heater temperature to stabilize before taking a reading and counting the hold time. The resistance at room temperature was measured by applying a very small current (0.33 mA), which produces negligible Joule heating.

In the first Joule heating test, the current was increased gradually in intensity and time in order to avoid a thermal shock that could cause a heater fracture. The experimental sequence was as follows: 1) 0.33 mA were passed through the heater to measure R_{rt} . 2) The current was raised to 123 mA, held for 30 s to allow temperature settling, and then a chronometer was started to count the hold time. The resistance R_1 was measured during this time. 3) After 15 min the timer was stopped, the current was turned off and the system was allowed to cool down for 3 min. 4) The current was raised again to 123 mA, but only held for 1 min in order to measure the resistance R_2. The difference $\Delta R = R_1 - R_2$ and its temperature counterpart (calculated from Eq. 5) $\Delta T = T_1 - T_2$ were used as a metric of the stability of the film. This sequence was repeated with 148 mA, and 172 mA using a hold time of 30 min at each level. Finally, the sequence was repeated one more

time, again at 172 mA and for 30 min, to ensure there was no additional change in R_2. After returning to the waterbath for the second calibration cycle, the second Joule heating test was performed. This second Joule heating test was performed in the same way as the first, but with adjustments; the current was raised to 172 mA directly, and the hold time was increased to 2 hr and 3 hr (from 30 min) for two consecutive tests. During these tests the heaters were monitored for fracture and other types of damage with a microscope.

We expected that the gradual increase of temperature and short hold time in the first test would bake the polymer in the heater area, resulting in a progressive increase in its glass transition temperature (T_g) resulting in higher hardness and mechanical stability. Previously [24], our research group measured the shift of T_g with baking temperature and time for KMPR. From this work we estimate that the initial T_g in our films is within 95–105 ºC, and reaches 120–130 ºC from the Joule heating tests.

8.4 Results and Discussion

8.4.1 Characteristics of the Al Film on KMPR

An example of the fabricated heater is displayed in Figure **33**. We found that a hard-bake of KMPR for shorter times or lower temperature (e.g. 15 min at 120 ºC) leads to ridge formation on the Al film and a non-linear resistance vs. temperature characteristic, which renders the heater unusable (data not shown). The observed ridges, shown in Figure **34**, are of the labyrinth-type (described in [12], [33]) and appear when baking the positive photoresist at 115 ºC, which we attribute to the stresses in the system. Since the Al deposition occurs at temperatures above room temperature, an intrinsic compressive stress develops in the film upon cooling due to differential thermal expansion [34]. KMPR also expands thermally during Al deposition and will also contribute to the total stress of the system. We believe that the T_g of KMPR with the aforementioned baking conditions is too low (70–80 ºC, estimated from [24]), and hence the KMPR softens substantially when heated to 115 ºC, to a point where the stress overcomes the mechanical strength of the

polymer and corrugates the metal. We observed that this corrugation/ridging is irreversible. We also found that sufficiently hard-baked KMPR was stable against these mechanical effects. If KMPR is baked at 130 ºC for 30 min, polymerization advances, T_g moves up to 95–105 ºC, and hardness increases [35], resulting in a KMPR film that is rigid enough to withstand these stresses and maintain the Al film smoothness.

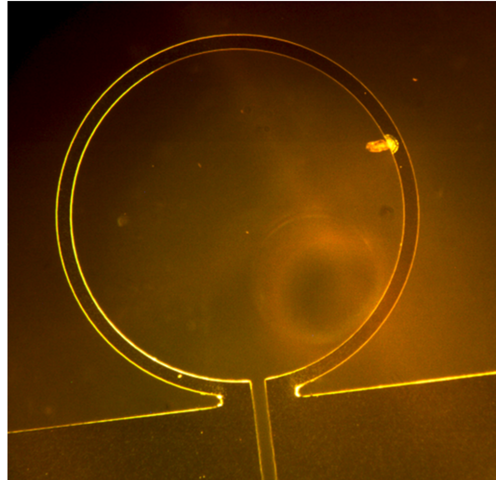

Figure 33. Optical image of an Al heater on KMPR during Joule heating tests. No discernible changes were detected in the metal at this level of magnification. In this heater, the defect on the right-hand side, possibly a bubble in KMPR, did not affect resistance stability, because there was good coverage of metal.

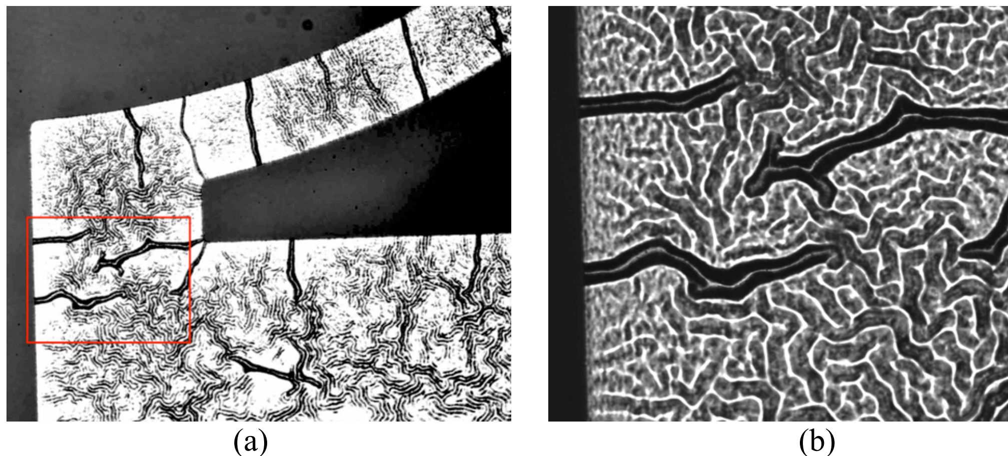

(a) (b)

Figure 34. Optical images of ridges on the Al film, formed by compressive stresses on insufficiently hard-baked KMPR (120ºC for 15 minutes). (a) Ridges on heaters caused significant hysteresis and nonlinear temperature vs. resistance curves; (b) zoomed-in image of the rectangular region in (a). Baking at 130ºC for 30 minutes raised T_g sufficiently to avoid such deformations.

Using these settings, four heaters of 211–241 ± 12.6 nm thickness were patterned on a 50 μm hard-baked KMPR layer. After sputtering, the Al film displayed a smooth glossy appearance that was preserved across the lithography and etching processes. The metal did not crack and did not develop ridges, meaning that KMPR had reached a high degree of polymerization and structural rigidity.

The chemical resistance of KMPR after hard-baking is less than that of SU-8, however it can still tolerate acetone in microchannels for 1 hr and immersion in isopropyl alcohol for 1.5 hr [36]. When hard-baked at 130 ºC for 30 min, KMPR survived lithography with no discernible negative effects, but we observed a degree of permeability to acetone that caused stresses and detachment from the substrate after a 30 min immersion. For shorter periods (3–5 min), the absorption of acetone in KMPR caused cracking of the Al film. For this reason we reduced exposure to acetone to the minimum (10 s) necessary to strip the positive resist. Using the tape test (described further in section 8.4.5), the Al heaters showed excellent adhesion to KMPR at room temperature.

8.4.2 Resistance Behavior

8.4.2.1 First Calibration Cycle and Joule Heating Test

Before the application of any current, the heaters displayed acceptable linearity and hysteresis levels in the first calibration cycle, as illustrated in Figure 35. However, the resistivity was clearly unstable, as the calibration curves were progressively shifting up, again clear from Figure 35. Furthermore, the slope across all the chips showed an important deviation of 2.1 x 10^{-4} Ω/ºC, which corresponds to a measurement error in a theoretical sensor of ±0.62 ºC (0.38%) at 164.5 ºC. This was calculated from Eq. 5 with m_{mean} = 4.82 x 10^{-2} Ω/ºC, T_{rt} = 23.30 ºC, R_{rt} = 15.48 Ω, R = 22.29 Ω. In these chips, contraction of KMPR was negligible, owing to the hard-bake significantly advancing the cross-linking and the waterbath temperatures being too low to produce any significant cross-linking or solvent loss in the KMPR. Therefore, the trend of the resistance to increase

over calibration runs may be due to a combination of thermal strain and a small degree of recrystallization, occurring mainly at 80 ºC [34].

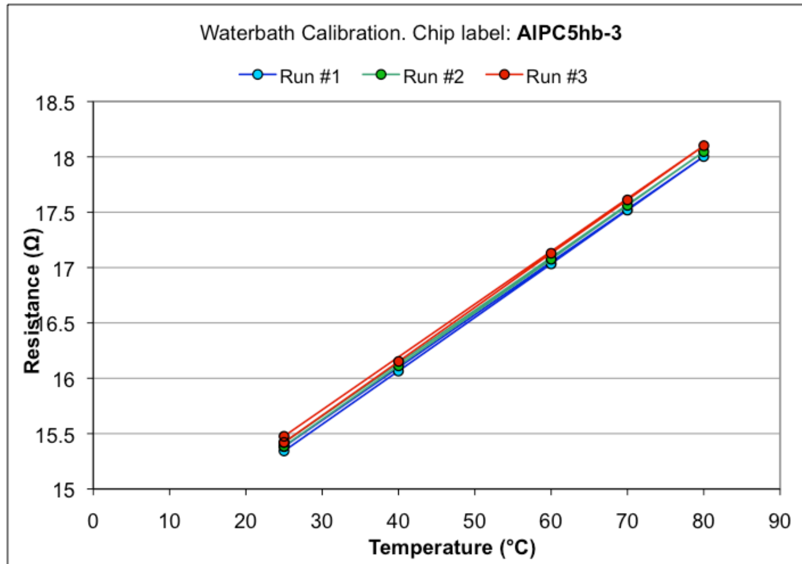

Figure 35. First calibration cycle of a typical Al heater on KMPR, comprising three calibration runs in a row. The plot contains three curves that show a trend between calibration runs of ncreasing resistivity. Blue – run #1; green – run #2; red – run #3.

The first Joule heating test was aimed to determine whether the Al-KMPR system could survive temperatures above 100 ºC for short periods of time, as is often required for LOC devices to perform fundamental operations, such as PCR.

The results of the test are summarized in Table 6. We attained heater temperatures of up to 165 ºC, corresponding to 22.3 Ω (Eq. 5), for periods no longer than 30 min. Gardner and Flinn [34] observed that temperatures between 100 to 200 ºC induce substantial recrystallization in sputtered Al films. Therefore, we expected that this test could anneal the film and stabilize its resistivity. The current through the heater was raised to the same level two consecutive times, with a cooling period in between, as explained in section 8.3.2. The resistance and temperature were measured each time, and the mismatch ΔR and ΔT was used to evaluate the stability of the heater.

The worst stability in terms of calculated temperature ΔT was 0.74 ºC at 86 ºC, after holding the 123 mA current for 15 min. At the highest temperature reached

(165 ºC) ΔT was 0.42 ºC after holding the current for 30 min. In both cases, the variation was less than 1 %. A clear trend of ΔR and ΔT to become smaller indicated that the film was actually being annealed. Holding a current of 172 mA for 30 min seemed to stabilize the film thereafter. The maximum current density through the heater was 7.81 mA/µm^2 at steps 3 and 4 in Table 6. The best and average stability recorded across all the chips was 0.06 ºC and 0.35 ºC, respectively. Notably, defects of up to ~75 µm (caused by particles, bubbles, etc.) did not have a discernible impact on the heater's resistance, as long as there was good coverage of metal, showing that the heaters are tolerant to defects. None of the heaters fractured with the temperature cycling and no adhesion loss was observed.

Step	Hold time [min]	Applied current [mA]	Reached temperature [ºC]	Resistance Mismatch ΔR [mΩ]	Temperature Mismatch ΔT [°C]
1	15	123	86	-36	- 0.74
2	30	147	121	31	0.65
3	30	172	166	20	0.42
4	30	172	165	20	0.42

Table 6. First Joule heating results of a prototype Al heater on KMPR. At each step, the current was turned on, held for the times specified in the second column, turned off to allow the heater to reach room temperature, and finally turned on again. Resistances were measured with the applied current and the mismatch between the two values reflects the film's stability.

8.4.2.2 Second Calibration Cycle and Joule Heating Test

The heaters were calibrated again (another three-run cycle) and the curves obtained, shown in Figure **36**, revealed a highly linear, stable and hysteresis-free behavior, clearly enhanced compared to the first cycle (Figure 35). This result suggests that resistive annealing occurred with a significant degree of recrystallization and stress-relief of Al, again since recrystallization has been observed to take place between 100–200 ºC when the metal is strained by thermal expansion [34]. This phenomenon creates new unstrained grains and removes dislocations in aluminum crystallites caused by sputtering, thereby softening the material and decreasing stress [34]. No deformation/reflow of KMPR nor ridging

of Al were observed, possibly indicating that KMPR acquired higher mechanical stability by advancing polymerization in the heater area, shifting up T_g to 120–130 ºC (estimated from [24] for a 160 ºC bake), and further increasing its hardness as reported in [35].

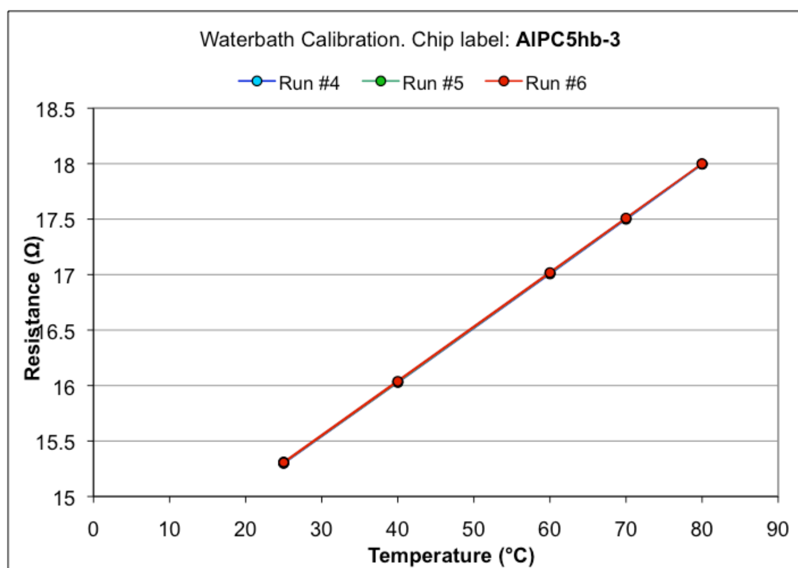

Figure 36. Second calibration cycle of a typical Al heater on KMPR, comprising three calibration runs in a row. The plot contains three curves that overlap each other. It is clear that resistive annealing substantially improves the heater performance.

The surface oxide plays an important role in the film's stability, as it prevents corrosion even at the higher temperatures reached in Joule heating. Lu *et al*. [37] found that further growth of the surface oxide of sputtered Al films is not significant below 250 ºC, even exposed to 100 sccm of pure oxygen flow and plasma.

The second Joule heating test was aimed to establish the feasibility of the Al-KMPR system to sustain a PCR reaction for the minimum time necessary, which can be up to 3–4 hr [38]. During this length of time the resistivity needs to be highly stable as PCR temperatures must be precisely controlled for efficient and selective amplification [24]. To this end, the same maximum current was passed through but for longer hold times.

The results of the test in Table 7 show that the film's resistivity is almost unchanged for over 5 hours of sustained heating. The worst ΔT observed was 0.26 ºC (ΔR = 13 mΩ), after three hours. Compared to the worst ΔT of the first experiment (0.74 ºC), this was an improvement in stability of 2.8 times, and a temperature variation of less than 0.2 %, which can be due to systematic error. This degree of stability is the result of resistive annealing.

Step	Hold time [hr]	Applied current [mA]	Reached temperature [ºC]	Resistance Mismatch ΔR [mΩ]	Temperature Mismatch ΔT [ºC]
1	2	172	162	12	- 0.25
2	3	172	160	13	0.26

Table 7. Second Joule heating test results of a prototype Al heater on KMPR. At each step the current was turned on, held for the times specified in the second column, turned off, allowing the heater to reach room temperature, and finally turned on again. Resistances were measured with the applied current, and the mismatch between the two values reflects the film's stability.

After more than 6 hr of total sustained heating at 140–165 ºC, the duration of both the first and second tests, no change in the film's surface uniformity was detected (see Figure **33**). Although KMPR was exposed to these temperatures that are much higher than the hard-bake (130 ºC), the metal did not develop ridges. The CTE of KMPR, assuming it comparable to that of SU-8 (52–150 ppm/K [8]), is significantly higher than for Al (~23.1 ppm/K [34]). This mismatch generates tensile stresses on the Al film. However, even after repeated heating/cooling cycles, no cracks or fractures of Al were detected. Adhesion was maintained, as confirmed by the tape test. This behavior of the Al-KMPR system suggests that the temperature can be increased beyond 165 ºC, up to the limit of the decomposition temperature of KMPR (200 ºC, which produces 5 % mass loss [24]).

8.4.3 Resistivity and TCR

Final values for the TCR (α) and room temperature resistivity (ρ_o) of the Al film were calculated using the length to cross-section area ratio *L/a* of the heaters and the data of calibration run #6. The *L/a* ratio was calculated for each heater from

their individual thicknesses, ranging from 211 to 241 ± 12.6 nm. The results are shown in Table 8, along with values for other film and bulk materials for comparison.

	α [10^{-3} K^{-1}]	ρ_o at 22 ºC [10^{-8} Ω-m]
Al on KMPR (this work)	3.52 ± 0.059	4.39 ± 0.16
Bulk Aluminum [31], [39]	3.90 – 4.71	2.67 – 2.82
Platinum thin film on SiN_X, Si [23] or SiO2 [40]	1.96 – 3.30	15 – 30
Bulk Platinum [31], [23]	3.92 – 4.00	10.55 – 10.58

Table 8. Mean temperature coefficient of resistivity and resistivity at room temperature of Al on KMPR after annealing. Values for other film and bulk materials are shown for comparison.

The TCR of the Al film is 75 to 90 % of the bulk value. The resistivity is 1.6 times higher than the bulk value but still in the range reported by others on inorganic substrates [41], [42], [43], [44]. The measured α for the Al film is of the same order as for a Pt film. In the test range the observed behavior is also as linear as for Pt. Therefore the Al film can readily replace Pt in integrated heater and temperature sensor applications.

The oxide fraction in Al films does not have a significant impact on the resistivity until it reaches a certain limit. Faith *et al*. [43] used the resistivity as a measure of the oxygen content in Al films, with the resistivity being insensitive to the oxygen content until about a 5% content, corresponding to O_2 pressures of ~10^{-3} Pa (7.5 µTorr), but depending on deposition rates, sputtering distance etc. Kubovy and Janda [44] noted that at low residual gas pressures the resistivity remained approximately at 5 x 10^{-8} Ω-m, but showed a sharp increase when the oxide content exceeded 20%. We therefore estimate that the oxide content in our films is on the order of 5 to 20%, and has the effect of moderately increasing the resistivity of the film.

8.4.4 Resistance Repeatability and Measurement Precision

8.4.4.1 Same Chip Repeatability

The variation of the slope of the curves in Figure **36** was found negligible in all the chips tested. In runs #4–6, after 11 hr effective test time in the waterbath, the slope changed with a standard deviation of $\sigma \approx 7 \times 10^{-5}$ Ω/ºC, i.e. 0.13 %, corresponding to a measurement error of ±0.2 ºC at 162 ºC. This is the heater temperature precision that can be ensured by performing a per-chip calibration, as estimated from Eq. 5. A table that summarizes this calculation is available in [32]. We are typically concerned with temperature accuracy to within 1 ºC. Therefore, in sensor applications only one calibration run after annealing is necessary to obtain parameters for highly accurate temperature measurements.

8.4.4.2 Chip-to-Chip Repeatability

The slope standard deviation after annealing, as measured from chip-to-chip, was $\sigma \approx 1.3 \times 10^{-3}$ Ω/ºC, representing ±2.3 % variation, corresponding to ±3.7 ºC at 162 ºC. However, the slope is highly influenced by variations of film thickness. In other words, a change in slope may be due to variations in both thickness and resistivity. Since we measured a relatively large thickness deviation of ±12.6 nm (5.6 %) across different heaters, it is better to use the TCR (α) to calculate measurement error. At the same temperature, the resistivity at each point of the wafer is different, meaning that α is also different; therefore, the deviation of α is a measure of the wafer-wide uniformity of the resistivity. The standard deviation of α was measured to be $\pm 0.059 \times 10^{-3}$ K^{-1} or ±1.7 % (see Table 8). In a heater of standard dimensions, this produces a measurement error of about ±1.5 %, corresponding to ±2.4 ºC at 162 ºC. Please refer to [32] for details of this calculation.

Therefore, in a process with good thickness control, only one chip in the wafer would need to be calibrated if a maximum error of 1.5 % is acceptable. The error decreases with temperature. For instance, at 100 ºC, the error is calculated to be 1.3 %. Therefore, in the worst-case scenario of a PCR system, the error in heater

temperature *Th* would be about ± 1.4 ºC at the denaturation temperature (94ºC). In a typical PCR device, however, the temperature in the PCR chamber (*Tc*) is a fraction of *Th* and therefore variations of *Th* attenuate at the chamber level, and hence the error in *Tc* will be under 1.3 %.

8.4.4.3 Batch to Batch Repeatability

In unpatterned Al on KMPR we observed that films sputtered at Ar pressures between 7 to 11 mTorr did not develop defects, i.e. ridges or cracks, even after being annealed in an oven at 200 ºC. This mechanical stability was also associated with a consistent resistivity. This property was measured at 22 ºC on the unpatterned metal using a 4-point probe. We confirmed that the resistivity and deposition rate are significantly sensitive to deposition pressure. In the aforementioned pressure range, the resistivity of annealed samples at room temperature varied within ±10 %. From this we estimate a worst case TCR deviation of ±6.3 %. We believe that constraining the deposition pressure to 7 ± 0.5 mTorr or better, the TCR deviation can be reduced to the ±2% level, although per-wafer calibration and annealing will still be necessary for high accuracy applications.

8.4.5 Al-KMPR Adhesion

As mentioned throughout the work in this paper, the adhesion of the Al heaters to the underlying KMPR structure is exceptionally strong. Immediately following the initial sputtering step, the blanket-deposited Al-on-KMPR passed the tape test at all tested locations of the wafer. After the first Joule heating test in which the heater was brought to 165ºC, the patterned aluminum again passed the tape test. Finally, after a total of more than 6 hours at high temperature, the heater yet again passed the tape test, showing its robust adhesion to the KMPR layer underneath. Indeed, standard tape tests were performed at each step of the fabrication and testing processes, and the metal-KMPR adhesion never failed. This level of metal adhesion is not observed on other polymer materials. In fact, it is often very difficult to achieve even moderate adhesion [45], [46], [47]. Adhesion between

other metals and polymers often fails at room temperature, let alone at the high temperatures required for PCR, where thermal mismatch causes high stresses. Our process did not require any chemical adhesion promoters, surface treatments (such as O_2 plasma) or additional adhesion layers such as Cr or Ti. Furthermore, over time, adhesion has been maintained – our older samples still pass the tape test 12-months after patterning.

To qualitatively demonstrate the exceptional adhesion of aluminum on KMPR in comparison to other commonly used LOC polymers, an additional tape test on various substrate materials was done. Al was deposited as described in section 8.2 onto substrates of PMMA, polycarbonate (PC), SU-8 on Si and KMPR on Si. All substrates were processed the same way, with no adhesion promotion or surface treatment of any kind. The PMMA and PC substrates were cleaned gently with water and IPA to remove contaminant oils and dust prior to Al sputter-deposition. Both the SU-8 and KMPR were spun to a thickness of 20 µm, pre-baked for 10 min at 100 ºC, and blanket-exposed with a dose of 1 J/cm^2. The SU-8 on Si was post-baked for 30 min at 100 ºC and the KMPR for 60 min at 150 ºC. Aluminum was sputter-deposited to a thickness of 200 nm, and all four substrates were in the chamber together, so as to ensure identical films.

Crystal Clear tape (Grand & Toy, product code 99110) was used for the tests. From preliminary tests on glass we observed that this product has aggressive adhesion, even stronger than that of typical packing tape. Figure 37 clearly displays the key result of the test; the aluminum was easily and completely removed from the PC, PMMA and SU-8 substrates, yet maintained excellent adhesion to KMPR.

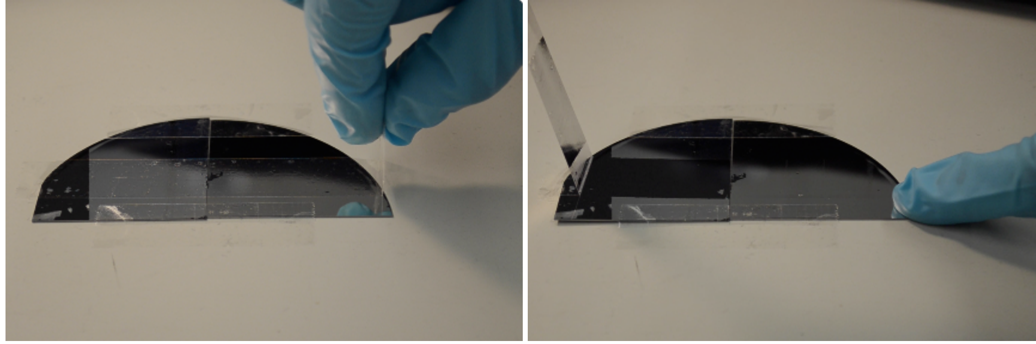

Figure 37. Aluminum on KMPR (right quarter wafer) and Al on SU-8 (left quarter wafer) tape-test. Both polymers were layered on silicon substrates. Al is completely removed from the SU-8 but remains on the KMPR, clearly showcasing exceptional metal-polymer adhesion.

While this test lacks rigorous quantitative values, it shows the significant difference in adhesion strength of aluminum deposited on KMPR compared to other common LOC substrate materials. Since the patterned metal exhibited such strong adhesion compared to results typical of metallization on other polymers, quantification of the adhesion strength should be explored. Such quantification does not have a significant impact on the focus of this particular work, however, and as such will be relegated to future publications.

8.4.6 Electromigration Effects

For pure Al connected to DC power, a conservative electromigration limit is 1–2 mA/μm^2 for conductors at 110 ºC [28, p. 240]. In our experiments, this limit was greatly exceeded (7.8 mA/μm^2, 165 ºC). We expected that these conditions would cause severe electromigration and heater failure in a short time. Contrary to our expectations, the heaters survived all the experiments (~6 hours) with no apparent damage. Closer inspection revealed electromigration-induced hillocks, with highest incidence and largest size at the interconnections of the heater ring to the contact pads. We found by simulation (see Figure 38) that these are the areas of maximum combined current density and temperature, which supports the electromigration origin of the hillocks.

In our work, electromigration progressed at a low rate along the experiments, as shown in Figure 39, without creating voids. Electromigration did not have a measurable effect on the resistance characteristics of the heaters. We believe that the addition of oxides to the film increased its resistance to electromigration, giving an effect similar to doping Al with Cu. Al-Cu alloys, however, are susceptible to corrosion [27], [30], and thus their properties are at risk of changing when exposed to oxygen and other corrosives. The Al-Al_2O_3 heaters of this work are not, however, susceptible to corrosion due to the highly stable surface passivation oxide of the film. The increase in electromigration resistance may be caused by the oxide crystallites (microscopic crystalline grains) in the film creating stress fields that oppose the transport of Al [48].

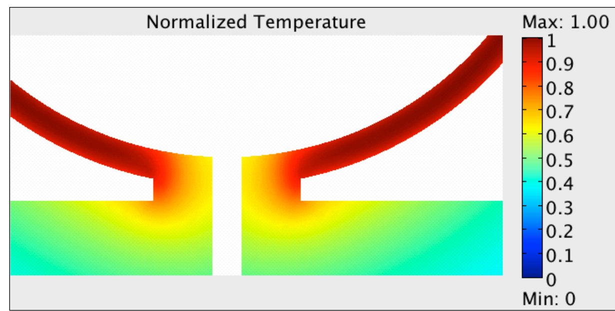

(a)

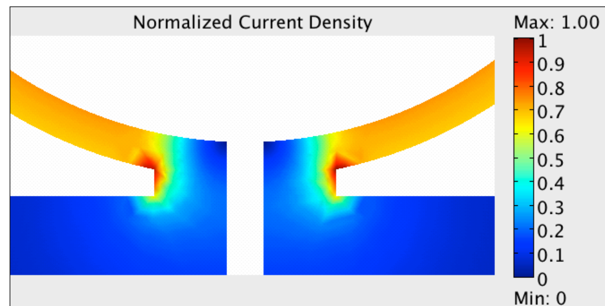

(b)

Figure 38. Coupled Joule-heating/heat-transfer 3D simulation of an Al heater on KMPR in normalized values. The area of highest combined current density and temperature is at the ring-pad interconnect. Electromigration will occur at the highest rate in these areas. (a) normalized temperature; (b) normalized current density. The simulation was performed in COMSOL 3.5a using the base model of PCR/CE-4 described in section 3.7. The Electrical Conduction in Shells physics was added to the base model to simulate Joule heating, much as described in section 4.1.

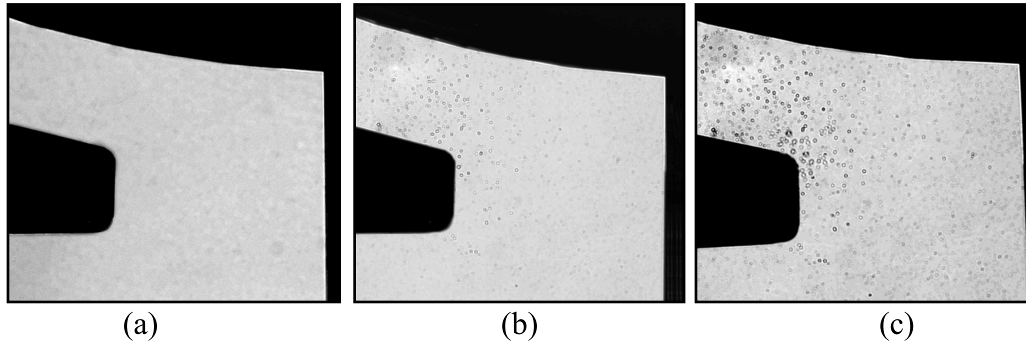

Figure 39. Optical images of Al heaters on KMPR. The size and density of hillocks due to electromigration increase with operation time. (a) Film before application of current; (b) film after 1 hr of ~165 ºC Joule heating; (c) film after 6 hr of ~160 ºC Joule heating. Deliberate shallow scratches to the film (d, e, f) confirmed that hillocks proliferate on defects.

8.4.7 Resistive vs. Batch Annealing

The annealing of the metal film was accomplished via resistive Joule heating, as described. It should be noted, however, that annealing could have been accomplished by oven-heating the entire device. Such batch-annealing is cost effective and simple, but per-device resistive annealing offered significant advantages. Firstly, annealing and calibrating devices in one step yields information about how the stability of the microfabricated heaters changes. Furthermore, in applications where a heater must be fabricated with other, more temperature-sensitive layers or processes, a batch-annealing process may not be possible. The resistive annealing method is selective in its heating, allowing for a wider range of fabrication possibilities. For example, membranes and cantilever MEMS structures often depend on careful thermal stress management, and may be adversely affected by a batch anneal step. In considering the purposes of this research, the resistive annealing method was more desirable.

8.5 Conclusions

We presented a method to produce a stable non-noble metal film that can be patterned by standard lithography on a photopolymer and then stabilized through resistive annealing. The film has a sufficiently high resistivity and TCR for use as a heater or temperature sensor. We demonstrated that the film is mechanically and

electrically stable in contact with air for at least 6 hr at ~160 ºC and 7.8 mA/μm^2 current density.

The stability shown at temperatures greater than 100 ºC makes the film suitable for use as a heater or sensor in disposable PCR LOC systems. In sensor applications, a temperature measurement error of ± 0.13 % can be ensured by performing per-chip calibration, since the slope of the resistance vs. temperature curve of a typical heater varies by 7 x 10^{-5} Ω/ºC. If only one chip per wafer is calibrated, the error will be within ± 1.5 %, since the TCR of all the chips in the wafer varies by 59 x 10^{-6} K^{-1}. In a typical PCR system, the error at the chamber level will be smaller since the chamber temperature is a fraction of the heater temperature, and hence variations attenuate.

In this work, the addition of oxides to the Al film provides resistivity above the bulk value, and is thought to increase its resistance to electromigration. In contrast to the effects of Cu in a Cu-Al alloy, the oxides likely protect the film from corrosion, even at high temperatures. The film showed adequate surface uniformity and strong adhesion to the photopolymer, without any additional adhesion layers or other treatments. This is an important point, since avoiding additional adhesion layers or chemical promoters simplifies the fabrication process and reduces time and cost significantly. Finally, and perhaps most significantly, the fabrication process and materials are compatible with CMOS technology, enabling the possibility of true integration of electronic infrastructure and microfluidics. To the best of our knowledge, this is the first demonstration of a stable, non-noble metal thin film heater/sensor fabricated on a photopatternable polymer in the LOC field.

8.6 References

[1] E. J. Geiger, A. P. Pisano, and F. Svec, “A Polymer-Based Microfluidic Platform Featuring On-Chip Actuated Hydrogel Valves for Disposable Applications,” Journal of Microelectromechanical Systems, vol. 19, no. 4, pp. 944–950, Aug. 2010.

[2] P. Abgrall and A.-M. Gué, “Lab-on-chip technologies: making a microfluidic network and coupling it into a complete microsystem—a review,” Journal of Micromechanics and Microengineering, vol. 17, no. 5, pp. R15–R49, May 2007.

[3] S. Park, Y. Zhang, S. Lin, T.-H. Wang, and S. Yang, “Advances in microfluidic PCR for point-of-care infectious disease diagnostics,” Biotechnol. Adv., vol. 29, no. 6, pp. 830–839, Dec. 2011.

[4] C. Liu, “Recent Developments in Polymer MEMS,” Adv. Mater., vol. 19, no. 22, pp. 3783–3790, Nov. 2007.

[5] S. H. Ng, Z. F. Wang, R. T. Tjeung, and N. F. Rooij, “Development of a multi-layer microelectrofluidic platform,” Microsystem Technologies, vol. 13, no. 11–12, pp. 1509–1515, Jan. 2007.

[6] M. Graff, S. K. Mohanty, E. Moss, and A. B. Frazier, “Microstenciling: a generic technology for microscale patterning of vapor deposited materials,” Journal of Microelectromechanical Systems, vol. 13, no. 6, pp. 956– 962, Dec. 2004.

[7] J. N. Patel, B. Kaminska, B. L. Gray, and B. D. Gates, “A sacrificial SU-8 mask for direct metallization on PDMS,” Journal of Micromechanics and Microengineering, vol. 19, no. 11, p. 115014, Nov. 2009.

[8] T. C. Duc, G. K. Lau, and P. M. Sarro, “Polymeric Thermal Microactuator With Embedded Silicon Skeleton: Part II—Fabrication, Characterization, and Application for 2-DOF Microgripper,” Journal of Microelectromechanical Systems, vol. 17, no. 4, pp. 823–831, Aug. 2008.

[9] S. R. Nugen, P. J. Asiello, and A. J. Baeumner, “Design and fabrication of a microfluidic device for near-single cell mRNA isolation using a copper hot embossing master,” Microsystem Technologies, vol. 15, no. 3, pp. 477–483, Aug. 2008.

[10] W. Watanabe, S. Onda, T. Tamaki, K. Itoh, and J. Nishii, “Space-selective laser joining of dissimilar transparent materials using femtosecond laser pulses,” Applied Physics Letters, vol. 89, no. 2, p. 021106, 2006.

[11] W. A. MacDonald, M. K. Looney, D. MacKerron, R. Eveson, R. Adam, K. Hashimoto, and K. Rakos, “Latest advances in substrates for flexible electronics,” J. Soc. Inf. Disp., vol. 15, no. 12, pp. 1075–1083, Dec. 2007.

[12] Z. Huang, W. Hong, and Z. Suo, “Evolution of wrinkles in hard films on soft substrates,” Phys. Rev. E, vol. 70, no. 3, p. 030601, 2004.

[13] C. E. Dube, J. O. Fiering, and M. J. Mescher, “A Si-based FPW sensor array system with polymer microfluidics integrated on a PCB,” in Proceedings of IEEE Sensors, 2002, 2002, vol. 1, pp. 460– 465 vol.1.

[14] "DuPont Corp. - Pyralux Technical Information." [Online]. Available: http://www2.dupont.com/Pyralux/en_US/tech_info/index.html. [Accessed: 10-Jan-2012].
[15] J. El-Ali, I. R. Perch-Nielsen, C. R. Poulsen, D. D. Bang, P. Telleman, and A. Wolff, "Simulation and experimental validation of a SU-8 based PCR thermocycler chip with integrated heaters and temperature sensor," Sensors and Actuators A: Physical, vol. 110, no. 1–3, pp. 3–10, Feb. 2004.
[16] G. V. Kaigala, M. Behnam, A. C. E. Bidulock, C. Bargen, R. W. Johnstone, D. G. Elliott, and C. J. Backhouse, "A scalable and modular lab-on-a-chip genetic analysis instrument," Analyst, vol. 135, no. 7, pp. 1606–1617, 2010.
[17] N. Beyor, L. Yi, T. S. Seo, and R. A. Mathies, "Integrated Capture, Concentration, Polymerase Chain Reaction, and Capillary Electrophoretic Analysis of Pathogens on a Chip," Analytical Chemistry, vol. 81, no. 9, pp. 3523–3528, May 2009.
[18] Z.-Y. Wu, K. Chen, B.-Y. Qu, X.-X. Tian, X.-J. Wang, and F. Fang, "A thermostat chip of indium tin oxide glass substrate for static polymerase chain reaction and in situ real time fluorescence monitoring," Analytica Chimica Acta, vol. 610, no. 1, pp. 89–96, Mar. 2008.
[19] S. R. . Kumar and S. Kasiviswanathan, "Transparent ITO-Mn:ITO Thin-Film Thermocouples," IEEE Sensors Journal, vol. 9, no. 7, pp. 809–813, Jul. 2009.
[20] "Kurt J. Lesker Company, Sputtering Targets," http://www.lesker.com/newweb/menu_depositionmaterials.cfm?section=targets&init=skip. .
[21] D. Resnik, D. Vrtačnik, M. Možek, B. Pečar, and S. Amon, "Experimental study of heat-treated thin film Ti/Pt heater and temperature sensor properties on a Si microfluidic platform," Journal of Micromechanics and Microengineering, vol. 21, no. 2, p. 025025, Feb. 2011.
[22] U. Schmid and H. Seidel, "Influence of thermal annealing on the resistivity of titanium/platinum thin films," Journal of Vacuum Science & Technology A: Vacuum, Surfaces, and Films, vol. 24, p. 2139, 2006.
[23] A. Giani, F. Mailly, F. Pascal-Delannoy, A. Foucaran, and A. Boyer, "Investigation of Pt/Ti bilayer on SiN[sub x]/Si substrates for thermal sensor applications," Journal of Vacuum Science & Technology A: Vacuum, Surfaces, and Films, vol. 20, no. 1, p. 112, 2002.
[24] M. Reynolds, A. Elias, D. G Elliott, C. Backhouse, and D. Sameoto, "Variation of thermal and mechanical properties of KMPR due to processing parameters," Journal of Micromechanics and Microengineering, vol. 22, no. 12, p. 125023, Dec. 2012.
[25] V. M. Blanco Carballo, J. Melai, C. Salm, and J. Schmitz, "Moisture resistance of SU-8 and KMPR as structural material," Microelectronic Engineering, vol. 86, no. 4–6, pp. 765–768, Jun. 2009.
[26] V. M. Blanco Carballo, M. Chefdeville, M. Fransen, H. van der Graaf, J. Melai, C. Salm, J. Schmitz, and J. Timmermans, "A Radiation Imaging Detector Made by Postprocessing a Standard CMOS Chip," IEEE Electron Device Letters, vol. 29, no. 6, pp. 585–587, Jun. 2008.

[27] T. Boettcher, M. Rother, S. Liedtke, M. Ullrich, M. Bollmann, A. Pinkernelle, D. Gruber, H.-J. Funke, M. Kaiser, K. Lee, M. Li, K. Leung, T. Li, M. L. Farrugia, O. O'Halloran, M. Petzold, B. Marz, and R. Klengel, "On the intermetallic corrosion of Cu-Al wire bonds," in Electronics Packaging Technology Conference (EPTC), 2010 12th, 2010, pp. 585 –590.
[28] N. H. E. Weste and D. F. Harris, CMOS VLSI design: a circuits and systems perspective. Boston, US: Pearson/Addison-Wesley, 2005.
[29] S. D. Senturia, Microsystem Design. New York, US: Springer, 2000.
[30] G.-L. Gong, L. Li, W. Liu, M.-J. Song, X.-S. Xu, D.-H. Ye, and J.-Z. Yao, "Characterization of Al/Cu/W bond pad micro-corrosion," in Advanced Packaging Materials (APM), 2011 International Symposium on, 2011, pp. 234 –238.
[31] D. R. Lide, CRC Handbook of Chemistry and Physics, 90th ed. Boca Raton, US: CRC Press, 2009.
[32] J. Martinez-Quijada, S. Caverhill-Godkewitsch, M. Reynolds, L. Gutierrez-Rivera, R. W. Johnstone, D. G. Elliott, D. Sameoto, and C. J. Backhouse, "Fabrication and Characterization of Aluminum Thin Film Heaters and Temperature Sensors on a Photopolymer for Lab-On-Chip Systems," Sensors and Actuators A: Physical, vol. 193, pp. 170–181, Apr. 2013.
[33] Z. Y. Huang, W. Hong, and Z. Suo, "Nonlinear analyses of wrinkles in a film bonded to a compliant substrate," Journal of the Mechanics and Physics of Solids, vol. 53, no. 9, pp. 2101–2118, Sep. 2005.
[34] D. S. Gardner and P. A. Flinn, "Mechanical stress as a function of temperature in aluminum films," IEEE Transactions on Electron Devices, vol. 35, no. 12, pp. 2160–2169, Dec. 1988.
[35] K.-S. Ou, H.-Y. Yan, and K.-S. Chen, "Mechanical Characterization of KMPR by Nano-Indentation for MEMS Applications," Strain, vol. 44, no. 3, pp. 267–271, 2008.
[36] L. Convert, V. Aimez, P. Charette, and R. Lecomte, "Rapid prototyping of integrated microfluidic devices for combined radiation detection and plasma separation," in Microsystems and Nanoelectronics Research Conference, 2008. MNRC 2008. 1st, 2008, pp. 105–108.
[37] F.-H. Lu, H.-D. Tsai, and Y.-C. Chieh, "Plasma oxidation of Al thin films on Si substrates," Thin Solid Films, vol. 516, no. 8, pp. 1871–1876, Feb. 2008.
[38] T.-T. Huang, J.-S. Wang, C.-S. Yu, and Y.-C. Hu, "A novel rapid-reaction nucleic-acid amplification device using micro-volume chips," in Instrumentation and Measurement Technology Conference (I2MTC), 2011 IEEE, 2011, pp. 1 –3.
[39] R. A. Serway, Principles of Physics. Fort Worth, US: Saunders College Pub., 1998.
[40] I. Elmi, S. Zampolli, E. Cozzani, M. Passini, G. C. Cardinali, and M. Severi, "Development of Ultra Low Power Consumption Hotplates for Gas Sensing Applications," in 5th IEEE Conference on Sensors, 2006, pp. 243–246.
[41] F. D'Heurle, "Aluminum films deposited by RF sputtering," Metallurgical and Materials Transactions B, vol. 1, no. 3, pp. 725–732, 1970.

[42] H. Takatsuji, T. Arai, S. Tsuji, K. Kuroda, and H. Saka, “Al-based sputter-deposited films for large liquid-crystal-display,” Thin Solid Films, vol. 337, no. 1–2, pp. 235–239, Jan. 1999.
[43] T. J. Faith, R. S. Irven, J. J. ONeill, and F. J. Tams, “Oxygen monitors for aluminum and Al-O thin films,” Journal of Vacuum Science and Technology, vol. 19, no. 3, pp. 709 –716, Sep. 1981.
[44] A. Kubový and M. Janda, “The influence of residual gas pressure on the stress in aluminium films,” Thin Solid Films, vol. 42, no. 2, pp. 169–173, Apr. 1977.
[45] D. Sameoto, S.-W. Lee, and M. Parameswaran, “Electrical interconnection through optimized wirebonding onto SU-8 structures and actuators,” Journal of Micromechanics and Microengineering, vol. 18, no. 7, p. 075023, Jul. 2008.
[46] J. Ge and J. K. Kivilahti, “Effects of surface treatments on the adhesion of Cu and Cr/Cu metallizations to a multifunctional photoresist,” Journal of Applied Physics, vol. 92, no. 6, pp. 3007 –3015, Sep. 2002.
[47] R. K. Ulrich, M. Wasef, J. Im, P. Garrou, and D. Scheck, “Thermosonic gold wirebonding to electrolessly-metallized copper bondpads over benzocyclobutene,” in Proceedings-SPIE The International Society For Optical Engineering, 1999, pp. 260–265.
[48] Y. Luo and P. U. M. Engineering, Modeling Stress and Stressmigration in Microelectronics Interconnects. Purdue University, 2007.

9 A Novel Design Method for Thin Film Heaters

A version of this chapter will be submitted for publication (Article 3 – J. Martinez-Quijada 2014).

In Chapter 5 we concluded that calibration procedures could be greatly simplified by immersing the chamber, heat source and temperature sensor in a uniform temperature environment. High temperature uniformity is also required for efficient PCR and is critical in other key operations in LOC devices, such as melting curve analysis (MCA). However, spatial thermal control of localized fluid volumes is a major challenge in the LOC field. Uniform heating, particularly, is difficult to achieve due to complex patterns of heat loss to a variable external environment. Moreover, the conventional design approach for thin film heaters is to iterate from an initial best guess towards reaching an optimal design, but without knowledge of the exact power distribution that is required to produce the desired temperature profile. Such an iterative process enormously increases the time and cost of the design process. This chapter presents a novel methodology for rapid-turnaround design of thin film heaters that produce a pre-determined, high resolution, spatially-controlled power density field that produces uniform temperature or any other temperature profile in a planar structure. High temperature uniformity in PCR chambers of arbitrary shape and size is achieved with a single metal layer heater, while maximizing energy efficiency and minimizing the footprint. Furthermore, our method enables the use of aluminum as an effective replacement to platinum and other expensive materials commonly used in LOC devices

A novel PCR LOC system with robust thermal control is the platform where the method presented herein is implemented. Four different heater designs clearly demonstrate fast, highly selective and uniform heating repeatably within ± 1.25 ºC at an average chamber temperature of 95 ºC. The thermal system is briefly introduced in section 9.2 and is explained in detail in the next chapter.

The author along with Dr. Duncan Elliott developed the presented method. The author analyzed and simulated several heater topologies, including concentric ring heaters, which led to the development of the method. The author developed the design flow, simulation models and step-by-step procedures of the method. The author developed the mathematics and algorithm to automatically generate the mask layout of the heaters and implemented the algorithm in MATLAB code. The author implemented the method to produce four heater designs helped by Saul Caverhill-Godkewitsch, Matthew Reynolds and David Sloan. In this implementation the author performed the 2D simulations of Step 1 and the operations involved in Step 2 of the method. Saul Caverhill-Godkewitsch performed the 3D simulations of Step 1 and Step 3 of the method. The author wrote the corresponding paper with feedback and corrections from Saul Caverhill-Godkewitsch. Saul carried out other 3D simulations, including sensitivity and transient simulations, and generated the 2D and 1D plots from COMSOL for the article. Matthew Reynolds developed the lift-off process to fabricate the heaters. Matt connected the tracks of the heaters manually and laid out the fabrication masks in L-Edit. He fabricated the devices and calibrated them to determine the TCR of the Al film. David Sloan developed the instrumentation to perform lifetime and transient response tests and ran these tests along with Matt. David validated the MATLAB code developed by the author and ported the code to C# for future use. The author wrote all the documents of the provisional patent application.

9.1 Introduction

The advent of lab-on-chip (LOC) devices for genetic diagnosis has revolutionized our vision for the future of health care. To date, however, LOC systems remain confined to the laboratory setting due to the need for off-chip infrastructure [1], [2], and other factors including the high cost of design and fabrication. One critical step in many gold-standard genetic analysis methods is the polymerase chain reaction (PCR). The temperature uniformity in a PCR microreactor has a profound impact on the efficiency of the reaction [3], [4], and on the accuracy of

quantitative real-time PCR (qPCR) and melting curve analysis (MCA) [5], [6]. The speed of the reaction, on the other hand, is typically limited by temperature ramping rates [1]. Therefore, to achieve widespread use of LOC devices it is fundamentally important to develop an inexpensive technique for fast, uniform heating.

Uniform temperature in LOC PCR can be obtained by heating entire devices with external sources such as temperature-controlled blocks [7], infrared lamps [8], Peltier cells [6] and other commercial heaters [9]. These methods are power-inefficient and typically show poor heating/cooling rates [10]. Recently, infrared laser has been proposed as a more selective heating alternative [11], [12]. Regrettably, the methods above require off-chip components and/or precision optical instrumentation that are bulky and too costly for an inexpensive LOC or implementation and eventually the integration of LOC functionality on CMOS.

Integrated thin-film heaters can be batch-produced in cost effective mass production. These elements have small thermal mass and can be constructed in close proximity to the PCR chamber, which results in fast heating/cooling rates and efficient use of power. In some instances it is also possible to use the heater as a temperature sensor [13], [14]. Unfortunately, controlling temperature gradients across the heater and in the PCR chamber is difficult, and this problem exacerbates with the use of low-conductivity materials such as polymers [4], [15], and certain geometrical factors. Some designs, such as the drive-wheel heater [16], produce better uniformity than other heaters with tracks connected in series or parallel. Generally, however, the uncompensated high heat loss at the edges of planar heaters results in poor temperature uniformity. Moreover, thin film heater materials must show stability at high temperatures and resistance to electromigration. Because platinum exhibits these characteristics, it is the most commonly used metal for LOC thin film heaters [14]. Platinum, however, is expensive, requires Ti or Cr adhesion layers and patterning is difficult as it requires lift-off [14] or etch in aqua regia at 90 ºC [9]. Therefore, Pt is not

compatible with CMOS processing since aqua regia attacks Si, Al, photoresist and other materials used in CMOS fabrication [17], [18].

The use of inexpensive non-noble metals such as Al is vital to achieving a truly inexpensive LOC system. Al metallization is cheap, easy to pattern, and compatible with CMOS technology. Current density is a key parameter to consider in the heater design to enable the use of aluminum without risking failure electromigration. Previously we demonstrated the favorable characteristics of Al as a suitable alternative to Pt for the fabrication of thin film heaters/sensors on a polymer [19] (in Chapter 8).

Array-type heaters are made of intersecting tracks of dissimilar metals forming an array of low and high resistance spots. These heaters have been shown to achieve higher temperature uniformity than conventional serpentine heaters, parallel track heaters and block heaters [20], [21], [22]. Wang *et al*. [22] reported on 6 x 6 mm Pt/Au array microheaters that provided uniformity of ± 2 ºC around an average of 94 ºC over 98.5% of a 5.2 x 5.2 mm area. Hsieh *et al*. [21] presented a 6-track Pt/Au array-type heater that compensated for edge cooling by widening the outermost tracks, and achieved approximately ± 0.5 ºC uniformity in 90.3% of a 5 mm diameter circular chamber around an average of 95 ºC. Unfortunately, these heater designs are expensive, as they require two superimposed layers of noble metals.

In addition to the costs associated with expensive thin film materials, the design methodology used to create the heaters listed above is rigid, time-consuming and costly. Typically, a heater geometry is proposed and then tested or simulated. Results are then fed back into the design flow to correct uniformity issues, and the process is iterated until an acceptable temperature profile is obtained. However, if the geometry, materials or boundary conditions of the device change, the heater is no longer optimized and the design process will have to be repeated. Such inefficiencies in design methodology limit the number of systems that can be produced and contribute to the high costs of PCR heater designs for LOC

platforms. Modern LOC implementations often require frequent changes of structure, materials, and chamber size/shape during the design process to improve their functionality. Therefore, a well-organized and flexible method to rapidly produce heater designs optimized for the newest system configurations is required.

One of the most advanced heater design methods presented to date is from Selva *et al*. [23]. The method optimizes the shape of a single-layer Pt heater in order to minimize its size in relation to the chamber to save power and to compensate for edge cooling. Starting from an initial suggested shape, a genetic algorithm generates variations of the shape and then tests them via finite element simulation until obtaining an optimal geometry. This method, however, is still iterative, extremely complex and computationally intensive. Furthermore, a low-resolution design is obtained at the output (8 metal tracks for a 600 x 600 μm area), which yields uniformity of ± 6 ºC around an average chamber temperature of 37.5 ºC, in 82 % of the area of the chamber. The uniformity at higher temperatures is not clear. At PCR temperatures (60–95 ºC), uniformity was not reported; at those temperatures, especially at 95 ºC, the gradients are much more difficult to control.

To the best of our knowledge, a general, non-iterative technique to automatically layout inexpensive thin film heaters that compensate for uneven heat loss and edge effects has not been reported. This chapter presents a methodology for rapidly generating thin-film heaters that produce a highly uniform temperature across a PCR chamber of arbitrary shape and size by applying an optimal pre-determined power density profile. The resulting single-layer thin film heaters compensate for areas of higher heat loss and maximize the area of uniform temperature. Furthermore, power requirements are minimized and low current densities are maintained for a wide range of suitable voltages.

Instead of departing from a best-guess or arbitrary geometry, the power density distribution required to produce a desired uniform temperature is pre-determined. The power density field is then discretized into a grid of very small segments,

where the resolution can be freely selected in two axes. The local track width that satisfies the power density in each segment is then calculated. The result is a heater with continuous tracks of varying width that recreates the pre-determined power density field when passing a current through it, producing uniform temperature in the PCR chamber within ±1.25 ºC.

In our method, the discretization, track width calculation and geometric layout of the heater are fully automated. This methodology allows for rapid prototyping of power density-determined high-resolution heaters for arbitrary chamber shapes and sizes, different structural layer thicknesses, new materials, adjusted boundary conditions and different chip architectures. Although in this study we focused on producing a uniform temperature field, uneven temperature patterns can be produced in the same way for other applications, such as continuous-flow PCR. In other words, complex temperature patterns in arbitrary shapes are possible in addition to highly uniform temperature distributions. Such flexibility allows for the design of miniaturized devices that can fit into USB key or SD card packages.

The work presented herein provides for the first time a simple and deterministic technique to design fast, selectively uniform, customized heating solutions for the LOC community and beyond.

9.2 Target System

The method presented here is used to design four different heaters for a system suitable for PCR. The system consists of a circular chamber and a thin film heater embedded in a layered polymer structure fabricated on a Si substrate. The device placed on a heatsink forms a thermally robust system, as explained in the next chapter. Figure 40 shows the cross section of the system. For a detailed list of the materials and their properties please refer to the next chapter.

In this configuration, the heat loss at the edge is greater than at the center. To maintain temperature uniformity, the heater must provide a higher power input at the edge. At the same time, the heater must be designed with low current-density

levels in order to enable the use of an Al film and prevent early damage due to electromigration. Moreover, the voltage and current requirements must be kept low to allow the use of low-power electronic components and CMOS integration.

We aimed to produce ±1 ºC temperature uniformity at the highest PCR temperature (95 ºC). We selected 95 ºC as since this temperature causes the worst-case gradients in the chamber. Also, at this temperature the system imposes the highest current and voltage requirements. To show the flexibility of our method, heaters were designed for two different chamber sizes (r_c = 500 µm and 1200 µm radius), and two power density (Q) profiles (non-uniform and uniform). The "non-uniform Q" heaters compensate for edge effects with an increased perimeter power density. However, the metal is exposed to higher current densities that may reduce the lifetime of the device. The "uniform Q" heaters substantially reduce the current density levels, but are larger and use more power. These two Q profiles accommodate a broad range of potential applications.

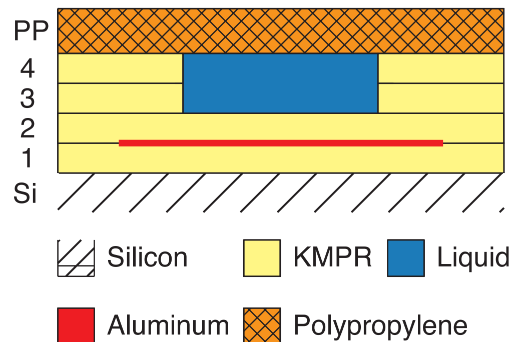

Figure 40. Schematic cross-section of the target PCR system. The thickness of the KMPR layers is (from 1 to 4) 20, 20, 20 and 25 µm. The thickness of the sealing polypropylene layer and Si substrate are 40 µm and 500 µm, respectively. The thin-film Al heater is 100 nm thick.

9.3 Heater Design Methodology

Integrated thermal LOC systems often suffer from a lack of spatial control over the power density distribution of the heat source. As a result, regions with lower thermal isolation experience a drop in temperature; such temperature drops are typically at the edges of a heated area. The purpose of our method is to determine

the exact power density profile required to maintain uniform temperature in all regions of a PCR chamber, and to produce that profile by designing a thin-film heater appropriately.

The PCR chamber in our target system is circular. To achieve high power efficiency, the heater must follow the shape of the chamber while avoiding excessive heating of regions outside that radius. To this end, we initially implemented our design concept in a drive-wheel heater configuration, proposed by Lee *et al*. [16], and a parallel-type configuration, depicted in Figure 41.

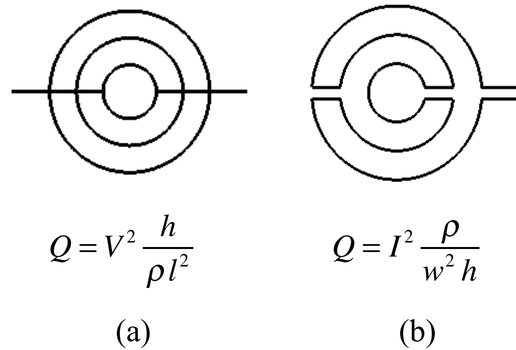

Figure 41. (a) Parallel-type heater (b) Series-type drive wheel heater. Q – power density along the metal tracks; V and I – applied voltage and current; h – thickness of the metal film; ρ – resistivity of the metal film; l and w – length and width of the tracks.

The parallel-type heater, however, has very high amperage requirements and the radial power density is difficult to control as it depends quadratically on the track radius (length), as shown in Figure 41a. In contrast, the drive-wheel heater is independent of track radius, as shown in Figure 41b, allowing the power density across the heater to be shaped precisely and with flexibility. However, since a high track density is required to attain acceptable power density resolution, the voltage requirement of these heaters may become extremely high for heaters of large radii. Moreover, the use of these designs is limited to systems with axial symmetry.

To circumvent these problems, we developed a novel topology that we call *grid heaters*, as they originate from a grid of small segments. The method is divided into three steps: 1) calculation of the Q profile, 2) discretization/layout and 3)

verification. In the first step, a finite element model (FEM) of the system is used to determine the power density field Q that produces uniform temperature in the system geometry of interest. In the second step, the Q field from step 1) is divided into small rectangular segments and the track width for each is calculated; the width information is then used to construct the layout of the heater that is to be fabricated. In the third step, the heater layout is embedded into a 3D FEM of the system and is simulated with an applied voltage to verify the temperature uniformity and current density levels.

One of the novel aspects of this methodology is that the Q field is discretized in order to calculate the local width of metal traces that will provide that required power density. With the calculated track widths, the heater design is laid out by software with no manual intervention. This is a significant achievement because it is a deterministic design method as opposed to an artisanal or guess-and-check method. Furthermore, if the system changes in terms of geometry, materials or boundary conditions, the FEM model can be updated and the process repeated, resulting in a new heater pattern that produces uniform temperature in the new system. Since the width of the metal tracks is calculated per-segment, the heater can take any shape defined within the input Q field. This process has been automated as a MATLAB® program in order to rapidly generate customized heater patterns that employ a single metal layer.

9.3.1 Step 1: Calculation of the Q Field

A key step in the design flow is to build a model wherein an idealized heater is forced to maintain a defined two-dimensional temperature profile T. In the present work, T is a scalar so as to produce a uniform temperature across the 2D space. Therefore, the heat flux Q that meets T in the system of interest is the power density field that the actual heater needs to produce in order to obtain the desired T profile. The uniform temperature in the heater will also produce uniform temperature in the chamber if the heater radius is larger than the chamber radius by a distance Δrh. The extension distance Δrh is determined from the ΔT vs. Δrh

curves of the system as explained below. All the simulations in this chapter, Chapter 10 and Chapter 11 were performed in COMSOL 4.3 using the Heat Transfer and AC/DC modules. Details of materials and boundary conditions are given throughout the text.

The geometry, material properties and boundary conditions of the system are first captured in a heat-transfer FEM model. For best results, the model must be as similar as possible to the real device and target operation environment. For systems with axial symmetry (like the one presented here), a 2D model can be used to speed up simulation. Otherwise, a 3D model must be constructed. The heater is then defined as a surface underneath the PCR chamber and is prescribed a uniform temperature boundary condition. With this condition applied, the heater surface will behave as a heat source. In this step of the design process the chamber temperature uniformity, ΔT, is defined as the maximum temperature minus the minimum temperature across the chamber volume:

$$\Delta T = Tc_{\max} - Tc_{\min} \qquad \textbf{Eq. 6}$$

At this stage of the process we target ΔT < 1 ºC (or ~0.5 ºC) to allow room for the temperature non-uniformities caused by the process of turning the ideal heater into a discrete set of tracks.

A parametric 2D axisymmetric simulation is run where the heater radius (r_h) is progressively increased beyond the radius of the chamber (r_c). In the designs demonstrated here r_h was increased from r_c to r_c + 500 µm in steps of 50 µm. The uniformity ΔT is recorded at each simulation point. The optimal value of Δrh is then readily determined from the resulting ΔT vs. Δrh curves. Since this is a simple heat-transfer 2D simulation, the solution is obtained in a few minutes.

The extension distance Δrh is obtained just once. This parameter is relevant for any changes in planar geometry or power density distribution. In our demonstration, we selected a circular geometry and uniform temperature –

however, the Δrh found above will hold true for any shape (e.g., a square). The margins only need to be adjusted if the fabrication parameters or materials change significantly. For example, if the thickness of the chamber layer is increased to yield a cubic chamber, then Δrh should be recalculated to obtain the specified ΔT. Since Δrh needs to be calculated only once per fabrication scheme, a high degree of flexibility in design is provided. The flexibility of this technique is demonstrated by the following concepts:

- The temperature (and therefore power density) *distribution* and *resolution* in a 2D plane are free to choose.
- The 2D geometry of the thermal space is free to choose.
- A Δrh is calculated once per fabrication scheme, and is applicable to any adjustments to the temperature field and geometry.

Once Δrh has been determined, the heat flux being sourced across the heater plane is extracted. Areas with higher heat loss, such as heater edges, will show that a higher power density is required to comply with the uniform temperature boundary condition. This power density field must be reproduced by the actual heater to achieve the temperature distribution selected. This is the key to making the method deterministic.

The upward and downward heat flux values are sampled in the solved model at a resolution of choice. For example, values could be found in a 5 μm grid in the x-y plane and exported from COMSOL in the form of a matrix. The pointwise sum of these fields is performed in MATLAB® in order to obtain the total power density generated by the heater, i.e. the Q field. The resulting map/matrix is the input to the MATLAB® code that carries out the discretization process in step 2.

For the purpose of reducing the current density in the Al film we also designed heaters that produce a uniform power density profile. For these designs a uniform power density boundary condition was prescribed along the heater. The extension distance required to obtain $\Delta T < 1$ ºC was determined from the corresponding ΔT vs. Δrh curves.

9.3.2 Step 2: Discretization and Automatic Layout Generation

The discretization process starts by dividing the Q field extracted in step 1) into segments of length L and width s that form a grid, as shown in Figure 42. The segment width s also represents the pitch of the heater tracks to be designed. The pieces along a y-direction column of segments are connected in series and form one of these tracks. Each segment contains a small track piece of width w plus spacing. All the tracks are connected to a common voltage, and the tracks may in turn be connected in series within groups to fit particular voltage/current requirements, to control the track width and to limit the current density.

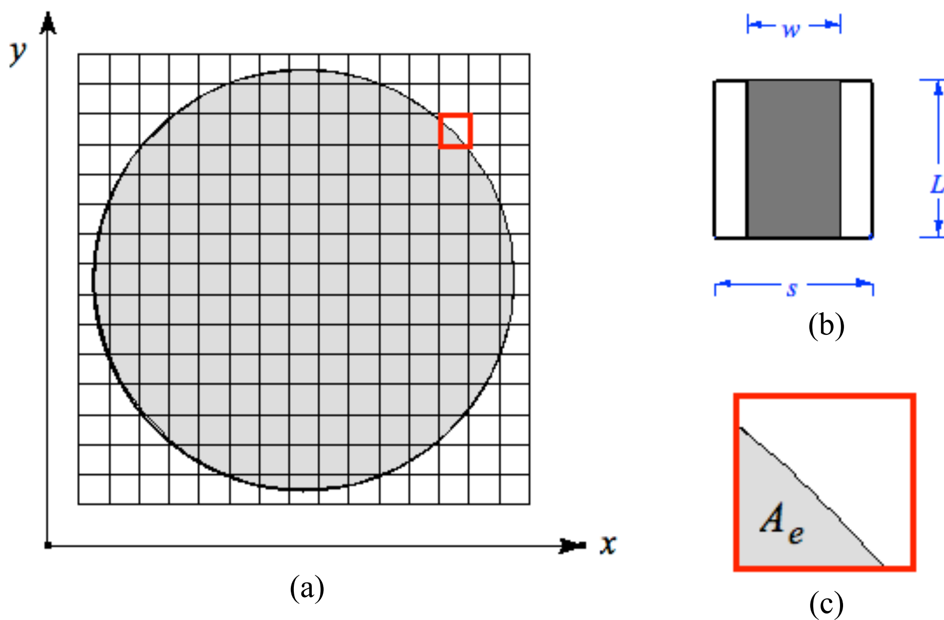

Figure 42. (a) Discretization of the Q field into segments. The circular area represents the non-zero elements of the matrix. (b) Segment structure. Each segment in the heater is comprised of a track segment and an empty space on each side. L – segment length; s – segment width; w – track width. L and s are controlled independently. (c) Effective area A_e that the heater occupies in an edge segment.

The extracted Q field is a square matrix with zeros outside the perimeter of the heater. Each segment shown in Figure 42 is a sub-matrix of the Q field. The track width w is calculated only for the segments containing non-zero elements. The all-zero segments are assigned $w = 0$. The result is a matrix (**W**) of the track widths (w) that the layout generator employs to construct the heater. The shape of the

heater is defined by drawing a polygon only for the non-zero elements in **W**. Therefore, the shape of the heater can be arbitrary (e.g. rectangular, oval, rhomboidal, etc). The circular shape, despite its convenience for axisymmetric simulations, is the most challenging because the slope of the edge ranges from 0 to infinity (it passes from the x-axis to the y-axis).

The power P_s delivered by each segment is calculated by integrating the power density over the segment area:

$$P_s = \int^L \int^s Q\,dx\,dy \qquad \textbf{Eq. 7}$$

The total power of a track P_T is calculated by summing the power delivered by all the segments along a y-direction column,

$$P_T = \sum_{i=1}^{m} P_{si} \qquad \textbf{Eq. 8}$$

where m is the number of segments of the track. Therefore, the total current through each segment is:

$$I = \frac{P_T}{V} \qquad \textbf{Eq. 9}$$

Where V is the applied voltage. Once the track current is known, the resistance R of each track segment necessary to dissipate P_s can be calculated as:

$$R = \frac{P_s}{I^2} \qquad \textbf{Eq. 10}$$

The segment resistance can be also defined as:

$$R = \frac{\rho L}{w h} \qquad \textbf{Eq. 11}$$

Where h is the thickness of the metal film and ρ is the resistivity of the metal at the average target heater temperature (95 ºC). Combining Eq. 9 and Eq. 11, the width of each track segment can be deterministically calculated from:

$$w = I^2 \frac{\rho L}{P_s h} \qquad \textbf{Eq. 12}$$

In terms of power density, however, w is independent of the length of the segment, L:

$$w = I^2 \frac{\rho}{Q_s h\, s} \qquad \textbf{Eq. 13}$$

Where Q_s is the average power density of the segment and is defined $P_s / L\, s$. The track piece in the segment, with area Lw, must deliver all the power necessary to meet Q_s over a larger area Ls. Therefore, the power density on the metal Q_t needs to be higher than the power density of the segment Q_s by a factor s/w:

$$Q_t = Q_s \frac{s}{w} \qquad \textbf{Eq. 14}$$

Accordingly, the temperature on the metal will be higher than 95 ºC, while on the gaps it will be lower, achieving an average temperature across the entire segment of 95 ºC. As a first validation of this concept, Eq. 14 is used at the end of the discretization process to verify that the calculated w produces the expected Q_s in each segment, as designed.

The resistivity of the metal film, ρ, is approximated linearly from:

$$\rho = \rho_0 \left(1 + \alpha \left(T - T_0\right)\right) \qquad \textbf{Eq. 15}$$

Where ρ_o is the resistivity of the heater material at reference temperature (4.39 x 10 $^{-8}$ Ω-m for Al); $\boldsymbol{\alpha}$ is the temperature coefficient of resistivity – TCR (3.518 x 10 $^{-3}$ K^{-1}) and T_o is the reference temperature (22 ºC). These values were measured

previously for Al films on KMPR [19]. In [19], we also verified that the resistivity vs. temperature curve of the film is highly linear, and therefore Eq. 15 is a valid approximation.

In order to decrease the current requirement of the heater and the current density levels, the heater can be divided into groups of tracks connected in series. In this case, the width of the track segments is calculated from Eq. 12, but the current through all of them is calculated from the total power P_G delivered by the group:

$$I = \frac{P_G}{V} \qquad \textbf{Eq. 16}$$

Where P_G is the sum of the power of all the segments in the group:

$$P_G = \sum_{j=1}^{n} \sum_{i=1}^{m} P_{s,i} \qquad \textbf{Eq. 17}$$

Here, n is the number of tracks in the group, and can take on only odd values. The case for $n = 1$ means that all tracks are connected in parallel. Grouping tracks causes a higher current flow through the segments. However, the current density, defined as $J = I/(wh)$ decreases because the width increases quadratically with the current, as stated by Eq. 12 and Eq. 13.

A MATLAB® program was written to carry out the discretization process and draw the heater layout automatically. The program scans the input Q field from step 1), calculating the power of each segment, one at a time, from Eq. 7. If a segment sub-matrix contains zeros, it is identified as an edge segment. In these segments, the effective area A_e occupied by the heater is a fraction of Ls. A_e is compared to a pre-determined minimum allowable segment-fill area A_{min}. If $A_e \geq A_{min}$, the power of the segment is calculated and inserted in a matrix **P** that contains the power of every segment P_s. **P** is then subdivided into groups to calculate the power and current of each one using Eq. 16 and Eq. 17 Finally, the width of each segment is calculated from Eq. 12, storing the result in **W**.

The layout generation section of the program reads **W** and generates a polygon for each track segment. Finally, the polygons are merged into a single polygon track. By making the walls of the individual segments slanted, tracks acquire a continuous shape, which yields smooth current density transitions. Figure 43 illustrates how the process creates a polygon for each segment. In this example where all the tracks are designed to be connected in parallel (in groups of $n = 1$). In practice the current density levels in a design like this are too high to enable the use of Al. By grouping the tracks in series ($n > 1$) their width increases and the current density is lowered.

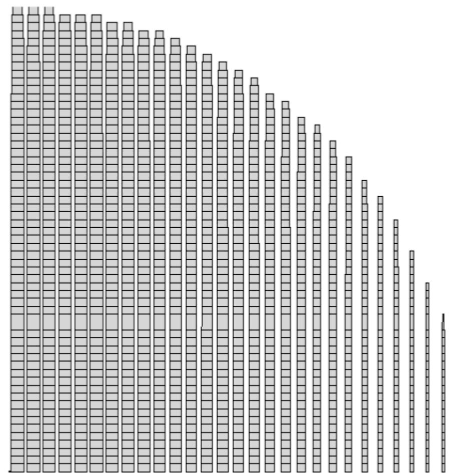

Figure 43. Stack of polygons forming a grid heater (only ¼ of the heater is shown). The x and y resolution can be freely selected. In this example the tracks are all connected in parallel. Far from the center the tracks become shorter, thus they need to become thinner to limit the current and maintain the same power input.

9.3.3 Step 3: Verification

After the calculation of the Q field in step 1) and the automatic heater layout in step 2), the final step is to check that the result achieves the parameters set in step 1). Of course, it should always be “correct” since the method is deterministic.

The thermal and electrical characteristics of the generated layout are tested by simulation. As shown in Figure 43, the generated heater layout is an unconnected set of tracks. This layout is tested as-is, through the use of *virtual connections* between tracks. These connections are a special type of boundary condition pair

that conveys the current from one track to another with zero electrical resistance. This allows for the detection of any issues early, before the physical connections are made. In this stage of verification the heaters normally show excellent agreement with the parameters set in step 1) and discretized/calculated in step 2). Refer to Appendix C: Layout Verification for more information on this step. Upon successful simulation, the physical connections between tracks and to the power bus are added. This procedure was performed manually taking about one hour per heater, however this connection layout operation can be also automated. The physical connections are drawn in L-Edit® (Tanner EDA) and are made as wide as possible in order to minimize their resistance. However, the accumulated resistance of these connections may lead to significant voltage drops that can deteriorate the temperature profile of the heater, as shown in Appendix C: Layout Verification. For this reason, a second verification stage is performed on the full heater layout, including the pads for contact with external connections.

For the simulations in this step, the Joule heating equation set was added to the model used in step 1), in order to construct a fully-coupled 3D heat-transfer/Joule-heating model of the system. In order to make the meshing of the heater manageable, the heater layout is embedded in the model as a 2D surface and is set up as a Highly Conductive Layer (HCL), which allows the software to treat the heater as a volume (100 nm thick). This *HCL* condition assumes that no vertical temperature gradients exist in the thin volume, which is a reasonable assumption for a metal. Additionally, the heater layer is assigned the thermal properties of aluminum (k = 237 W/m-K, c_p = 897 J/kg-K, ρ = 2700 kg/m^3 [24]. When the heater is tested through virtual connections, a *ground* and *electric potential* are assigned to each group of tracks, using the same electric potential value for all of them. When the full heater layout is tested, the ground and electric potential conditions are prescribed to contact areas on the main power bus. The resistivity of the film is calculated pointwise as a function of temperature by the simulation software using Eq. 12, with the same values for ρ_o, α, and T_0 used in step 2).

9.4 Results and Discussion

9.4.1 Heater Extension and Calculation of the Q Field

The ΔT vs. Δrh curves of the designed heaters as obtained from 2D simulation are shown in Figure 44. The power curves (diamond and circle markers) are obtained by integrating the heat flux over all the external boundaries of the chip. The uniform temperature condition on the ideal heater causes a non-uniform power density distribution, therefore the prefix NU is used to identify the heaters built to meet this condition. The heaters built to provide a uniform power density distribution are identified by the prefix U. Heaters of the NU and U types were designed for 500 µm and 1200 µm radius chambers. Figure 44(a) and Figure 44(b) correspond to the heaters designed for a 500 µm and a 1200 µm radius chamber, respectively. From these plots we find that for NU designs extending the heater by Δrh = 250 µm brings the uniformity ΔT to within the < 1 ºC target (triangle-markers). Therefore, the appropriate r_h for a 500 µm chamber is 750 µm and for a 1200 µm chamber is 1450 µm. The U designs require Δrh = 350 µm to reach the same level of uniformity (square-markers). Therefore, for U designs the appropriate r_h for a 500 µm chamber is 850 µm and for a 1200 µm chamber is 1550 µm. The exact values of ΔT for NU and U designs are listed in **Table 9**.

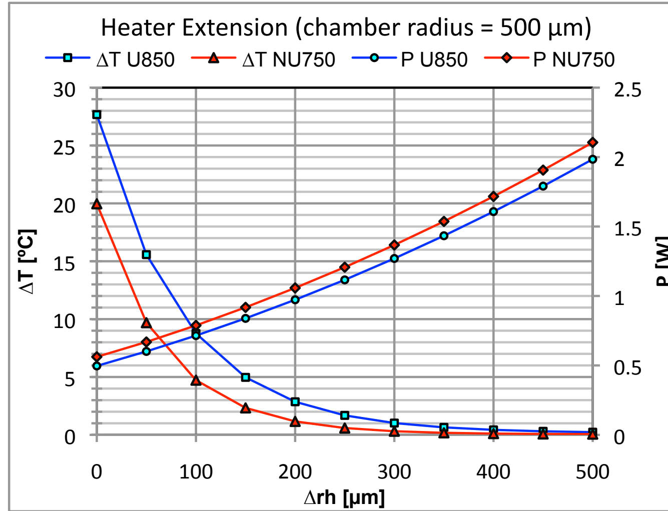

(a)

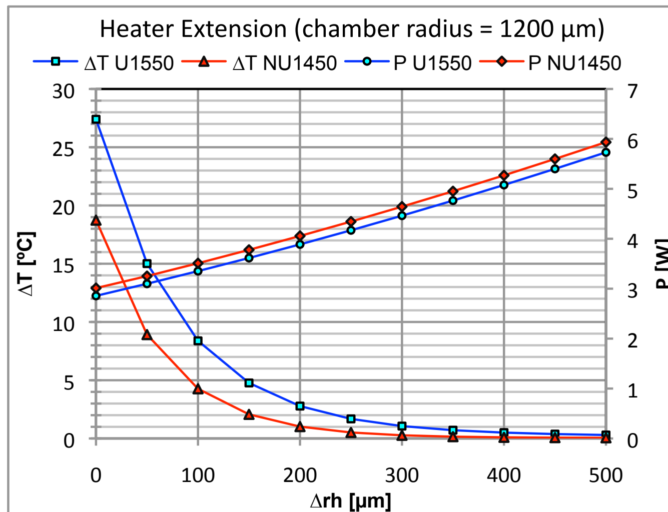

(b)

Figure 44. Trade-off between chamber temperature uniformity (ΔT), power consumption (P) and extension distance (Δrh), for uniform and non-uniform power density heaters. The curves were obtained from 2D simulation using an ideal heater. (a) Curves for designs with a 500 µm radius chamber. (b) Curves for designs with a 1200 µm radius chamber. At $\Delta rh = 0$ the radius of the heater is equal to the radius of the chamber. For NU designs a uniform temperature condition of value $Th = 95$ ºC is prescribed along the heater. For U designs a uniform power density condition of value $Q = 6.32 \times 10^{5}$ W/m^2 is prescribed along the heater. $Ths = 30$ ºC, $Tamb = 22$ ºC.

At any given Δrh the NU designs consume slightly higher power than the U designs since higher power at the edge is spent to meet the uniform temperature condition. However NU designs achieve the target uniformity 100 µm before U designs, resulting in lower power consumption and smaller footprint. Although

higher uniformity could be achieved by extending the heater further, the extension distance is limited so as to respect the power constraints. For designs with a 500 µm radius chamber the power consumption is limited to 2 W (to enable operation from a USB port) and for designs with a 1200 µm radius chamber the power is limited to 5 W.

Table 9 summarizes the design specifications resulting from this analysis. The uniformity ΔT not only depends on Δrh, but also on the increment in average chamber temperature Tc_{avg} above the heatsink temperature, Ths. The chamber temperature Tc_{avg} in turn depends on the extension distance Δrh. Therefore the estimated ΔT is accurate only near the target < 1 ºC. Table 9 shows the variation in Tc_{avg} when the heater is extended from 0 to 500 µm. We employ the relative uniformity, denoted B, as a measure of uniformity that is independent of the chamber and heatsink temperatures. The target uniformity ΔT < 1 ºC corresponds to a relative uniformity $B \approx 0.01$ (1 %). For an explanation and plots of relative uniformity please refer to Appendix A: Heater Extension .

Heater Identifier	*Q* field distribution	Chamber radius [µm]	Heater radius (µm)	Power P [W]	ΔT [ºC]	Tc_{avg} @ Δrh=0 [ºC]	Tc_{avg} @ Δrh=500 µm [ºC]
NU 750	Non-uniform	500	750	1.21	0.59	92.00	94.94
NU 1450	Non-uniform	1200	1450	4.34	0.65	93.87	94.94
U 850	Uniform	500	850	1.43	0.52	87.84	94.74
U 1550	Uniform	1200	1550	4.77	0.71	92.47	94.90

Table 9. Dimensions and type of power density distribution of the designed heaters. The power, uniformity (ΔT) and average chamber temperature (Tc_{avg}) were calculated on the 2D model of the system driven by an ideal heater. Ths = 30 ºC. For NU 750 and NU 1450 Th = 95 ºC. For U 850 and U 1550 $Q = 6.314 \times 10^{5}$ W/m^2.

To better visualize the effect of extending the heater, consider a system with a 500 µm radius chamber. Figure 45 shows a plot of the temperature along the ideal continuous heater and the PCR chamber, obtained by prescribing uniform temperature on the heater boundary. It is clear that if the heater is not extended (i.e. rh = 500 µm, Δrh = 0) the temperature uniformity in the chamber does not meet the < 1 ºC requirement (circle markers). However, extending the heater by Δrh = 250 µm, as predicted from the plots in Figure **44**(a), brings the gradients in

the chamber to within 1 ºC (no markers). This is, in fact, the case of the NU 750 design.

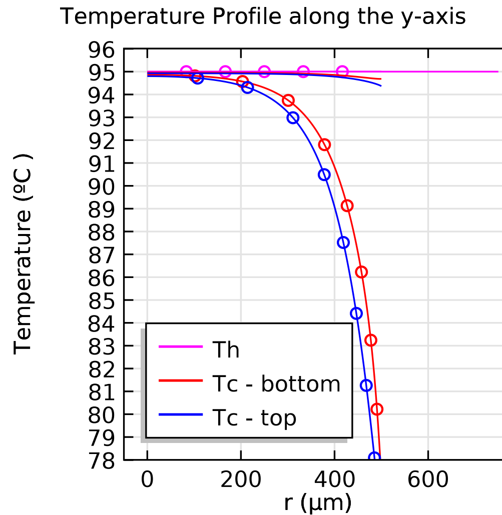

Figure 45. Temperature along a 500 µm PCR chamber induced by a 500 µm (circles) and 750 µm (no markers) radius ideal heater. The temperature of the ideal heater is maintained at 95 ºC across its entire surface.

By forcing the ideal heater to maintain uniform temperature, the exact heat flux distribution necessary to meet this condition can be calculated from the solved model. This heat flux distribution is the *Q* field that will be employed to calculate the width of the metal tracks in step 2).

In NU designs the heat flux is nearly flat in the center region and becomes exponentially higher at the edges, as shown in **Figure 70**. This higher power input at the edges is required to compensate for the high heat loss at that location, caused by the proximity to the unheated KMPR layers. The plot of **Figure 70** shows the *Q* field of the NU 750, resulting from the pointwise sum of the upward and downward fluxes exported from COMSOL. The *Q* field resolution for the smaller heaters is 1 µm and for the large heaters is 5 µm for faster processing.

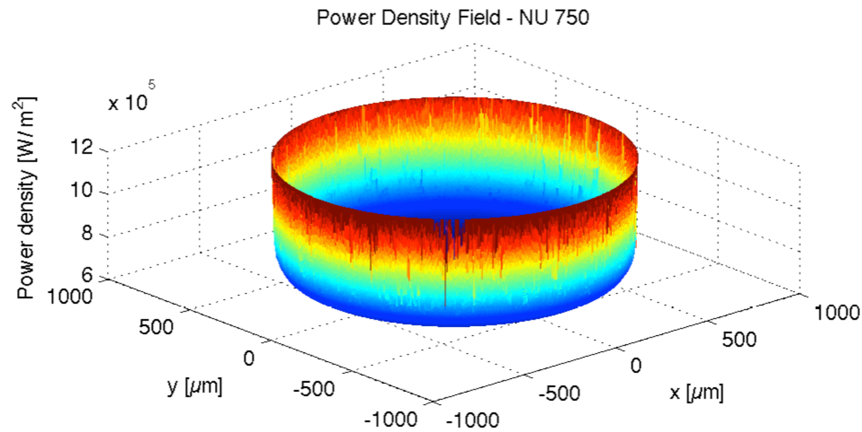

Figure 46. Heat flux along the surface of the ideal NU 750 heater. This is the power density field necessary to maintain uniform temperature in the PCR chamber. An exponentially increasing power density radially towards the edge compensates for the high losses outside the heater.

The higher power density at the edge leads to thinner track width and higher current density. At high current densities, electromigration on the Al film may accelerate and substantially reduce the heater's lifetime. This potential issue motivated the design of the U-type heaters, which produce a uniform power density profile, yielding a layout that keeps the current density constant along the tracks. These heaters (U 850 and U 1550) are constructed from a single value of power density and do not require an exported Q field.

If uniform power density, instead of uniform temperature, is prescribed on the ideal heater, the temperature drops much faster before reaching the edge and hence the heater must be extended further by 350 μm to reach the target uniformity. The heat flux prescribed to obtain 95 ºC at the center of the heater/chamber was 0.6314×10^6 W/m^2 (value obtained from the analytical model of the system presented in Chapter 10).

It is important to again highlight the advantage that this method is independent of geometry. Since we are not dealing with "tracks", but instead with small pieces of tracks, the total length of a heater trace does not need to be specified at all. Since we calculated values per element, the shape does not matter; all geometry is cared for by the power distribution from Step 1. That information is stored in a matrix,

and every discretized region that has a non-zero power density will have a piece of metal defined for it.

9.4.2 Discretization

The heaters were designed using a heater temperature *Th* = 95 ºC and heatsink temperature *Ths* = 30 ºC. The operation voltage was constrained to 3.4 V for the NU 750 and U 850 and 9–10 V for the NU 1450 and U 1550. For effective etching between tracks during lithography, a minimum gap of ~5 μm between tracks was allowed. The pitch *s* was chosen small enough to provide a high power density resolution without compromising lithography.

Table 10 summarizes the parameters of the heaters obtained from the discretization process. The total power calculated by the algorithm agrees with that calculated by simulation in step 1 (see Table 9). By making groups of tracks in series, the power density levels were reduced from 160–180 mA/μm^2 to a maximum of 26.67 mA/μm^2, occurring in only the ends of one of the tracks. Table 10 lists the calculated widths and current densities of the four heater designs. The last row in Table 10 shows the number of groups and tracks per group on each half of the heater. In U 1550 for example, each half is made up of three groups of five tracks connected in series plus one group of nine tracks connected in series. The mirrored halves make a total of 48 tracks. The groups with fewer tracks are at the center portion of the heater.

In edge segments that contain zeros, the average power density of that segment is low in comparison to the rest of the segments of that track. To accommodate the low power, the algorithm rapidly widens the track, lowering the power density. The additional figure shown in Appendix B: Heater Track Widths and Current Densities shows this effect clearly. The width of the tracks is constrained to be less than the pitch distance *s*, to ensure that the tracks do not overlap each other in the algorithm's effort to reduce power density.

Parameter	U 1550	NU 1450	U 850	NU 750	Unit
P	4.578	4.194	1.402	1.130	W
V	10.0	9.0	3.4	3.4	V
R	21.84	19.31	8.24	10.23	Ω
I	0. 458	0.466	0.412	0.332	A
J_{max}	13.66	19.83	16.36	26.67	mA/μm^2
J_{min}	11.62	11.13	10.94	11.89	mA/μm^2
w_{max}	52.56	45.73	27.60	24.54	μm
w_{min}	37.83	28.99	14.53	10.23	μm
g_{min}	9.44	4.27	6.40	5.46	μm
Pitch	62	50	34	30	μm
No. tracks	48	58	50	50	---
Groups of Tracks	3 of 5	4 of 5	6 of 3	6 of 3	n/a
	1 of 9	1 of 9	1 of 7	1 of 7	n/a

Table 10. Specifications of the heater designs, as obtained from the discretization process. Heaters were designed with Th = 95 ºC and Ths = 30 ºC. For uniform power density heaters Q = 6.314 x 10 ^{5} W/m^2.

9.4.3 Steady State Uniformity

A sample of the generated mask layouts (the NU 1450) is shown in Figure 47(a). The heaters are operated simultaneously as 4-point sensors, wherein the drive current is applied through terminals A and B, and the voltage is probed across terminals C and D. As discussed earlier, the tracks are connected in series within groups and all the groups are connected in parallel to the power bus in order to reduce the current density levels and the total current requirement of the system. The inset of Figure 47(a) displays a narrowing track width at the edge of the heater that causes higher power dissipation, which maximizes the area of uniform temperature and minimizes the total power consumption. This narrowing of the tracks at the edge is present in non-uniform designs (NU 1450 and NU 750). In uniform designs (U 1550 and U 850) the track width is constant across the entire length of the tracks. The 3D heat-transfer/Joule-heating model used for virtual connection and full layout verification is shown in Figure 47(b).

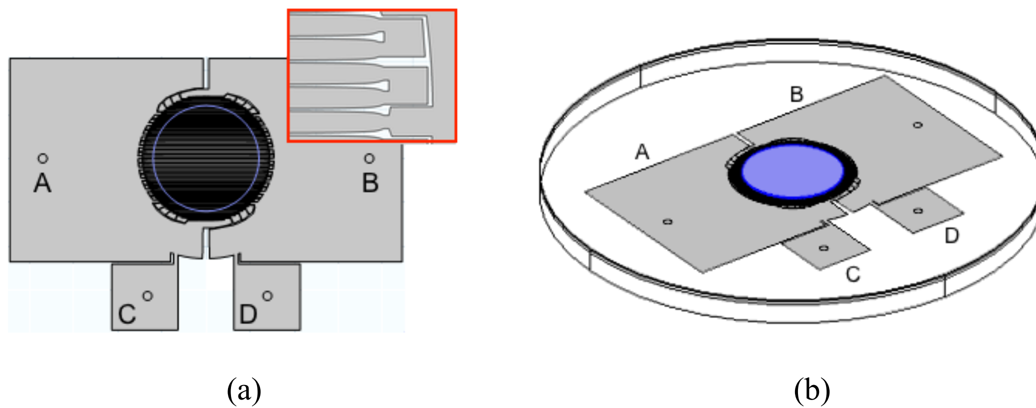

(a) (b)

Figure 47. (a) Layout of the NU 1450 design. The blue circle in (a) indicates the perimeter of the 1200 µm radius chamber. The drive current is applied through terminals A and B; the output voltage is probed between terminals C and D. The circles indicate points of contact for terminals (pogo pins). The inset in (a) is a zoom-in of the heater's edge, where the tracks thin down to increase the power input. (b) 3D FEM model used to characterize the designed heaters. The full layout of the heaters is embedded in the model; the chamber is indicated in blue.

Figure 48 show the temperature at the bottom of the PCR chamber for the four designs. Recall that this is the plane of the chamber that shows the worst non-uniformities. The obtained uniformities are ± 0.43, ± 0.57, ± 0.97 and ± 1.25 ºC around an average of ~95 ºC for the NU 750, U 850, NU 1450, and U 1550, respectively. In general, the non-uniform power density heaters are remarkably uniform in temperature compared to uniform power density designs. The temperature uniformity at lower PCR temperatures (~ 60 and 70 ºC) is better, as observed by others [25] and verified in our work (data not shown). Taken together, the results of the four heater designs demonstrate that this method of generating system-customized uniform temperature heaters is repeatable.

In literature it is common to express uniformity as the portion of the chamber whose temperatures fall within a given temperature band (see section 9.1). According to this metric of uniformity > 99 % of the temperatures in the chamber volume fall within a 1 ºC band for the non-uniform designs, as shown in the histograms of Figure 49(a). For uniform designs, 94 % of the chamber volume is within a 1 ºC band, as shown in the histograms of Figure 49(b). This metric of

uniformity can be used to compare the performance of our designs to that of other reported devices.

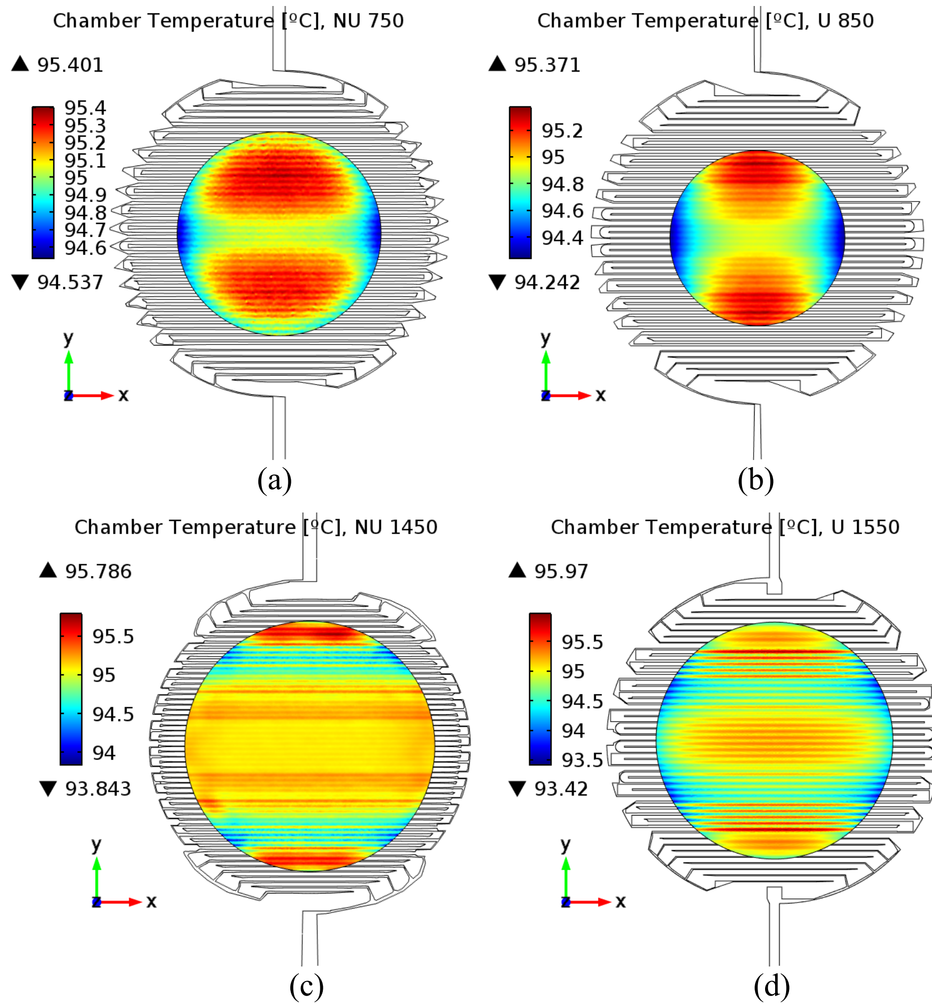

Figure 48. Temperature field at the bottom of the PCR chamber, predicted by 3D heat-transfer/Joule-heating simulation of the full layouts. (a) NU 750, (b) U 850, (c) NU 1450, (d) U 1550. The voltages applied to reach an average *Tc* = 95 ºC are: 3.89, 3.95, 9.72, 10.62 The heaters in the full layout require higher voltages than those shown in Table 10, due to the voltage drops introduced by the power bus and elbows; therefore the voltages need to be adjusted to reach 95 º in the chamber.

Note that although the ripple on the heater plane may reach ± 7 ºC, it is greatly attenuated at the chamber level (to within ±1.25 ºC, depending on the design). The relatively high conductivity of water contributes to dissipating the ripple. This ripple attenuation is depicted for NU 750 and NU 1450 in Figure 50, where *Th* is compared to *Tc* in one-dimensional plots.

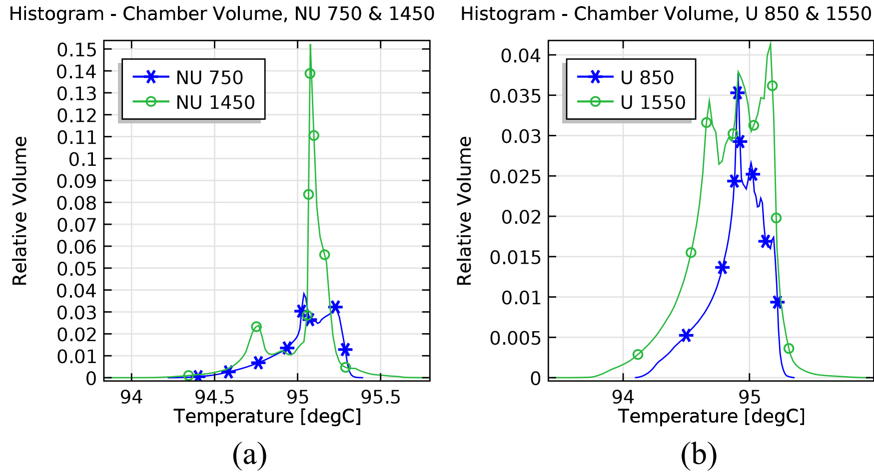

Figure 49. Histograms of temperatures across the entire volume of the PCR chamber of non-uniform (a) and uniform (b) power density heaters. The temperatures in > 94 % of the chamber volume fall within a 1 ºC band in all cases, while the volume outside this band is negligible.

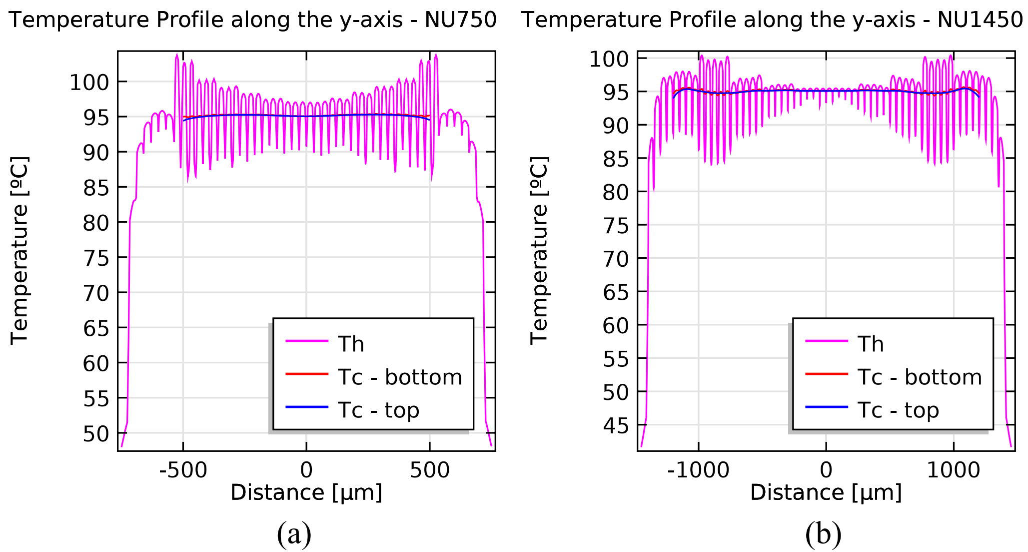

Figure 50. Temperature along the middle of the chamber and heater. (a) NU 750; (b) NU 1450.

9.4.4 Current Density Considerations

The current density field of the full layout of the NU 1450 calculated by 3D simulation is displayed in Figure 51. The maximum current density in the simulation agrees with that calculated in the discretization step (19.83 mA/µm^2, see Table 10. Observe that in this heater the current density is higher at the track ends, as designed.

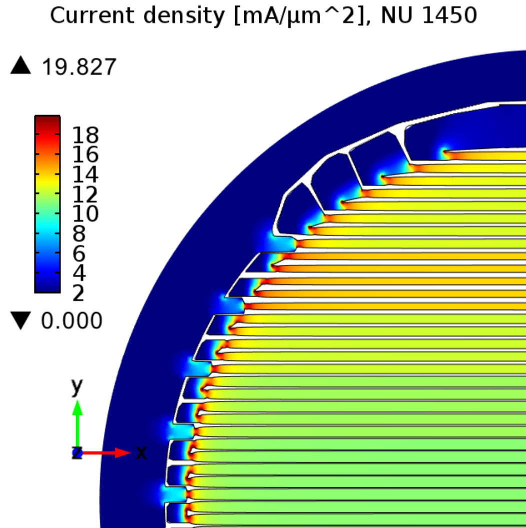

Figure 51. Current density field in the NU 1450 heater. Notice the sharp increase at the track ends. The current density on the elbows and connections to the power bus is 1-2 orders of magnitude lower than the densities found on the tracks.

We developed an automated electromigration lifetime test system that applies a current through the element under test and simultaneously measures resistance in four-point mode. The system adjusts the current in order to maintain the target temperature based on the TCR of the element. With this system we measured the failure (open circuit) time of straight 10 x 100 µm Al tracks fabricated on KMPR. The tracks showed a failure time of 145 min at 57.5 mA/µm^2 constant current density, and 13.5 min at a current density decreasing from 300 to 250 mA/µm^2. The test was performed at ~ 120 ºC target temperature. Analytically we have estimated that our devices have the potential to run a full PCR reaction in 3 min, and transient response experiments support this estimate (data not shown). If such a speed could be achieved, the lifetimes measured in these experiment would be more than enough to run the reaction. These results were the first evidence that the levels of current density calculated for the heaters are low enough to allow the use of aluminum metallization.

9.4.5 Selectivity

On a chip-wide scope we can see, from Figure 52, the sharp transition between the heated volume and the rest of the chip. This characteristic allows the designer

to place other components as close as ~250 µm without affecting the thermal system or being damaged by heat. This also means that several PCR chambers could coexist in the same chip without thermal crosstalk between them. Compared to the PC6-K design, this system achieves far better uniformity and selectivity (refer to Figure 22 and Figure 23). For PC6-K a uniformity of ~4 ºC was obtained for a much smaller chamber (250 µm radius).

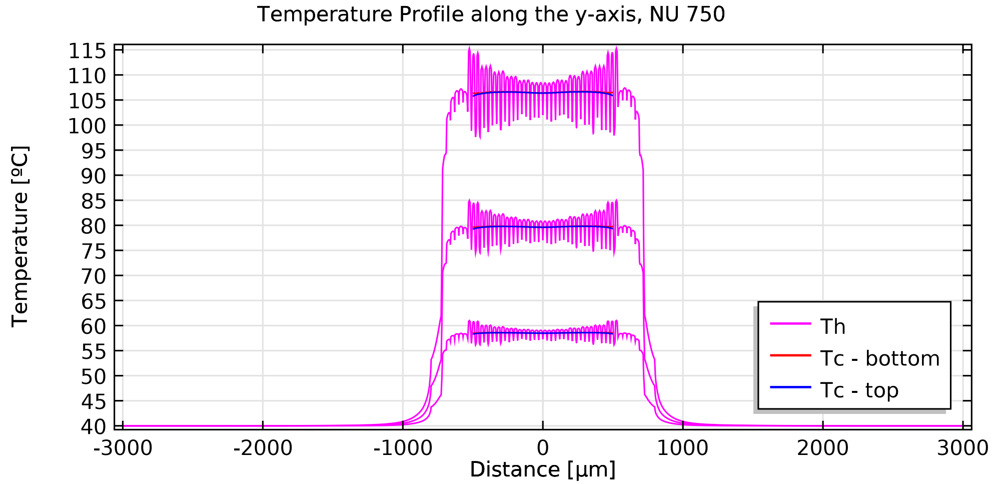

Figure 52. *Tc* and *Th* of NU 750 over a chip-wide scope for an applied voltage of 2, 3, 4 V. At a distance 250 µm from the edge of the heater the chip remains at the temperature of the heatsink. Uniformity is better at lower temperatures. Other objects can be placed in contact or other structures can be built in the chip at this distance without affecting the thermal system. This establishes the potential for building several chambers in the same chip.

9.4.6 Experimental Results

Examples of the fabricated device are shown in Figure 53. The fabrication process is discussed in Appendix C of Chapter 10.

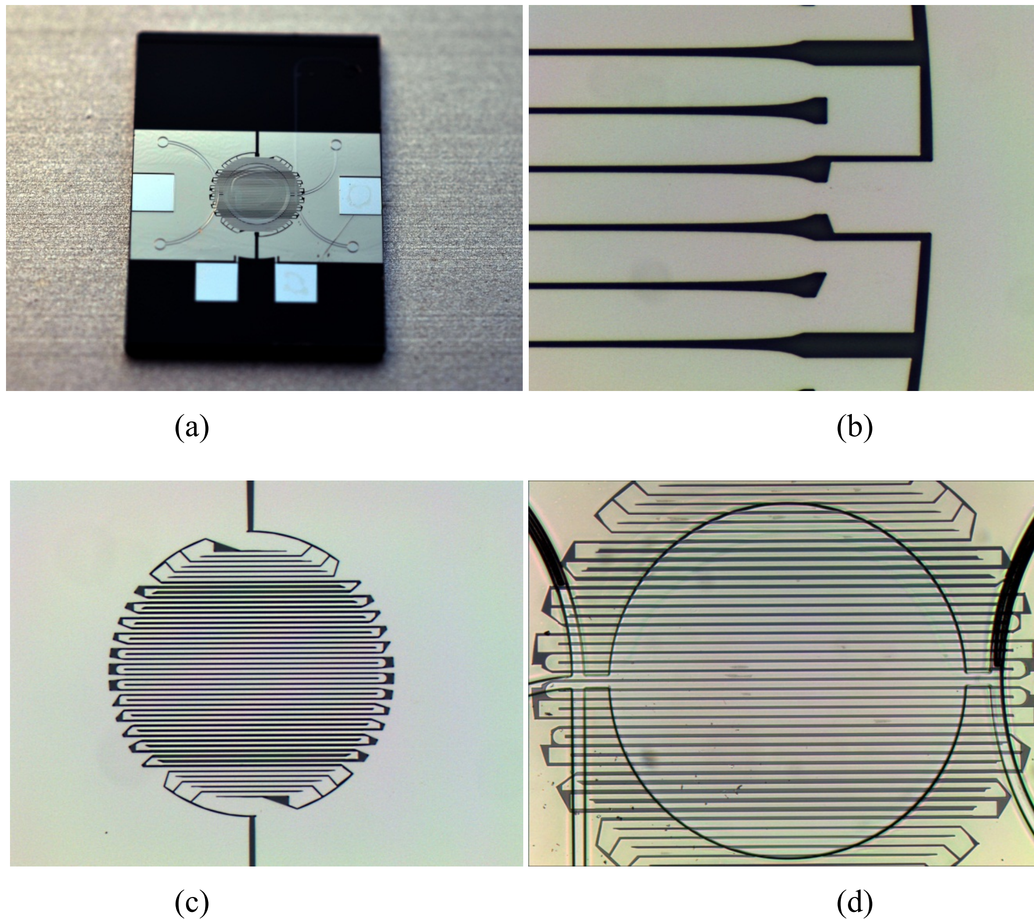

Figure 53. (a) Photograph of the fabricated target system (U 1550) as a silicon die, including the KMPR microfluidic layer. (b) Zoomed-in image of the NU 1450 aluminum traces showing the narrowing of tracks towards the heater perimeter. (c) U 850 heater tracks with no KMPR fluidics. (d) U 1550 configuration including KMPR fluidics.

9.4.6.1 Device Lifetime.

The proper operation of the heaters could be compromised by the combined high temperature and high current density that they are exposed to. The NU 750 is at the highest risk, as it has the highest current density. Therefore, a lifetime test was performed on an NU 750 chip, with an Al thickness of 180 nm. Electrical connections were made to the chip by using Field's metal obtained from Rotometals.com (32.5 % Bi, 51% In, 16.5 % Sn: melting point 62 ºC) as a low-temperature solder to bond to the exposed aluminum pads shown in Figure 53(a). Connections to the Field's metal were made using spring-loaded "pogo" pins (Digikey Corporation). Resistance measurements were made using a 4-point

connection. The chip was heated on a hotplate to 95 ºC and the resistance was measured in order to determine the target resistance for the lifetime test (found to be 11.43Ω). The chip was placed on an Al block, acting as a heatsink, to match our expected operating conditions of high conductivity through the substrate. The current and voltage were set and controlled in order to maintain a resistance of 11.43Ω. Values of 3.59V and 0.314A were measured for the voltage and current respectively. This current corresponded to a current density of 14.2 mA/µm2 (lower than the designed value). This is because the resistivity of the aluminum with the processing conditions used in this work was found to be $12.9 \pm 0.2 \times 10^{-8}$ Ω-m (vs. 4.39×10^{-8} Ω-m found earlier) and also had a much lower TCR $2.07 \pm 0.02 \times 10^{-3}$ K^{-1}). In this case, the higher resistivity is advantageous in lowering the risk of failure by electromigration because smaller current densities are needed to obtain the same power dissipation in the aluminum tracks. These changed values however, were confirmed by simulation to not affect the uniformity of the heater chamber, just the calibration voltages necessary to achieve the expected temperatures. These lifetime test conditions were held for 41 hours and 25 minutes until the first track failure occurred (800 times the intended operating time of a single-use device), which resulted in the voltage and current values reducing to 2.83V and 0.247A to maintain the same constant resistance. These conditions were held for an additional 8 hours and 35 minutes before the chip failed completely.

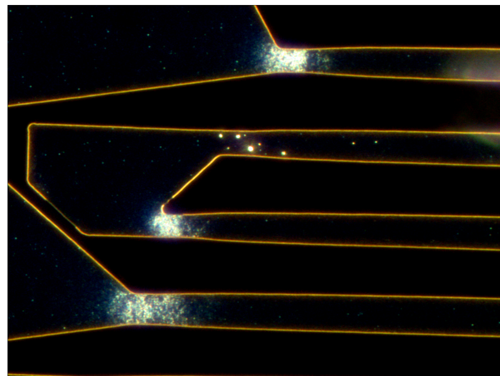

Figure 8. A dark field microscope image of the NU 750 Al tracks after the lifetime tests showing hillock formation from electromigration (bright spots) at the narrowing ends of the heater tracks, as would be expected by the higher current concentrations at these locations.

9.5 Conclusion

We presented here a novel and widely applicable method for rapidly designing system-customized thin-film heaters. This deterministic method yields heaters that compensate for uneven heat loss and produce an isothermal environment. Using a predetermined power density distribution desired by the designer, the proposed method is independent of the size and shape of the micro-chamber that is to be heated. This independence is by virtue of the discretization step, which calculates the local width of heater elements for any region that requires a non-zero power density. Additionally, the uniformity of the heater designs is not significantly affected by changes in metal resistivity, thickness or TCR, although these will have an impact on the lifetime, and voltage and current requirements of the heater. The method allows for enormous reduction of current density levels, enabling safe operation of Al heaters and potential CMOS integration, replacing Pt and Au – by far the most commonly used metals in lab-on-chip research.

We demonstrate this method by designing and fabricating thin film Al heaters that produce temperatures within approximately ±1 ºC at temperatures up to 95 ºC with an expected heatsink temperature of 30 ºC in a polymer structure. Achieving such a high degree of uniformity makes the method well-suited for designing LOC heater applications such as PCR, and substantially reduces measurement uncertainty. By designing, building and testing four different heater designs, two with uniform power density profiles and two with non-uniform profiles, we clearly show how the method can produce successful results in a repeatable fashion.

We believe that this work is a solid step towards solving the problem of spatial thermal control in LOC systems. Since the outlined method is easy to follow and lends itself to automation, it has the potential to become a design standard, allowing researchers to concentrate on new challenges.

9.6 Appendix A: Heater Extension Based on Relative Uniformity

In Step 1 of the process (section 9.4.1) the extension distance Δrh was calculated to meet a target absolute uniformity $\Delta T < 1$ ºC, where ΔT is the difference between the maximum and minimum temperatures in the chamber, as stated by Eq. 6. However the uniformity ΔT is not only determined by Δrh but also by the increment in the chamber temperature above heatsink temperature, ΔTc, defined as:

$$\Delta Tc = Tc_{avg} - Ths \qquad \textbf{Eq. 18}$$

Where Tc_{avg} is the volumetric average chamber temperature, defined as the volume integral of temperature divided by the total chamber volume; and Ths is the heatsink temperature. To find the proportionality between ΔT and ΔTc we define the relative chamber temperature uniformity, B, as:

$$B = \frac{\Delta T}{\Delta Tc} \qquad \textbf{Eq. 19}$$

Since ΔTc depends on the difference between Tc and Ths, rather than on their absolute value, B can be used as a more general design criterion that works for any target chamber temperature and any expected heatsink temperature. Figure **54** shows the B vs. Δrh curves of the designed heaters as calculated from the 2D simulation data obtained in section 9.4.1. The curves of power are the same as those in Figure **44**.

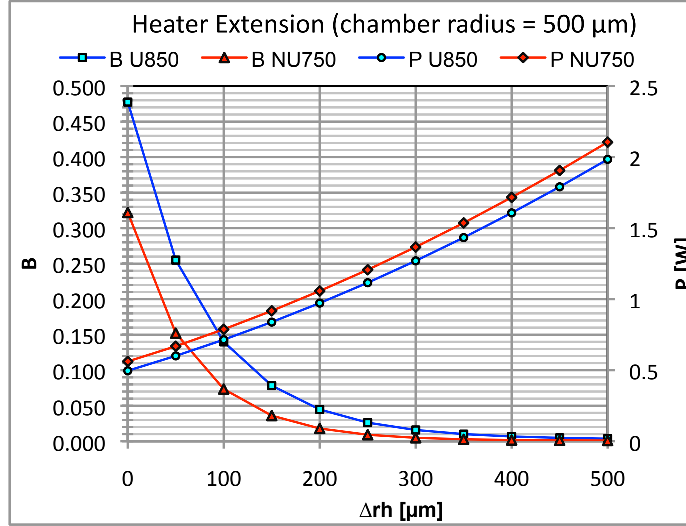

(a)

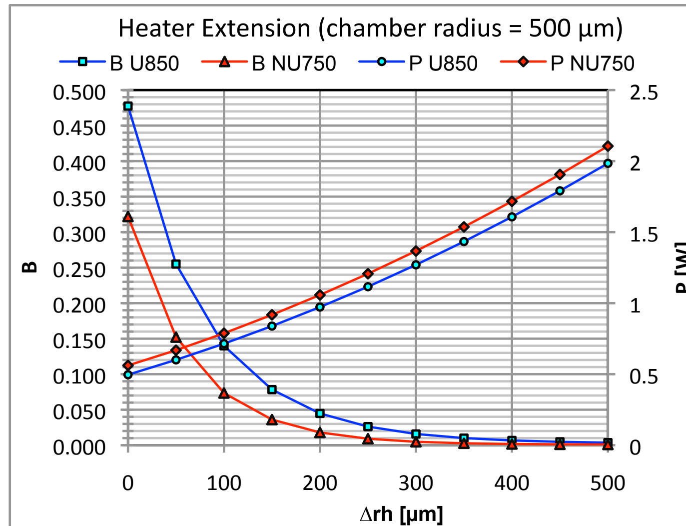

(b)

Figure 54. Trade-off between relative chamber temperature uniformity (B), power consumption (P) and extension distance (Δrh), for uniform and non-uniform power density heaters. The curves are calculated using the data obtained from the 2D simulations of section **9.4.1**. (a) Curves for designs with a 500 µm radius chamber. (b) Curves for designs with a 1200 µm radius chamber.

By comparing the uniformity curves in Figure **44** and Figure **54** we find that in all the designs the desired absolute uniformity, ΔT, is reached when the relative uniformity, B, is approximately 0.01 (1 %). Table 11 shows the exact values of ΔT and B that result from extending the NU designs by Δrh = 250 µm and the U designs by Δrh =250 µm. Therefore B = 0.01 can be used as a target for future designs.

Heater Identifier	ΔT [ºC]	B [unitless]
NU 750	0.59	0.009
NU 1450	0.65	0.008
U 850	0.52	0.010
U 1550	0.71	0.011

Table 11. Absolute and relative chamber temperature uniformity of the designed heaters (applicable to Step 1 of the process), calculated on the 2D model of the system driven by an ideal heater.

9.7 Appendix B: Heater Track Widths and Current Densities

Figure 71 (a-b) below shows a quarter of the layouts for the NU750 and U850 designs. Notice the widening of the tracks at their tips, rapidly lowering current density. (c-d) display the track width along the track for the same two designs. Finally, (e-f) displays how the current density varies along the length of the track.

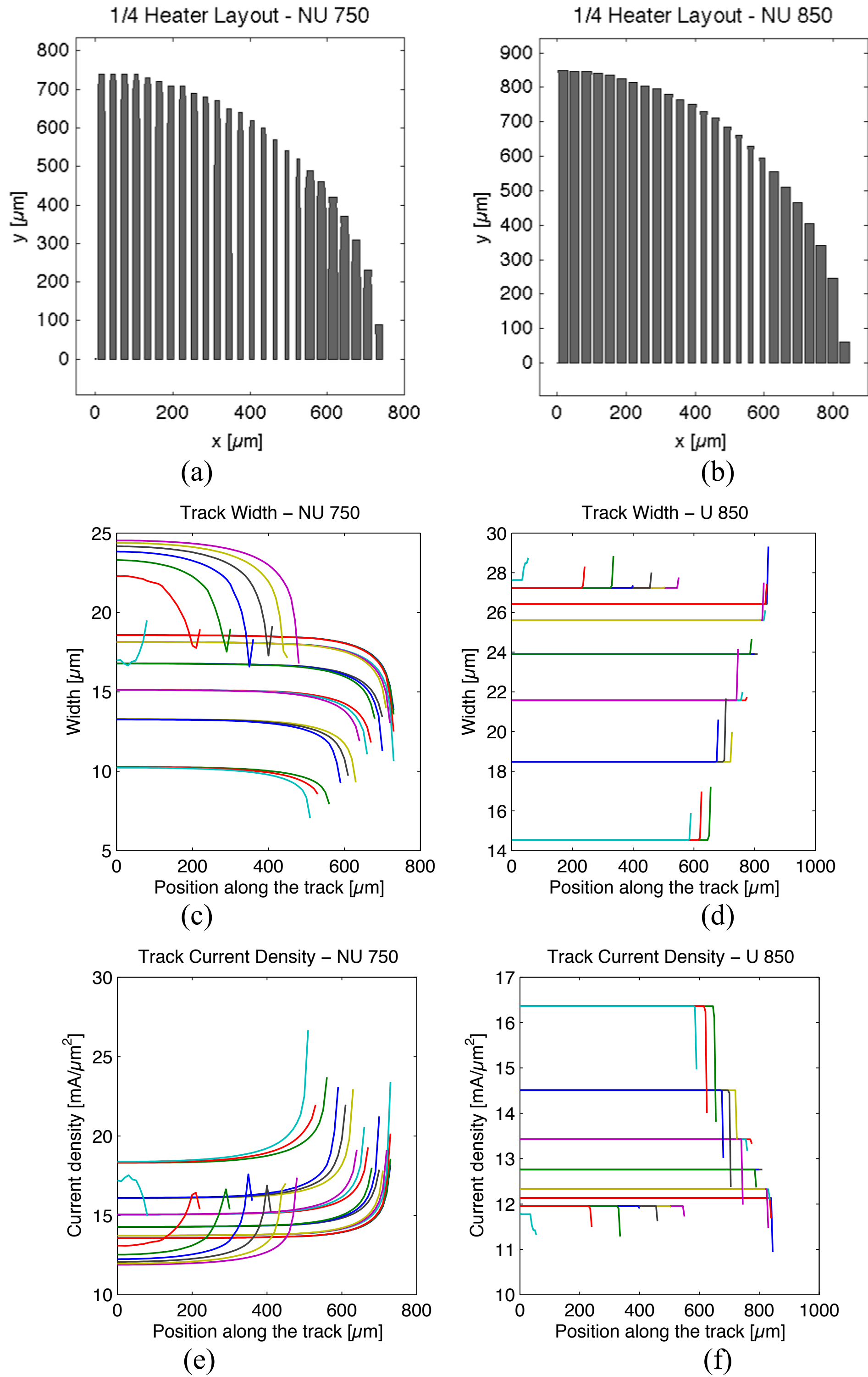

Figure 55. (a, b) Automatically generated NU 750 and U 850 heater tracks. (c, d) Width of the tracks for the NU 750 and U 850 heaters. Note the significant tapering of track width near the heater edge. (e,f) Current density along the tracks.

9.8 Appendix C: Layout Verification

9.8.1 Virtual Connection Test

In order to simulate the heater generated automatically in MATLAB®, we connected the tracks through virtual connections. With this simulation we confirmed that the heater conformed to the ± 1 ºC *Tc* uniformity requirement. Figure 56 shows the temperature distribution at the bottom of the U 1550 heater and its corresponding Tc histogram.

The discretization of the ideal *Q* field causes a ripple that introduces non-uniformities. Histograms are generated by sampling temperature across the entire volume of the chamber and counting the volume/frequency of temperature values. This is the best metric of uniformity, as it accounts for vertical gradients and clearly indicates the relative volume of the chamber at various temperatures. The most recent heater design techniques [23] aim for uniformity on one of the surfaces, rather than on the volume, of the chamber. Our method is developed to attain volumetric uniformity and we test for it with the histograms.

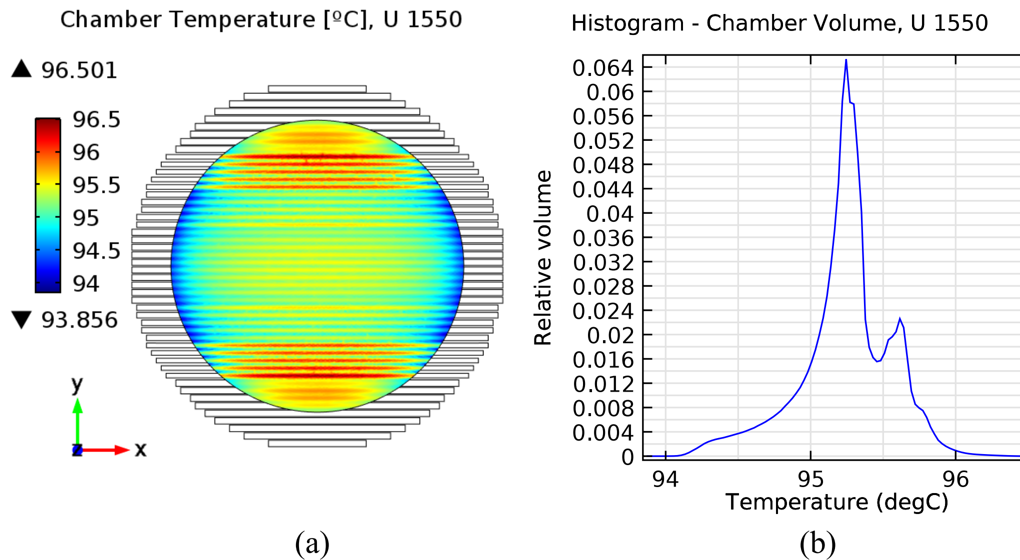

(a) (b)

Figure 56. (a) Temperature field at the bottom of the PCR chamber in U 1550. (b) Histogram of the temperatures across the volume of the PCR chamber. The heater tracks are connected through zero-resistance virtual connections. The uniformity is good which validates the result of the discretization and generated layout.

The average chamber temperature can reach the target of 95 ºC even with a low track count. However, the uniformity largely depends on the resolution of the heater, and this virtual connection test allows us to check the uniformity. To understand the effect of low resolution on uniformity, refer to Figure 57. It is obvious that there is a significant ripple in the heater and chamber temperature, deteriorating uniformity to approximately 2 ºC.

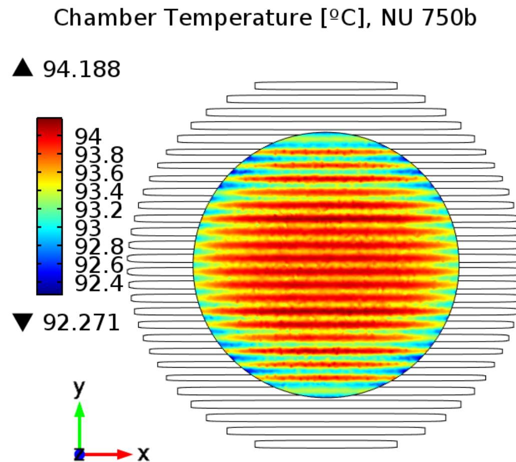

Figure 57. Temperature field at the bottom of the PCR chamber in the NU 750, using a pitch of 50 µm (30 tracks resolution).

9.8.2 Physical Connection Test and Optimization

In our first attempt at using this novel methodology, the heater in the physical connection layout showed poor uniformity caused by the end groups not reaching the temperature of the rest of the groups. It was clear that the voltage drop accrued across the track “elbow” connections, causing the problem. The more elbows in a group, the greater the voltage drop within that group, and worse the effect on uniformity. For this reason, the effect was immediately obvious in the larger heaters, which were designed with groups of a higher number of tracks at the ends than in the middle (shown clearly in Figure 58 of U 1550 at the top of the color plot). The total voltage drop across the elbows in the end groups was 0.47 V compared to only 0.16 V for the middle groups in the U 1550 model. This

difference resulted in a decline of uniformity to about ±2.5 ºC, down from the target ±1 ºC.

To mitigate these effects we increased the elbow size to lower the voltage drop across them. On its own, this adjustment was not enough to make up the significant difference in voltage dropped across the elbows between the end and middle groups. To make up for this loss, we decided to reduce the length of the very last track in the end group, thereby compensating for the increased voltage drop across the elbows. The last track was adjusted by laying a polygon on part of the track to widen it, making the resistance negligible in comparison to the normal track width. To determine up to where the track should be widened, the difference between the voltage drop for the center and end groups (0.31 V) was summed to the voltage at the ground end of the track. This yielded the lower absolute voltage that the end groups must see in order to have a total voltage equal to that on the center groups. Probing a 2D electric potential color-plot of the heater allowed us to find the coordinate easily. With the track adjusted, uniformity was restored. The restoration of uniformity is also shown in Figure 58 at the bottom of the color plot where the last track has been widened for part of its length.

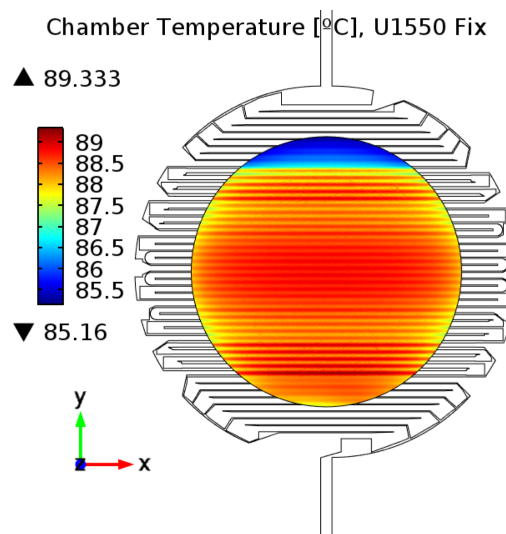

Figure 58. Temperature field at the bottom of the PCR chamber in U 1550, when the physical connections are added. The voltage drop at the end group at the bottom, caused by the large number of elbows, was corrected by reducing the length of the first track. The top group was not corrected, in order to show the difference. The non-uniformity in this group reaches ~ 5 ºC.

9.9 References

[1] S. Park, Y. Zhang, S. Lin, T.-H. Wang, and S. Yang, "Advances in microfluidic PCR for point-of-care infectious disease diagnostics," *Biotechnology Advances*, vol. 29, no. 6, pp. 830–839, Nov. 2011.

[2] F. Ahmad and S. A. Hashsham, "Miniaturized nucleic acid amplification systems for rapid and point-of-care diagnostics: A review," *Analytica Chimica Acta*, vol. 733, no. 0, pp. 1–15, Jul. 2012.

[3] J. Noh, S. W. Sung, M. K. Jeon, S. H. Kim, L. P. Lee, and S. I. Woo, "In situ thermal diagnostics of the micro-PCR system using liquid crystals," *Sensors and Actuators A: Physical*, vol. 122, no. 2, pp. 196–202, Aug. 2005.

[4] P.-C. Chen, D. Nikitopoulos, S. Soper, and M. Murphy, "Temperature distribution effects on micro-CFPCR performance," *Biomedical Microdevices*, vol. 10, no. 2, pp. 141–152, Apr. 2008.

[5] C. D. Bennett, M. N. Campbell, C. J. Cook, D. J. Eyre, L. M. Nay, D. R. Nielsen, R. P. Rasmussen, and P. S. Bernard, "The LightTyper: high-throughput genotyping using fluorescent melting curve analysis," *BioTechniques*, vol. 34, no. 6, pp. 1288–1292, 1294–1295, Jun. 2003.

[6] K. Hu, Z. Chen, and J. Huang, "Research on temperature measuring positions selection and verification for Polymerase Chain Reaction instruments," in *2011 4th International Conference on Biomedical Engineering and Informatics (BMEI)*, 2011, vol. 3, pp. 1165 –1169.

[7] H. Nagai, Y. Murakami, K. Yokoyama, and E. Tamiya, "High-throughput PCR in silicon based microchamber array," *Biosensors and Bioelectronics*, vol. 16, no. 9–12, pp. 1015–1019, Dec. 2001.

[8] M. G. Roper, C. J. Easley, L. A. Legendre, J. A. C. Humphrey, and J. P. Landers, "Infrared Temperature Control System for a Completely Noncontact Polymerase Chain Reaction in Microfluidic Chips," *Analytical Chemistry*, vol. 79, no. 4, pp. 1294–1300, Feb. 2007.

[9] N. Beyor, L. Yi, T. S. Seo, and R. A. Mathies, "Integrated Capture, Concentration, Polymerase Chain Reaction, and Capillary Electrophoretic Analysis of Pathogens on a Chip," *Analytical Chemistry*, vol. 81, no. 9, pp. 3523–3528, May 2009.

[10] C. Zhang and D. Xing, "Miniaturized PCR chips for nucleic acid amplification and analysis: latest advances and future trends," *Nucl. Acids Res.*, vol. 35, no. 13, pp. 4223–4237, Jul. 2007.

[11] H. Kim, S. Dixit, C. J. Green, and G. W. Faris, "Nanodroplet real-time PCR system with laser assisted heating," *Opt. Express*, vol. 17, no. 1, pp. 218–227, 2009.

[12] N. Pak, D. C. Saunders, C. R. Phaneuf, and C. R. Forest, "Plug-and-play, infrared, laser-mediated PCR in a microfluidic chip," *Biomedical Microdevices*, vol. 14, no. 2, pp. 427–433, Jan. 2012.

[13] G. V. Kaigala, M. Behnam, A. C. E. Bidulock, C. Bargen, R. W. Johnstone, D. G. Elliott, and C. J. Backhouse, "A scalable and modular lab-on-a-chip genetic analysis instrument," *Analyst*, vol. 135, no. 7, pp. 1606–1617, 2010.

[14] D. Resnik, D. Vrtačnik, M. Možek, B. Pečar, and S. Amon, "Experimental study of heat-treated thin film Ti/Pt heater and temperature sensor properties on a Si microfluidic platform," *Journal of Micromechanics and Microengineering*, vol. 21, no. 2, p. 025025, Feb. 2011.

[15] Q. Zhang, W. Wang, H. Zhang, and Y. Wang, “Temperature analysis of continuous-flow micro-PCR based on FEA,” *Sensors and Actuators B: Chemical*, vol. 82, no. 1, pp. 75–81, Feb. 2002.
[16] S. M. Lee, D. C. Dyer, and J. W. Gardner, “Design and optimisation of a high-temperature silicon micro-hotplate for nanoporous palladium pellistors,” *Microelectronics Journal*, vol. 34, no. 2, pp. 115–126, Feb. 2003.
[17] K. R. Williams, K. Gupta, and M. Wasilik, “Etch rates for micromachining processing-Part II,” *Journal of Microelectromechanical Systems*, vol. 12, no. 6, pp. 761–778, 2003.
[18] Y.-F. Chang, Q.-R. Chou, J.-Y. Lin, and C.-H. Lee, “Fabrication of high-aspect-ratio silicon nanopillar arrays with the conventional reactive ion etching technique,” *Appl. Phys. A*, vol. 86, no. 2, pp. 193–196, Feb. 2007.
[19] J. Martinez-Quijada, S. Caverhill-Godkewitsch, M. Reynolds, L. Gutierrez-Rivera, R. W. Johnstone, D. G. Elliott, D. Sameoto, and C. J. Backhouse, “Fabrication and Characterization of Aluminum Thin Film Heaters and Temperature Sensors on a Photopolymer for Lab-On-Chip Systems,” *Sensors and Actuators A: Physical*, vol. 193, pp. 170–181, Apr. 2013.
[20] T.-M. Hsieh, C.-H. Luo, F.-C. Huang, J.-H. Wang, L.-J. Chien, and G.-B. Lee, “Enhancement of thermal uniformity for a microthermal cycler and its application for polymerase chain reaction,” *Sensors and Actuators B: Chemical*, vol. 130, no. 2, pp. 848–856, Mar. 2008.
[21] T.-M. Hsieh, C.-H. Luo, J.-H. Wang, J.-L. Lin, K.-Y. Lien, and G.-B. Lee, “A two-dimensional, self-compensated, microthermal cycler for one-step reverse transcription polymerase chain reaction applications,” *Microfluidics and Nanofluidics*, vol. 6, no. 6, pp. 797–809, Oct. 2008.
[22] J.-H. Wang, L.-J. Chien, T.-M. Hsieh, C.-H. Luo, W.-P. Chou, P.-H. Chen, P.-J. Chen, D.-S. Lee, and G.-B. Lee, “A miniaturized quantitative polymerase chain reaction system for DNA amplification and detection,” *Sensors and Actuators B: Chemical*, vol. 141, no. 1, pp. 329–337, Aug. 2009.
[23] B. Selva, P. Mary, and M.-C. Jullien, “Integration of a uniform and rapid heating source into microfluidic systems,” *Microfluidics and Nanofluidics*, vol. 8, no. 6, pp. 755–765, 2010.
[24] W. M. Haynes and D. R. Lide, *CRC Handbook of Chemistry and Physics - A Ready-Reference Book of Chemical and Physical Data: 2011-2012*, 92nd ed. Boca Raton FL; London; New York: CRC Press, 2011.
[25] P.-C. Chen, W. Fan, T.-K. Hoo, L. C. Z. Chan, and Z. Wang, “Simulation guided-design of a microfluidic thermal reactor for polymerase chain reaction,” *Chemical Engineering Research and Design*, vol. 90, no. 5, pp. 591–599, May 2012.

10 A Robust and Manufacturable LOC Thermal System

A version of this chapter will be submitted for publication (Article 4 – J. Martinez-Quijada, 2014).

The technologies that we developed enabled the design and fabrication of a system that, to our knowledge, is the first manufacturable implementation of a thermally robust, CMOS-compatible LOC system. A key advantage of this new technology is that the temperature of the PCR chamber can be estimated with high accuracy from the heater's resistance without the need for per-device calibration, making mass-manufacture viable. We successfully demonstrated the system by simulation and experiment. A manuscript for this work is in the final stages of preparation and will be submitted for publication.

The presented system is a joint development of the research groups of Dr. Chris Backhouse and Dr. Duncan Elliott. The author carried out the analysis, modeling and simulation tasks that led to the understanding and optimization of the design. The author performed different numerical analyses including the calculation of correction factors. The author wrote the corresponding article. Saul Caverhill-Godkewitsch contributed simulations and plots from COMSOL that were obtained as part of the work in Chapter 9. Saul reviewed and corrected the article in its first stages of development and later Dr. Backhouse reviewed and restructured the article. The infrared imaging experiment was performed by the author, Saul Caverhill-Godkewitsch, Matthew Reynolds and Dan Sameoto. The author and Saul analyzed the images after the experiment. The group of Dr. Backhouse at the University of Waterloo developed the fluid handling system of the device, which includes the polypropylene membrane. They also designed the arrangement of the microchannels in the chip. Tianchi Ma and Gordon Hall performed the fluorescence temperature measurements. The author developed an analytical model of the system that describes its dynamic response and performed

transient simulations that validated the analytical model and the results of transient experiments performed by David Sloan.

10.1 Introduction

This chapter presents a manufacturable LOC implementation where a thin film Al heater is intimately integrated with a PCR chamber and is simultaneously used as a temperature sensor. The thermal resistance from the heater to the chamber is orders of magnitude lower than the resistance from the chamber to the environment. This configuration has several distinct advantages: 1) the system becomes largely insensitive to variations of external conditions; 2) the chamber and heater temperatures are essentially the same; 3) the thermally controlled regions are isolated and can be operated independently. Although the effects of boundary variables such as ambient temperature are greatly attenuated, they can still shift the chamber temperature slightly. However by making use of a controller these shifts can be compensated, effectively preventing those boundary variables from affecting the system.

The heater and PCR chamber are embedded in a low thermal conductivity thin polymer structure built on a high conductivity Si substrate. Because the thermal interface between the polymer and the Si is well controlled (at the fabrication level), this design is thermally robust - insensitive to external parameters to the extent that it need not be calibrated before use if the temperature coefficient of resistivity (TCR) of the Al film is known. With tight control of the fabrication parameters, i.e. repeatable layer thicknesses, lithography, material properties, etc., the only boundary variable affecting the system significantly is the substrate temperature. Variations in this temperature can be easily measured and compensated for with a controller, making the system highly insensitive to this boundary variable as well.

In the system the vertical thermal conduction towards the Si substrate dominates, so that convective and lateral losses are negligible, leading to uniform temperatures that can be characterized by a single temperature value. The heater,

which provides a uniform power density field, is extended beyond the radius of the chamber to ensure approximately ±1 ºC uniformity within the chamber.

Other devices made of thin polymer layers on substrates of high or relatively high conductivity have been presented before [1], [2]. Lee *et al*. [1] developed a PCR chip comprising a PMMA structure bonded on top of a thin Si membrane, aimed to isolate the system thermally. The PMMA structure contained a 250 µm deep PCR chamber and the membrane contained a thin film Pt heater and a sensor. In 2013 Deng *et al*. [2] presented a 1 x 1 cm PCR chip with 12 chambers of 1 x 1.5 mm each. The chambers were patterned in a 60 µm thick SU-8 layer built on a SiO_2 substrate. Each chamber was equipped with a thin film Pt heater and a sensor that were separated from the liquid in the chamber by a 300 nm layer of SiO_2. In these examples the heater was not used as a sensor. Perhaps more importantly, they did not employ a heatsink and instead natural convection was the dominant heat release mechanism. Therefore these systems were vulnerable to changes in environmental parameters.

There have been reports of designs comparable to ours using integrated heaters and polymers, the closest of all being from Selva *et al*. [3]. In that work, a Cr/Au heater underlying a chamber was embedded in a SU-8/PDMS structure built on silicon. The heater was optimized to compensate for edge cooling and provide uniform temperature constrained within the chamber area. A uniformity of ±6 ºC at 37.5 ºC in 82 % of the chamber was achieved. The authors, however, did not utilize the heater as a sensor, and instead relied on fluorescence thermometry to measure the temperature in the chamber during operation. Moreover, the SU-8/PDMS structure was 4.15 mm thick, which allows a significant lateral heat loss, hence preventing the heat from being constrained to flow vertically in a way that the substrate temperature dominates.

More recently, Jung *et al.* [4] presented Pt/Ti heaters on silicon that were coated with a thin SU-8 layer loaded with Rhodamine-B, enabling high resolution surface temperature imaging via fluorescence thermometry. The heaters, however,

remained only as a heat source. A calibration curve of fluorescence intensity vs. temperature was constructed to allow for temperature monitoring and control. However solutions relying on fluorescence thermometry (or other contact-less methods) at the time of use are not compatible with single-chip integration or are not suitable for point of care use.

In the work presented herein the heater is used simultaneously as a sensor and its resistance is measured in 4-point mode. The temperature in the chamber is estimated from the measured resistance, the TCR of the heater's material and scaling factors obtained by simulation. The chamber temperature is estimated with a maximum uncertainty of ±0.6 % and chamber temperature uniformity within ±1.25 ºC. We show the analytical development of the system in a 1D model and verify the design via 3D simulation. As a final test of the robustness of this design we fabricated the devices and, without prior calibration, showed that the measurement of their operation temperature by several means gives identical temperatures. This validates the design and indicates that it is suitable for CMOS-compatible mass-manufacture.

As a result of the robustness of the system, if the temperature coefficient of resistivity (TCR) of the metal film is known within ± 1%, the chamber temperature can be estimated to within ± 0.73 ºC error, potentially enabling operation without device-level calibration. Simplifying the calibration procedure is key to the reduction of the production time and cost of the devices. To the best of our knowledge, our work represents for the first time a robust and accurate thermal control of a LOC system that is insensitive to all external variables, except one that is easily controllable. We have implemented the solution in an inexpensive, integrated chip architecture that enables medical diagnostic instruments to be built in a USB-key format, driving cost to as low as a few dollars and encouraging widespread use.

10.2 Design, Methods and Materials

10.2.1 System Description

It has been noted that thick substrates of low thermal conductivity, e.g. glass or polycarbonate, may cause large temperature non-uniformities [5], [6]. On the other hand, the high thermal conductivity of Si bonded to glass-based PCR chips can make the temperature differences in the chamber very small [6]. In addition, due to its small heat capacity, Si can also acquire the temperature of a heated surface extremely rapidly upon contact [7] and this makes Si an excellent thermal interface. The use of polymer materials in LOC architectures often results in large temperature differences [5], [8], due to the low conductivity of polymers. In our system, however, this property is used to limit power consumption and obtain a compact heated volume. In order to prevent large temperature differences (and non-uniformities) resulting from the polymer we fabricated a thin polymer structure on top of a Si substrate.

The system consists of a thin film aluminum heater that underlies a circular PCR chamber. The heater is embedded in a multilayer KMPR polymer structure built on a Si substrate, as shown in Figure 59(a). The entire device is placed onto a heatsink. The thickness of each KMPR layer is (from bottom to top) 20, 20, 20 and 25 µm. The thicknesses of the polypropylene (PP) roof and Si substrate are 40 µm and 500 µm, respectively. The expected thickness of the Al heater is 100 nm.

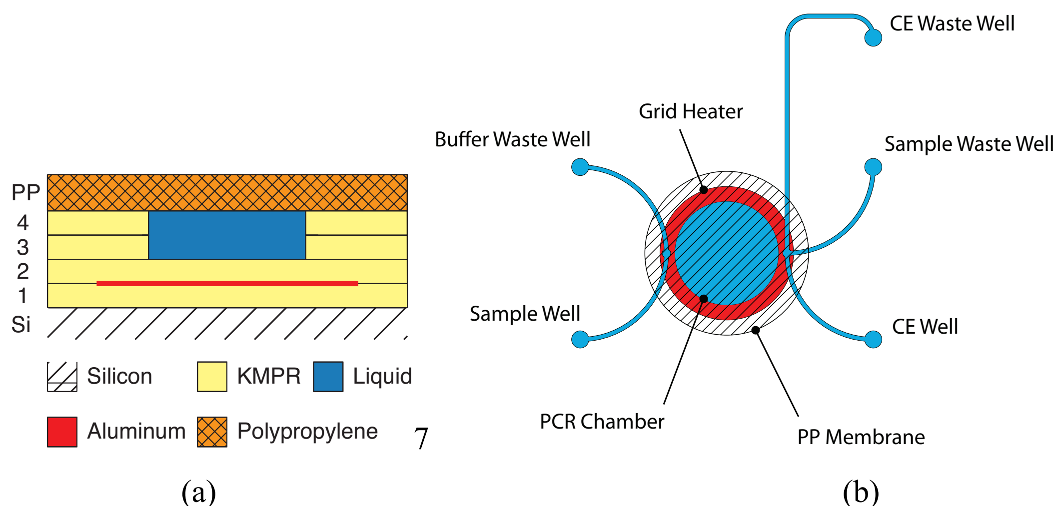

Figure 59. Construction of the thermally robust LOC system. (a) Cross sectional view of the stack of KMPR layers forming the system. The device is placed onto a heatsink prior to operation. (b) Top view schematic of the system, showing the PCR chamber, the heater and the polypropylene lid that seals the chamber. The wells and microchannels are part of the fluidic system intended to fill up the PCR brew into the chamber and perform capillary electrophoresis on the PCR product.

We fabricated the heater on top of the first KMPR layer to limit the power consumption of the device by insulating the heater from the Si substrate. Layer 2 isolates the PCR sample from the heater/sensor and smoothes out the large temperature ripple of the heater. Layers 3 and 4 are patterned to make up the chamber, channels and fluidic ports. Finally, the polypropylene lid on top seals the chamber and contains the pressure generated by the heated liquid.

The top view of the system is depicted in Figure 59(b) showing that, to conserve power, the heater is extended only enough beyond the chamber to ensure uniformity in the chamber. The extension distance, Δrh, depends non-linearly on the thickness of the structure and depends strongly on the specific power density profile of the heater. Because of this the most effective way to determine Δrh is from the design curves of the heaters, depicted in Figure **44**. These curves constructed by 2D simulation allow for finding the best trade-off between uniformity, power consumption, device footprint and extension distance. From these curves we determined that for the total thickness of the structure (125 µm) the optimal extension distance for uniform power density heaters is 350 µm.

Therefore, we would expect that edge effects can be (at least to first order) neglected as long as the heater extends by 350 μm. For uniform power density heaters the extension distance as a function of the total thickness of the structure, *l*, can be estimated from $\Delta rh = 175 \ln(l) - 500$, with *l* in μmeters (calculated from 2D simulation for an average heater temperature of 95 ºC and heatsink temperature of 30 ºC).

10.2.2 Analytical Model

With the heater suitably extended the temperature in the chamber region is expected to be uniform. This allows the use of a 1D approximation wherein we primarily consider the heat to flow vertically through the various layers. The 1D model of the system is depicted in Figure 60. The resistances R_{Si}, *R1, R2, Rc* and *Rm* are the vertical resistances due to conduction, which can be calculated from:

$$R = \frac{1}{k} \cdot \frac{h}{A} \qquad \textbf{Eq. 20}$$

Where *k* is the thermal conductivity, *h* is the layer thickness and *A* is the top-view surface area. Our 1D model can be visualized as a cylinder where all the resistances have the same radius. The properties of the materials in the system are listed in Table 12. The properties for KMPR (k, ρ_m ,c_p) have not been reported, so those of SU-8 are used as this is the epoxy-based photo-polymer most similar to KMPR [9], [10], and is well-characterized.

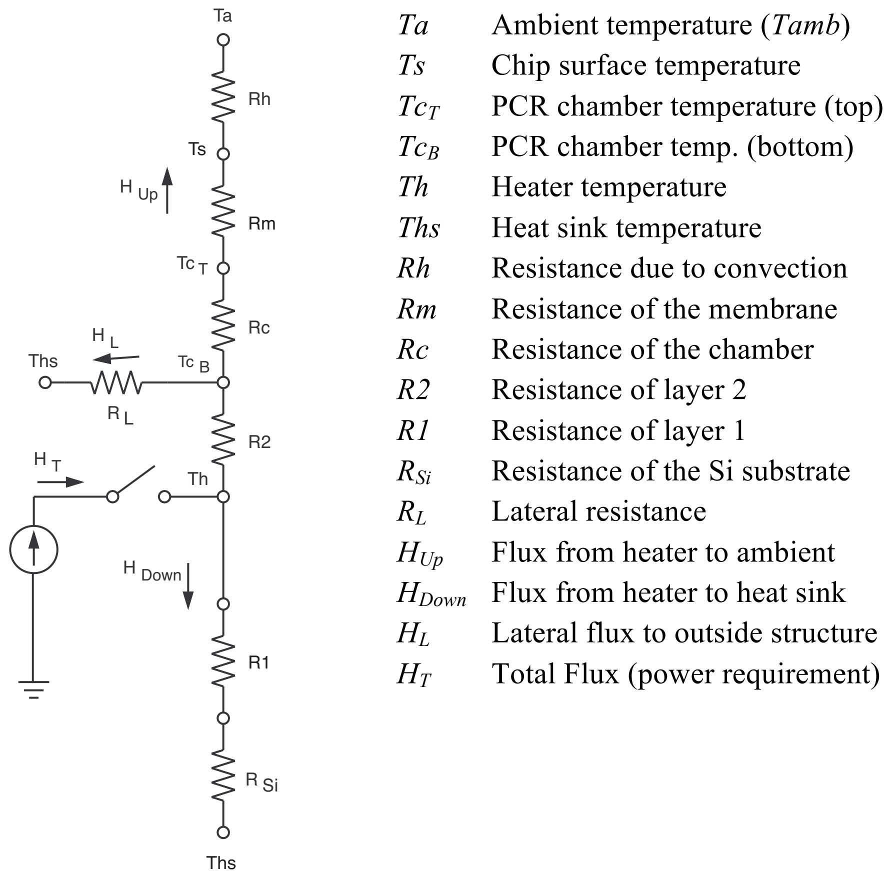

Figure 60. Analytical model of the system, with layers as labeled in Figure 59.

Material	Thermal conductivity k - [W/m-K]	Mass Density ρ_m - [kg/m^3]	Specific Heat c_p - [J/kg-K]	Comment
KMPR	**0.2** [12], [13]	**1200 [12]** 1190 **[13]**	**1500** [12], [14]	Typical values for crosslinked SU-8.
Polypropylene	**0.22 @ 20 ºC** [15]	**900** [15], [16]	**2100** @ 100 ºC [15]	Typical values
Water	0.6262 @ 25 ºC [16] **0.6729** @ 100 ºC [16]	**1000** @ 25 ºC [12] 998.21 @ 20 ºC [16]	4182 [14] 4200 [12] **4184** @ 20 ºC [16]	In simulation these properties are calculated pointwise as a function of temperature.
Silicon	**163** [17] 168 [7]	2329 [16] **2330** [18, p. 585]	702 @ 300 K [19] **700** [18, p. 585]	Typical values
Aluminum	237 [16]	**2700 [16]**	**897 [16]**	Bulk values

Table 12. Properties of the materials in the system. The values in bold were used in analytical calculations.

R_L is the lateral resistance to heat loss from the chamber to the rest of the KMPR structure. At some distance from the chamber, the temperature of the structure drops to the heatsink temperature, thus R_L connects to *Ths*. This resistance can be approximated from the radial thermal resistance of a hollow cylinder [11]:

$$R_L = \frac{1}{2\pi k l} \ln\left(\frac{r_2}{r_1}\right) \qquad \textbf{Eq. 21}$$

Where *r1* is the inner radius; *r2* is the outer radius; *k* is the thermal conductivity; and *l* is the thickness of the cylinder, which may simply be taken as the total thickness of the structure, i.e. $l = 125$ µm. From simulation and IR imaging experiments we observed that most of the temperature change occurs within 100 µm at the outer edge of the the heater, i.e. the transition from the maximum temperature to the heatsink temperature (about 60 ºC change) occurs over a distance of 100 µm. Therefore, for the purpose of estimating R_L we take $r1 = 1500$ µm and $r2 = r1 + 100$ µm. Although this is a rather crude approximation our 3D simulations will show that these are reasonable values for *l*, *r1* and *r2*.

From Eq. 21 it is clear that a very thin, low-conductivity structure can dramatically increase the lateral resistance, thereby reducing substantially the horizontal heat loss. If this loss is made negligible, the heat will be constrained to flow vertically, turning the device into a one-dimensional system. If the polymer layers are sufficiently thin, the heated area will be fairly insensitive to anything occurring outside, such as variable airflow, ambient temperature fluctuations or even an object touching the chip. Since only conduction in the vertical direction is expected to be significant, a uniform temperature field can be produced from a heater that generates uniform heat flux. Our U 850 and U 1550 designs were crafted to produce such a uniform flux over the entire heater area.

Heat loss at the top surface of the chip is taken to occur by natural convection with a heat transfer coefficient (*htc*) of 5.6 W/m^2-K [20], resulting in an effective thermal resistance *Rh* given by [11]:

$$Rh = \frac{1}{htc\ A} \qquad \textbf{Eq. 22}$$

Although *htc* varies non-linearly with the difference between the surface and ambient temperatures [21], in the operating range (22–95 ºC) its variation is small enough and can be neglected.

If a controller keeps the heater at a constant temperature, *Th*, the temperature at the bottom of the PCR chamber can be estimated from:

$$Tc_{B_} = \left(\frac{Th}{R2} + \frac{Ths}{R_L} + \frac{Tamb}{Rc + Rm + Rh} \right) \cdot \left(\frac{1}{R2} + \frac{1}{R_L} + \frac{1}{Rc + Rm + Rh} \right)^{-1} \qquad \textbf{Eq. 23}$$

Since the temperatures of the chamber and heater vary spatially, we define *Th* as the average temperature across the surface of the heater. Similarly, Tc_B and Tc_T are the average temperatures across the bottom and top surfaces of the chamber. Eq. 23 allows estimating the robustness of the system to variations in heatsink and ambient temperature. A very thin, low-conductivity structure that maximizes R_L will render the system highly insensitive to changes of *Ths*. On the other hand, a system that minimizes the convective losses, i.e. that maximizes *Rh*, will be insensitive to fluctuations in ambient temperature.

The thermal resistances for the U 1550 design estimated from Eq. 20 and Eq. 22 (considering a radius of 1550 µm) are shown in Table 13. The lateral resistance, R_L, is calculated from Eq. 21 with l = 125 µm, $r1$ = 1500 µm and $r2 = r1$ + 100 µm.

Parameter	Value [K/W[
Rh	2.37×10^4
Rm	26.50
Rc	8.86
$R2$	13.25
$R1$	13.25
R_{Si}	0.41
R_L	410.86

Table 13. Estimated resistances of the system using a U 1550 heater design, whose chamber and heater radii are 1200 µm and 1550 µm, respectively.

The resistance due to convection is at least two orders of magnitude greater than the rest of the resistances in the system, as the surface in contact with air is very small. With Rh and R_L relatively so large we can expect very low sensitivity to Ths and $Tamb$. By substituting the resistance values into Eq. 23 we obtain the relative contribution of the different variables to the chamber temperature:

$$Tc_B = 0.967Th + 0.032Ths + 0.00054Tamb \quad \textbf{Eq. 24}$$

The contribution of Ths and $Tamb$ is, in fact, very small and $Tc_B \approx Th$. Therefore, in the limit of a sufficiently thin structure the system is thermally robust against variations of Ths and $Tamb$ if a controller holds Th constant.

The coefficients of the Ths and $Tamb$ terms are denoted β and γ, respectively. To better understand the meaning of these factors let us consider separately the two main branches of the system that determine the conductive lateral loss and the convective loss. For the conductive loss through R_L we can write:

$$Th - Tc_B = \frac{R2}{R2 + R_L}(Th - Ths) \quad \textbf{Eq. 25}$$

And we define β such that:

$$Th - Tc_B = \beta(Th - Ths) \quad \textbf{Eq. 26}$$

The factor β is, therefore, the amount of change in the average chamber temperature that will be introduced if the heatsink temperature changes by a degree Kelvin when the heater temperature is held constant. The parameter β is unitless and is approximately proportional to 1/ R_L. From the calculated value of β (0.031) we expected a change of 0.3–0.4 ºC in chamber temperature if *Ths* varies by 10 ºC. It is clear that the vertical loss by conduction towards the heatsink dominates over the lateral loss to the extent that even a large change in the heatsink temperature does not affect the result significantly. For the convective loss we can write:

$$Th - Tc_B = \frac{R2}{R2 + Rc + Rm + Rh}(Th - Tamb) \qquad \textbf{Eq. 27}$$

Similarly, we define γ such that:

$$Th - Tc_B = \gamma\,(Th - Tamb) \qquad \textbf{Eq. 28}$$

The factor γ is the amount of change in the average chamber temperature that will be introduced if the ambient temperature changes by a degree Kelvin when the heater temperature is held constant. The paramter γ is unitless and is approximately proportional to 1/*Rh*.

The reported values of *htc* for free convection on heated surfaces facing upwards may differ by a factor of four [21], depending on conditions and the difference between the surface and ambient temperatures (*htc* increases by ~1 W/m^2 K with an increase in the temperature difference of 10 ºC [21]). However, it is clear that the vertical loss by conduction is dominant to the point that even a large change in the *htc* value (e.g. a factor of 4) or ambient temperature (e.g. 10 ºC) does not affect the factor γ significantly and hence the effect of these variations is expected to be negligible.

The calculation of β and γ in this section is intended to provide only an estimate of the overall sensitivity to changes in the heatsink temperature, ambient temperature and airflow. A far more accurate calculation of these factors is performed by 3D simulation, as explained in section 10.2.4.

10.2.3 Physical Layout

We designed our devices for ±1 ºC temperature uniformity (or better) at the denaturation temperature (95 ºC) as described in Chapter 9. As part of Step 1 of the heater design process we constructed curves of uniformity (ΔT) and power (P) vs. extension distance (Δrh). In this step a uniformity $\Delta T < 1$ ºC (the difference between the maximum and minimum temperatures in the chamber) was set as a target to allow room for the non-uniformities introduced by the discretization process in Step 2. From the design curves we found that heaters that produce uniform power density (U 850 and U 1550) need to be extended by 350 μm to reach the target uniformity. The construction of the curves is explained in sections 9.3.1 and 9.4.1.

Figure 61 shows the generated mask layout of the U 1550. The heater is operated simultaneously as a 4-point sensor, wherein the drive current is applied through terminals A and B, and the voltage is probed across terminals C and D. To reduce the total current requirement of the system while maintaining the same power generation, the tracks are connected in series in groups of 3 to 9, and all the groups are connected in parallel to a common power bus. In uniform designs the track width is constant across the length of the tracks. A table of specifications, including track widths and current densities, is available in section 9.4.2. Lifetime experiments in section 9.4.6.1 demonstrate the stability of the devices operating at ~100 ºC with 14.2 mA/μm^2 maximum current density (on the thinnest tracks) for > 40 hr – more than enough time for PCR applications.

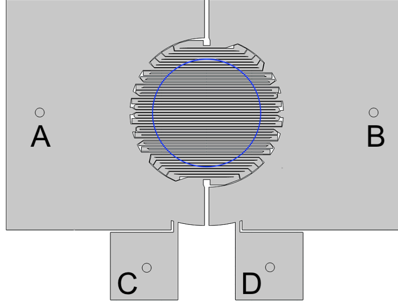

Figure 61. Layout of the U 1550. The horizontal lines at the center of the figure are the heater tracks. The blue circle at the center of the figure indicates the perimeter of the 1200 µm radius chamber. The driving current is applied through terminals A and B; the output voltage is probed between terminals C and D.

10.2.4 3D Simulation of the System

The sensitivity of the system to variations in *Ths* and *Tamb* was assessed by simulation on the full 3D model of the system by embedding the actual mask layout shown in Figure 61 in a fully coupled Joule-heating/heat-transfer 3D FEM model. The default boundary conditions were uniform temperature of value *Ths* on the bottom surface of the Si substrate, and heat loss by convection on the other boundaries. The condition for convection used in 2D and 3D simulations is defined as:

$$Q(T) = htc\,(Tamb - T) \qquad \textbf{Eq. 29}$$

Where *htc* = 5.6 W/m^2-K for natural convection in air [20]; *Tamb* is the ambient air temperature; and *T* is the temperature at the surface where convection occurs. The heater is modeled as a 100 nm thick Highly Conductive Layer with the thermal conductivity of aluminum; the simulation tool calculates its resistivity pointwise as a function of temperature via Eq. 30 with TCR $\alpha = 3.52 \times 10^{-3}\ K^{-1}$, reference resistivity $\rho_o = 4.39 \times 10^{-8}$ Ω-m and reference temperature T_o = 22 ºC. We reported these values for Al films on KMPR previously [22]. The correction factors are independent of the values used for the TCR, resistivity and Al thickness. This is fortunate since these parameters will vary considerably depending on deposition conditions such as base pressure.

$$\rho = \rho_0 \left(1 + \alpha (T - T_0)\right) \qquad \textbf{Eq. 30}$$

In the simulation the applied voltage *Vapp* across terminals A and B in Figure 61 is specified and the current through the heater, *I*, is determined. In order to quantify the sensitivity to *Ths* the system is first simulated with *Ths* = 20 ºC for eight different values of *Vapp* from 1.5 to 12 V in steps of 1.5 V. The value of *Tamb* is fixed to 20 ºC. The average chamber temperature *Tc* and the heater's resistance *R* are recorded at each simulated point. The average *Tc* is calculated as the volume integral of the temperatures in the chamber divided by the total chamber volume. The resistance is calculated from the output voltage between C and D, *Vo,* divided by the total current, *I.* The simulation is repeated for *Ths* = 30 ºC and 40 ºC.

Lines of *Tc* vs. *Rh* were then fitted through the sets of data obtained for each of the three values of Ths. If a controller holds the heater temperature constant (and hence its resistance) the spacing between the three lines represents the change in *Tc* brought about by the variation in *Ths*. By dividing the vertical distance (in *Tc*) between the fitted lines by the change in *Ths* we can obtain a value for β. The sensitivity to *Tamb* is determined much in the same way: the applied voltage is ramped from 1.5 V to 12 V for three different values of *Tamb* (20, 30, 40 ºC), and *Ths* is fixed at 20 ºC. The resulting data can be treated the same as for the *Ths* sensitivity to provide a value for γ.

To find the most accurate values for β and γ, a linear model of the following form is fitted to the full set of data obtained from 3D simulation:

$$R = Ro + m1Tc + m2\;Ths + m3\;Tamb \qquad \textbf{Eq. 31}$$

Dividing each of the slopes, *m1, m2* and*, m3* by the product *Ro* α yields the sensitivity of the heater's resistance, *R,* to *Tc*, *Ths* and *Tamb.* These sensitivities are denoted *k1, k2* and *k3*, respectively. The factor *Ro* is the intercept and α is the TCR of the Al film. The sensitivity *k1* is equivalent to the correnction factor ε that

will be introduced in section 10.2.6.2. The correction factors are then calculated as $\varepsilon = k1$, $\beta = k2 / k1$ and $\gamma = k3 / k1$ (these relations are found by solving Eq. 31 for Tc). Since $\varepsilon \approx 1$, $\beta \approx k2$ and $\gamma \approx k3$.

10.2.5 Power Considerations

We designed the structure as thin as possible to minimize the lateral heat loss. Although thinner KMPR layers can be fabricated, we maintained enough thickness for the chamber to hold a useful volume of PCR sample. The thickness of layer 1 was kept to a thickness which limited the power consumption to within 5 W. The total power consumption of the system can readily be estimated from:

$$H_T \approx \frac{Th - Ths}{R1 + R_{Si}} \qquad \textbf{Eq. 32}$$

With Th = 95 ºC, Ths = 30 ºC we estimate for the U 1550 heater a total power H_T = 4.76 W. The lateral loss can be estimated from:

$$H_L = \frac{Tc_B - Ths}{R_L} \qquad \textbf{Eq. 33}$$

Solving the 1D model for Tc_B yields 92.93 ºC (equation not shown), which gives H_L = 0.15 W. Therefore, if the lateral loss is considered the total power consumption would be 4.9 W, suggesting that the lateral loss is ~ 3.1 % of the total generated power. The total power calculated for the U 1550 design from 3D simulation when holding the chamber at an average temperature of 95 ºC is 5.03 W (calculated from Eq. 35 with m = 12.91 ºC/W, Tc = 95 ºC, Ths = 30 ºC). This agreement indicates that Eq. 32 and Eq. 33 are reasonable approximations. If the heater was directly patterned on the Si substrate, i.e. $R1$ = 0, the power consumption would be ~160 W, which shows the strong isolation effect of the KMPR layer 1.

Since R_{Si} is very small compared to $R1$ the power density over the heater can be approximated from Eq. 32 as:

$$Q \approx \frac{k_{KMPR}}{h1}(Th - Ths) \qquad \textbf{Eq. 34}$$

With Th = 95 ºC, Ths = 30 ºC, k_{KMPR} = 0.2 W/m-K and $h1$ = 20 µm we estimate Q = 6.32 x 10^5 W/m^2 . The uniform power density designs (U 1550 and U 850) were designed in Chapter 9 to provide this Q value for Tc = 95 ºC. Since our 1D model is independent of the area this value is the same for any heater size. It is clear that the thickness of layer 1 and the radius of the heater control the power requirement at the fabrication level, while during operation the power consumption depends primarily on the difference between heater and heatsink temperatures.

From the 1D model we estimate a loss by convection of 0.00298 W, which is < 0.1 % of the total generated power. With such a small flux upwards we expected < 1 ºC difference across the thickness of the chamber and the average Tc and Th to be equal within ~2 ºC at Th = 95 ºC. By minimizing the difference between Th and Tc the power is used more efficiently and the polymer's integrity is better protected since extremely high values for Th are not required (as in our glass/PDMS technology) to reach the target Tc. Most importantly, when used as a sensor, the chamber temperature can be estimated from the heater temperature, i.e. from the heater's resistance. This makes the Tc vs. Th calibration (see section 3.2 and Chapter 5) unnecessary, thereby avoiding the observer effect so common in LOC systems. The observer effect is the disturbance caused by a calibration transducer that impedes observing the true temperature of the system. In principle, obtaining an accurate resistance-temperature curve of the heater/sensor would be enough to know the temperature in the chamber accurately. Moreover, if the thickness of the aluminum film is carefully controlled and its properties are repeatable within a narrow range, the same curve can be valid for all the devices in a wafer, eliminating the need for per-chip calibration.

10.2.6 Electrical Temperature Measurement

10.2.6.1 Temperature Measurement from Power

From Eq. 32 we derive that *Tc,* which is approximately equal to *Th*, can be estimated from the total input power with:

$$Tc = m\,H_T + Ths \qquad \textbf{Eq. 35}$$

Where *m* is the slope of the *Tc* vs. *P* curve and it is approximately equal to *R1*. An accurate value of *m* for the U 1550 calculated by 3D simulation is 12.91 ± 0.003 ºC/W. The advantage of this type of measurement is that it does not depend on the TCR value. However the accuracy of the estimation depends on how accurately *Ths* can be measured. Additionally, the measurement accuracy is compromised by variations in the thermal contact resistance at the interface between the Si and the heatsink. Therefore this measurement technique is not robust. However, it is a useful measure for comparison with the more difficult to obtain, but more accurate optical measurements.

10.2.6.2 Temperature Measurement from Resistance

We can estimate *Th* directly from the heater resistance following:

$$Th = To + \frac{Re - Ro}{Ro\,\alpha} \qquad \textbf{Eq. 36}$$

Where α is the TCR of the Al film in units of K^{-1}, *Re* is the electrical resistance of the heater measured during operation and *Ro* is the resistance measured at the reference temperature *To*. Since not all of the heater is at a uniform temperature during operation (as opposed to when it is being calibrated in a hotplate or oven), a more accurate expression would be:

$$Th = To + \frac{Re - Ro}{Ro\,\varepsilon\alpha} \qquad \textbf{Eq. 37}$$

Where ε accounts for the fact that a small portion of the heater (mainly the edge) is not at uniform temperature. Since this cooler region is small, we expect ε to be slightly smaller than 1. We refer to the product $\varepsilon\alpha$ as being the *effective TCR* (α_e) whereas the TCR itself (i.e. α) is determined experimentally from calibration. Much as described in section 10.2.2, the size of the coldest portion of the heater might be taken as half of the transition region between *r1* and *r2* (i.e. about 50 μm). An estimate for ε then would be:

$$\varepsilon = \frac{\pi(1550\ \mu m)^2}{\pi(1550\ \mu m + 50\ \mu m)^2} = 0.938 \qquad \textbf{Eq. 38}$$

A far more accurate estimate of ε will be obtained from a 3D simulation in section 10.3.1.

In summary, a consideration of the thermal convection and conduction paths in a resistive divider indicates that this analysis will require correction factors to estimate the chamber temperature from the heater temperature. Fortunately, β and γ are small and $\varepsilon \approx 1$, and these can be determined quite accurately. As a result, we can estimate the chamber temperature from:

$$Tc = Th - \beta(Th - Ths) - \gamma(Th - Tamb) \qquad \textbf{Eq. 39}$$

Where *Th* is given by Eq. 37. Eq. 39 results from solving Eq. 26 and Eq. 28 for *Tc* and combining the individual solutions. Accurate values for β and γ can be found in Table 14. Nevertheless, the magnitude of β and γ is such that we expect robust thermal control.

We can visualize the heater as an electrical resistance composed of two resistances, one kept at *Th*, i.e. the temperature of the uniformly heated region, and one kept at *Th*s at the edge. Given the approximate linearity of the system we expect that the resistance heated at *Th* would account for ε times the total

resistance (R_T), and the resistance heated at *Ths* would comprise the remaining (1 - ε):

$$R_T = R_{Th} + R_{Ths} = \varepsilon R_T + (1-\varepsilon) R_T \qquad \textbf{Eq. 40}$$

Where R_{Th} and R_{Ths} are the resistances at *Th* and *Ths*, respectively. On the other hand, from Eq. 26 we know that *Tc* is determined for the most part by the relative contribution of *Th* and *Ths*:

$$Tc = Th(1-\beta) + \beta Ths \qquad \textbf{Eq. 41}$$

Consider an imaginary experiment in which the polymer structure is significantly thinned down. In such a situation the lateral thermal resistance, R_L, would increase and hence β would approach zero, as stated by Eq. 25, making $Tc \approx Th$. As a consequence of the increment in R_L, the lateral loss would be reduced, narrowing the cooler portion at the heater's edge, thereby reducing the temperature differences across the heater, driving ε to 1 and making $R_T \approx R_{Th}$. From this we speculate that ε and β are complementary and we can express this relation as:

$$\varepsilon \propto 1-\beta \qquad \textbf{Eq. 42}$$

10.2.7 TCR Measurement

The TCR and reference resistivity of the Al film were measured in 4-point mode by placing the devices on an aluminum heatsink (72.5 x 40 x 6.5 mm) atop a hotplate (Torrey Pines Scientific Echotherm™ HS40). Spring-loaded Au-coated pogo pins of 1 mm diameter (Interconnect Devices Inc.) soldered to a custom-designed PCB were used to contact the heater terminals without scratching the Al film. A very thin film of thermal paste (T630 THERM-A-GAP Dispensed Thermal Gel, Parker Chomerics) was applied at the chip-heatsink and heatsink-hotplate interfaces to ensure good thermal contact. It was verified through simulation that the temperature drop between the hotplate surface and the heater

at 100 ºC is negligible, and heating is highly isothermal, owing to the high conductivity of aluminum and Si. The hotplate heated the entire aluminum plate and chip to known temperatures with accuracy < ±1 ºC. The resistance was measured with a multimeter (HP-34401A, Hewlett Packard) in 4-point mode at 22, 40, 60, 80 and 100°C (on both a ramp-up and ramp-down) and again at 22°C to verify film stability. A pause of 20 min at each temperature were allowed for the hotplate to stabilize before taking a reading. This procedure yielded nine data points in total.

Matthew Reynolds built the test hardware for this measurement and performed the experiments along with Saul Caverhill-Godkewitsch. The author analyzed the experimental data and performed the calculations of section 10.4.1 to determine the TCR and reference resistivity.

10.2.8 IR Temperature Measurement

IR camera imaging was used to verify the uniformity and robustness of the design. Although the accuracy of this method is compromised by the uncertainty in surface emissivity, it is useful in showing temperature variations with great resolution even if the exact emissivity and temperature levels are not known.

A device with a U 1550 heater was imaged with an infrared camera (SC5600-M, FLIR Systems) sensitive in the mid-IR range (2.5–5.1 μm) and pre-calibrated by the manufacturer with a proprietary process. Details of the experimental setup can be found in Appendix C. Unfortunately; experimental constraints required us to place the chip in direct contact with the heatsink - without thermal paste. This is an extreme case of poorly controlled boundary conditions.

10.2.9 Fluorescence-based Temperature Measurement

As implemented by Ross *et al*. [23], fluorescence thermometry has been used to non-invasively measure in-chamber temperature in lab-on chip devices. Although such a method would not be suitable for inexpensive point of concern applications, the method is entirely suitable for confirming the absolute

temperature of the chamber over a range of applied currents. In this work the method of Ross *et al*. [23] was used to demonstrate that the average temperature of the chamber can be estimated accurately from electrical resistance under varying boundary conditions.

To perform this measurement the chamber of a U 1550 was filled with a 100 µM solution of Rhodamine-B in a buffer of 1xTBE. The fluorescence intensity of the solution was measured as the applied electrical current was gradually stepped up. The temperature in the chamber, Tc_F, was estimated from a fluorescence-intensity vs. temperature calibration curve corrected for ongoing photobleaching. Simultaneously, the temperature in the chamber, *Tc*, was calculated from the heater's resistance measured in 4-point mode (with 0.004 Ω precision) and the TCR of the Al film using Eq. 39. The input power was also calculated from the voltage and current of the 4-point measurement.

The temperature uniformity in the PCR chamber was also verified by imaging the fluorescence in the chamber. An LED with center wavelength of 465 nm was used as an excitation source and the image was taken with a CCD camera (MU900, Amscope) mounted on a microscope (Micromaster, Fisher). An absorbing color filter (wavelength cut at ~560 nm) was adapted to the microscope. The current was ramped up until reaching *Th* ≈ 40 ºC and then kept steady while electrical and optical signals were recorded. This procedure was repeated for successively higher temperatures at intervals of ~5 C. The fluorescence was scaled to account for any photobleaching measured (about 1% per hour.

These measurements were carried out by Tianchi Ma and Gordon Hall at the University of Waterloo under supervision of Dr. Chris Backhouse.

10.3 Simulation Results

10.3.1 Calculation of Correction Factors via 3D Simulation

In this section we calculate the correction factors that allow us estimate *Tc* from measured values of *Th*, *Ths* and *Tamb* using Eq. 37 and Eq. 39.

The three sets of data obtained for the system simulated with different values of *Ths* are shown in Figure 62. The lines fitted to each data set are indicated as a dashed line. The average slope of the lines is 17.39 ºC/Ω ± 0.0032 ºC/Ω. Note that *Tc* moves nearly along the same line regardless of changes in *Ths*, making the fitted lines appear overlapped. Therefore, to first order *Tc* could be estimated accurately from *R* without the need for measuring *Ths*.

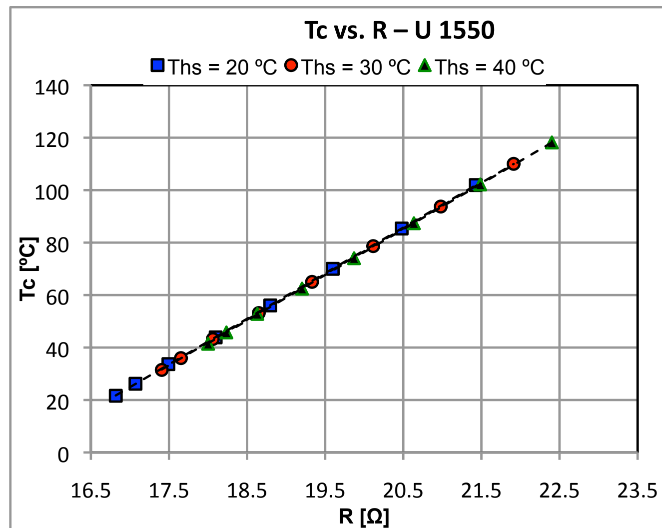

Figure 62. Average chamber temperature vs. resistance curves calculated by 3D simulation for U 1550. In the simulation the applied voltage is ramped from 1.5 to 12 V for three different values of *Ths*, causing *R* and *Tc* to increase. The plot shows the three sets of data corresponding to *Ths* = 20, 30, 40 ºC. A line is fitted to each data set (dashed lines) and these lines overlap on each other, indicating a very small sensitivity to changes in *Ths*.

A zoomed-in image of Figure 62 is shown in Figure 63. This zoom in reveals that although the deviation of the slope is negligible, there is a small offset caused by changes of *Ths*. Figure 62 shows that if a controller was capable of keeping the resistance constant, *Tc* would still vary by ~0.048 ºC by a change in *Ths* of 10 ºC (thereby giving $\beta = 0.0486$). This value agrees with that predicted from the 1D model (0.031), suggesting that the net lateral resistance in the real device is in the order of 410 K/W, as estimaged in secton 10.2.2. For the *Tamb* data the fitted lines offset by ~0.04 ºC by a 10 ºC change in *Tamb*, thereby giving $\gamma \approx 0.004$. Although this value is an order of magnitude higher than that predicted by the 1D

model (0.00054), it is still very small and confirms that variations in *Tamb* and airflow have a negligible effect on *Tc*.

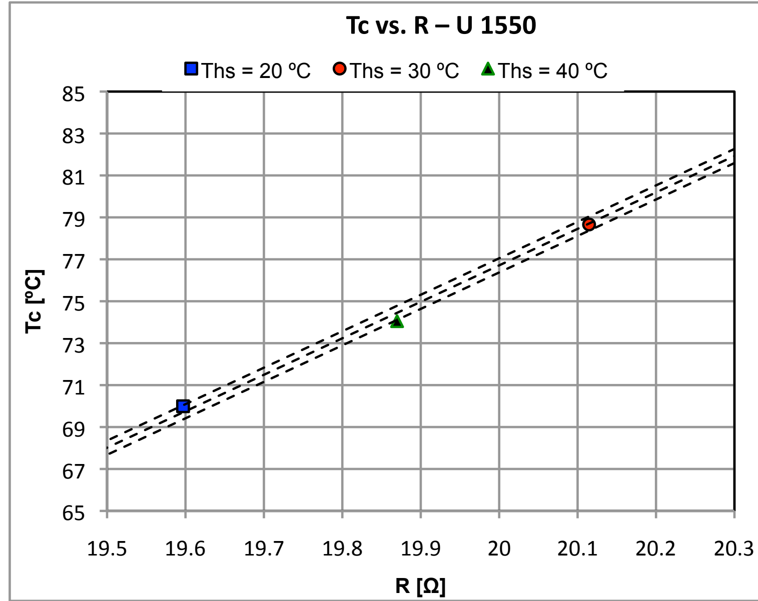

Figure 63. Zoomed-n image of the plot in Figure 62. If a controller keeps *R* constant, *Tc* would shift by 0.76 ºC with variations of 20 ºC in *Ths*.

The factor ε is calculated by comparing the TCR measured from the 3D simulation (in which the Al is at non-uniform temperature) to the TCR of the Al film measured experimentally from calibration (in which the Al is at uniform temperature). To calculate ε consider the fitted line for *Ths* = 30 ºC in Figure 62. The equation for this line is *Tc* = 17.393 *R* - 271.15. Solving for resistance gives *R* = 0.05749 *Tc* + 15.5896. The TCR of this line is the effective TCR (α_e), and is calculated by dividing the slope *m* = 0.05749 by the intercept *Ro*. Since we measure all TCR values at a reference temperature of 22 ºC, we first calculate *Ro* = 0.05749 x 22 + 15.5896 = 16.8545 Ω. Thus, the effective TCR is $\alpha_e = m/Ro$ = 3.41 x 10^{-3} K^{-1}. On the other hand, the TCR of the Al film obtained from calibration in the work of Chapter 8 and used in these simulations is α = 3.52 x 10^{-3} K^{-1}. Therefore, $\varepsilon = \alpha_e / \alpha$ = 0.9691. Repeating the calculation for the three lines in Figure 62 gives the average ε = 0.9693 ± 0.0013.

In order to verify that the correction factors are constant the full set of simulations was repeated using the electrical properties (α and ρ_o) and Al thickness (h) measured in the fabricated devices: $\alpha = 2.06 \times 10^{-3}$ K^{-1}, $\rho_o = 1.29 \times 10^{-7}$ Ω-m, h = 150 nm. The calculated β, γ and ε were averaged with those obtained above and the reuslting values are shown in Table 14. The number (indicated ±) after the average value is the variability introduced by changing the electrical properties and Al thickness in the simulation.

β	γ	ε
0.0486 ± 0.0028	0.00436 ± 0.0022	0.9625 ± 0.0010

Table 14. Correction factors determined from 3D simulation for U 1550. The parameters β and γ are defined in section 10.2.2 (Eq. 26 and Eq. 28, respectively). The parameter ε is defined in section 10.2.6.2.

By changing the values of α, ρ_o and h in the simulation, the parameter ε varied by approximately ± 0.1 %, which confirms that ε is essentially a constant. The factor β varied by ±5.8 %, suggesting a small dependence on the electrical properties and thickness of the Al film. A ~50 % uncertainty in γ, possibly introduced by numerical error, does not allow us to confirm whether γ is a constant, however it is clearly very small, which predicts that the system will be highly insensitive to variations in ambient temperature and airflow rate.

As expected, β and ε were approximately complementary consistently across the various simulations. Following Eq. 46 the value of β can be approximated as 1 – ε. Taking the analytical value for ε from Eq. 38 gives β = 1 - 0.938 = 0.062. Taking the simulation value for ε from Table 14 gives β = 1 - 0.9625 = 0.0375. The average error of these estimates with respect to the value obtained from simulation (β = 0.0486) is ± 25.2 %. Therefore a good estimate of β can be obtained without the need for complex 3D simulations from:

$$\beta \approx 1 - \varepsilon \qquad \textbf{Eq. 43}$$

These results confirm that the system is robust to variations of *Ths* and *Tamb*. The simulation of the system under different sets of conditions confirms that ε is constant and therefore can be used to estimate and control the chamber temperature with remarkable accuracy from the heater's resistance using Eq. 37 and Eq. 39. This ε is a general purpose result that is valid for this design (U 1550) for any TCR. If the TCR changes we would expect that the new value could simply be updated in Eq. 37. As long as fabrication parameters such as KMPR thicknesses are tightly controlled, the calculated ε will not vary from run to run or device to device. The simulation also confirmed that *Ths* has a minor impact on the accuracy of the measurement ant the *Tamb* term could be neglected.

10.3.2 Temperature Uniformity in 3D

Reaching an average chamber temperature of 95 ºC in the 3D model required the application of 10.62 V, with *Ths* = 30 ºC and *Tamb* = 22 ºC. The solution temperature field, displayed in Figure 64, predicts a uniformity of ± 1.25 ºC around an average of 95 ºC. This temperature field corresponds to the bottom of the chamber, where the worst-case non-uniformities were observed. These results confirm that the combination of thin polymer layers on a highly conductive substrate plus the extension of the heater result in high temperature uniformity within the chamber. Clearly, the uniformity at lower chamber temperatures would be proportionally better still.

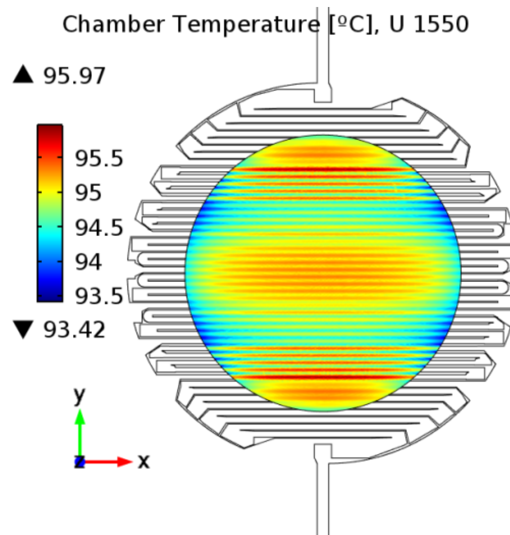

Figure 64. Temperature field at the bottom of the PCR chamber in U 1550, predicted by 3D simulation. Applying a voltage of 10.62 V gives an average chamber temperature of 95 ºC and a uniformity of ±1.25 ºC.

10.4 Experimental Results

An example of one of the fabricated devices is shown in Figure 65. For details of the fabrication process refer to Appendix A: Device Fabrication.

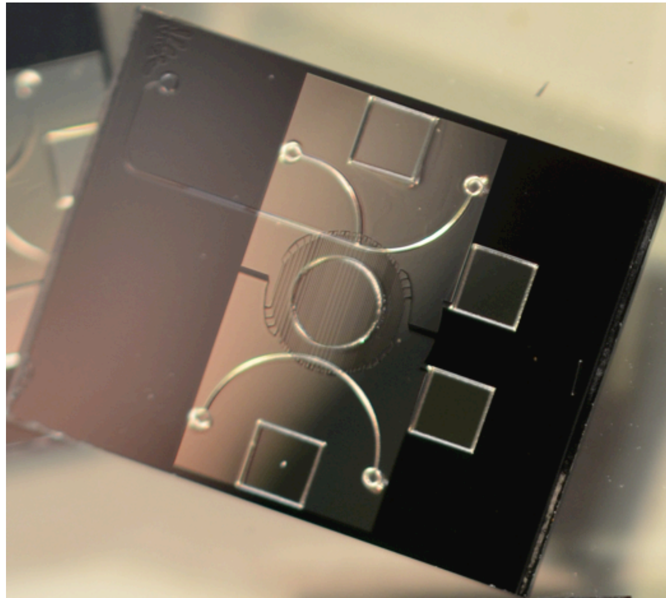

Figure 65. Photograph of the fabricated device.

In order to demonstrate the robustness of our thermal design we measured the TCR of the Al film in order to obtain an accurate estimate of the temperature in the PCR chamber from the heater's resistance. Then we performed infrared (IR) thermometry (preliminary work completed) and fluorescence-based thermometry (preliminary work completed, further work underway). The IR thermometry measurements confirmed that the spatial uniformity of the temperature was within the range expected from the design simulation. The fluorescence thermometry confirmed that the chamber temperature was in agreement with the temperature expected from simulation and from electrical measurement. This agreement, under varied operating conditions, confirms the robustness of the thermal design.

10.4.1 Determination of TCR

The TCR and resistivity of the Al film was measured on a NU 750 heater of the same batch as the U 1550 tested herein. The obtained resistance vs. temperature curve showed highly linear behavior. Fitting a line to the calibration data yields $R = 0.0332\,T + 15.416$ with a correlation of 0.9961. The TCR (α) depends on the slope of the calibration curve m and the resistance measured at reference temperature R_o:

$$\alpha = \frac{m}{R_0} \qquad \textbf{Eq. 44}$$

From the calibration curve, $R_o = 16.146$ at $To = 22$ ºC, yielding $\alpha = 2.06 \times 10^{-3}\ K^{-1}$. Calibrating other chips of the same batch yielded an average TCR of $2.07 \pm 0.019 \times 10^{-3}\ K^{-1}$. A consistent TCR of $2.06 \pm 0.05 \times 10^{-3}\ K^{-1}$ was obtained by the group of Dr. Chris Backhouse at the University of Waterloo from calibrating a U 1550 of the same batch as the above chips using an oven-based method.

The fabricated and simulated heaters are nearly identical, except by their thickness. Thus, to approximate the resistivity ρ_o of the fabricated heater, we visualize the heaters as simple rectangular-section resistors with the same $K = L/w$ ratio but with thicknesses h and hs. Accordingly, the reference resistance of the

fabricated and simulated heater would be $R_o = \rho_o K/h$ and $Rs_o = \rho s_o K/hs$, respectively. Combining and solving for ρ_o yields:

$$\rho_0 = \rho s_0 \frac{R_0 h}{Rs_0 hs} \qquad \textbf{Eq. 45}$$

The Al thickness measured in the fabricated devices was $h = 150 \pm 10$ nm and the thickness used in the simulation was $hs = 100$ nm. With this the resistivity of the Al film in this batch is $\rho_o = 2.93\ \rho s_o$, where $\rho s_o = 4.39 \times 10^{-8}$ Ω-m. The geometric factor G of the heater is $R_o/\rho_o = 1.25 \times 10^{8}$ m^{-1}.

10.4.2 IR Temperature Measurement

Figure 66(a) displays the captured thermograph of a U 1550 driven by 3.34 ± 0.01 W power. The temperature in the image is estimated by the camera software with an assumed value for the emissivity of 0.9. Figure 67(b) presents the temperature sampled along a horizontal line crossing through the heated region in Figure 66(a), with indices of 70–510 corresponding to the chamber. These plots show periodic apparent temperature variations (a ripple) of up to ~1.5 ºC that match the pattern of the designed heater tracks. Since these are present even with the heater off and since the heater tracks appear cooler than the nearby regions, such variations are thought to arise primarily from emissivity fluctuations from the areas with and without aluminum. An explanation of these effects and the device imaged with the heater off are presented in Appendix B: Details of the IR Imaging Experiments.

There appears to be an annulus of a higher temperature around the chamber that reaches ~6 ºC above a 49 ºC baseline. In Figure 66(b) the annulus corresponds to indices 1–70 and 510–566. We believe that this annulus results from differences in emissivity as well as from the KMPR structure being thicker outside the chamber (85 µm vs. 40 µm). These artifacts and associated image distortion are discussed in more detail in Appendix B: Details of the IR Imaging Experiments.

Aside from these artifacts, the long-range variation in intensity within the chamber suggests a real temperature variation of ±1 ºC. This is consistent with the

simulation results in section 10.3.2. The image also demonstrates that the use of thin polymer layers atop a highly conductive substrate results in negligible heating outside the heater's perimeter. This can be appreciated from the sharp temperature transition near the heater edge (indices 30 and 560 in Figure 66(b)).

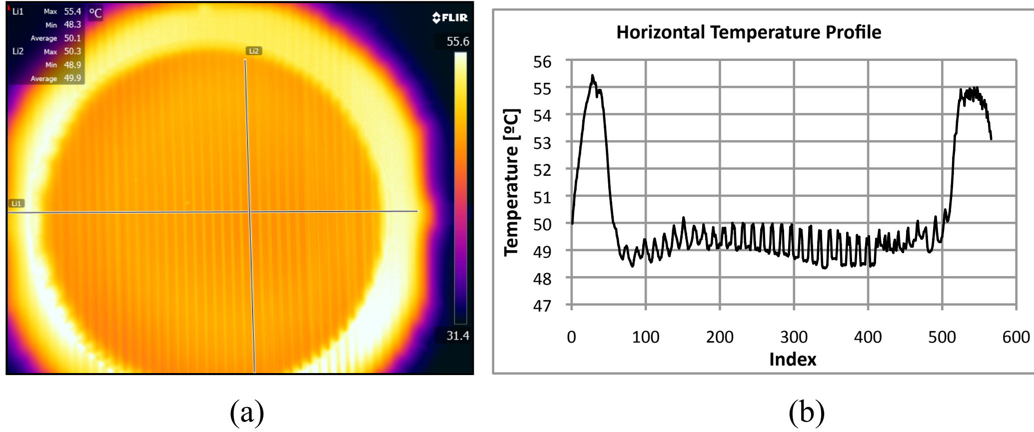

(a) (b)

Figure 66. (a) Infrared image of U 1550 using driven by 3.34 ± 0.01 W power. (b) Temperature sampled along a horizontal line crossing through the heater in (a).

The captured image gives reasonably accurate information about the temperature variation across the chamber. However the uncertainty in the emissivity causes a large error in the absolute temperatures detected by the instrument. As shown in section 10.2.6.2 the actual chamber temperature can be estimated from the heater's resistance and TCR using Eq. 37 and Eq. 39.

The resistance of the heater changed from Ro = 32.82 ± 0.01 Ω at room temperature (To = 22.7 ± 0.38 ºC) to Re = 37.0 ± 0.09 Ω at the applied power (3.34 ± 0.01 W). The measured TCR is $\alpha = 2.07 \pm 0.019 \times 10^{-3}\ K^{-1}$, and ε = 0.9625 and β = *0*.0486. The *Tamb* term is neglected. With these parameters the temperature calculated from Eq. 39 is 86.48 ºC. This estimation has an error of ± 0.4 ºC due to variations in To and ± 0.6 ºC due to the TCR uncertainty. The maximum observed increment in heatsink temperature was 3 ºC, which causes an error of ±0.1 ºC.

The error of the IR camera due to the uncertainty in emissivity can be calculated from the Stefan-Boltzmann's law with a correction for a non-unity emissivity [11]:

$$J = \varepsilon \sigma T^4 \qquad \textbf{Eq. 46}$$

Where J is the radiated power, $\boldsymbol{\varepsilon}$ is the surface emissivity, σ is the Stefan-Boltzmann constant and T is the absolute temperature (in degrees Kelvin). The temperature calculated by the instrument, Tc, is calculated from an assumed emissivity, $\boldsymbol{\varepsilon}_A$. Given the above relationship, the real emissivity $\boldsymbol{\varepsilon}_R$ is given by:

$$\varepsilon_R = \varepsilon_A \frac{Tc^4}{Tr^4} \qquad \textbf{Eq. 47}$$

Where Tr and $\boldsymbol{\varepsilon}_R$ are the real temperature and real emissivity, respectively. The temperature calculated from the heater's resistance is accurate (86.48 ± 0.6 ºC) and therefore we take this value as Tr. The temperature calculated by the camera (within the chamber area) is 49 ºC and $\boldsymbol{\varepsilon}_A$ is the emissivity set in the instrument (0.9). These parameters yield a real emissivity $\boldsymbol{\varepsilon}_R = 0.58 \pm 0.004$. Substituting $\boldsymbol{\varepsilon}_A$ and $\boldsymbol{\varepsilon}_R$ in Eq. 47 we obtain:

$$Tr = 1.116\ Tc \qquad \textbf{Eq. 48}$$

Figure 67 shows the data of Figure 66(b) corrected for the real emissivity using Eq. 48. The temperatures within the chamber area are centered at ~85 ºC as would be expected. Note that since the absolute temperature (in Kelvin) did not change substantially, the temperature uniformity is essentially unchanged at about ± 1 ºC. Recall that we assess temperature uniformity based on the chamber-wide temperature variation rather thatn on the height of the apparent ripple, which is an optical artifact (explained in Appendix B: Details of the IR Imaging Experiments).

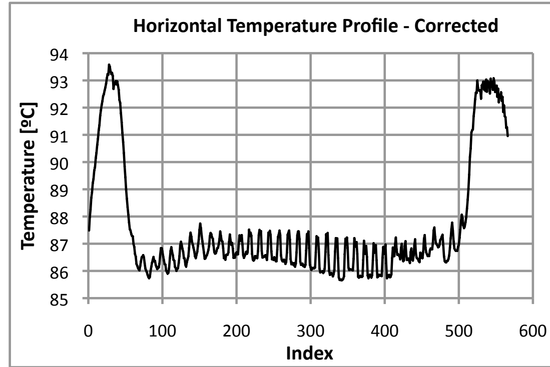

Figure 67. Temperature corrected for the real emissivity in U 1550.

Although SU-8 (a similar epoxy-based photopolymer) has been reported to have an emissivity of 0.85–0.95, the substantially lower value estimated here (0.59) is not surprising since we observed that KMPR is semi-transparent in the wavelength range of the camera and roughly 50–60 % of the area under the KMPR surface is covered by low-emissivity Al.

The robustness of this thermal design hinges upon there being reasonably good thermal contact to the heat sink. In order to establish how good the thermal contact needs to be to maintain acceptable temperature uniformity, a 3D simulation of U 1550 was carried out using $\alpha = 2.07 \pm 0.019 \times 10^{-3}$ K^{-1}, $\rho_o = 1.27 \pm 0.022 \times 10^{-7}$ Ω-m, *Ths* = 22 ºC, and Al thickness *h* = 150 nm. In order to emulate the effect of poor thermal contact, a 1 µm thick air layer was included in the model between the chip and the heatsink. The thickness of this layer was chosen based on the average surface roughness ($R_a = 1.01 \pm 0.23$ µm) that we have measured in our in-house metal milling process. It is difficult to establish an exact uncertainty for thermal contact since it depends not only on surface roughness but also on the contact pressure and other factors. Moreover, the contact is typically non-uniform [24]. However, the simulation shows that for the power levels used here the uniformity is still acceptable (± 1.4 ºC). However, a simulation with a thicker air layer (by 50%) caused the temperature to increase by ~5 ºC and the uniformity to deteriorate to ± 2.2 ºC.

IR thermometry has therefore confirmed that this design produces excellent temperature uniformity even under challenging conditions of thermal contact. However, the method was not able to accurately corroborate the absolute temperature of the chamber (only the spatial uniformity).

10.4.3 Fluorescence-based Temperature Measurement

The temperature in the chamber calculated from the heater's resistance agreed with that determined from simulation and from temperature-dependent fluorescence. Successive runs at temperatures less than 45 ºC showed excellent agreement between the fluorescence and electrical temperature measurements, which confirms the validity of the present robust design.

From simulations we expect that Tc can be known to within ± 0.73 ºC due to a TCR variation of 1 %, with the resistance changing from 32.81 Ω at 22 ºC to 34.31 at 45 ºC within ± 0.05 Ω error (calculated from $R = 0.0651\ Tc + 31.378$). In the experiment the current was ramped up until reaching $Tc \approx 40$ ºC. Thereafter the current was kept constant, but Tc drifted up slowly by ~3 ºC due to the heatsink warming up. At all times Tc and Tc_F were equal to within ± 0.3 ºC regardless of the fluctuating heatsink temperature level, which confirms that the system is robust in terms of temperature measurement accuracy when the resistance-based method is used. Successive runs showed the same Tc - Tc_F differences until bubbles formed at 45–70 ºC and altered the fluorescence intensities.

As established in section 10.2.6.1 the temperature can be calculated from power if the heatsink temperature is known with $Tc = m\ H_T + Ths$. For the U 1550 the value of m predicted by simulation is 12.54 ± 0.01 ºC/W. The temperature calculated from this relation using the measured power agreed to within 1.3 ºC with the temperature calculated from resistance until the heatsink started to warm up significantly at ~40 ºC, causing these two temperatures to diverge significantly. The 1.3 ºC error is thought to arise primarily from the thermal contact resistance at the Si-Al interface, which in simulation is assumed to be zero.

From these results we expect the Tc_F measured by fluorescence and the Tc measured from resistance to always be similarly accurate. The temperature measured from power, however, depends on the quality of the Si-Al thermal interface, i.e. the thermal contact resistance, which is very difficult to control. Moreover, the power-based method relies on how accurately the heatsink temperature can be measured near the bottom of the chip. Therefore, a robust system can be effectively implemented by using the temperature measured from resistance or fluorescence as a feedback for a controller.

The chamber filled with the Rhodamine-B solution was imaged at an average temperature of ~40 ºC, as estimated from the fluorescence intensity calibration curve. Difficulties of low and non-uniform illumination produced distortion and a significant amount of noise in the image. By subtracting an image taken at room temperature and performing a running average we were able to correct for these artifacts and extract the true temperature profile of the chamber. This profile showed a uniformity of ± 0.65 C, which is in agreement with the 3D simulation and IR camera results.

10.4.4 Measurement Error

Table 15 summarizes the main sources of error in the measurement of the chamber temperature. From Eq. 37 and Eq. 39 we estimate that a ± 1 % variation in the TCR will cause an error of ± 0.73 ºC at denaturation (To = 22 ºC, Ro = 32.82 Ω, Re = 37.85 Ω, $\alpha = 2.07 \times 10^{-3}$ K^{-1}, ε = 0.9625, β = 0.0486, Ths = 22 ºC, yielding average values Th = 98.92 ºC and Tc = 95.18 ºC for the U 1550 heater). From the calculated value of β = 0.0486, a 10 ºC variation in heatsink temperature may cause an error of approximately ± 0.5 ºC at denaturation. In addition, the fluorescence experiments indicate that electrical measurements are accurate within ± 0.3 ºC at Tc = 40 ºC. Assuming a linear relationship, this error may reach ± 0.7 ºC at Tc = 95 ºC. The non-uniformity in the chamber temperature could also be considered part of the measurement error. 3D simulations predict that Tc will be uniform within ±1.25 ºC at Tc = 95 ºC. Therefore, in a worst-case scenario the

sum of these errors would result in ±3.08 ºC uncertainty in the estimation of *Tc* at denaturation. This uncertainty is significant and suggests that these sources of error must be carefully controlled. The heatsink temperature, in particular, may vary by more than 10 ºC if the device is operated in extreme climate conditions or if a small heatsink is used. However the heatsink temperature, or directly the substrate temperature, can be monitored to enable the controller to compensate for these variations. This leaves the TCR being the most important parameter to control at the fabrication level. Adjusting the value of the correction factors ε and β according to experimental data could reduce the error in electrical measurements. This adjustment therefore relies on improving the accuracy of the fluorescence measurements or using another more accurate non-invasive thermometry method. Using an edge-compensated design can further reduce the uncertainty due to temperature non-uniformities. The NU 750 and NU 1450, for example, have a uniformity of ± 0.43 ºC and ±0.97 ºC, respectively. This uniformity values express the total temperature range around 95 ºC. However histograms of temperature (see Figure 49) reveal that the volume of water in the chamber that is actually exposed to the maximum and minimum (± 0.43 ºC and ± 0.97 ºC) is negligible, and actually > 99 % of the temperatures in the chamber volume is within a 1 ºC band. Therefore ± 0.5 ºC could be considered the standard uniformity of NU designs.

Source of Variability	**Estimated Erro in *Tc* [ºC]**
TCR variation by 1 %	± 0.73
Variation in heatsink temperature by 10 ºC	± 0.49
Variation in ambient temperature by 10 ºC	± 0.044
Experimental error with respect to fluorescence thermometry measurements	± 0.70
Temperature non-uniformity	± 1.25
Variation of Al film thickness	to be determined
Variation of thickness of KMPR layers	to be determined
Variation of thickness of KMPR layers	to be determined
Instrumetation and resistance measurements error	to be determined
Total of known errors	**± 3.21**

Table 15. Estimated error in chamber temperature measurements due to different sources of variability, estimated for the U 1550 design at *Tc* = 95 ºC, *Ths* = 20–30 ºC and *Tamb* = 20 ºC.

10.5 Conclusion

We have presented an integrated lab-on-chip heater design for which we have been able to show the chamber temperature is the same (± 0.65 ºC) whether measured electrically or optically. In addition, to first order, the chamber temperature is not affected by any external variables except the (easily controlled for) heatsink temperature. The close relation between heater/sensor and chamber is independent of variables at the chip-to-world interface and as a result, if the temperature coefficient of resistivity (TCR) of the metal film is known within ± 1%, the chamber temperature can be estimated to within an uncertainty of ± 0.73 ºC - an uncertainty that is sufficiently small to enable many molecular biology protocols. Together, these enable direct and inexpensive electrical control of the device temperature. As long as the TCR and other fabrication parameters are tightly controlled to ensure repeatable devices, the need for per-device-level calibration can be removed. In closed-loop control, such repeatable devices can compensate for any remaining effect of fluctuations in external variables, becoming highly robust. Reliable operation can then be expected regardless of changing airflow rate or ambient temperature, as well as packaging variability in aspects such as thermal paste compound and thickness, and chip-to-world gantry/interface materials and configuration.

By restricting the vast majority of the generated heat to flow vertically the device was turned into a 1D system that can be effectively represented using a resistive divider model. This model allows for a good understanding of the underlying mechanisms of the system and shows that the major determinant of the robustness is the β factor. This is a small enough correction factor that could be neglected, even for the most demanding of the PCR stages (annealing, near 50 ºC). If this correction is made then we might expect to have a temperature uncertainty within ± 1 ºC.

We have validated our designs and devices by showing a good agreement between models, simulations and an experimental measurement of temperature

via three independent techniques. This shows that we can accurately control the chamber temperature via electrical signals in a way that is largely independent of external conditions. We demonstrated this without run-time calibrations.

A simple mechanism to explain the edge effects led to surprisingly accurate estimates of the correction factors, suggesting that this mechanism has predictive value. This mechanism predicts that the edge effects will scale with the length of the heater perimeter, suggesting that:

$$\beta \propto \frac{2\pi r}{\pi r^2} \qquad \textbf{Eq. 49}$$

This predicts that, for half the radius (where the power consumption is about 1 W and where several chambers would easily fit on a standard CMOS die), we would expect that this parameter would be twice as large. Since this factor seems to be intrinsically related to edge effects it would appear to suggest that edge compensation, i.e. higher power input at the edges, as designed for non-uniform power density heaters (NU 750 and NU 1450) could reduce the sensitivity of the devices to external parameters.

Recently we observed that the absorption of water into KMPR softens the polymer, leading to wrinkling of the Al film (for details refer to Appendix C: Moisture Sensitivity). The phenomenon appears to arise due to a combination of moisture, elevated temperatures and residual stress of the aluminum. This moisture sensitivity and wrinkling of the Al film must be controlled to minimize changes in the electrical properties of the film, which will ensure robust thermal control. In the past we successfully tested Al/KMPR structures in the presence of both moisture and temperatures up to 80 ºC (work of Chapter 8). However in the recently developed devices the Al/KMPR structure withstood moisture and heat only at temperatures below 50 ºC. This may be a reflection of the more challenging structure or a change in the process parameters. Therefore, although the system was shown to be thermally robust, it would not have sufficient structural stability to run PCR under the present processing conditions. We expect

that by adjusting our fabrication protocol this moisture sensitivity would no longer be an issue. With functional microchannels, the PCR chamber could be pressurized to suppress bubble formation. In summary then, although the present protocol leads to KMPR that is not moisture tolerant at high temperatures, the design has been shown to be thermally robust in a manner not previously reported. Further work will use a more moisture-tolerant fabrication process or impermeable coatings, and this is expected to enable low cost PCR that could be fully integrated onto CMOS devices.

To our knowledge, this is the first demonstration of a thermally robust, CMOS-compatible design for thermal control without the need for device-level calibration - a key requirement for any inexpensive point-of-care diagnostic.

A detailed manuscript for this work will be submitted for publication.

10.6 Appendix A: Device Fabrication

Devices were fabricated on test grade 4” Si substrates. The silicon was cleaned and prepared for use by immersion in a freshly prepared solution of 3:1 H_2SO_4:H_2O_2 for 15 min prior to being rinsed with deionized water and dried using N_2. The substrates were then dehydrated on a hotplate at 150 ^oC for 15 min. To form layer 1 of the device, KMPR 1025 (Microchem Corp) was spin-coated onto the substrates (4000 RPM, 60 s, 10 s ramp) to a thickness of approximately 20 μm. The substrates were then soft-baked for 10 min at 100 degrees. The KMPR was blanket-exposed with a UV dose of 1.33 J/cm^2 (calculated using the intensity of the 365 nm line) to activate the majority of the photoactive compounds in the resist. Following exposure, the substrates were placed on a hotplate at 150 degrees for 1 hour to crosslink the KMPR and provide a stable surface on which the heaters could be formed.

Previously we reported on the patterning of Al heaters on KMPR by standard lithography [22]. In this work, however, the power density profile produced by the

heaters is highly dependent on the width of the metal tracks. Therefore, lift-off was used to avoid undercut and respect the designed shape of the tracks.

A 50 nm thin Cr film was sputtered (300 W, magnetron sputtering) onto the crosslinked KMPR using an Ar deposition pressure of 8.5 mTorr to reduce film stress. This film served to protect the KMPR during the lift-off process. The lift-off resist used in our process was HPR 504 positive photoresist. A 1.25 μm thick film of the resist was patterned on top of the Cr film to form the heater shapes. Following development, the newly exposed Cr was etched away to allow the heaters to be deposited directly onto the KMPR. Once etching was completed, a Al film was deposited by sputtering (300 W, 7 mTorr Ar), aiming for 100 nm thickness.

Lift-off was performed by sonicating the substrates in acetone to remove the remaining 504 resist (and the Al deposited on top of the resist). Lift-off typically required between 5 and 10 min to fully remove the excess Al. Once lift-off was complete (and verified using an optical microscope), the remaining Cr on the substrate was stripped off to leave only the heaters remaining on top of the KMPR film.

Once the heaters were successfully formed, the KMPR layer 2 was spin-coated (4000 RPM, 60 s) on top. The KMPR was soft-baked at 100 ºC for 10 min following spinning. This layer of KMPR was then patterned by contact lithography, with the majority of the substrate being exposed to UV light (same dose as previously), except the outer 0.5 cm of the substrate (the edge bead) and the KMPR above the heater connections. The KMPR was post-exposure baked at 100 ºC for 5 min to cross-link the KMPR, but was not yet developed.

Following the post-exposure bake (PEB), the KMPR layer 3 was spin-coated (4000 RPM, 60 s) onto the substrate, and a 10 minute soft-bake at 100 ^{o}C was again performed. This layer was then patterned to define the PCR chamber and other fluidic channels (0.60 J/cm^2). A PEB was performed (5 min, 100 ºC) following exposure to cross-link the KMPR. The substrates were then developed

in SU-8 developer for 8 min (visual endpoint) and baked for 30 min at 100 ºC to increase the cross-linking level of the KMPR and stabilize its mechanical properties [10].

The channel roof (layer 4) was fabricated on a separate carrier wafer. The carrier wafers were 4" square Borofloat® substrates coated with a 5 µm thick layer of PDMS (Sylgard 184, Dow Corning) acting as a low-adhesion layer for the bonding process. The PDMS was prepared by mixing the base and curing agent in a 10:1 ratio, spin coating at 3000 RPM for 60 s, and curing the film at 120 ^{o}C for 1 hr. A 0.5 cm wide, 10 nm thick gold border was sputtered onto the PDMS in order to reduce de-wetting effects. KMPR was spun onto the PDMS film at 4000 RPM for 60 s to produce a 25 µm thick film, and was soft-baked at 100 ºC for 10 min. The KMPR was patterned as before, but with a dose of 0.90 J/cm^2, and a PEB was performed on a ramp from 50 to 100 ºC along 40 min prior to development in MF-319.

Bonding of layer 4 was performed using a hot embosser (Jenoptik HEX02), with a force of 10 kN at 100 ºC for 15 min. The glass carrier wafer was carefully released using a scalpel to apply pressure between the substrates, and allowing the KMPR to release from the PDMS. The devices were diced in a diamond-tipped dicing saw (Diamond Touch Technology Inc.).

10.7 Appendix B: Details of the IR Imaging Experiments

The fabricated U 1550 was imaged using the FLIR SC5600-M infrared camera with an attached microscope lens. The camera's cooled sensor is sensitive to wavelengths between 2.5 and 5.1 µm, and is factory-calibrated with a FLIR's proprietary process called CNUC [25]. With this calibration the camera is accurate within ± 1%, assuming that the emissivity is known[3]. The instrument computes surface temperature from the radiated power and the emissivity using Stefan-Boltzmann's law [3] ($J = \varepsilon \sigma T^4$) [11]).

The device was imaged with the PCR chamber open to air. As confirmed by simulation, with the chamber containing air the system is expected to reach the same (within 0.3 ºC) temperatures as it would if it contained water. The device was affixed without thermal paste to a heatsink with an unpolished (milled) surface with average roughness, R_a = 1.01 ± 0.23 µm. The chip was held in place by spring-loaded pogo pins pressing on it far from the heater. The heatsink in turn was attached to a large aluminum box to improve heat dissipation. Joule heating was induced by applying a regulated DC current, and resistance was measured in 4-point mode throughout the test. The experiment was carried out in a room with uncontrolled temperature and the chip was not protected from ambient air drafts.

Our devices are built from a variety of materials (Si, Al, KMPR), and the KMPR was observed to be partially transparent in the IR range of the camera. Al has a very low emissivity (~0.06 [16]) while the emissivity of KMPR has not been reported, but could be close to that of SU-8 (0.85—0.95 [26], [27]), since this is the epoxy-based resist most similar to KMPR. Since this experiment was meant to be qualitative we set up in the instrument a generic value of emissivity of 0.9.

Due to the radical differences in emissivity across the heated region, as well as the partial IR transparency of KMPR, an apparent temperature ripple is visible even when the heater is off, as shown in Figure 68.

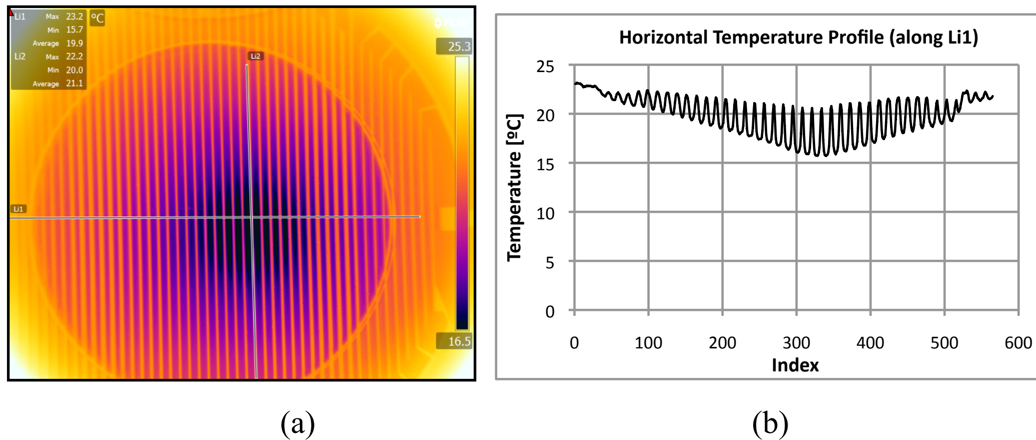

(a) (b)

Figure 68. (a) Infrared image of a U 1550. The image was taken with no power applied. (b) Temperature sampled along a horizontal line crossing through the heater in (a).

In the image of the powered chip (Figure 66) there appears to be an annulus of a hotter temperature outside the chamber. We hypothesize that each KMPR layer contributes to the total emission, and hence the heated areas outside the chamber, where the KMPR is 85 µm thick radiate higher power than in the chamber area, where the total KMPR thickness is 40 µm. The increased emission intensity outside the chamber is then translated by the IR camera as a higher temperature. Simulation of the empty chip showed that these areas should not be at higher temperature than the chamber, supporting this hypothesis. Notice that even in the unpowered chip (Figure 68) the areas outside the chamber appear to be hotter.

In the images of the powered chip (Figure 66) and the unpowered chip (Figure 68) the heater tracks appear to be cooler than the gaps. Following the same reasoning, we speculate that the total emission in the gaps is higher than on the tracks because the KMPR in the gaps (in the chamber area) is 40 µm thick (layer 1 + layer 2), while above the tracks the KMPR is 20 µm thick (layer 2 only), and Al contributes little to the total emission (its emissivity is ~0.06 [16]). The conversion of emmitted power into temperature, therefore, results in the tracks looking cooler than the gaps, which originates the apparent ripple.

10.8 Appendix C: Moisture Sensitivity

The operation of the devices in a dry environment did not produce any damage to the Al film, except for that caused by electromigration (reported in section 9.4.6.1). However we noted that heating the devices in a moist environment leads to wrinkling of the Al film. Matthew Reynolds first observed this wrinkling when he calibrated the devices in a waterbath. In our standard calibration protocol the devices are enclosed in a thick plastic bag and then immersed in the water. The automated calibration system then ramps the temperature from 20 to 80 ºC, in steps of 20 ºC, along ~ 2.5 hr. The resistance vs. temperature curves obtained by Matthew were far from linear and microscope inspection revealed the formation of labyrinth-like wrinkles across the Al film. The water diffused through the bag seemed to be responsible for this wrinkling. In view of this damage we moved to

a hotplate calibration method (with the chip exposed to air), which preserved the integrity of the film.

The aluminum always wrinkled in our recent attempts to calibrate the devices (made with the new process) in the waterbath. In order to confirm the relation between water and the wrinkling phenomenon a hard-baked chip was placed in a bag that contained a few drops of water. The bag was then immersed in the waterbath for 2 hr at 80 ºC. The water in direct contact with KMPR caused severe wrinkling across the Al film, including those areas not covered by KMPR (i.e. contact pads). The wrinkles were 2–5 times taller than those of chips hard-baked at the same temperature (180 ºC) placed in a dry bag. It is believed that the absorption of water into KMPR softens the material to a point that the compressive residual stress of the Al film overcomes the mechanical strength of the polymer, which corrugates the metal. Baking waterbath-tested chips on a hotplate (at ~100 ºC for 5 min) reduced the height of the wrinkles by 50–80 %. This reversible nature of the wrinkles suggests that a compressive stress results from swelling of the KMPR, contributing to the total stress over the aluminum. The evaporation of water, therefore, releases part of the stress and smoothes out the Al film.

The performance of the heater may be affected by changes in the thermal conductivity of KMPR induced by the intake of water, whose conductivity is ~0.67 W/m-K. Depending on how much water is absorbed into KMPR, its thermal conductivity may increase from the expected value (0.2 W/m-K), reducing the lateral thermal resistance, R_L, and hence increasing edge cooling effects. If the conductivity of KMPR was increased by a factor of two the value of β would also duplicate. However, even with such a large increase this factor is still very small and hence the robustness of the system would not be affected significantly. The most concerning effect of the wrinkling are the variations in the electrical resistivity and TCR of the film. Such variations may lead to loss of temperature uniformity since the power at each segment of the heater tracks is

determined by the square of the current, which in turn depends on the resistivity. A non-uniform distribution of resistivity, therefore, will distort the power density profile of the heater leading to poor temperature uniformity. On the other hand, if the TCR shifts the electrical measurement of temperature will lose accuracy as it relies on repeatable TCR values. For these reasons the wrinkling of the Al film must be controlled in order to ensure robust thermal control.

In order to investigate how fast water absorption occurs and how the current affects the wrinkling, David Sloan prepared a system to test the heaters in wet conditions. In this system a gantry keeps a column of water on top of the heater, filling the PCR chamber (the polypropylene membrane is not included in the setup). The controller initially sets a temperature of 85 ºC (corresponding to ~19.4 Ω) and keeps the resistance constant by adjusting the current. In the experiment the heater, videotaped under the microscope, did not show clear signs of wrinkling after 3 min. However the measured power started to decrease exponentially as soon as the experiment started. Over the period of 3 min the power decayed by 19.6 % (from 1.212 to 0.947 W), indicating that the actual resistance of the heater had increased in similar proportion. By the end of the test (116.7 min) the power had decayed by 83.5 % (from 1.212 to 0.2 W), corresponding to a temperature of ~ 54 ºC. The resistance measured with a DMM after the experiment was ~200 Ω, about 11.7 times higher than the original value at room temperature. The Al surface was severely wrinkled. The wrinkling does not seem to be related to the current since wrinkles also appeared in unheated areas in contact with water. Footprints of the O-rings used to seal the column of water around the chamber were left on the KMPR, which demonstrates the softening effect of water. Clearly, a moisture-resistant KMPR is needed to maintain stable electrical properties and hence enable robust temperature measurement and control.

Although the current fabrication process leads to KMPR that is not moisture-tolerant at high temperatures, the group of Dr. Chris Backhouse at the University

of Waterloo was able to demonstrate robust thermal control by operating the system at low temperatures. In their fluorescence thermometry experiments (discussed in sections 10.2.9 and 10.4.3 an aqueous solution of Rhodamine-B was heated in the PCR chamber up to a maximum of ~ 45 ºC. The electrical temperature measurement was stable and tracked the optical measurement, despite heatsink temperature variations, in successive experiments of ~ 4.5 min each. No wrinkling or irreversible changes in resistance were detected, suggesting that there is a threshold of temperature under which the intake of water and damage to the Al film are negligible.

In the work of Chapter 8 we were able to produce a moisture-resistant KMPR. In that work the patterned Al heaters were calibrated six times in the waterbath (for 11 hr effective time), following the same protocol as in our present experiments. No discernible wrinkling was detected under the microscope and the resistance was highly stable. A key characteristic of the KMPR produced at that time was its relatively low surface energy. With a contact angle of ~ 80º (see section 7.3.3) the KMPR was close to hydrophobic, to the point that water could hardly fill up 50 x 100 µm cross-section KMPR channels by capillarity. Understanding the tradeoffs between the variables that determine the surface energy, including the crosslinking level and solvent content of the polymer, will enable us to control the wettability and moisture resistance of KMPR. Note that in Chapter 8 (section 8.4.1) an irreversible wrinkling of the Al film is reported. However that wrinkling appeared during the fabrication process in dry conditions (during an oven bake), not in the waterbath. A hard bake of 130 ºC for 30 min prevented that wrinkling thereafter. Other researchers have also produced moisture-tolerant KMPR [28]. Blanco *et al.* [28] sputtered and patterned Al films on KMPR and SU-8 structures built onto an Al-coated Si substrate. The structures were exposed to a relative humidity of 95 %, maintaining a temperature of 30 ºC. After one day under such conditions KMPR showed superior adhesion to Al and the structures did not show significant swelling or other kind of damage. No wrinkling of the Al film on top of KMPR was reported. After three days the polymer became more elastic, as

detected by the shear tool used to measure adhesion strength (the exact amount of change in elasticity was not reported). To our knowledge other Al/KMPR structures exposed to moisture at temperatures higher than 30 ºC have not been presented.

The old fabrication process used in the work of Chapter 8 to produce the heater chips is summarized in Table 16 (data verified in the corresponding paper [22]). The new process used to fabricate the devices presented in chapters 9 and 10 is summarized in Table 17 (data verified in the thesis of Matthew Reynolds). The major differences between the two processes are listed in Table 18.

Substrate	1.1 mm thick, 4” x 4” borosilicate glass
KMPR layer 1	
Spin-coat	50 µm, 1000 rpm for 60 s
Soft-bake	105 ºC for 20 min
Exposure	1.00 J/cm^2 365 nm UV. Blanket-exposed.
Post-bake	105 ºC for 3 min
Hard-bake	130 ºC for 30 min
Metal deposition	
Al sputtering	210–240 ± 13 nm. 1.4 µTorr base pressure, 7 mTorr Ar dep. pressure, 300 W.
Al Patterning	
Al lithography	3 µm thick HPR-504 positive photoresist, bake, expose to define heater, develop, Al etch, resist stripping in acetone for 10 s.

Table 16. Old Al/KMPR fabrication processes used in the work of Chapter 8 (section 8.2). The heater chips were fabricated by Luis Gutierrez-Rivera and tested by the author.

In both processes the Al film deposition conditions were similar and hence the stress should remain approximately the same (~70 MPa, compressive, measured after deposition). The wrinkling, therefore, could be attributed to a softer KMPR. Higher baking temperatures increase the crosslinking level of the polymer, hardening the material and increasing its glass transition temperature, T_g, (as noted in the work of Chapter 8). Higher crosslinking levels also reduce the wettability of the polymer (as noted in the work of Chapter 7). In recent experiments performed by Matthew Reynolds we confirmed that hard-baking the KMPR at higher temperatures increases the crosslinking level, resulting in significantly less wrinkling. A chip whose layer 1 was baked at 120 ºC placed in a

dry bag in the waterbath at 80 ºC for 2 hr experienced severe wrinkling, and its resistance increased by ~50 % with respect to that measured before the experiment. A chip whose layer 1 was baked at 180 ºC, tested under identical conditions, showed wrinkles 50–70 % smaller and the resistance changed by ~5 %. The wrinkles, however, could not be completely eliminated. This could be due to the fact that the rest of the layers are only post-baked at a maximum temperature of 100 ºC, suggesting a that those layers are significantly less rigid and more hydrophilic. Recall from Chapter 7 that it is temperature, not time, what makes a significant change in the crosslinking level of the polymer. Hard-baking all the layers at > 130 ºC could therefore improve these aspects.

Substrate	500 μm thick, 4” dia. test grade Si
KMPR layer 1	
Spin-coat	20 μm, 4000 rpm for 60 s
Soft-bake	100 ºC for 10 min
Exposure	1.33 J/cm^2 365 nm UV. Blanket-exposed.
Post-bake	150 ºC for 1 hr. Recently it was increased to 180 ºC for 1 hr
Metal deposition	
Cr Sputtering	50 nm. 8.5 mTorr Ar deposition pressure, 300 W. Protects KMPR from acetone during lift-off.
Cr lithography	1.25 μm thick HPR-504 positive photoresist, bake, expose to define heater shape, develop. Cr etch to allow Al heater to be directly deposited on KMPR.
Al sputtering	150–180 ± 10 nm. 1 μTorr base pressure, 7 mTorr Ar dep. pressure, 300 W.
Al Patterning	
Al lift-off	Sonicate in acetone for 5–10 min to remove remaining HPR-504 and Al on top.
Cr etch	Strip remaining Cr to leave the finalized Al heater on KMPR.
KMPR layer 2	
Spin coat	20 μm, 4000 rpm for 60 s
Soft-bake	100 ºC for 10 min
Exposure	1.33 J/cm^2 365 nm UV. The mask covers the heater contact pads (A–D).
Post-bake	100 ºC for 5 min
Development	Not developed yet
KMPR layer 3	
Spin coat	20 μm, 4000 rpm for 60 s
Soft-bake	100 ºC for 10 min
Exposure	0.60 J/cm^2 365 nm UV. The mask covers the chamber and channels.
Post-bake	100 ºC for 5 min
Development	MF-319 (SU-8 developer) for 8 min
2nd post-bake	100 ºC for 30 min (expected to increase crosslinking level)
KMPR layer 4	
Spin coat	25 μm, 4000 rpm for 60 s on PDMS-coated carrier wafer
Soft-bake	50 ºC for 10 min, 80 ºC for 10 min, 100 ºC for 20 min
Exposure	0.90 J/cm^2 365 nm UV. The mask covers the chamber and fluidic ports.
Post-bake	100 ºC for 5 min
Development	MF-319 (SU-8 developer) for 8 min
Bonding	Thermocompression. 10 kN, 100 ºC for 15 min. Release carrier.

Table 17. New Al/KMPR fabrication processes used in the work of Chapter 10 (section 10.6). The devices were fabricated by Matthew Reynolds and recently tested by him and David Sloan.

The lower soft-bake temperature for shorter time in the new process indicates that the content of solvent may be higher in the new KMPR. Since the solvent of KMPR (Cyclopentanone) is water-soluble, it may facilitate the transport of water into the polymer. This effect could be reduced with a more aggressive soft-bake of all layers (105 ºC for at least 20 min). The exposure of KMPR to the MF-519 may have also increased the wettability or water absorption capacity of KMPR.

The effects of this developer should be studied separately, e.g. through a contact angle analysis, and if necessary consider the use of a different developer.

Old Process	**New Process**
Chips withstood moisture at 80 ºC.	Chips did not withstand moisture at 80 ºC.
Device structure is one KMPR layer with Al on top.	Device structure is one KMPR layer with Al on top plus three KMPR layers on top of the Al.
Heater design is a single ring of 1.15 mm inner radius and 100 µm width.	Heater design is far more complex. Heaters are made of 48–58 parallel tracks distributed over a region of 750–1550 µm radius. Track width varies from 10.23 to 52.56 µm. There is significant coverage of Al outside the heater.
Al was patterned by contact lithography.	Al was patterned by lift-off.
KMPR was soft-baked at higher temperature for twice the time (105 ºC for 20 min)	KMPR layers 1–3 were soft-baked at 100 ºC for 10 min. Only KMPR layer 4 was soft-baked for longer time (it was baked on a ramp from 50 to 100 ºC along 40 min).
KMPR was hard-baked at 130 ºC.	KMPR layer 1 was hard-baked at 150 ºC or more, but the subsequent layers were not.
KMPR was not patterned, i.e. it was never exposed to MF-519 developer.	KMPR layer 1 was not patterned but all other layers were patterned and developed with MF-319.

Table 18. Major differences between the old and new Al/KMPR fabrication processes.

From these observations we expect that the process parameters can be tuned up to the point that water absorption will no longer be an issue. This will ensure high stability of the electrical properties of aluminum, enabling low cost PCR that could be fully integrated onto CMOS devices. Further investigation of the wrinkling phenomenon is underway and the use of impermeable coatings is being considered.

10.9 References

[1] D. S. Lee, S. H. Park, H. S. Yang, K. H. Chung, T. H. Yoon, S. J. Kim, K. Kim, and Y. T. Kim, “Bulk-micromachined submicroliter-volume PCR chip with very rapid thermal response and low power consumption,” *Lab on a Chip*, vol. 4, no. 4, pp. 401–407, 2004.

[2] T. Deng, M. Li, C. Zhao, J. Qin, C. Guo, and Z. Liu, “Characteristic investigation of a static micro polymerase chain reaction chip based on in situ electrochemical detection,” *IET Micro Nano Letters*, vol. 7, no. 12, pp. 1226–1229, 2012.

[3] B. Selva, P. Mary, and M.-C. Jullien, “Integration of a uniform and rapid heating source into microfluidic systems,” *Microfluidics and Nanofluidics*, vol. 8, no. 6, pp. 755–765, 2010.

[4] W. Jung, Y. W. Kim, D. Yim, and J. Y. Yoo, “Microscale surface thermometry using SU8/Rhodamine-B thin layer,” *Sensors and Actuators A: Physical*, vol. 171, no. 2, pp. 228–232, Nov. 2011.

[5] Q. Zhang, W. Wang, H. Zhang, and Y. Wang, “Temperature analysis of continuous-flow micro-PCR based on FEA,” *Sensors and Actuators B: Chemical*, vol. 82, no. 1, pp. 75–81, Feb. 2002.

[6] P.-C. Chen, D. Nikitopoulos, S. Soper, and M. Murphy, “Temperature distribution effects on micro-CFPCR performance,” *Biomedical Microdevices*, vol. 10, no. 2, pp. 141–152, Apr. 2008.

[7] H. Nagai, Y. Murakami, K. Yokoyama, and E. Tamiya, “High-throughput PCR in silicon based microchamber array,” *Biosensors and Bioelectronics*, vol. 16, no. 9–12, pp. 1015–1019, Dec. 2001.

[8] D. Erickson, D. Sinton, and D. Li, “Joule heating and heat transfer in poly(dimethylsiloxane) microfluidic systems,” *Lab Chip*, vol. 3, no. 3, pp. 141–149, Jul. 2003.

[9] L. Convert, V. Aimez, P. Charette, and R. Lecomte, “Rapid prototyping of integrated microfluidic devices for combined radiation detection and plasma separation,” in *Microsystems and Nanoelectronics Research Conference, 2008. MNRC 2008. 1st*, 2008, pp. 105–108.

[10] M. Reynolds, A. Elias, D. G Elliott, C. Backhouse, and D. Sameoto, “Variation of thermal and mechanical properties of KMPR due to processing parameters,” *Journal of Micromechanics and Microengineering*, vol. 22, no. 12, p. 125023, Dec. 2012.

[11] J. El-Ali, I. R. Perch-Nielsen, C. R. Poulsen, D. D. Bang, P. Telleman, and A. Wolff, “Simulation and experimental validation of a SU-8 based PCR thermocycler chip with integrated heaters and temperature sensor,” *Sensors and Actuators A: Physical*, vol. 110, no. 1–3, pp. 3–10, Feb. 2004.

[12] R. Mackay, H. Le, and R. Keatch, “Design optimisation and fabrication of SU-8 based electro-thermal micro-grippers,” *Journal of Micro - Nano Mechatronics*, vol. 6, no. 1, pp. 13–22, 2011.

[13] K. Colinjivadi, J.-B. Lee, and R. Draper, “Viable cell handling with high aspect ratio polymer chopstick gripper mounted on a nano precision manipulator,” *Microsystem Technologies*, vol. 14, no. 9, pp. 1627–1633, 2008.
[14] D. Tripathi, *Practical guide to polypropylene*. Shawbury, U.K.: Smithers Rapra Technology, 2002.
[15] W. M. Haynes and D. R. Lide, *CRC Handbook of Chemistry and Physics - A Ready-Reference Book of Chemical and Physical Data: 2011-2012*, 92nd ed. Boca Raton FL; London; New York: CRC Press, 2011.
[16] Y. S. Shin, K. Cho, S. H. Lim, S. Chung, S.-J. Park, C. Chung, D.-C. Han, and J. K. Chang, “PDMS-based micro PCR chip with Parylene coating,” *Journal of Micromechanics and Microengineering*, vol. 13, no. 5, pp. 768–774, Sep. 2003.
[17] S. A. Campbell, *The science and engineering of microelectronic fabrication*, 2nd ed. New York: Oxford University Press, 2001.
[18] D. R. Lide, *CRC Handbook of Chemistry and Physics*, 90th ed. Boca Raton, US: CRC Press, 2009.
[19] J. H. Lienhard and J. H. Lienhard, *A heat transfer textbook*. Mineola, N.Y.: Dover Publications, 2011.
[20] Fontes, J., “Temperature Sensors,” in *Sensor Technology Handbook*, 2005th ed., Oxford: J.S. Wilson, Elsevier Inc., pp. 531–562.
[21] K. Abdul-Jabbar N, “Natural convective heat transfer coefficient – a review: I. Isolated vertical and horizontal surfaces,” *Energy Conversion and Management*, vol. 42, no. 4, pp. 491–504, Mar. 2001.
[22] J. Martinez-Quijada, S. Caverhill-Godkewitsch, M. Reynolds, L. Gutierrez-Rivera, R. W. Johnstone, D. G. Elliott, D. Sameoto, and C. J. Backhouse, “Fabrication and Characterization of Aluminum Thin Film Heaters and Temperature Sensors on a Photopolymer for Lab-On-Chip Systems,” *Sensors and Actuators A: Physical*, vol. 193, pp. 170–181, Apr. 2013.
[23] D. Ross, M. Gaitan, and L. E. Locascio, “Temperature Measurement in Microfluidic Systems Using a Temperature-Dependent Fluorescent Dye,” *Anal. Chem.*, vol. 73, no. 17, pp. 4117–4123, Sep. 2001.
[24] E. . Wolff and D. . Schneider, “Prediction of thermal contact resistance between polished surfaces,” *International Journal of Heat and Mass Transfer*, vol. 41, no. 22, pp. 3469–3482, Nov. 1998.
[25] FLIR Systems, “SC5000 User Manual.” [Online]. Available: http://www.flir.com/. [Accessed: 12-Apr-2013].
[26] M. Kubenz, U. Ostrzinski, F. Reuther, and G. Gruetzner, “Effective baking of thick and ultra-thick photoresist layers by infrared radiation,” *Microelectronic Engineering*, vol. 67–68, pp. 495–501, Jun. 2003.
[27] B. Solano, S. Rolt, and D. Wood, “Thermal and mechanical analysis of an SU8 polymeric actuator using infrared thermography,” *Proceedings of the Institution of Mechanical Engineers, Part C: Journal of Mechanical Engineering Science*, vol. 222, no. 1, pp. 73–86, Jan. 2008.

[28] V. M. Blanco Carballo, J. Melai, C. Salm, and J. Schmitz, “Moisture resistance of SU-8 and KMPR as structural material,” *Microelectronic Engineering*, vol. 86, no. 4–6, pp. 765–768, Jun. 2009.

11 A CMOS-Ready PCR System

We believe that integration is the key to achieve the goals of LOC. Such an achievement would lead to the emergence of high quality medical services, based on fast, accurate and accessible genetic diagnosis tests. The technologies that we developed, particularly the robust thermal control, are the foundation of a highly advanced generation of LOC systems equipped with CMOS instrumentation. We have already demonstrated the viability of aluminum thin film heaters/sensors on KMPR, which ensures the compatibility of our polymer architecture with standard CMOS processes.

This chapter presents the preliminary design of our next LOC implementation: a CMOS-ready robust genetic analysis system. Such a system works the same way and follows exactly the same principles of the system presented in Chapter 10, i.e. it depends on a single dominant variable. However the system will be smaller, will have even higher tolerance to changes of the external environment, will consume less power and will be faster. Indeed, the system will have real potential to run the shortest PCR ever reported. It will also provide highly selective and uniform heating through the application of our hearer design method. Indeed, no changes in the algorithm or design flow will be necessary to obtain an optimal design. In addition, the design makes use of the *air bridge* concept, developed in our early designs in Chapter 6. The bridge limits the power consumption and voltage requirement to within 2W and 5 V, which will make it possible powering the system from a USB port, similarly as in the system presented in Chapter 4. A system with these characteristics is well beyond the state of the art.

The author modeled analytically and simulated the presented system and implemented the method described in Chapter 9 to obtain a preliminary design of the heater.

11.1 Design Considerations

This new design is intended to enable the fabrication of a PCR LOC system, made with our multilayer polymer structure, on a CMOS pre-processed substrate. The CMOS die will contain the electronics to drive the heater and perform 4-point temperature measurements. The die may also include subsystems for data acquisition, control, communication, etc., in addition to high voltage circuitry for CE and planar electromagnets for SP. Since the cost per unit area of CMOS wafer is high, the thermal system must be miniaturized to fit all these components while keeping low fabrication costs. Preliminary layouts of the CMOS die show that the heater/sensor is indeed the component most difficult to accommodate. The system is to be packaged in a USB key and run from the power and voltage provided by the USB port The CMOS circuitry, in addition, imposes a constraint of 3.4 V on the maximum voltage across the heater. Keeping a small heater/sensor area will be fundamental to meet these requirements.

In the design of Chapter 10 the power was controlled by means of a 20 µm thick KMPR layer (layer 1). The use of a polypropylene membrane increased substantially the total thickness of the structure (by ~30 %). This made it necessary to extend the heater radius by 350 µm beyond the edge of the chamber in order to maintain ± 1 ºC temperature uniformity, at the cost of higher power consumption. Reducing the heater area therefore requires thinning the entire structure, but thinning layer 1 would raise the power demand beyond the capacity of the USB port. To overcome this problem, we have introduced a thin air bridge in the system. The cross section of the system is shown in Figure 69.

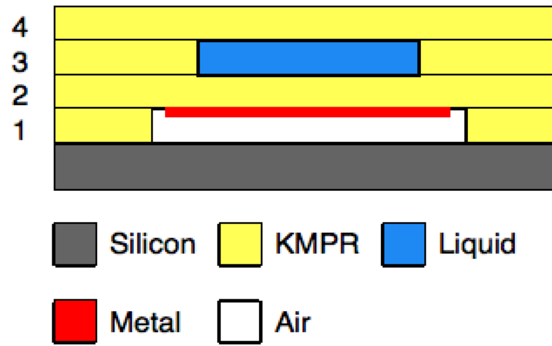

Figure 69. Cross section of the CMOS PCR system.

By thickening the bridge the power requirement could be made extremely small, but as we learned from Chapter 6, a thick bridge will also reduce the horizontal to vertical resistance ratio, elevating the lateral loss and cooling the edge. Compensating for this additional cooling would again require increasing the heater area. However, by using a thin bridge we ensure that the vertical conduction dominates. Simulation of this system has confirmed that it will behave just as the designs of the previous chapter, but with even better performance.

The use of the polypropylene membrane should be discontinued, as it would double the total thickness of the structure, increasing substantially the heater area. By increasing the heated area and adding a large thermal mass, the membrane would also slow down the response of the system. For this reason in the design presented here the membrane was removed and the top KMPR layer was left unpatterned to form a closed chamber. Filling of the chamber and other fluidic tasks will be carried out by means of built-in microvalves or an external hydraulic/pneumatic system. The use of microvalves would achieve the maximum level of integration and lowest cost per-device.

11.2 Preliminary Results and Specifications

The layers of the structure were made as thin as possible in order to minimize the lateral heat loss. Layer 2 was kept 20 μm thick to allow for a large volume of PCR brew. The new combination of layer thicknesses is (from layer 1 to 4): 2, 10, 20

and 10 μm. With a total thickness of 42 μm, the structure is only ~1/3 the thickness of the designs in Chapters 9 and 10. The new system is called NU 600.

In principle, the PCR chamber could be made very small to reduce the power requirements of the system. However, very small volumes of the PCR product may be excessively diluted when recovered from the chamber, weakening the signal strength in the CE detection stage. Another problem is the adsorption of reactants on the walls of the chamber, associated to high surface to volume ratios. For this reason the radius of the chamber *rc* was kept the same (500 μm) as for the NU 750 and U 850 designs.

As calculated in step 1 of our design flow, with the new thicknesses the heater radius *rh* for ± 1 ºC uniformity only needs to be extended by 100 μm beyond the chamber's edge, which results in a power consumption of ~1 W at 95 ºC. Running the calculation on a design that includes the polypropylene membrane shows that *rh* would need to be extended by additional 100 μm, increasing the power requirement to ~1.44 W (~ 50 % higher), meaning no gain with respect to the designs presented in chapters 9 and 10.

The parameters of the system in Figure 69 calculated using the analytical model of Chapter 10 are shown in Table 19. The resistance of the KMPR layer 1 has been replaced by the resistance of the airbridge, *Rb*. The properties of air used in the calculation are displayed in Table 20. Please refer to Chapter 10 for the properties of the other materials.

Parameter	Value	Units
rh	600	µm
Rh	1.58 x 10^5	K/W
R4	44.21	"
Rc	26.28	"
R2	44.21	"
Rb	58.95	"
R_{Si}	2.71	"
Th	95.03	ºC
Tc_T	94.98	"
H_{Up}	6.01 x 10^{-4}	W
H_T	1.06	"
Q	9.33 x 10^5	W/m^2
C4	2.04	10^{-5} J/K
Cc	9.46	"
C2	2.04	"
Cb	0.000264	"
C_{Si}	92.23	"
τ	~ 20	ms

Table 19. Parameters calculated in the analytical model of the system with *Tc* = 95 ºC, *Ths* = 30 ºC, *htc* = 5.6 W/m^2 K. The parameters C_{Si}*, Cb, C2, Cc* and *C4* are the heat capacities associated to the Si substrate, airbridge, layer 2, the chamber and layer 4, respectively. The parameter τ Is the time constant of the system.

Material	Thermal conductivity [W/m-K]	Mass Density [kg/m^3]	Specific Heat [J/kg-K]	Comment
Air	0.0264 @ 26.85 ºC [19] **0.030** @ 100 ºC 0.0335 @ 126.85 ºC [19]	**1.161** @ 300 K [19]	**1007** @ 300 K [19]	In simulation these properties are calculated pointwise as a function of temperature.

Table 20. Properties of air. The values in bold were used in analytical calculations.

Notice that despite the thinness of the air bridge, its resistance is the highest in the chip. In fact, the bridge largely controls the power demand of the system. Without the presence of the bridge, i.e. solid KMPR under the heater, the power requirement would be 5.63 W. The resistance due to convection *Rh*, being ~50 % higher than for NU 750 (the smallest previous design), indicates that this system will be more robust to external factors, including changes of airflow rate and ambient temperature. This increased *Rh* as well as the thinner layer 2 will likely improve the coupling of the chamber to the heater, and with this the measurement accuracy. In the previous work the *Tc*-*Th* coupling was 99.907 %, while in this design is 99.955 %, as calculated analytically. The power density in the inner

regions of the heater will increase from 6.32 x 10 ^{5} W/m^{2} to 9.33 x 10 ^{5} W/m^{2} in this design, because the 2 µm bridge presents lower resistance per unit area than the 20 µm KMPR used previously for layer 1.

Compared to the previous designs, the system will be substantially faster because: (1) the thermal mass of the membrane was removed; (2) the thermal mass of layers 2 and 4 is significantly smaller; (3) the capacity under the heater *Cb* is four orders of magnitude smaller than that of the previous designs (called *C1*); (4) the heated volume is reduced. This combination will shorten the transient equilibrium time from 0.32 s to ~0.1 s, as calculated analytically and confirmed by simulation. Calculated as in Chapter 10 (for SpeedSTAR™ polymerase), the total time for 35-cycle, 3-step PCR would be 2 min 30 s. This is only 10 s faster than previous designs, but shows that for the first time the total PCR time will no longer be limited by the heating/cooling transients, but may only depend on the processing speed of the polymerase.

Since the air bridge is the dominant resistance in the downward direction, changes of its thickness will significantly affect temperatures. The thickness of the bridge may change due to the pressure generated in the PCR chamber during thermal cycling. This pressure would tend to deflect the diaphragm under the chamber (layer 2), producing a cold spot at the center, and hence a substantial loss of uniformity. Other factors such as thermal expansion can also buckle the diaphragm during operation. In addition, during fabrication the diaphragm could be distorted permanently to a random shape, rendering a bridge with different thicknesses. To overcome these problems and obtain repeatable thickness (and temperatures), an array of KMPR pillars is to be fabricated within the bridge. The number and area of the pillars must be carefully chosen in order to keep a low power requirement, which will translate into low current densities. A large number of pillars could deteriorate temperature uniformity. We estimated that the power density on a KMPR pillar will be ~6 times higher than in the 'air' arias

We estimated through a structural mechanics simulation that for a 1 atm pressure in the chamber, an array of 3 x 5 µm pillars spaced on a 100 µm square grid will suffice to prevent deflections of the diaphragm greater than 0.05 µm. The total area of the pillars represents ~ 1 % of the bridge area. Therefore the presence of the pillars will have minor effect on the power and average temperature levels. The local heat loss through the pillars, however, is significant and must be compensated to maintain temperature uniformity.

As this technology moves close to manufacture, the developed heater design method and software tools are being applied to prototype the NU 600 and other heaters for the new CMOS system. Figure 70 shows the power density field for NU 600 resulting from step 1 of our method. Figure 71 shows the heater layout resolved by the algorithm in step 2 of the method. Note that the algorithm thins down the tracks at the pillar locations to a precise width to compensate for the higher heat loss at those points. The next step in the design would be grouping the tracks to reduce the current density levels down to ~25 mA/µm^2, or less. We previously demonstrated that the lifetime of the Al film at these current densities is more than enough to run a PCR. After grouping the tracks the design will be essentially completed. Simulating the full heater layout embedded in a 3D model of the system (step 3 of the process) should show approximately ± 1 ºC uniformity, as it was normally the case in the designs of chapters 9 and 10. Depending on the results the pillar locations may need to be adjusted, but an optimal design should be reached within two iterations of the thermal and structural designs.

From these preliminary results we believe that this system may become the first manufacturable and robust LOC implementation on CMOS. By extrapolating the results from the work presented in Chapters 9 and 10, we expect that this design will perform as per simulation. The experimental results for this system will be reported on by others.

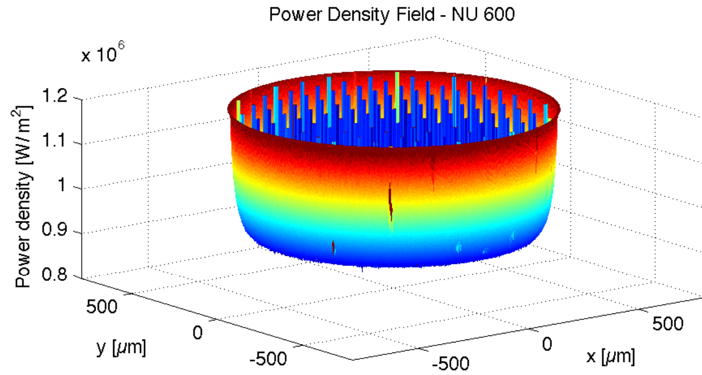

Figure 70. Heat flux along the surface of the ideal NU 600 heater. This is the power density field necessary to maintain uniform temperature in the PCR chamber of the LOC CMOS system. The exponential increment of power density towards the edge compensates for the high losses at the heater's edge. The heat loss at the pillar locations is also compensated with sharp power steps.

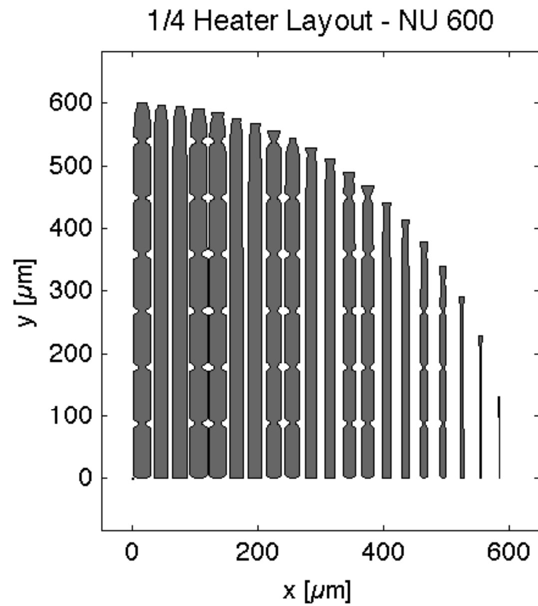

Figure 71. Automatically generated NU 600 heater tracks for the CMOS PCR system. The algorithm compensates for the high heat loss through the pillars by thinning the tracks at the pillar locations. This design demonstrates the flexibility of our heater design method.

12 Conclusions

Most LOC systems to date face two central problems: a vulnerability to external variables that are difficult to measure and control; and the measurement uncertainty due to the observer effect and poor sensor-to-chamber coupling. These issues derive into a need for costly infrastructure and complex per-device or per-instrument calibration procedures. As a consequence, LOC systems in general are not manufacturable.

In this work we developed several new technologies to address these problems. Notably, we presented a novel robust thermal management approach to build LOC systems with the ability to operate repeatably in uncontrolled environments. This robustness was achieved by making the system dependent upon a single variable that dominates over all those variables that are difficult to control. As a result, run-to-run repeatability is ensured without the need for lab infrastructure or hardware, specialized in keeping stable external conditions. External variables can still shift slightly the system temperatures. These shifts, however, can be rapidly detected and compensated for with an uncomplicated closed loop controller, effectively eliminating any external influence. The key to rapid and accurate compensation is the strong coupling of the built-in heater/sensor to the reaction chamber. In fact, this coupling is so strong that *Tc* can be known accurately from *Th* regardless of changes of the external environment. Therefore, complicated or Invasive calibration methods that suffer from the observer effect are no longer required.

The system can be seen as a closed universe with a small, clearly defined, connection to the macro-world. Within this universe there are variables that can also affect the system, such as layer thickness and material properties, but differently from the outside variables, internal variables can be controlled with high precision in the cleanroom. The system is made in a lithography-based

multilayer polymer process that allows for controlling layer thicknesses and alignment precisely. This leaves the TCR of the heater/sensor metal film being the most influential internal variable, which we expect can be stabilized within less than 1.7 % in the industrial setting. Thus, once the TCR is under control, the fabricated devices will all be essentially the same. We estimated that if the TCR varies across devices by 1 %, *Tc* can be known within a ±0.73 ºC uncertainty. With this, calibrating one device in dozens or hundreds could potentially be enough to calibrate the entire batch. Moreover, since *Tc* and *Th* are so close, the calibration will simply consist on measuring the resistance of the heater at different temperatures. *Tc* can them be mapped from *Th* with a small correction obtained by simulation.

In the first part of this research we underwent a learning process to identify the major limitations of the standard thermal control approach. Along this process several designs were presented, including a PCR device that enabled some of the smallest genetic analysis instruments reported to date, which in addition can be powered from a USB port. That PCR device, however, still suffered from the problems of the standard thermal control approach. One of such problems is to estimate the true *Tc* from a measurement that has been biased by the observer effect. A method that corrected for the observer effect was then developed, resulting in a significant improvement in the PCR efficiency and reproducibility. We understood, however, that a manufacturable robust system should be designed in a way that the calibration complexity is removed, and this would require solving the core problem: the distant heater-chamber relation.

The work done throughout this research enabled a large number of new alternate projects and demonstrations in our group. The latest achievements presented here will provide a solid foundation for our group to continue on developing more advanced LOC technologies.

Moving towards manufacture, we developed a new multilayer polymer chip architecture and its associated process. Being entirely based on lithography and standard microfabrication steps, the process yields highly repeatable, affordable, batch-producible devices that can be fabricated onto a CMOS substrate. The designs made in this chip architecture showed that it allows for more efficient thermal control. We introduced the concept of air bridges, which achieve high levels of thermal isolation within very thin structures. With air bridges we designed a viable flow-through PCR system that would be remarkably easy to control and fabricate, and could certainly be the beginning of a new research branch in our group. In these initial designs we discovered that thinning the structure would tightly constrain the heated area, yielding a high level of robustness as well as uniform, selective heating. We also understood the urgent need for deterministic methods to design thin film heaters. However, to make this polymer technology affordable and eventually move it to a CMOS process, those heaters would need to be made in a non-noble metal, such as TiW or Al.

We then developed a polymer metallization method to fabricate Al heaters/sensors on KMPR and treat them for stability. Many favorable characteristics of the Al-KMPR system were documented, including strong adhesion to KMPR, mechanical/electrical stability at high temperatures, and a resistance to electromigration high enough to sustain a PCR reaction. Aluminum was then found to be a viable substitute for platinum, which has been used in the LOC community for decades.

An automated heater design method was developed to produce a controlled spatial distribution of heat that creates a highly uniform temperature environment in our devices. This uniformity is key to efficient and reliable PCR reactions, as well as to the accurate measurement of temperatures. A fundamental feature of this method is that allows for reducing the current density on the heater to levels that aluminum can withstand, giving the device more than enough lifetime to perform a PCR reaction. The high flexibility of the developed design tools allows for rapid

prototyping of system-customized heaters of arbitrary size and shape and complex temperature/power-density patterns. With such a flexibility, optimal heaters for the flow-through PCR design presented in Chapter 6 could be generated in few minutes. The heaters in that design require either three distinct contiguous temperature zones or a linear temperature ramp. The CMOS LOC system presented in Chapter 11 requires a heater that compensates for the high heat loss caused by the pillars that support the airbridge structure. With the developed tools, prototyping all those heaters now seems highly feasible and straight forward.

These tools enabled us to build a truly robust thermal control system, presented in Chapter 10. Prior to fabrication, the system was designed through analytical models and thoroughly tested via simulation. Devices of different size and power density profiles were fabricated. All the designs showed approximately ± 1 ºC temperature uniformity in simulation, demonstrating that our tools can generate heaters that produce user-defined temperature/power-density profiles repeatably. The rigorous design process resulted in fabricated devices that worked as per simulation at the first trial.

Through a set of simple experiments we demonstrated the thermal and electrical functionalities of the system. IR imaging of the powered system showed highly selective heating, which is an important part of the robustness of the system. This selectivity potentially enables the integration of multiple PCR chambers in a single chip. A repeatability test and calibration revealed highly linear and stable resistance vs. temperature characteristics. A lifetime test at full power demonstrated that the devices can safely run PCR with an aluminum heater. The experiments in general were remarkably consistent with simulation and with previous experiments on Al films on KMPR. Our current fabrication process leads to a KMPR that does not resist the combination of moisture and high temperatures, resulting in deterioration of the Al film (for details please refer to Appendix C: Moisture Sensitivity). We expect that the process parameters can be

tuned to the point that this moisture sensitivity will no longer be an issue. Further testing of the thermal system as well as the PCR performance will be demonstrated by others.

We also demonstrated that the heater can be used as a sensor despite its complex geometry. Analytical and numerical calculations revealed that, if the moisture sensitivity issue were solved, the system would allow for robust thermal control at very high speeds, possibly requiring only 3 min to run a 35-cycle 3-step PCR. To our knowledge such a short time has only been achieved in truncated 2-step PCR. Remarkably, this speed could be achieved without an elaborate 'overshooting' controller, due to the rapid natural response of the system. A simpler controller algorithm will then reduce the memory and processing power requirements, allowing for cheaper and smaller electronics and easier CMOS integration. We seem to have reached the point were making the transient shorter will no longer yield faster PCR, since the reaction time would mostly be dictated by the DNA building speed of the polymerase. So far the long transient times of thermal systems in static LOC PCR have been considered in literature as the major limitation for PCR speed, which motivated the development of alternatives such as continuous-flow PCR. We also explored this approach in section 6.2 using our multilayter polymer chip architecture.

These results give us the confidence to believe that our designs can be batch fabricated with standard process steps onto a CMOS substrate. The resulting LOC CMOS unit, will be ~ 5 x 5 mm or smaller. We have already made a preliminary design of this device, which predicts a highly robust and fast behavior, and shows the feasibility of integrating an air bridge in the system. This bridge will reduce the power/voltage requirements of the system to fit comfortably within the capabilities of the USB interface, which will enable the construction of the first genetic analysis instruments fully contained in a USB key. Owing to the robustness of the thermal system, the designer of genetic diagnosis tests will be able to concentrate on the biochemistry aspects of the PCR reaction, rather than

on stabilizing the instrument and creating repeatable conditions. The only major infrastructure required by the thermal system will be a regular commercial-grade heatsink. The final user will insert a chip in a portable instrument that will self-calibrate. From a tiny drop of the clinical sample, the user will obtain in few minutes an accurate diagnosis, even under extreme ambient conditions.

We believe that this work represents a new state of the art in LOC thermal control, and it may greatly contribute to consolidate the LOC technology, someday making human life longer, healthier and happier.